TECHNISCHE UNIVERSITÄT MÜNCHEN

Ingenieurfakultät Bau Geo Umwelt

Lehrstuhl für Statik

MODELING AND SIMULATION OF WIND-STRUCTURE INTERACTION OF SLENDER CIVIL ENGINEERING STRUCTURES INCLUDING VIBRATION MITIGATION SYSTEMS

Andreas Winterstein

Vollständiger Abdruck der von der Ingenieurfakultät Bau Geo Umwelt der Technischen Universität München zur Erlangung des akademischen Grades eines

Doktor-Ingenieurs

genehmigten Dissertation.

Vorsitzender:

Prof. Dr.-Ing. habil. Michael Manhart

Prüfer der Dissertation:

1. Prof. Dr.-Ing. Kai-Uwe Bletzinger
2. Prof. Dr. Rainald Löhner
3. Prof. Riccardo Rossi, Ph.D.

Die Dissertation wurde am 07.04.2020 bei der Technischen Universität München eingereicht und durch die Ingenieurfakultät Bau Geo Umwelt am 17.09.2020 angenommen.

Schriftenreihe des Lehrstuhls für Statik TU München

Band 44

Andreas Winterstein
(Geb. Mini)

MODELING AND SIMULATION OF WIND-STRUCTURE INTERACTION OF SLENDER CIVIL ENGINEERING STRUCTURES INCLUDING VIBRATION MITIGATION SYSTEMS

München 2020

Veröffentlicht durch

Kai-Uwe Bletzinger
Lehrstuhl für Statik
Technische Universität München
Arcisstr. 21
80333 München

Telefon: +49(0)89 289 22422
Telefax: +49(0)89 289 22421
E-Mail: kub@tum.de
Internet: www.bgu.tum.de/st

ISBN: 978-3-943683-61-5

für Elisabeth und unsere Tochter Anna

Abstract

This thesis deals with the multiphysics problem of wind-structure interaction of civil engineering structures, including vibration mitigation systems, to reduce wind-induced vibrations. The work is subdivided into two major parts.

The first part presents the solution of the general fluid-structure-control interaction problem by an iterative, partitioned approach, utilizing Gauss-Seidel formulations. Therefore, the fluid-structure interaction (FSI) problem is extended by a control unit, which is actively influencing the dynamics of the structure. The behavior and sensitivity of the fluid-structure-control interaction problem are investigated by a simplified model problem. Based on this simplified model problem, three different algorithmic variants for the coupling of fluid flow, structure, and controller in a partitioned way by a Gauss-Seidel scheme are derived. Finally, the resulting algorithms are applied to a complex, nonlinear, multi-degree of freedom problem. This benchmark problem is well-tested for FSI and is thus extended to fluid-structure-control interaction. It is demonstrated, that the flow-induced structural vibrations can be reduced significantly by actively influencing the structure's dynamics with a controller.

In the second part, the newly developed methods and general findings from the first part are applied to high-rise, tower-like structures from civil engineering subjected to wind. Those structures are a television tower and an elevator test tower. To further validate the simulation environment, the results of fully coupled FSI simulations for the television tower are compared to on-site measurements. Finally, the findings from the numerical studies for the television tower, combined with the best variant of the algorithms presented in the first part of this work, are applied to the elevator test tower simulation. This tower is equipped with a hybrid mass damper, which is utilized to reduce wind-induced vibrations but can also be used to actively excite tower oscillations. Different configurations of the elevator test tower are modeled and investigated by the algorithms and concepts developed throughout this work.

Zusammenfassung

Diese Arbeit behandelt das multiphysikalische Problem der Wind-Struktur-Interaktion von Strukturen des Bauingenieurwesens, inklusive Systemen zur Reduktion windinduzierter Schwingungen. Die Arbeit ist in zwei wesentliche Teile gegliedert:

Im ersten Teil wird die Lösung des generellen Fluid-Struktur-Regelungs-Interaktions Problems mit einem iterativen, partitionierten Ansatz unter der Verwendung einer Gauß-Seidel-Formulierung vorgestellt. Dafür wird das FluidStruktur-Interaktions (FSI) Problem mit einem Regler, der aktiv die Dynamik der Struktur beeinflusst, erweitert. Das Verhalten und die parametrische Sensitivität des Problems der Fluid-Struktur-Regelungs-Interaktion (FSCI) wird anhand eines vereinfachten Modellproblems untersucht. Auf Basis dieses vereinfachten Modellproblems werden drei verschiedene Varianten für einen Algorithmus zur partitionierten Kopplung von Fluid, Struktur und Regelung mit einem Gauß-Seidel Verfahren abgeleitet. Letztlich werden diese Algorithmen auf ein komplexes, nichtlineares Mehrfreiheitsgrad Problem angewandt. Bei diesem Problem handelt es sich um ein vollumfänglich getestetes Beispiel aus dem Bereich der FSI, das entsprechend für die FSCI erweitert wird. Es wird gezeigt, dass die fluid-induzierten Strukturschwingungen durch die aktive Beeinflussung der Strukturdynamik durch einen Regler stark reduziert werden können.

Im zweiten Teil werden die neu entwickelten Verfahren und generellen Ergebnisse aus dem ersten Teil auf hohe, turmartige Strukturen aus dem Bauingenieurwesen unter Windeinwirkung angewandt. Es handelt sich dabei um einen Fernsehturm und einen Aufzugstestturm. Zur weiteren Validierung des Simulationskonzepts werden die Ergebnisse von voll gekoppelten FSI Simulationen für den Fernsehturm mit Messungen vor Ort verglichen. Schließlich werden die Erkenntnisse der numerischen Studien für den Fernsehturm in Kombination mit der besten Variante des Algorithmus, der im ersten Teil dieser Arbeit vorgestellt wurde, für die Simulation des Aufzugstestturms verwendet.

Dieser Testturm ist mit einem hybriden Massendämpfer ausgestattet, der zur Reduktion windinduzierter Schwingungen eingesetzt wird. Der hybride Massendämpfer kann aber auch dazu verwendet werden, den Turm aktiv zu Schwingungen anzuregen. Verschiedene Konfigurationen des Aufzugstestturms werden mit den in dieser Arbeit entwickelten Verfahren modelliert und untersucht.

Acknowledgments

This work would not have been possible without the support of several people and institutions. First of all, I want to thank Prof. Dr.-Ing. Kai-Uwe Bletzinger for the opportunity to work as a member of the Chair of Structural Analysis and the freedom to work on this thesis. I want to thank my mentor PD Dr.-Ing. habil. Roland Wüchner for his guidance and all the discussions. I thank the examiners for their effort in reviewing my thesis. I especially thank all my colleagues and students at the Chair of Structural Analysis and the International Centre for Numerical Methods in Engineering (CIMNE) in Barcelona for the motivation and excellent collaboration. I gratefully acknowledge the Gauss Centre for Supercomputing e.V. (www.gauss-centre.eu) for funding this thesis by providing computing time on the GCS Supercomputer SuperMUC-NG at Leibniz Supercomputing Centre (www.lrz.de).

Ich danke allen, die meine Träume belächelt haben.
Sie haben meine Phantasie beflügelt.

Ich danke allen, die mich in ihr Schema pressen wollten.
Sie haben mich den Wert der Freiheit gelehrt.

Ich danke allen, die mich belogen haben.
Sie haben mir die Kraft der Wahrheit gezeigt.

Ich danke allen, die nicht an mich geglaubt haben.
Sie haben mir zugemutet, Berge zu versetzen.

Ich danke allen, die mich abgeschrieben haben.
Sie haben meinen Mut geweckt.

Ich danke allen, die mich verlassen haben.
Sie haben mir Raum gegeben für Neues.

Ich danke allen, die mich verraten und missbraucht haben.
Sie haben mich wachsam werden lassen.

Ich danke allen, die mich verletzt haben.
Sie haben mich gelehrt, im Schmerz zu wachsen.

Ich danke allen, die meinen Frieden gestört haben.
Sie haben mich stark gemacht, dafür einzutreten.

Ich danke allen, die mich verwirrt haben.
Sie haben mir meinen Standpunkt klar gemacht.

Vor allem aber danke ich all jenen,
die mich lieben, so wie ich bin.
Sie geben mir die Kraft zum Leben!
DANKE

von Paulo Coelho

Andreas Winterstein im April, 2020

Contents

Contents **xiii**

List of Abbreviations **xvii**

List of Symbols **xix**

1 Introduction **1**
1.1 Background and Motivation 1
1.2 Previous Related Studies 2
1.3 Starting Point and Goals of the Thesis 3
1.4 Present Contributions 4
1.5 Outline of the Thesis 6

2 Theoretical Background **9**
2.1 Computational Structural Dynamics (CSD) 10
2.1.1 Dynamic Eigenvalue Analysis 13
2.1.2 Finite Element Formulations 14
2.1.2.1 Shell Elements 15
2.1.2.2 Beam Elements 15
2.1.2.3 Plane Stress Plate Elements 16
2.2 Computational Fluid Dynamics (CFD) 16
2.3 Control Theory for Structural Systems (SC) 20
2.3.1 Description of Mechatronic Systems 20
2.3.2 Open- and Closed-Loop Control 21

2.3.3 System Representation in the Frequency and the Time Domain 24
2.3.4 Controller Design 26
2.3.5 Stability Considerations and Important Definitions 26
2.4 Fluid-Structure Interaction (FSI) 29
2.4.1 Communication Pattern 32
2.4.2 Mapping 35
2.4.3 Mesh Motion 36
2.4.4 Notation for Coupled Problems 38
2.5 Time Integration 39
2.6 Software Environment and Simulation Time 41

3 Fluid-Structure-Control Interaction 43
3.1 The Simplified Model Problem 44
3.1.1 Monolithic Approach 46
3.1.1.1 Analysis of the Time-Continuous Problem 46
3.1.1.2 Analysis of the Time-Discrete Problem 47
3.1.2 Partitioned Approach 48
3.2 Extension of the Notation for the FSCI Problem . . 51
3.3 Alternatives of the Gauss–Seidel Pattern for Three Different Physical Fields 53
3.3.1 No Nesting FSCI 53
3.3.2 Nesting of the FSI Sub-Problem ([FS]CI) . . 55
3.3.3 Nesting of the SCI Sub-Problem (F[SC]I) . . 59
3.4 Numerical Results for a Multi-Degree of Freedom FSCI Problem 64
3.4.1 Description of the Subsystems Involved . . . 65
3.4.2 Residual Calculation and Numerical Accuracy 73
3.4.3 Presentation and Interpretation of the Results 75
3.5 Chapter Summary 79

4 The Numerical Wind Tunnel for Civil Engineering Structures 81
4.1 Characteristic Dimensionless Numbers and Coefficients 82
4.2 Numerical Generation of Natural Wind 83

4.3 Wind Effects on High-Rise Civil Engineering Structures . . . 88
4.4 Basic Convergence and Validation Study . . . 89
4.5 The Olympic Tower in Munich . . . 93
4.5.1 Numerical Wind Generation for the Wind Acting on the Olympic Tower in Munich . . . 93
4.5.2 CSD Model of the Olympic Tower in Munich 98
4.5.3 FSI Simulations of the Olympic Tower in Munich . . . 102
4.5.4 Acknowledgments . . . 110
4.6 The thyssenkrupp Elevator Test Tower in Rottweil . 110
4.6.1 Wind Conditions for the thyssenkrupp Elevator Test Tower . . . 111
4.6.2 CSD Model of the thyssenkrupp Elevator Test Tower . . . 116
4.6.3 Wind Effects on the thyssenkrupp Elevator Test Tower . . . 122
4.6.4 FSI Simulations thyssenkrupp Elevator Test Tower . . . 123
4.6.5 CFD vs. FSI and Weak vs. Strong Coupling . 134
4.6.6 Artificial Oscillations and Oscillation Reduction of the thyssenkrupp Test Tower . . . 136
4.6.7 Procedure for the Numerical Wind Generation 142
4.6.8 Acknowledgments . . . 145
4.7 Chapter Summary . . . 145

5 Conclusions and Outlook 149

A Algorithms 151

B Calculation of Descriptive Statistics 159
B.1 Mean Value . . . 159
B.2 Median Value . . . 159
B.3 Root Mean Square (RMS) . . . 160
B.4 Standard Deviation . . . 160
B.5 Spectral Density . . . 160
B.6 Auto Correlation . . . 160

C Integral Transform Methods 161
C.1 The Laplace-Transform . . . 161
C.1.1 Differentiation . . . 162

C.1.2 Integration 162
C.2 The Z-Transform 163

D Dynamic System Modeling in Control Theory 165
D.1 Modeling in the Frequency Domain 166
D.2 Modeling in the Time Domain 169

Bibliography 171

List of Abbreviations

AE	algebraic equation
ABL	atmospheric boundary layer
ALE	arbitrary Lagrangian-Eulerian
AMSL	above mean sea level
BDF	backwards differentiation formula
BIBO	bounded input bounded output
BIM	building information modeling
CFD	computational fluid dynamics
CGL	geometric conservation law
CSD	computational structural dynamics
CR	corotational
CWE	computational windengieering
DFT	discrete Fourier transform
dfvb	”Drachenfliegerverein Bösingen”
DSG	discrete shear gap
EICR	element-independent corotational
FEM	finite element method
FFT	fast Fourier transform
FSCI	fluid-structure-control interaction
FSI	fluid-structure interaction
FS	fluid-structure
GCL	geometric conservation law
GL	Green-Lagrange
GS	Gauss-Seidel
HMD	hybrid mass damper

J	Jacobian
LES	large eddy simulation
LQR	linear-quadratic regulator
LTI	linear time-invariant
MIMO	multiple-input multiple-output
M50	measurement number 50
NSE	Navier-Stokes equations
ODE	ordinary differential equation
OT	Olympic Tower in Munich
PDE	partial differential equation
PSD	Power Spectral Density
PVW	principle of virtual work
PK2	second Piola-Kirchhoff
SC	structural control
SCI	structure-control interaction
SDoF	single-degree of freedom
SISO	single-input single-output
SWM	Stadtwerke München
TkT	thyssenkrupp test tower in Rottweil
VMS	variational multiscale method

List of Symbols

$(\cdot)_{\mathrm{B}}$	value of the state observer
$(\cdot)_{\mathrm{C}}$	property of the control subsystem
$(\cdot)_{\mathrm{CG}}$	value for galloping
$(\cdot)_{\mathrm{D}}$	property of the Dirichlet boundary
$(\cdot)_{\mathrm{F}}$	property of the fluid subsystem
$(\cdot)_{\mathrm{FS}}$	property of fluid-structure coupling
$(\cdot)_{\mathrm{FSI}}$	property of fluid-structure interaction
$(\cdot)_{\mathrm{FSCI}}$	property of fluid-structure-control interaction
$(\cdot)_{\mathrm{GL}}$	Green-Lagrange
$(\cdot)_{\mathrm{I}}$	property of the interface
$(\cdot)_{\mathrm{N}}$	property of the Neumann boundary
$(\cdot)_{\mathrm{M}}$	property of the mesh
$(\cdot)_{\mathrm{PK2}}$	second Piola-Kirchhoff
$(\cdot)_{\mathrm{S}}$	property of the structural subsystem
$(\cdot)_{\mathrm{SC}}$	property of structure-control coupling
$(\cdot)_{\mathrm{cm}}$	secant value
$(\cdot)_{\mathrm{crit}}$	critical value
$(\cdot)_{\mathrm{ext}}$	external
$(\cdot)_{\mathrm{g}}$	equilibrium
$(\cdot)_{i}$	i^{th} vector component
$(\cdot)_{\mathrm{int}}$	internal
$(\cdot)_{\mathrm{kin}}$	kinematic
$(\cdot)_{\mathrm{lin}}$	linearized value
$(\cdot)_{\mathrm{max}}$	maximum value
$(\cdot)_{\mathrm{meas}}$	measured value
$(\cdot)_{\mathrm{norm}}$	norm value

$(\cdot)_{\mathrm{opt}}$	optimal value
$(\cdot)_{\mathrm{ref}}$	reference value
$(\cdot)_{\mathrm{x}}$	x-value
$(\cdot)_{\mathrm{y}}$	y-value
$(\cdot)^{h}$	approximated values in the FEM context
$(\cdot)^{\mathrm{init}}$	initial value
$(\cdot)^{n}$	n^{th} time step
${}^{k}(\cdot)$	k^{th} iteration
${}_{l}(\cdot)$	l^{th} iteration
${}_{1}(\cdot)$	unrelaxed value
${}_{\beta}(\cdot)$	relaxed value
$\widetilde{(\cdot)}$	median value; approximated value of the state observer
$\hat{(\cdot)}$	approximation in the general context
$\overline{(\cdot)}$	mean value
$(\cdot)'$	fluctuating part
$(\cdot)_{\perp}$	value perpendicular to streamwise direction
$\dot{(\cdot)}$	first derivative w.r.t. time
$\ddot{(\cdot)}$	second derivative w.r.t. time
Δ	difference of two scalars or vectors, second derivative
Γ	domain boundary
Λ	logarithmic decrement
Ω	domain
α	mass ratio; exponent for power law
α_{R}	Rayleigh coefficient
β	relaxation parameter
β_{crit}	critical relaxation parameter
β^{*}	optimal relaxation parameter
β_{R}	Rayleigh coefficient
δ	Dirac delta function
δt	discrete time step
δW	virtual work
ε	error
φ	rotation angle; phase angle
γ	scaling factor
η	exponent for mesh motion, principal axes
λ	Lamé constant, eigenvalue
μ_{F}	dynamic viscosity
μ	mass ratio ${}^{m_D}/_{m_H}$; Lamé constant
μ_{S}	distributed sectional mass
ν_{F}	kinematic viscosity

ν_S	Poisson's ratio
ω	circular eigenfrequency
ω_i	i^{th} circular eigenfrequency
ρ	density, spectral radius
ξ	principal axes
∇	gradient operator
$\nabla\cdot$	divergence operator
A	area; with an index iteration factor
D	damping ratio, Lehr's damping
$\mathrm{C_d}$	drag coefficient
E	Young's modulus
$\overline{E}$	modified Young's modulus
$\widetilde{EI}$	distributed sectional stiffness
F_G	gravity force
F_{in}	inertia force
F_{rad}	radial force component
F_{tan}	tangential force component
$\hat{F}$	general external force
$\hat{F}_M$	actuator force
G	transfer function
I	turbulence intensity for one component of $\boldsymbol{u}_\mathrm{F}$
J	quadratic cost functional
K	inverse scalar stiffness $^1/_k$
L	turbulence length for one component of $\boldsymbol{u}_\mathrm{F}$
M	reaction moment
Ma	Mach number
N_dof	number of degrees of freedom
R	reaction force
Re	Reynolds number
Sc	Scruton number
St	Strouhal number
T	final time or oscillation period
T_0	initial time
T_phys	physical time
U	system input or manipulation variable in frequency domain
V	amplification function
Y	system output or controlled variable in frequency domain

a_G	stability parameter for galloping
b	characteristic length
c	scalar damping coefficient
d	degree of stability
e	error signal
c_{air}	speed of sound in air
f	frequency
f_i	i^{th} eigenfrequency
g	gravity constant ($g = 9.81\,\mathrm{m}/\mathrm{s}^2$)
h	height
i	complex unit $i = \sqrt{-1}$
k	scalar stiffness
k_{R1}	constant controller parameter
k_{R2}	constant controller parameter
ℓ	length
m	scalar mass or controller output variable
m_D	HMD mass
$m_{i,e}$	equivalent structural mass per unit length
m_H	relevant mass of the structure
n_i	grid points
p	pressure
r	feedback variable
r_i	grid exponent
s	$s \in \mathbb{C}$, i.e. $s = a + bi$
t	time
t	thickness
u	system input or manipulation variable
w	reference variable
w	width
y	system output or controlled variable
z	z from Z-transform; disturbance variable
z_0	roughness height
z_{ref}	reference height for inlet generator
$\mathcal{G}$	system transfer operator
$\mathcal{I}$	interface constraint operator
$\mathcal{L}$	Laplace transform operator
$\mathcal{M}$	mapping operator
$\mathcal{R}$	residual operator
$\mathcal{Z}$	Z-transform operator

$\mathbb{C}$	space of complex numbers
$\mathbb{R}$	space of real numbers
$\|\| \ \|\|$	L^2-norm
$\boldsymbol{A}$	system matrix; iteration matrix
$\boldsymbol{B}$	input matrix
$\boldsymbol{C}$	system damping matrix; output matrix
$\boldsymbol{\mathcal{C}}$	material tensor
$\boldsymbol{D}$	direct input-output matrix
$\boldsymbol{H}$	mapping matrix
$\boldsymbol{M}$	system mass matrix
$\boldsymbol{N}$	shape functions
$\boldsymbol{K}_e$	elastic system stiffness matrix
$\boldsymbol{K}_{\mathrm{eff}}$	effective system stiffness matrix
$\boldsymbol{K}_{\mathrm{dyn}}$	dynamic system stiffness matrix
$\boldsymbol{K}_g$	geometric system stiffness matrix
$\boldsymbol{K}_T$	tangent system stiffness matrix
$\boldsymbol{K}_u$	initial system displacement matrix
$\boldsymbol{\mathcal{R}}$	residual vector
$\boldsymbol{X}$	reference coordinate
$\boldsymbol{b}$	vector of constant values during iteration; right hand side
$\mathbf{b}$	vector of body forces
$\boldsymbol{d}$	vector of nodal displacements with components $[u, v, w]^T$
$\mathbf{d}$	vector of displacements with components $[u, v, w]^T$
$\delta\mathbf{d}$	vector of virtual displacements
$\boldsymbol{f}$	vector of nodal forces
$\boldsymbol{n}$	surface normal vector
$\boldsymbol{q}$	general vector of nodal unknowns
$\mathbf{u}$	vector of velocities with components $[u, v, w]^T$
$\boldsymbol{u}$	input vector
$\mathbf{w}$	vector of convective velocities
$\boldsymbol{x}$	state vector
$\boldsymbol{x}_0$	initial state vector
$\boldsymbol{y}$	output vector
$\boldsymbol{z}$	vector of disturbance forces
ε	strain tensor
$\boldsymbol{\delta\varepsilon}$	virtual strains
$\boldsymbol{\Phi}$	modal matrix
$\boldsymbol{\varphi}$	eigenvector
$\boldsymbol{\sigma}$	stress tensor
$\boldsymbol{\sigma}_0$	prestress tensor
$\boldsymbol{\chi}$	convective coordinate

Chapter 1

Introduction

1.1 Background and Motivation

Especially in civil engineering, ongoing climate change will cause new challenges soon. This work examines the field of computational wind engineering (CWE), which is one of those areas affected by climate change and where it will have an essential influence. The unfavorable effects of wind mostly play a role in high-rise and slender civil engineering structures, particularly sensitive to wind effects. The trend in recent years is the increase of height and length of those types of structure. Additionally, the reduction of material used also for smaller buildings to save resources and costs comes more into play and is one of the future challenges. Those developments lead to an increased sensitivity of such structures and, in combination with climate change, increases the importance of focusing more on assessing the wind effects. The aim must be to design structures with adequate stiffness and damping characteristics, which meet the safety and habitability requirements. In the case of high-rise civil engineering structures, according to [91] several techniques exist that make those structures meet those requirements in the context of wind. Fig. 1.1 depicts the most followed approaches. They include a) the application of additional damping and motion control devices, b) the modification of the structural system, and c) aerodynamic modifications. In practice, often, a combination of

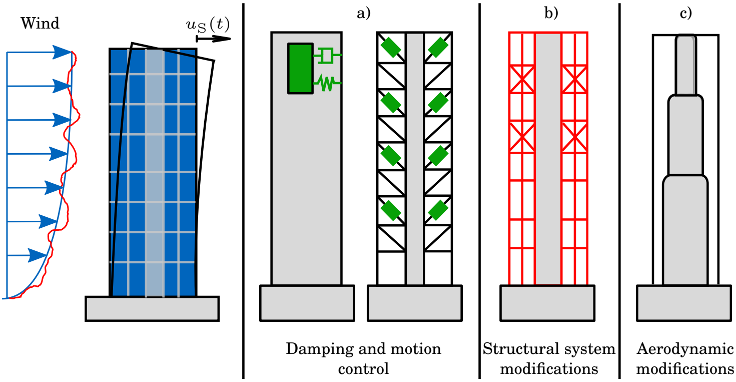

Figure 1.1: Techniques for the control and reduction of wind-induced vibrations, adopted from [91] p. 379.

methods a), b), and c) will lead to the best result. This work focuses on method a), which is the application of auxiliary damping and motion control devices.

1.2 Previous Related Studies

Starting from [107] and [56] to [70] and finally [4], several investigations concerning the numerical treatment of wind effects on different civil engineering structures on the way to a numerical wind tunnel have been carried out. Particular investigations for high-rise buildings were, for example, conducted in [74].

In the works of [107], and [56], the first investigations concerning computational wind-structure interaction were made. Although at that time, generally large scale FSI simulations of practically relevant problems from civil engineering were hardly possible because of limited computational resources and the lack of an appropriate software environment. Thus only basic assessments were possible. In [70] first serious investigations on computational wind-structure interaction, including a numerically generated wind field for a lightweight civil engineering structure, were made. The advantage here was an extensive measurement campaign on-site and in the physical wind tunnel. Those measurements provided the necessary data for the numerical generation of the wind field. The simulations conducted within this work were compared to the experiments from the physical wind tunnel. The modeling of the fluid flow herein was conducted with a finite volume solver. In [4] further investigations concerning the numerical modeling of natural wind were made. Additionally, in contrast to [70], finite elements were used to model the fluid flow. In the wind-structure interaction simulations for a solar trough collector performed therein, the structure was modeled by a single degree of freedom model in a 3D simulated wind field. Nevertheless, the extensive experimental validation and the cross-comparison between the numerical approaches showed good results. For a further review of the development in CWE and especially the numerical wind tunnel, over the past years, the reader is referred to [108].

Besides the CWE community's developments, the development in the community of coupled problems tends to deal with multiphysics problems containing more than two physical fields. One of the first contributions to the partitioned treatment of such issues has been made in [37], which gives a general overview of the treatment of coupled problems by a partitioned approach. More recent developments are, for example, fluid-structure interaction with electromagnetics [10], fluid-structure-contact interaction [67] or general n-field coupling [87] and [18]. [18] and [87] mostly focus on the theoretical algorithmic treatment and not on practical applications, especially not for wind effects on civil engineering structures. This links to the concept of a digital twin, which is referred to as the connection of a physical system (”real world”) with a digital representation (”virtual world”) and the interaction between each other [81]. The digital twin is just now of significant interest in other disciplines, e.g., the mechanical engineering community or in supply chain management, but will gain more importance in the civil engineering context.

1.3 Starting Point and Goals of the Thesis

The aim of this thesis is the coupled simulation of the wind-structure interaction problem in combination with damping and motion control devices. The open-source software Kratos Multiphysics [27], [53] is employed. The Kratos serves as a basis for the simulations conducted and as a platform for new implementations in this thesis's context. The research within the present thesis is devoted to the following topics:

a) Numerical treatment of complex wind-structure interaction problems of civil engineering structures.

b) The general algorithmic extension of the partitioned FSI problem by open- or closed-loop control devices.

c) The combination of a) and b) for the simulation of a complex, high-rise, tower-like structure in natural wind conditions, including a vibration mitigation system.

1.4 Present Contributions

Considering the described goals, this thesis comprises the following contributions to the simulation of multiphysics problems, the modeling of mechatronic systems and the field of CWE:

a) Development of a robust and practically applicable approach for numerically dealing with complex wind-structure interaction problems in civil engineering, on basis of an open-source software (in this case [53]).

    - Assessment of different structural finite elements for their application for the simulation of nonlinear dynamic problems of practical relevant size in civil engineering and extension of the StructuralMechanicsApplication of [53].
    - Implementation of a MeshMotionApplication in [53], containing different, robust and efficient mesh motion strategies which are also applicable for problems beyond the body fitted FSI context (e.g., in node based structural optimization).
    - Extension of the inclusion of the numerical inlet generator [5] into the simulation approach concerning the application of the numerically generated wind as an inlet condition of the fluid domain.

  - Concise schematic concept for the numerical generation of realistic natural wind conditions for civil engineering structures on basis of on-site measurements, values from surrounding measurement stations, numerical meteorological simulations, design codes, and their combination. Including the identification of the important statistic quantities, which are reasonable for a comparison of the values coming from the different sources.
  - Validation of the developed approach by fully coupled wind-structure interaction simulations for a physical time of 41 min. and comparison of their results with on site measurements of reaction moments for a complex, high-rise, civil engineering structure. This also includes the error development over simulation time of important statistic measures in CWE.
  - Evaluation of different coupling strategies (implicit/explicit) for partitioned FSI in the context of efficient and robust simulation of practical wind-structure interaction problems and confirmation of the findings of [4].

b) Algorithmic extension of the partitioned FSI problem by open- or closed-loop control, utilizing a Gauss-Seidel pattern. The algorithm is generally applicable to all types of partitioned FSI problems.

  - Evaluation of existing algorithms for the coupling of multiple physical problems concerning the inclusion of control into FSI.
  - Developed algorithms and the ideas behind them are a contribution to the CoSimulationApplication implemented in [53].
  - Derivations of the algorithms for fluid-structure-control interaction from a simplified model problem, which is easily accessible.
  - Application of the developed algorithms to a well-known benchmark problem from FSI with large deformations, extended by a controller.

  - Modeling approach, which is different from the standard procedure in control of mechanic structures, which simulates a fully nonlinear high fidelity model of the structure and the interaction between the mechanic structure, the disturbances and the controller. This inherits the exchange of information between all system parts in every time step.

c) Application of the combination of a) and b) to a complex, high-rise civil engineering structure in natural wind conditions, including a vibration mitigation system, which is capable of actively influencing the dynamics of the structure.

  - Thorough FSI studies of different structural configurations and the identification of the main excitation mechanism.
  - Modeling of the hybrid mass damper (HMD) as a pendulum and its implementation into [53], including the interaction properties, i.e., information transfer, with the structural system.
  - Coupled, partitioned simulation of the structure and the HMD, where the HMD excites the structure to forced vibrations.
  - Coupled, partitioned simulation of the wind-structure interaction problem including the HMD for vibration mitigation.

1.5 Outline of the Thesis

The remaining Chapters of this thesis are organized as follows:
CHAPTER 2 offers a short introduction into the theoretical background and the assumptions necessary to understand the content of this work and the results of the simulations. The reader also finds references to literature for additional information concerning the different subproblems and their coupling.
CHAPTER 3 shows the partitioned algorithmic treatment of a general FSI problem, which is extended by an open- or closed-loop control device, by a Gauss-Seidel pattern. It is added for completeness and summarizes the content published in [72] and [104].

CHAPTER 4 introduces the numerical wind tunnel and its application to high-rise, tower-like civil engineering structures subjected to wind. It contains a validation study comparing simulation and measurements for the Olympic Tower in Munich. It shows how to find the prevailing wind conditions from measurements and generate those wind conditions with the synthetic inlet generator developed in [4]. Finally, the best variant of the algorithm from CHAPTER 3 and the previous findings from CHAPTER 4 are applied to the simulation of the thyssenkrupp elevator test tower in Rottweil, including a hybrid mass damper (HMD).

CHAPTER 5 summarizes the outcomes of this work and gives some recommendations for future research.

APPENDIX A shows the algorithms developed in CHAPTER 3 in pseudo-code notation.

APPENDIX B summarizes the basic methods of discrete, descriptive statistics, which are applied in this work.

APPENDIX C offers a short introduction into integral transform methods.

APPENDIX D exercises the two different modeling approaches in control theory for dynamic systems on a simple mechanical problem.

Chapter 2

Theoretical Background

This Chapter contains the fundamental governing equations, assumptions, and definitions necessary to understand this thesis's content. This thesis deals with the multiphysics problem of fluid-structure-control interaction (FSCI), making it essential to give the reader a fundamental idea of the subproblems involved. This chapter can only provide a rough overview. Hence the reader is referred to the literature, which is cited in the respective subsections for more detailed information. The FSCI problem is treated by a partitioned approach, which means it can be subdivided into three subproblems in the following called subsystems:

a) Computational structural dynamics (CSD)

b) Computational fluid dynamics (CFD)

c) Structural control (SC)

The subsystems can be solved independently and are coupled by appropriate coupling conditions on their common interfaces. This also means the theory of the different subsystems can be presented in the following independently of each other. While the subsystems CFD and CSD are field problems, the SC subsystem is a signal problem. A field has a coherence in space and time, whereas signals do not have the spatial coherence. The conditional equations for the CFD and CSD subsystem are derived from the balance equations of continuum mechanics, which can be found in every textbook for basic continuum mechanics like [63], [66] or [44]. To be able to solve the problems resulting from the balance equations; they are discretized in space by the finite element method (FEM). The basics for the FEM can be found, for example, in [7]. In the following a short overview for the CSD subsystem is given in section 2.1, for the CFD subsystem in section 2.2 and for the SC subsystem in section 2.3.

2.1 Computational Structural Dynamics (CSD)

The CSD subsystem is generally formulated in terms of displacements denoted by the vector $\mathbf{d}_\mathrm{S}(t)$, with its components $[u_\mathrm{S}, v_\mathrm{S}, w_\mathrm{S}]^T$. The labeling with (t) might be omitted for better readability if appropriate. The kinematics of the structural dynamics problem is described by the the total Lagrangian formulation in a Cartesian coordinate system. Therefore, the basic initial-boundary value problem for structural dynamics in total Lagrangian kinematics can be expressed by the balance of linear momentum as

$$\rho_\mathrm{S}\ddot{\mathbf{d}}_\mathrm{S} - \nabla \cdot (\boldsymbol{\sigma} + \boldsymbol{\sigma}_0) - \rho_\mathrm{S}\mathbf{b} = 0 \quad \text{in} \quad \Omega_\mathrm{S} \times [0, T), \tag{2.1}$$

in a structural domain Ω_S. Herein ρ_S is the density of the structure, $\boldsymbol{\sigma}$ the stress tensor, $\boldsymbol{\sigma}_0$ the prestress tensor and $\mathbf{b}$ the vector of body forces. $\dot{(\cdot)}$ and $\ddot{(\cdot)}$ denote the first and second derivative w.r.t. time. On the boundary Γ_S of Ω_S, which consists of a Neumann part $\Gamma_{\mathrm{S},N}$ and a Dirichlet part $\Gamma_{\mathrm{S},D}$ as well as the respective initial conditions can be defined as:

$$\begin{aligned} \mathbf{d}_\mathrm{S} &= \mathbf{d}_\mathrm{S}^\mathrm{init} && \text{in } \Omega_\mathrm{S} \text{ for } t = T_0, \\ \dot{\mathbf{d}}_\mathrm{S} &= \dot{\mathbf{d}}_\mathrm{S}^\mathrm{init} && \text{in } \Omega_\mathrm{S} \text{ for } t = T_0 \end{aligned} \tag{2.2}$$

and the boundary conditions as:

$$\begin{aligned} \mathbf{d}_\mathrm{S} &= \mathbf{0} && \text{on } \Gamma_{\mathrm{S},D}, \\ \boldsymbol{\sigma} \cdot \boldsymbol{n} &= \mathbf{t} && \text{on } \Gamma_{S,N}. \end{aligned} \tag{2.3}$$

Herein $\mathbf{d}_\mathrm{S}^\mathrm{init}$ are the initial displacements and $\dot{\mathbf{d}}_\mathrm{S}^\mathrm{init}$ the initial velocities of the domain Ω_S. All or one component of $\mathbf{d}_\mathrm{S}$ on $\Gamma_{S,D}$

can be set to zero or to a prescribed value and $\boldsymbol{n}$ represents the outer normal vector with $\boldsymbol{t}$ being the traction vector on $\Gamma_{S,N}$. For the strains the Green-Lagrangian (GL) strain measure is chosen, which is defined for the general non-linear case as

$$\varepsilon_{GL} = \underbrace{\frac{1}{2} \cdot \big(\nabla \mathbf{d}_{\mathrm{S}} + (\nabla \mathbf{d}_{\mathrm{S}})^T}_{\varepsilon_{\mathrm{lin}}} + \nabla \mathbf{d}_{\mathrm{S}} \cdot \nabla \mathbf{d}_{\mathrm{S}}\big). \tag{2.4}$$

It can be linearized by neglecting the last two terms. The energy conjugated stress measure to the GL strains are the second Piola-Kirchhoff (PK2) stresses. Stresses and strains are related throughout this work by the St. Venant-Kirchhoff constitutive law as

$$\boldsymbol{\sigma}_{\mathrm{PK2}} = \boldsymbol{\mathcal{C}} : \varepsilon_{\mathrm{GL}}. \tag{2.5}$$

Herein $\boldsymbol{\mathcal{C}}$ denotes the fourth order material tensor, which represents a linear elastic, isotropic material. The equilibrium is fulfilled weakly by applying the principle of virtual work (PVW) to Eq. (2.1). Generally, the PVW is defined as

$$\delta W = \delta W_{\mathrm{int}} - \delta W_{\mathrm{ext}} + \delta W_{\mathrm{kin}} = 0. \tag{2.6}$$

Therein, the overall virtual work δW consists of the internal virtual work δW_{int}, the external virtual work δW_{ext} and the kinetic virtual work δW_{kin}. The weak form of Eq. (2.1) is

$$\begin{aligned} \delta W = & \underbrace{\int_{\Omega_{\mathrm{S}}} \delta \mathbf{d}_{\mathrm{S}} \cdot \rho_{\mathrm{S}} \ddot{\mathbf{d}}_{\mathrm{S}} \, \mathrm{d}\Omega_{\mathrm{S}}}_{\delta W_{\mathrm{kin}}} + \underbrace{\int_{\Omega_{\mathrm{S}}} \delta \boldsymbol{\varepsilon} : (\boldsymbol{\sigma}_{PK2} + \boldsymbol{\sigma}_0) \, \mathrm{d}\Omega_{\mathrm{S}}}_{\delta W_{\mathrm{int}}} \\ & \underbrace{- \int_{\Omega_{\mathrm{S}}} \delta \mathbf{d}_{\mathrm{S}} \cdot \rho_{\mathrm{S}} \mathbf{b} \, \mathrm{d}\Omega_{\mathrm{S}} - \int_{\Gamma_{S,N}} \delta \mathbf{d}_{\mathrm{S}} \cdot \mathbf{t} \, \mathrm{d}\Gamma_{S,N}}_{\delta W_{\mathrm{ext}}} . \end{aligned} \tag{2.7}$$

It contains the virtual displacements $\delta \mathbf{d}_{\mathrm{S}}$ and the virtual strains $\delta \boldsymbol{\varepsilon}$. The weak form in Eq. (2.7) is discretized in space by the FEM. The straight forward approach in structural mechanics is a purely displacement based formulation. Therefore, the continuous functions for $\mathbf{d}_{\mathrm{S}}$ and $\delta \mathbf{d}_{\mathrm{S}}$ are chosen on a discrete subspace. The space is formulated on element level and is spanned by a set of shape functions $\boldsymbol{N}_i$. The continuous displacements $\mathbf{d}_{\mathrm{S}}$ and their temporal derivatives are approximated by the nodal quantities $\boldsymbol{d}_{S,i}$, $\delta\boldsymbol{d}_{S,i}$, $\dot{\boldsymbol{d}}_{S,i}$ and $\ddot{\boldsymbol{d}}_{S,i}$ as

$$\begin{aligned}
\mathbf{d}_{\mathrm{S}}^{h}(\boldsymbol{X},t) &= \sum_{i=1}^{N_{\mathrm{dof}}} \boldsymbol{d}_{S,i}\boldsymbol{N}_i(\boldsymbol{X}), \qquad & \delta\mathbf{d}_{\mathrm{S}}^{h}(\boldsymbol{X}) &= \sum_{i=1}^{N_{\mathrm{dof}}} \delta\boldsymbol{d}_{S,i}\boldsymbol{N}_i(\boldsymbol{X}), \\
\dot{\mathbf{d}}_{\mathrm{S}}^{h}(\boldsymbol{X},t) &= \sum_{i=1}^{N_{\mathrm{dof}}} \dot{\boldsymbol{d}}_{S,i}\boldsymbol{N}_i(\boldsymbol{X}), \qquad & \ddot{\mathbf{d}}_{\mathrm{S}}^{h}(\boldsymbol{X},t) &= \sum_{i=1}^{N_{\mathrm{dof}}} \ddot{\boldsymbol{d}}_{S,i}\boldsymbol{N}_i(\boldsymbol{X}).
\end{aligned} \tag{2.8}$$

Herein i is the counter for the N_{dof} number of degrees of freedom and $\boldsymbol{X}$ denotes the reference to the undeformed configuration. Applying the approximation of Eq. (2.8) to Eq. (2.7), performing a numerical integration by Gaussian quadrature in space, assembling quantities on element level to system matrices and applying the boundary conditions, the semidiscrete system of equations can be written in matrix form as

$$\boldsymbol{M}\ddot{\boldsymbol{d}}_{\mathrm{S}} + \boldsymbol{C}\dot{\boldsymbol{d}}_{\mathrm{S}} + \boldsymbol{f}_{\mathrm{int}}\left(\boldsymbol{d}_{\mathrm{S}}\right) = \boldsymbol{f}_{\mathrm{ext}}, \tag{2.9}$$

for the general non-linear case. Herein $\boldsymbol{M}$ denotes the system mass matrix, $\boldsymbol{C}$ the system damping matrix, $\boldsymbol{f}_{\mathrm{int}}$ is a non-linear function of $\boldsymbol{d}_{\mathrm{S}}$ containing the system stiffness matrix $\boldsymbol{K}$ and $\boldsymbol{f}_{\mathrm{ext}}$ the system vector of external forces. The nonlinearity of $\boldsymbol{f}_{\mathrm{ext}}$ is neglected, because taking it into account would be numerically very costly and also thwarts the partitioned concept followed later. It is possible to obtain a lumped or a consistent version of $\boldsymbol{M}$. Throughout this work, the lumped version is applied. Eq. (2.9) is a system of nonlinear ordinary differential equations (ODEs), which is still continuous in time. This system has to be linearized and discretized in time in order to solve it for the nodal unknowns $\boldsymbol{d}_{\mathrm{S}}$. The time integration is performed by the BDF2 method, which is presented in section 2.5. A detailed review and assessment of time integration schemes for CSD can be found in [55]. Applying the time integration scheme to Eq. (2.9) leads to a modified system of the semi-discrete equations, which is a non-linear system of algebraic equations (AE). Therefore, a linearization of $\boldsymbol{K}$ is necessary, which results in the tangential system stiffness matrix $\boldsymbol{K}_T$. $\boldsymbol{K}_T$ can be subdivided into $\boldsymbol{K}_T = \boldsymbol{K}_e + \boldsymbol{K}_g + \boldsymbol{K}_u$, where $\boldsymbol{K}_e$ is the linear part, $\boldsymbol{K}_g$ the geometric system stiffness matrix and $\boldsymbol{K}_u$ the initial system displacement matrix. Finally, this gives an incremental system of equations to be solved in every time step, which is

$$\boldsymbol{K}_{\text{eff}} \Delta \boldsymbol{d}_{\text{S}} = \boldsymbol{\mathcal{R}}. \tag{2.10}$$

Herein $\boldsymbol{K}_{\text{eff}} = \boldsymbol{K}_T + \boldsymbol{K}_{\text{dyn}}$, in which $\boldsymbol{K}_{\text{dyn}}$ contains the dynamic parts of the system depending on the time integration scheme applied. $\boldsymbol{\mathcal{R}}$ is the residual vector defined as $\boldsymbol{f}_{\text{ext}} - \boldsymbol{f}_{\text{int}}$. The system is solved iteratively by a Newton-Raphson scheme updating $\Delta \boldsymbol{d}_{\text{S}}$ in every nonlinear iteration. More details about the solution procedure can, for example, be found in [7] p. 755 ff., and p. 826.

The damping matrix $\boldsymbol{C}$ is approximated by the Rayleigh damping approach [82]. Therein, the damping matrix is created by a linear combination of mass and stiffness as

$$\boldsymbol{C} = \alpha_R \boldsymbol{M} + \beta_R \boldsymbol{K}_T. \tag{2.11}$$

The coefficients α_R and β_R can be obtained by the first two angular eigenfrequencies ω_1, ω_2 and the damping ratio D as

$$\begin{bmatrix} \alpha_R \\ \beta_R \end{bmatrix} = \frac{2D}{(\omega_1 + \omega_2)} \cdot \begin{bmatrix} \omega_1 \cdot \omega_2 \\ 1 \end{bmatrix}. \tag{2.12}$$

The structural damping is generally not known. In practice it is possible to measure the logarithmic decrement Λ defined as

$$\Lambda = \frac{1}{k} \cdot \ln\Big(\frac{d_{S,i}^{n}}{d_{S,i}^{n+k}}\Big). \tag{2.13}$$

Therefore the amplitude of one component i of $\boldsymbol{d}_{\text{S}}$ is measured for a certain number of subsequent oscillations k. The damping ratio D can be determined from Λ as

$$D = \frac{\Lambda}{\sqrt{4\pi^2 + \Lambda^2}}. \tag{2.14}$$

This has been a short overview of the basics for discretization and solution of the CSD problem and how it has been basically performed throughout this work. For more detailed information the reader is referred to [109], [10] or [11].

2.1.1 Dynamic Eigenvalue Analysis

The structures treated in this work are only lightly damped. Thus the eigenfrequencies and eigenforms can be calculated from the general eigenvalue problem by a numerical Eigenvalue analysis, solving the equation:

$$(\boldsymbol{K}_e - \omega^2 \boldsymbol{M})\boldsymbol{\varphi} = \boldsymbol{0}. \tag{2.15}$$

Herein $\boldsymbol{M}$ is the system mass matrix and $\boldsymbol{K}_e$ is the linear part of the system stiffness matrix resulting from the finite element discretization of the system. The solution results in n eigenvectors $\boldsymbol{\varphi}_i$ and n circular eigenfrequencies ω_i. The eigenvectors are normalized and and summarized columnwise in the modal matrix $\boldsymbol{\Phi}$.

The eigenfrequencies f_i result from the eigen angular frequencies ω_i by:

$$f_i = \frac{\omega_i}{2\pi}. \tag{2.16}$$

The dynamic eigenvalue problem presented above is solved by the algorithm in [8], which recently has been enhanced in [50].

2.1.2 Finite Element Formulations

Civil engineering structures generally consist of plate, shell, or beam like construction components like slabs, columns, or girders. Thus the general balance equations for the continuum can be spatially reduced by applying certain assumptions to better match those construction components. In the case of a FEM, this means the discretization by shell and beam elements, also called structural elements. Those types of elements often suffer from problems, mostly caused by stiffening effects called ”locking.” A detailed summary of all types of locking effects is given in [51] p. 59-81 and [12] p. 99-124. Subsequently, shell and beam element formulations used for calculating the results in this work are shortly presented. The case for plates in bending is covered as a part of the shell elements. For shell and beam elements in this work, another type of Lagrangian kinematics, the corotational (CR) approach, is applied. In the CR kinematics, the deformation is split into a rigid body motion and a deformational motion. The CR approach can be modified such that it leads to an element-independent corotational (EICR) formulation, which is implemented in [53] and is described in detail in [36]. In [36] one can find the major derivations of this type of kinematics, a differentiation from total and updated Lagrangian kinematics, and a detailed historical review. One of the advantages of the EICR formulation is the possibility of re-using small-strain elements for large deformations. Hence for most civil engineering structures, it offers a reasonable balance between practical accuracy and computational speed.

2.1.2.1 Shell Elements

The shell elements applied for the simulations throughout this work are based on a five parameter Reissner-Mindlin shell theory. For further insight into different parameterizations of shell formulations and for a general overview of the different types of shell modeling, the reader is referred to [13]. For the spatial discretization, triangular elements with linear shape functions and six degrees of freedom at each node, i.e., three displacements and three rotations, are used. As mentioned in section 2.1.2 those purely displacement-based structural elements face locking problems. The locking problem also occurs for this type of element when the shell slenderness ratio increases. The locking phenomenon occurring here is transverse shear locking. The exact theory behind this phenomenon is described for example in [51] p. 72, ff. Different approaches exist as remedies for the transverse shear locking problem. Here, the Discrete Shear Gap (DSG) method proposed by [14] is utilized. Shortly summarized, the DSG applies an enhanced shear strain formulation to mitigate the locking. Additionally, the performance of the DSG element is improved by the approach first presented in [62] for MITC-4 elements as proposed in [13] and [101] p. 253-263. The details of the implementation can be found in [53] or in [103] p. 55-67, where the element was also tested in detail.

2.1.2.2 Beam Elements

In this work, the kinematics of the beam element is also formulated in the EICR formulation. The rigid body rotation is, in this case, calculated by quaternions [43]. Those have the advantage above other rotation strategies of not having the risk of singular results for particular angles and are more compact and numerically stable than, for example, rotation matrices. Furthermore, full circle rotations can be modeled because only half of the rotation angle is taken into account for the calculations. Further insights concerning the calculation of the quaternion parameters can be gained in [54] p. 63-68. Since the EICR is applied, it is possible to utilize a linear beam formulation in which the geometric nonlinearity is obtained by the motion of the local element coordinate system. The beam element used throughout this work has been implemented according to [54] p. 100 - 139. It is based on a Timoshenko beam theory and applies linear shape functions for the interpolations of longitudinal deformations, torsion (St. Venant torsion), and for the curvatures. Like for the shell elements mentioned in section 2.1.2.1, the element also suffers from the transverse shear locking problem. In [54] p. 91, 92, this is taken into account more in detail, and on p. 94-96, it is suggested how to solve the problem by applying modified bending and shear stiffness parameters. Looking closer at this approach, this has the same effect as interpolating the curvatures by cubic shape functions. The exact implementation of the element can be found in the code of [53] or in [84] p. 49 - 97, where the element was also tested in detail.

2.1.2.3 Plane Stress Plate Elements

Structures in two dimensions are discretized by a fully integrated, quadrilateral plane stress elements with total Lagrangian kinematics. The derivation and implementation of this element follow the standard approach, which can be found at the beginning of this section and every classical FEM textbook e.g., [7] p. 355, ff.

2.2 Computational Fluid Dynamics (CFD)

This thesis investigates the wind-effects on civil engineering structures. Airflow is a Newtonian fluid flow, which means it has a linear, viscous flow behavior. It follows that the properties of the fluid flow depend on the viscosity of the fluid and its density. Furthermore, under certain circumstances, air can be treated as an incompressible fluid flow. The validity can be examined by the dimensionless Mach number, which is defined as

$$\mathrm{Ma} = \frac{u_F}{c_{\mathrm{air}}}. \tag{2.17}$$

Herein c_{air} is the speed of sound in air, depending on the density and thus on the temperature and u_F is the component of the flow velocity in streamwise direction of the undisturbed flow. The effects of compressibility of air can be generally neglected as long as $\mathrm{Ma} < 0.3$. For natural wind the most unfavorable value for Ma will occur during a winter storm, where the temperature is low and the flow velocity is high. Thus for a temperature of -25 °C, the speed of sound in air c_{air} is approximately $315\ {}^{\mathrm{m}}/_{\mathrm{s}}$ and the maximum velocity is assumed to be $70\ {}^{\mathrm{m}}/_{\mathrm{s}}$, which corresponds to the highest measured wind speed until now during hurricane "Lothar" on the Wendelstein at a height of 1838 m AMSL in the year 1999 [32]. Inserting those values into Eq. (2.17) results in $\mathrm{Ma} = 0.22$. This clearly shows for this worst case scenario that air can be treated as an incompressible flow, when modeling wind effects on civil engineering structures.

From the considerations above it follows that the fluid flow can be modeled by the incompressible Navier-Stokes equations (NSE). For consistency with the remainder of this work, dealing with body fitted FSI, the NSE are written in the following in arbitrary Eulerian-Lagrangian (ALE) formulation. More details about the different coordinate systems in the ALE formulation can be found in [33] p. 8-12 and p. 18 or in [34]. Its application to the NSE is for example described in [100] p. 136. The NSE for an incompressible fluid flow consist of equations for the balance of linear momentum and the balance of mass

$$\begin{aligned} \rho_{\mathrm{F}}\left(\left.\frac{\partial \mathbf{u}_{\mathrm{F}}}{\partial t}\right|_{\boldsymbol{\chi}} + (\mathbf{w}\cdot\nabla)\mathbf{u}_{\mathrm{F}}\right) + \nabla p - \mu_{\mathrm{F}}\Delta\mathbf{u}_{\mathrm{F}} = \mathbf{f} \quad &\text{in} \quad \Omega_{\mathrm{F}}\times[0,T), \\ \nabla\cdot\mathbf{u}_F = \mathbf{0} \quad &\text{in} \quad \Omega_{\mathrm{F}}\times[0,T), \end{aligned} \tag{2.18}$$

in a fluid domain Ω_{F}. Herein, ρ_{F} is the fluid density, μ_{F} the dynamic viscosity, $\mathbf{u}_{\mathrm{F}}$ the fluid velocity vector with its components $[u_{\mathrm{F}}, v_{\mathrm{F}}, w_{\mathrm{F}}]^T$, p the pressure and f the external forces. Since the ALE formulation is applied, the convective velocity $\mathbf{w} = \mathbf{u}_{\mathrm{F}} - \mathbf{u}_{\mathrm{M}}$ between fluid flow and mesh motion is added, where $\mathbf{u}_{\mathrm{M}}$ is the mesh velocity. Furthermore, the spatial description is applied, which means the spatial derivatives are calculated on the spatial coordinate system and the time derivatives on the arbitrarily moving reference coordinate system χ. Details concerning the mesh motion are discussed in section 2.4. The problem can only be solved by applying suitable boundary conditions. The domain boundary of the fluid flow is denoted by Γ_{F}. It can be subdivided into a Dirichlet part $\Gamma_{\mathrm{F,D}}$ and a Neumann part $\Gamma_{\mathrm{F,N}}$. It has to hold that $\Gamma_{\mathrm{F}} = \Gamma_{\mathrm{F,D}} \cup \Gamma_{\mathrm{F,N}}$ and $\Gamma_{\mathrm{F,D}} \cap \Gamma_{\mathrm{F,N}} = \emptyset$. With this, the initial and boundary conditions can be expressed as:

$$\mathbf{u}_{\mathrm{F}} = \mathbf{u}_{\mathrm{F}}^{\mathrm{init}} \qquad \text{in} \quad \Omega_{\mathrm{F}}, t = 0, \quad \text{with} : \nabla \cdot \mathbf{u}_{\mathrm{F}}^{\mathrm{init}} = 0, \tag{2.19}$$

$$\mathbf{u}_{\mathrm{F}} = \mathbf{u}_{\mathrm{F,D}} \qquad \text{on} \quad \Gamma_{\mathrm{F,D}} \times [0, T) \text{ and} \tag{2.20}$$

$$\boldsymbol{\sigma} \cdot \boldsymbol{n} = \mathbf{t} \qquad \text{on} \quad \Gamma_{\mathrm{F,N}} \times [0, T). \tag{2.21}$$

Herein, $\mathbf{u}_{\mathrm{F}}^{\mathrm{init}}$ is the initial velocity field, $\mathbf{u}_{\mathrm{F,D}}$ the imposed velocity at the Dirichlet boundary, $\boldsymbol{n}$ is the outer normal vector, $\boldsymbol{\sigma}$ represents the stress tensor and $\mathbf{t}$ the imposed traction vector at the Neumann boundary. Additionally, a boundary condition for the moving boundary Γ_{I} of the fluid domain due to the ALE formulation has to be defined, which is

$$\boldsymbol{n} \cdot \mathbf{u}_{\mathrm{F}} = \boldsymbol{n} \cdot \mathbf{u}_{\mathrm{M}} \qquad \text{in} \quad \Gamma_{\mathrm{I}} \times [0, \mathrm{T}). \tag{2.22}$$

The NSE are discretized by a stabilized finite element formulation on unstructured grids with triangular elements in 2D and tetrahedral elements in 3D, both with linear shape functions. The formulation is based on the variational multiscale method (VMS), first introduced in [45] and [46]. The exact formulation applied throughout this work and which is implemented in [53] can be found in [26] chapter 2. The approaches shown there for the standard NSE can be likewise applied to the ALE formulation of the NSE in Eq. (2.18). In [26] also, several tests have been conducted and the parallels of the VMS method to Large Eddy Simulation (LES) are shown. For additional insights about the parallels of the VMS method to LES the reader is referred to [41], [80] and [25]. Furthermore, it is explained how the VMS method can be interpreted as a turbulence model, which is the reason why, throughout this work, no particular turbulence models are applied.

In the case of numerical simulations, additional boundary conditions have to be defined. Those are the following:

a) Inlet condition: The boundary where the fluid flow enters the discretized fluid domain. Here a prescribed inlet velocity profile is applied.

b) Outlet condition: The boundary where the fluid flow leaves the discretized fluid domain. In the cases treated throughout this work, the pressure is set to zero at this boundary.

c) No-slip condition: The fluid-particle closest to the boundary adheres to it. The velocity on this boundary is set to zero for all components of the velocity vector. In the case of a moving boundary FSI the fluid velocity is equal to the mesh velocity.

d) Slip condition: The fluid-particle closest to the boundary does not adhere to it. It follows that only the component of the velocity vector normal to the boundary is set to zero.

The linearization and spatial discretization with the FEM, basically working the same way as described for the CSD part in section 2.2, leads to the semi-discrete version of the transient system of partial differential equations (PDEs), which is a system of time-continuous (ODEs). This system of ODEs has to be discretized in time to obtain a system of algebraic equations (AEs), which can be solved for the nodal unknowns of the fluid flow, $\boldsymbol{u}_{\mathrm{F}}$ and p. When following this consistent or monolithic way of solving the fluid problem, i.e., solving the whole equation system for $\boldsymbol{u}_{\mathrm{F}}$ and p at once, one may run into difficulties when dealing with large systems of equations arising from ”real size” CFD problems. Furthermore, additional numerical problems may occur due to the ill-conditioning of the system of equations resulting from the discretization of different variables and the stabilization terms. Because of the high number of degrees of freedom, it is not possible to use direct solvers. Iterative solvers, made to solve large systems of stiff equations, might also fail because of the poor conditioning of the system.

To overcome this problem, the fractional-step method has been developed ([21], [22] and [92]). It splits the problem into two more steps. Different schemes are existing, but all of them have in common, that they decouple pressure and velocity calculation to get smaller, well-conditioned systems of equations. The method applied in this work and which is implemented in [53] has been published in [23] and [24]. The detailed algorithm can be found in [4] p. 21, 22. More about the mathematical background of the fractional step method and its connection to the monolithic approach can be found in [6].

Within the fractional step method, the integration in time is performed by the BDF2 method presented in section 2.5. This results in a consistent application of time integration schemes for the CSD and CFD subsystem.

Conclusively, it can be said, although the fractional step method introduces an additional approximation, it can be seen as an optimal compromise between computational cost and numerical accuracy, especially for the simulation of wind in the context of civil engineering. A validation concerning this was carried out in [4] and in this work in section 4.5.

2.3 Control Theory for Structural Systems (SC)

This subsection gives an overview of the control of mechanical systems, also called mechatronics. The field of control theory and mechatronics is vast and has many applications. Thus in this subsection, only a rough overview with a focus on the main definitions, which are needed later in this work, can be given. For more detailed information, the reader is referred to the literature, for example, [97], [96], [61], [60] and [40] for the basics of control theory and to [73] for the special field of mechatronics. In addition, APPENDIX C provides some basic information about integral transform methods used in control theory. APPENDIX D gives a short introduction into some modeling approaches for dynamic systems applied in control theory.

2.3.1 Description of Mechatronic Systems

A mechatronic system is a dynamic system, which mainly consists of the controlled system, i.e., a mechanical structure besides a sensor (measuring element), a controller (controlling and comparing element), and an actuator as principally can be seen in Fig. 2.2. In the case of a mechatronic system, the physical quantities measured by the sensor are accelerations, velocities, displacements or forces. Depending on the type of controller, not only one but two or even all of those quantities are measured or calculated. The actuator element is a device applying a force to the structure, e.g., electronic motors or pneumatic devices. The controller consists of a device where the control law is implemented and a comparing element. It is possible to realize the controller in an analog or a digital way. The latter one is currently the common case and means the implementation of the control law on a microprocessor. The block diagram notation is handy to describe dynamic systems, which can be seen in Fig. 2.1 which shows the system concept with input and output quantities. Hereby scalar quantities are marked by single arrows and vector or matrix quantities (in Fig. 2.1 b) and Fig. 2.4) with double arrows. In the context of control theory, systems with scalar inputs and outputs are referred to as single-input, single-output systems (SISO), and with vector inputs and outputs as multiple-input, multiple-output systems (MIMO). Concerning the control theory aspect, i.e., the SC subsystems, only SISO systems are taken into account in this work. Additionally, the SC subsystems in this work are considered linear and time-invariant (LTI). This means if the controlled CSD subsystem is nonlinear, the equations implemented for the SC subsystem are linear.

As mentioned above, the block diagram notation is a nice tool to describe dynamic systems, thus it is also applied to the FSI problem later in this Chapter and the FSCI problem in CHAPTER 3. Applying the block diagram notation to the CFD and CSD subsystem results in contrast to the SC subsystem in MIMO systems.

2.3.2 Open- and Closed-Loop Control

The two principal control strategies applied to the mechatronic system are open- and closed-loop control. Fig. 2.2 shows the principle of closed-loop control in block diagram notation, sometimes referred to as feedback, for a mechanical structure. In closed-loop control, the output $y(t)$ of the controlled system is compared to the reference input $w(t)$ and an error signal $e(t) = w(t) - r(t)$ is calculated and passed to the controlling element which applies a correction by an actuator, as manipulation variable $u(t)$, to the controlled system. Fig. 2.2 is kept very general. In the case of this work, the controlled system is mechanical. Since we are dealing with dynamic systems, all quantities depend on the time

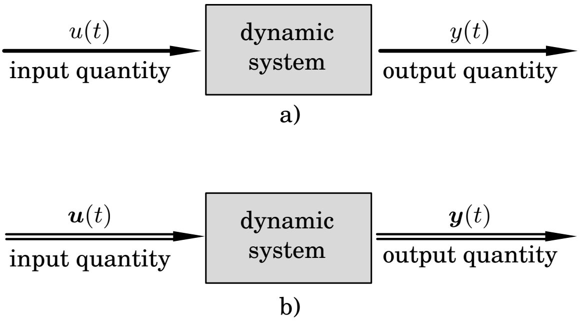

Figure 2.1: Symbolic presentation of the system concept for a SISO system a) and a MIMO system b) according to [97] p. 3.

t. If it is clear from the context, the addition (t) to the variables is omitted for better readability. Examples of closed-loop controlled, mechanical systems can be found in CHAPTER 3.

It exists an European standard for the naming in control theory. Unfortunately, the basic literature hardly uses it. Thus in this work, the notation, according to most of the standard literature, is applied. The variables in Fig. 2.2 are defined in Tab. 2.1.

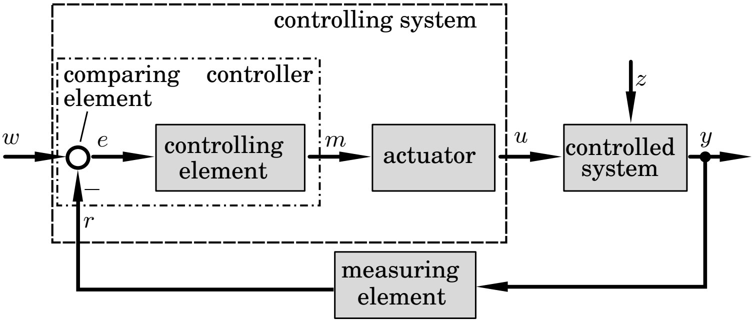

Figure 2.2: Block diagram for elementary closed-loop control according to [97] p. 185.

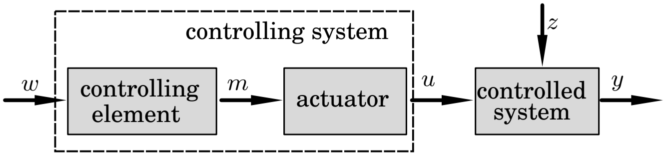

Figure 2.3: Block diagram for elementary open-loop control.

Table 2.1: Variables and symbols for block diagrams.

w	reference variable
e	control difference variable
m	controller output variable
u	manipulation variable
z	disturbance variable
y	controlled variable
r	feedback variable
●	branching point
○	summing point

Besides the closed-loop control, open-loop control, sometimes called feedforward, is also applicable for certain systems treated later in this work. The block diagram for open-loop control can be seen in Fig. 2.3. The corresponding variables can be found in Tab. 2.1. The main difference between open-loop and closed-loop control is the feedback loop in the closed-loop case. This means the open-loop control cannot react on arbitrary disturbances $z(t)$ acting on the controlled system. A remedy for this problem can be found if a signal correlated to the disturbance is available. If this is the case, adaptive filtering can be applied as suggested in [79]. The major advantage in this case is, that open-loop control does not necessarily need an explicit model of the system ([79] p. 10). The civil engineering structure which is investigated in Sect. 4.6 is an example of the type open-loop control described above.

2.3.3 System Representation in the Frequency and the Time Domain

A stable system might become unstable by applying the feedback loop when selecting the wrong parameters to tune the controller. Therefore, the controller design is a crucial part of influencing the dynamics of the controlled system suitably. The controller synthesis can either be performed in the frequency domain (classical approach) or in the time domain (modern approach).

In the time-continuous case, the Laplace-Transform is generally applied for the transformation into the frequency domain. In the time-discrete case, the transform is performed by the z-transform. Both types of transforms are shortly presented in APPENDIX C. It is common practice to write down the system's transfer function $G(s)$ (here in the time-continuous case), which is defined as

$$G(s) = \frac{Y(s)}{U(s)}. \tag{2.23}$$

It describes the relationship between the system output $Y(s)$ and its input $U(s)$. From $G(s)$ it is possible to determine the system's characteristic equation, which can be utilized to calculate the system poles. This applies to the time-continuous and the time-discrete case. The poles and zeros of the system can be depicted in the s-plane and the z-plane. The transfer function concept offers a basic platform for the analysis of the dynamic system and also for the controller design. Investigating those here more in detail would go far beyond the scope of this thesis, and the reader is referred to the vast amount of literature available for this topic. Some examples of this basic literature are cited at the beginning of this Section.

In the time domain the the equation Eq. (2.9) for the dynamic system can be written in state-space representation. This means the transformation of an ODE of order n into a system of ODEs with n equations of 1^{st} order [73] p. 68. The basic state-space representation for LTI systems is described by Eq. (2.24) and Eq (2.25) and its representation in a block diagram notation is shown in Fig. 2.4.

$$\dot{\boldsymbol{x}}(t) = \boldsymbol{A}\boldsymbol{x}(t) + \boldsymbol{B}\boldsymbol{u}(t) \qquad \text{(state equation)}, \tag{2.24}$$

$$\boldsymbol{y}(t) = \boldsymbol{C}\boldsymbol{x}(t) + \boldsymbol{D}\boldsymbol{u}(t) \qquad \text{(output equation)}. \tag{2.25}$$

Table 2.2: Variables and symbols for state-space representation.

$\boldsymbol{A}$	system matrix
$\boldsymbol{B}$	input matrix
$\boldsymbol{C}$	output matrix
$\boldsymbol{D}$	direct input-output matrix
$\boldsymbol{u}$	input vector
$\boldsymbol{x}$	state vector
$\boldsymbol{x}_0$	initial state vector
$\boldsymbol{y}$	output vector

The variables for the state-space representation are defined in Tab. 2.2. When dealing with SISO systems, the controller design is possible in the frequency and time domain. When dealing with MIMO systems, the controller design in the frequency domain is very challenging, and the design in the time domain by the state-space representation should be preferred ([73]). In this work, both types of representation are applied. APPENDIXD shows their application to a simple mechanical example.

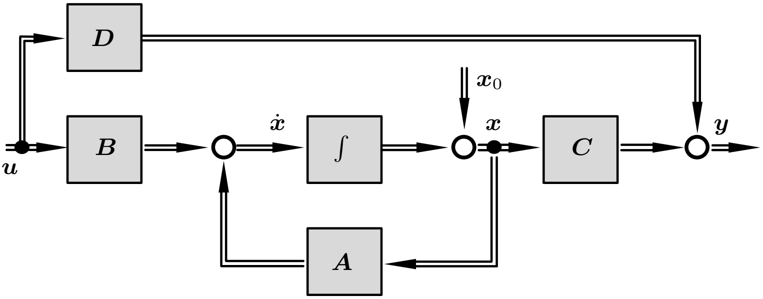

Figure 2.4: Block diagram for state-space representation according to [73] p. 69.

2.3.4 Controller Design

The choice of the control law and the selection of the controller parameters (controller design) is problem dependent and thus cannot be treated in a generalized way. Never the less, some brief statements applying for mechatronic systems are possible. The most common control law, which applies to most mechanic systems, is according to [73] p. 151 ff. the PD controller. The PD controller takes the control difference $e(t)$ multiplying it by a constant (P-Part) and also takes the first derivative w.r.t. time of it, i.e., $\dot{e}(t)$, multiplying it by a second constant (D-Part). An example of this type of control law can be found later in Eq. (3.3). Suppose the system is written in one of the ways presented in APPENDIXD; in that case, several tools for finding the optimal parameters to tune the controller, which can be found in the standard literature cited at the beginning of this Section, can be applied. One example of finding the optimal parameters for a controller can be found in Sect. 3.4. The high fidelity CSD model, simulated by the finite element method, can provide a very detailed description of the mechanical system's behavior. For controller design, the high-fidelity model is too extensive. Thus reduced-order models covering the most important dynamic aspects of the mechanical system (e.g., the first eigenmode), are utilized for the controller design and the implementation of the control law. An example of a basic reduced-order (low-fidelity) model is shown in Sect. 3.4.

2.3.5 Stability Considerations and Important Definitions

When manipulating a dynamic system, it is important to know if the system is stable. Therefore different stability definitions are of importance. We can distinguish between investigations in the frequency and in the time domain. As mentioned before, the system's poles can be depicted in the complex s-plane for the time-continuous case and in the z-plane for the time-discrete case. Generally, the desired degree of stability d is present if the real part of all poles s_i is smaller than $-d$. Fig. D.4 shows an example of the system pole's position in the s-plane with reference to the system behavior in the time domain for a simple example. A time-discrete system with the same degree of stability has only poles z_i located in a circle with a radius $\mathrm{e}^{-d\delta t} < 1$. This is depicted in Fig. 2.5

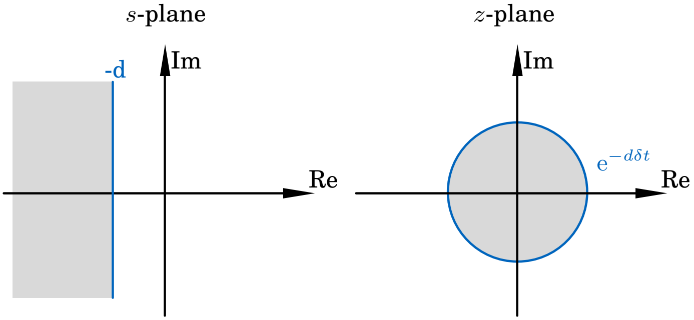

Figure 2.5: s-plane and z-plane

In the time domain, different stability criteria can be taken into account. The first one is bounded input bounded output (BIBO) stability, which is defined according to [60] p. 57 as follows:

Defintion 2.1: Bounded input bounded output (BIBO) stability

A linear system is BIBO stable if the output signal

$$||\boldsymbol{y}(t)|| < y_{\max} \quad \forall t > 0 \tag{2.26}$$

remains bounded for vanishing initial values $\boldsymbol{x}_0$ and an arbitrarily bounded input signal

$$||\boldsymbol{u}(t)|| < u_{\max} \quad \forall t > 0. \tag{2.27}$$

Another stability definition important in this work is the internal stability of a LTI system and its special case of asymptotic stability. The definition for internal stability is valid for linear, undisturbed systems, i.e. $\boldsymbol{u}(t) = \boldsymbol{0}$, with the initial values $\boldsymbol{x}_0 = \boldsymbol{x}^{\text{init}}$. Applied to Eq. (2.24) this results in

$$\dot{\boldsymbol{x}}(t) = \boldsymbol{A}\boldsymbol{x}(t). \tag{2.28}$$

This system is in equilibrium $\boldsymbol{x}_g$, if $\dot{\boldsymbol{x}} = 0$. It follows for non-singular matrices $\boldsymbol{A}$ that $\boldsymbol{x}_g = \mathbf{0}$. This means exactly one equilibrium state exists for the undisturbed, linear system if $\det\boldsymbol{A} \neq 0$. According to [61] p. 405 internal stability is defined as:

Defintion 2.2: Internal stability of LTI systems

The state of equilibrium $\boldsymbol{x}_g = \mathbf{0}$ of Eq. (2.28) is called stable (according to Ljapunow) or internally stable if a number $\alpha > 0$ exists for each $\gamma > 0$, such that for an arbitrary initial state, which fulfills the condition

$$||\boldsymbol{x}^{\text{init}}|| < \alpha, \tag{2.29}$$

the proper motion of the system in Eq. (2.28) fulfills the condition

$$||\boldsymbol{x}(t)|| < \gamma \quad \forall t > 0. \tag{2.30}$$

The state of equilibrium is called asymptotically stable if it is stable and if

$$\lim_{t \to \infty} ||\boldsymbol{x}(t)|| = 0 \tag{2.31}$$

holds.

Besides the stability definitions for a dynamic system, it is important to know if the system to be controlled can be influenced by an input vector $\boldsymbol{u}(t)$ in a prescribed way. The definition for the controllability is given in the following according to [60] p. 64:

Defintion 2.3: Controllability

A system defined by Eq. (2.24) is fully controllable if it can be transferred in a finite time interval T from any arbitrary initial state $\boldsymbol{x}^{\text{init}}$ to an arbitrarily defined final state $\boldsymbol{x}(T)$, by applying an appropriately selected input vector $\boldsymbol{u} \in [0, T]$.

In [60] p. 63 ff. also different ways for checking the controllability of a system are presented.

Finally, it might not be possible for most mechanical systems to measure all state variables of the system directly. It is often only possible to measure the output vector $\boldsymbol{y}(t)$. The problem is called observability and is defined according to [60] p. 93 as follows:

Defintion 2.4: Observability

A system defined by Eq. (2.24) and (2.25) is fully observable, if the initial state of the system $\boldsymbol{x}^{\text{init}}$ can be determined from a known distribution of the input vector $\boldsymbol{u}(t) \in [0, T]$ and the output vector $\boldsymbol{y}(t) \in [0, T]$ over a finite time interval $[0, T]$.

Again more detailed information how to determine the observability of a system is for example provided in [60] p. 92 ff.

2.4 Fluid-Structure Interaction (FSI)

This subsection describes the theoretical background for solving the coupled problem of fluid-structure interaction (FSI), i.e., coupling of the subsystems, CFD and CSD. Furthermore, the notation for coupled problems throughout this work is introduced, which is needed in CHAPTER 3.

FSI means the fully coupled, transient solution of a fluid flow interacting with a structure, in this work. In a physical context, this means the fluid flow applies a traction force onto the structure, the structure deforms, the fluid flow recognizes the deformed structure and adapts itself to the deformed geometry. Fig. 2.6 b) shows this concept, which is defined as two-way coupling. For comparison Fig. 2.6 a) also shows one-way coupling. One-way coupling treats the structure as a rigid object in the fluid flow, where the dynamic forces are applied to the structure. Fig. 2.6 a) also includes a pure CFD analysis, where the structure is not coupled to the fluid flow at all.

The next step describes how the problem defined above is approached numerically. The numerical solution can be either performed in a monolithic or a partitioned way. Fig. 2.7 depicts both possibilities. In FSI, monolithic means the coupled problem is formulated on a continuous level and is consistently linearized and discretized. This discretization results in one system of equations to be solved. The partitioned approach keeps the solution of the

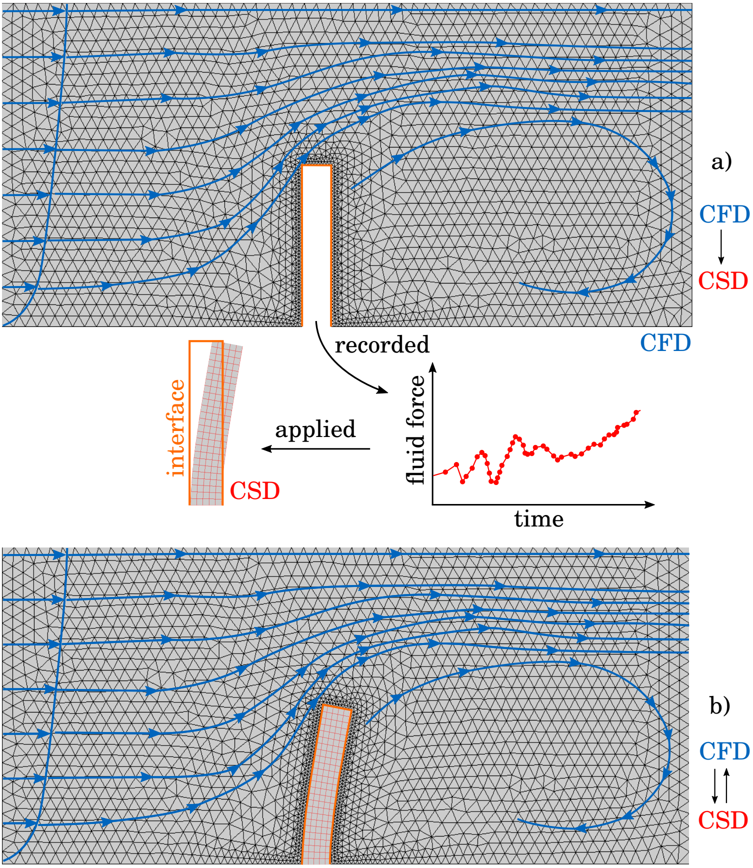

Figure 2.6: Difference of one-way and two-way coupling: a) one-way coupled FSI including pure CFD, b) two-way coupled FSI.

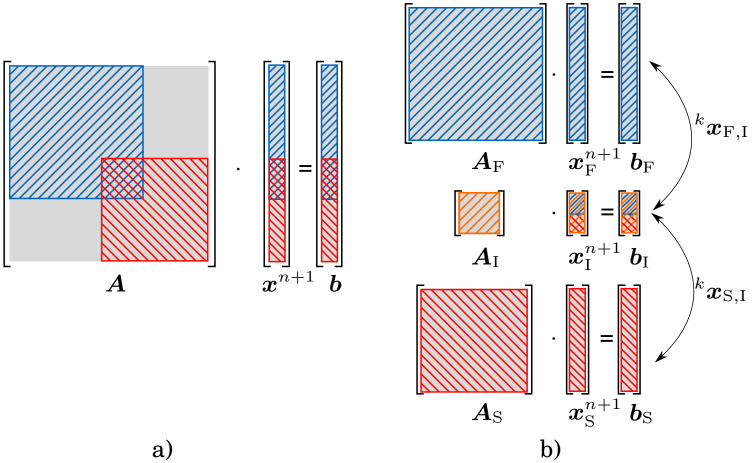

Figure 2.7: Scheme of a) monolithic and b) partitioned FSI. If the interface iteration counter $k = 0$, b) is a staggered solution scheme otherwise an iterative one.

subsystems involved independently of each other. The communication between the subsystems is shifted to the interface. In the context of FSI forces and displacements are communicated at the joint interfaces of fluid flow and structure. As can be seen in Fig. 2.7, additional conditions are necessary at the common interface (I) of the subsystems to communicate the respective quantities. Different ways of defining those conditions at the interface level exist and a comparison of the different types of decomposition can be found for a simple example [87] p. 60-65. The reader is also referred to as the literature cited there.

In this work, the classical decomposition approach for FSI, a Dirichlet-Neumann decomposition is applied, which means the traction forces are transferred from the boundary of the CFD subsystem to the CSD subsystem (Neumann condition) and displacements are transferred from the boundary of the CSD subsystem to the CFD subsystem (Dirichlet condition). As [87] p. 65 summarizes, the choice of the best decomposition of a coupled problem is highly problem dependent. The choice of Dirichlet-Neumann coupling has shown to be the best for FSI (e.g. [100], [57], [18]).

Furthermore, it is closest to the real physical problem of FSI and thus needs no additional assumptions.

2.4.1 Communication Pattern

Another crucial part of the partitioned simulation of the FSI problem is the communication pattern between the different subsystems. In [87] p. 58 and 59 and more in detail in [95] p. 31 the two fundamental communication patterns for partitioned FSI are presented, named Gauss-Seidel (GS) and Jacobian (J) pattern, following the naming of the splitting methods for solving linear equation systems. Accordingly, in the J pattern, communication between the subsystems only occurs after all subsystems have been solved. This offers the possibility of solving the subsystems in parallel but has the disadvantage of a slower convergence rate. The GS pattern solves the subsystems subsequently, and hence it is possible to transfer information between the subsystems throughout the solution process.

From the partitioning, an additional equation system is existing for the interface conditions. This system of equations has to be solved, too. Independent of the the CFD properties and the CSD problem, the interface equation system is a set of non-linear equations. For solving this set of non-linear interface equations, different approaches are possible. The standard schemes are fixed-point iterations with a convergence acceleration utilizing constant relaxation or a Newton scheme ([95] p. 37, Fig. 26 gives a good summary).

The general equation for a fixed point formulation can be written as

$$ {}^{k+1}\boldsymbol{x}^{n+1} = {}_{1}\boldsymbol{A}\ {}^{k}\boldsymbol{x}^{n+1} + \boldsymbol{b}^{n}. \tag{2.32} $$

Herein ${}_{1}\boldsymbol{A}^{k}$ is the iteration matrix, $\boldsymbol{b}^{n}$ is a vector remaining constant throughout the iteration process, k is the iteration counter, n the time step counter and x the vector of unknowns. Eq. (2.32) can be accelerated by relaxation ([90] p. 652 to 659) and can be rewritten as

$$ \begin{aligned} {}^{k+1}\boldsymbol{x}^{n+1} &= \beta\left({}_{1}\boldsymbol{A}\ {}^{k}\boldsymbol{x}^{n+1} + \boldsymbol{b}^{n}\right) + (1-\beta)\ {}^{k}\boldsymbol{x}^{n+1}, \\ {}^{k+1}\boldsymbol{x}^{n+1} &= {}_{\beta}\boldsymbol{A}\ {}^{k}\boldsymbol{x}^{n+1} + \beta\boldsymbol{b}^{n}. \end{aligned} \tag{2.33} $$

Herein β is a user-defined relaxation parameter and the relaxed iteration matrix ${}_{\beta}\boldsymbol{A}$ is defined as

$$ {}_{\beta}\boldsymbol{A} = \boldsymbol{I} + \beta({}_{1}\boldsymbol{A} - \boldsymbol{I}), \tag{2.34}$$

which becomes

$$ {}_{\beta}A = 1 + \beta({}_{1}A - 1), \tag{2.35}$$

in the case of a single degree of freedom system. In Eq. (2.33) the convergence behavior only depends on the relaxed iteration matrix ${}_{\beta}\boldsymbol{A}$. The relaxed iteration matrix itself depends on the relaxation parameter β and the unrelaxed iteration matrix ${}_{1}\boldsymbol{A}$ containing the system parameters and the time step. Convergence is guaranteed if in the multi-degree of freedom case if $\rho({}_{\beta}\boldsymbol{A}) < 1$ for the spectral radius ρ of the iteration matrix holds. For only one degree of freedom, i.e. the scalar case, this boils down to $|{}_{\beta}A| < 1$. For the scalar case, the following, closed-form statements can be derived:

$$\begin{aligned} \frac{2}{(1 - {}_{1}A)} = -\frac{2}{({}_{1}A - 1)} < \beta < 0, &\quad \text{if } {}_{1}A > 1 \text{ and} \\ 0 < \beta < \frac{2}{(1 - {}_{1}A)}, &\quad \text{if } {}_{1}A < 1\,. \end{aligned} \tag{2.36}$$

Additionally, for the scalar case, a statement for an optimal relaxation factor β^* can be deduced for ${}_{1}A \neq 1$ as

$$\beta^* = \frac{1}{(1 - {}_{1}A)}. \tag{2.37}$$

This means by combining Eq. (2.37) with Eq. (2.33) the solution of the iteration procedure is given as

$$\lim_{k \to \infty} \{{}^{k}x^{n+1}\} = \frac{b^n}{(1 - {}_{1}A)}, \tag{2.38}$$

which corresponds to Eq. (22) in [47] on p. 762. From this it can be concluded, if ${}_{1}A \neq 1$, a range of values for β, which lead to convergence, exist. Furthermore, inside this amount of values for β an optimal value β^* exists, which leads to convergence within one iteration.

For the fixed-point formulation, the relaxation parameter is rather set to a fixed value, which only works for exceptional cases, or an optimal relaxation parameter can be computed. The direct calculation of β^* only works for very simple cases ([47], p. 769) and is hardly possible for multi-degree of freedom problems.

The computation of the relaxation parameter has been part of active research in the past years. Examples are the Aitken acceleration proposed by [57] or more advanced schemes like the ones presented in [29] or [15], belonging to the group of quasi-Newton methods. Again [95] p. 36-37 provides a good summary and a historical overview of all different techniques. The schemes for computing the acceleration parameter can be applied to the GS pattern as well as to the J pattern in the context of a fixed point formulation. When solving the interface equation system by a Newton scheme as presented in [87] p. 75, the major problem is obtaining the interface Jacobian of the subsystems. Getting the exact values is theoretically possible because both CFD and CSD are discretized by the FEM. The information has to be condensed to the interface level by static condensation methods ([87] p. 78-80). The static condensation is a numerically costly operation, which has to be performed in every iteration step. Furthermore, the resulting condensed matrix is fully populated and ill-conditioned. Additionally, a parallelization of this kind of problem in a distributed memory environment leads to difficulties because the interface might belong to different computing partitions. Thus, additional communication throughout the solution procedure is necessary. Therefore, a better alternative and more efficient way is again applying quasi-Newton schemes to approximate the interface Jacobian.

For practical problems in the civil engineering context, the Aitken method is the most effective one. It is robust and is accessible to implement in the serial case but also for distributed memory parallelism.

Besides the variety of iterative/strong/implicit coupling schemes presented before, which perform an iteration at the interface in each time step, making them fulfill all interface constraints strictly, explicit/staggered/loose coupling schemes exist. No iterations at the interface are performed; hence the subsystems are only solved once per time step. Therefore, a good predictor is necessary for the subsequent time step. Especially the predictor presented in [31] has turned out to be a very robust and efficient alternative for practical problems, as it also has been shown in [4].

Which of the techniques for the partitioned solution of the FSI problem is to be applied is problem-dependent. The coupled problems in this work are solved by an explicit coupling approach using the predictor from [30] as long as possible. Otherwise, an implicit approach applying a GS pattern with Aitken acceleration is utilized.

2.4.2 Mapping

Following the partitioned approach for a coupled problem, here FSI, the communication between the subsystems is shifted to their common interface. The numerical solution of the subsystems by the FEM results in discrete systems. For practical problems, the different subsystems' discretizations do not coincide at the interface in most cases. Therefore, a reasonable mapping between the surface meshes of the common interfaces of the different subsystems is necessary. Many different algorithms exist for surface mapping operations ([28] and [38]) and a summary is given in [102] p. 43-60. According to [102] p. 47, the mapping for the example of the coupled FSI problem can be defined as

$$\boldsymbol{d}_{I,F} = \boldsymbol{H}_{FS}\boldsymbol{d}_{I,S}, \tag{2.39}$$

for the displacement fields. Herein $\boldsymbol{d}_{I,F}$ is the vector of the discrete interface displacements of the CFD subsystem, $\boldsymbol{H}_{FS}$ is the displacement mapping matrix and $\boldsymbol{d}_{I,S}$ is the vector of discrete displacements on the interface of the CSD subsystem. This is called a consistent mapping operation. For the mapping of the traction forces besides the consistent also a conservative mapping is possible. According to [102] p. 47 the conservative mapping operation reads

$$\boldsymbol{f}_{I,S} = \boldsymbol{H}_{FS}^{T}\boldsymbol{f}_{I,F}, \tag{2.40}$$

where $\boldsymbol{f}_{I,S}$ is the vector of traction forces on the CSD interface, $\boldsymbol{H}_{FS}$ is the same mapping matrix as for the displacement field and $\boldsymbol{f}_{I,F}$ is the vector of traction forces on the CFD interface. Eq. (2.40) is derived from the energy conservation equation and guarantees the conservation of the sum of the resultant forces and energy. [100] p. 48 gives no suggestion if consistent or conservative mapping should be applied to map the traction forces in

FSI. The reason is each of the methods returns different results. For the problems treated in this work only conservative mapping leads to correct results. The reason is that the CFD and CSD domain interface meshes generally show big differences in their discretizations.

For building the mapping matrix, different algorithms exist. This work applies the nearest element mapping. The details about the algorithm, which is also implemented in [53], can be found in [102] p. 48-50. [16] shows how to implement this algorithm for distributed memory parallelism, which is necessary to solve the large problems treated in CHAPTER 4.

2.4.3 Mesh Motion

The FSI simulations in this thesis work follow a body fitted approach. Following this approach has the consequence that the fluid mesh has to be moved according to the displacements on the common interface between the CFD and CSD domain. Therefore, the NSE in section 2.2 have been formulated in ALE kinematics. Several approaches exist to project and distribute the displacement of the interface into the fluid domain. In [71] the possibilities of performing this mesh updating are summarized. The main prerequisites for a good mesh updating scheme are defined as follows:

a) The mesh quality, especially in the regions where the flow characteristics are to be modeled most accurately, should be preserved as well as possible without re-meshing. The region where the mesh quality has to be the best is, in most cases, the region near the common interface of CFD and CSD domain.

b) The scheme should be robust, i.e., the simulation should not fail or produce wrong results due to inverted or poorly shaped elements.

c) The scheme should be efficient in order not to increase the overall computation time of the simulation severely. Additionally, it should easily be implementable for shared and distributed memory parallelism.

The scheme fulfilling each prerequisite and which is applied in this work treats the mesh similar to a linear solid in 3D and utilizes a plane stress formulation in 2D. The derivation directly follows the section 2.1. It is a modification of the scheme presented in [89], which was tested in detail and implemented in parallel in the context of [71] in [53]. It is repeated here for completeness. The approach modifies the Lamé constants in the material tensor the following way:

$$\mu_{\mathrm{M}} = \frac{\overline{E}_{\mathrm{M}}}{2(1+\nu_{\mathrm{M}})}, \; \lambda_{\mathrm{M}} = \frac{\nu_{\mathrm{M}}\overline{E}_{\mathrm{M}}}{(1+\nu_{\mathrm{M}})(1-2\nu_{\mathrm{M}})}, \tag{2.41}$$

with

$$\overline{E}_{\mathrm{M}} = E_{\mathrm{M}}\left(\frac{\mathrm{J}_0}{\det \boldsymbol{J}}\right)^{\eta}. \tag{2.42}$$

Herein J_0 is an arbitrary global scaling factor and $\det \boldsymbol{J}$ is the determinant of the Jacobian of the fluid elements. The exponent can be set as $\eta \in [0, 2.0]$ and the mesh's Poisson's ratio can be chosen in the interval $\nu_{\mathrm{M}} \in [0, 0.5]$. In the simulations conducted throughout this work the mesh motion showed the most robust behavior with the parameters $E_{\mathrm{M}} = 1.0$, $\nu_{\mathrm{M}} = 0.3$ and $\eta = 2.0$. With the approach presented here, the elements are stiffened proportionally to their element Jacobian matrix, making smaller elements behaving stiffer and larger elements behaving softer. The solution to this additional linear problem is the mesh displacement $\boldsymbol{d}_{\mathrm{M}}$ of the overall CFD domain. This means the additional mesh solution projects the displacements on the interface into the CFD domain. As can be seen in Eq. (2.18) the mesh velocity $\mathbf{u}_{\mathrm{M}}$ has to be computed to get the convective velocity w. The computation of w cannot be performed arbitrarily but has to fulfill the geometric conservation laws (GCL), firstly mentioned in [93]. Those result from the minimum prerequisite that the CFD solution on the time-varying domain has to preserve a homogeneous flow field's trivial solution. A detailed literature review concerning the GCL can be found in [100] p. 143, 144 and detailed information in [35].

In this work, the nodal mesh velocity $\boldsymbol{u}_{\mathrm{M}}$ is computed consistently with the time integration scheme of the CFD subsystem from the nodal mesh displacements $\boldsymbol{d}_{\mathrm{M}}$, i.e., by the BDF2. The test calculations in [71] show this approach fulfills the GCL conditions.

2.4.4 Notation for Coupled Problems

Finally, the notation for coupled problems, followed in this work, and which is also necessary to understand the contents of CHAPTER 3, is defined by the example of the FSI problem. The notation is in the style of the block diagram notation commonly applied in control theory, which has been introduced in Section 2.3. This kind of notation is also applied in [59] and [104].

In a first step, the blocks of the CFD and the CSD subsystem are presented with a description of their input and output quantities.

The block for the CFD subsystem is shown in Fig. 2.8 a). The CFD subsystem receives interface displacements $\boldsymbol{y}_{\mathrm{F}}^{n+1}$ as an input. The CFD subsystem with all its degrees of freedom (p, $\boldsymbol{u}$ and $\boldsymbol{u}_{\mathrm{M}}$) contained in the vector $\boldsymbol{x}_{\mathrm{F}}^{n+1}$, is described by the system transfer operator $\mathcal{G}_{\mathrm{F}}$. The CFD subsystem is solved for its unknowns $\boldsymbol{x}_{\mathrm{F}}^{n+1}$ in dependency of the displacements $\boldsymbol{y}_{\mathrm{F}}^{n+1}$ on its interface, given as an input, in order to gain the reaction forces on the interface $\boldsymbol{z}_{\mathrm{F}}^{n+1}$. Those reaction forces are then considered as the CFD subsystem's output.

For the CSD subsystem the same principle applies. The CSD block receives a disturbance force $\boldsymbol{z}_{\mathrm{S}}^{n+1}$ as an input. The CSD subsystem with all its degrees of freedom ($\boldsymbol{d}$), contained in the vector $\boldsymbol{x}_{\mathrm{S}}^{n+1}$, can be described by the transfer operator $\mathcal{G}_{\mathrm{S}}$. It is solved in dependency on the forces on its interface $\boldsymbol{z}_{\mathrm{S}}^{n+1}$. From the solution of the CSD subsystem the interface displacements $\boldsymbol{y}_{\mathrm{S}}^{n+1}$ can be gained, which are considered as the CSD subsystem's output.

It has to be emphasized again that the input and output quantities of the blocks in Fig. 2.8 are to be interpreted as quantities at the common interfaces of the subsystems. If the system only has a single degree of freedom, i.e., the interface degree of freedom coincides with the system degree of freedoms, the reference to the system quantities, indicated by the [ ] superscript for $\mathcal{G}$, is omitted for better readability.

After the description of the subsystems' blocks, they are linked by appropriate interface constraint equations summarized in the interface constraint operator $\mathcal{I}_{\mathrm{FS}}$. The index FS indicates the coupling of CFD (index F) and CSD (index S) subsystem in this case. Since a Dirichlet/Neumann coupling approach is followed here

(Sect. 2.4), the interface constraint equations contained in $\mathcal{I}_{\mathrm{FS}}$ are defined as follows:

$$\begin{aligned} \boldsymbol{y}_{\mathrm{F}}^{n+1} - \boldsymbol{y}_{\mathrm{S}}^{n+1} &= \mathbf{0}, \\ \boldsymbol{z}_{\mathrm{F}}^{n+1} + \boldsymbol{z}_{\mathrm{S}}^{n+1} &= \mathbf{0}. \end{aligned} \tag{2.43}$$

This results in the compact notation with the interface constraint operator in $\mathcal{I}_{\mathrm{FS}}(\boldsymbol{y}_{\mathrm{F}}^{n+1}, \boldsymbol{y}_{\mathrm{S}}^{n+1}, \boldsymbol{z}_{\mathrm{F}}^{n+1}, \boldsymbol{z}_{\mathrm{S}}^{n+1})$. The coupling of the blocks shown separated in Fig. 2.8 by applying the interface constraint operator is shown in Fig. 2.9 for the FSI case. The notation presented here is used later in this work to describe the extension of the FSI problem by an additional subsystem, i.e., a controller influencing the dynamics of the CSD subsystem.

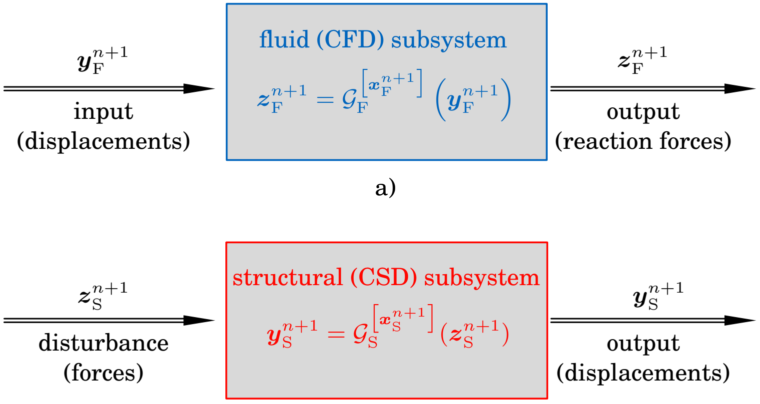

Figure 2.8: Single blocks for a) CFD and b) CSD subsystem

.

2.5 Time Integration

As mentioned in Section 2.1 and 2.2 the spatial discretization of the time depended PDEs leads to a system of ODEs of the type of Eq. (2.9), which is still continuous in time. For integrating this system of ODEs, which is a numerical initial value problem, the backward differentiation formulas (BDF) introduced in [42]

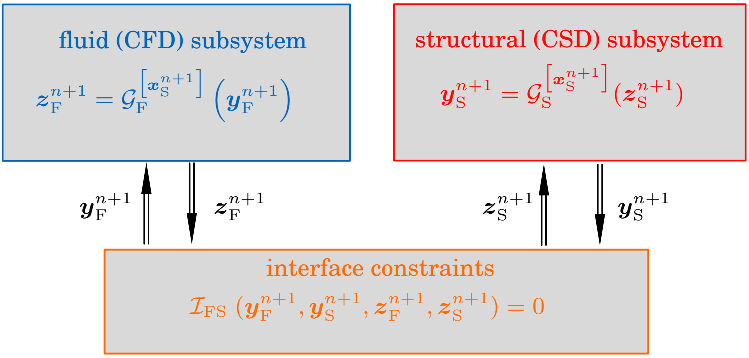

Figure 2.9: Application of the block diagram notation to the FSI problem.

can be applied. The BDF formulas can be characterized as an implicit, stiffly stable, one-level, multi-step method. In the following the BDF1 and BDF2, which are A-stable, are shortly introduced for a general vector of unknowns $\boldsymbol{q}(t) \in \mathbb{R}^{\mathrm{N_{dof}}}$. All strict mathematical stability proves of the BDF formulas and details for their derivation up to sixth order can be found in [42] p. 217, ff.
The BDF1 is defined as:

$$\begin{aligned} \boldsymbol{q}^{n+1} &= \boldsymbol{q}^{n} + \delta t \dot{\boldsymbol{q}}^{n+1}, \\ \dot{\boldsymbol{q}}^{n+1} &= \dot{\boldsymbol{q}}^{n} + \delta t \ddot{\boldsymbol{q}}^{n+1}. \end{aligned} \tag{2.44}$$

Rewriting those equations renders the approximation for the velocity

$$\dot{\boldsymbol{q}}^{n+1} = \frac{1}{\delta t}(\boldsymbol{q}^{n+1} - \boldsymbol{q}^{n}) \tag{2.45}$$

and for the acceleration

$$\ddot{\boldsymbol{q}}^{n+1} = \frac{1}{\delta t^2}(\boldsymbol{q}^{n+1} - 2\boldsymbol{q}^{n} + \boldsymbol{q}^{n-1}). \tag{2.46}$$

Herein δt is the discrete time step size and $\boldsymbol{q}^{n+1}$, $\boldsymbol{q}^{n}$ and $\boldsymbol{q}^{n-1}$ are the discrete instances of the variable, its first derivative in time $\dot{\boldsymbol{q}}$ and its second derivative in time $\ddot{\boldsymbol{q}}$ at time steps t^{n+1}, t^{n} and t^{n-1}, with n being the time step counter. In the context of mechanics the first derivative w.r.t. time are the velocities and the second derivative w.r.t. time the accelerations. The initial conditions are defined as

$$\boldsymbol{q}^0 = \boldsymbol{q}^{\text{init}} \tag{2.47}$$

and

$$\boldsymbol{q}^{-1} = \boldsymbol{q}^{\text{init}} - \frac{1}{\delta t}\dot{\boldsymbol{q}}^{\text{init}}. \tag{2.48}$$

The BDF1 has first order accuracy and suffers from numerical damping. Thus for practical applications, the BDF2 is a better choice. Accordingly, the approximation of the velocity by the BDF2 is defined as

$$\dot{\boldsymbol{q}}^{n+1} = \frac{1}{\delta t}\Big(\frac{3}{2}\boldsymbol{q}^{n+1} - 2\boldsymbol{q}^n + \frac{1}{2}\boldsymbol{q}^{n-1}\Big) \tag{2.49}$$

and the acceleration as

$$\ddot{\boldsymbol{q}}^{n+1} = \frac{1}{\delta t^2}\Big(\frac{9}{4}\boldsymbol{q}^{n+1} - 3\boldsymbol{q}^n + \frac{3}{4}\boldsymbol{q}^{n-1}\Big) + \frac{1}{\delta t}\Big(- 2\dot{\boldsymbol{q}}^n + \frac{1}{2}\dot{\boldsymbol{q}}^{n-1}\Big). \tag{2.50}$$

The BDF2 has second order accuracy and does not suffer from numerical damping. In order to obtain the initial conditions $\boldsymbol{q}^{\text{init}}$ and $\dot{\boldsymbol{q}}^{\text{init}}$ the first two time steps can be solved by the BDF1 method.

2.6 Software Environment and Simulation Time

The main problems when dealing with partitioned multiphysics simulations are the coupling of the software codes of the different subsystems and the computation time. Most of the codes available cannot deal with multiphysics problems inherently but are specialized in one type of physical problem. Thus in the past years, plenty of research has been conducted to develop coupling tools to couple those different types of software (e.g., [87], [95]). The application of those independent coupling tools works well, as long as the problems do not grow too large. As soon as real-world problems, like in CHAPTER 4 should be solved, those tools show their limits. Additionally, software development and solving multiphysics problems, especially in science, involves working in teams containing experts for the different subproblems. Furthermore, most of the scientific projects are supported by public funds and thus it should be evident that all outcomes of those projects, including the software code, should be accessible for everyone who is interested in them.

Hence for all simulations and developments carried out in the context of this thesis work, the open-source framework Kratos Multiphysics [27] was applied. The Kratos is freely accessible on GitHub [53], is written in C++ and is designed to allow collaborative development by large teams of researchers focusing on modularity as well as on performance. The Kratos features a ”core” and ”applications” approach where ”standard tools” (databases, linear algebra, search structures, etc.) come as a part of the core and are available as building blocks in the development of ”applications” which focus on the solution of the problems of interest. Its ultimate goal is to simplify the development of new numerical methods.

The Kratos also works on cluster systems, which makes it possible to solve large coupled problems. The simulations in CHAPTER 4 in this thesis work were conducted on the LRZ SuperMUC-NG cluster in the context of the project ”Wind-Structure Interaction Simulations for High-Rise, Wide-Span and Slender Civil Engineering Structures” (project id: pn56ba). To obtain calculation time on the SuperMUC-NG, a proposal, which undergoes a review by two independent experts in high-performance computing, was necessary. Besides basic project information, this proposal also had to include studies concerning the Kratos’ parallel performance. Those had been conducted for FSI problems testing CSD and CFD solver separately, but also FSI. As test case served the problem presented in Section 4.5, with up to $30e6$ elements. The Kratos shows good parallel scaling for such a case, whereby the optimal number of elements per CPU core for CFD is approximately $3\mathrm{e}4$ and for CSD with shell elements approximately $2\mathrm{e}3$. This results in approximately 300 CPU cores for an optimal performance of a typical FSI simulation with $10e6$ fluid and $3\mathrm{e}5$ shell elements. In this constellation the simulation time for a typical physical time $T_{\mathrm{phys}} = 600$ s with $\delta t = 0.02$ s is about 72 h, when running the simulation on the SuperMUC-NG.

Chapter 3

Fluid-Structure-Control Interaction

In this Chapter, the coupled problem of fluid-structure-control interaction (FSCI) is treated in a partitioned way. This means an open-loop or closed-loop control unit, which manipulates the structure's dynamics, is added to the well-known two field problem of fluid-structure interaction (FSI). This kind of problem statement was first mentioned in [37] (p. 3262 and 3263), but has not been followed in more detail. Also in [87], FSCI to reduce flow-induced structural displacements has been mentioned as a side note in the context of testing the algorithm developed therein.

In contrast to the present contribution, a rigid structure with one degree of freedom with small displacements and a very simple control-law is shown. Furthermore, [87] utilizes a Jacobi pattern instead of a Gauss-Seidel pattern.

The objective of applying a control unit to the FSI problem is getting a minimum or at best zero displacements.

In the case of the FSCI problem, the partitioned approach makes it simpler to add the controller to the problem. In the partitioned approach, an important issue is the stability of the overall simulation [10]. Analyzing the stability behavior of multiphysics problems, the superposition of many different effects may occur.

To get a good insight into the behavior of such complicated problems in computational FSI, it became the well-established practice to step back to highly simplified model problems for detailed investigations of different solution schemes. Such simplified models only represent the relevant properties of the actual FSI problem; thus, they give more insight and open the opportunity to formulate closed-form formulations. Within this chapter, such a simplified model problem, used for instance in [31] p. 4-6 and [48], p. 1365, is expanded. [31], Remark I p. 5-6 and conclusion p. 20, 21 as well as [20] show that this simplified model problem is sufficient for the analysis of a broad spectrum of solution schemes for FSI problems regarding properties like stability, convergence behavior, accuracy, and high-frequency damping. Thus the overall behavior of multi-degree of freedom, FSI problems, is explained quite well ([47] and [48]). The essential findings and algorithms obtained by the simplified model problem can be applied to more complex multi-degree of freedom examples.

The content and ideas of this Chapter, including figures and tables, have been published first in a short version in [72] and finally in their full version, including APPENDIX A in [104]. They have also been part of [58] and [59], which were written under essential scientific, technical and textual supervision of the author of this thesis. For the sake of completeness, the content of the sources mentioned before is included in this thesis work, too.

3.1 The Simplified Model Problem

A generic control unit extends the simplified model problem introduced by [31] and [48]. According to [31] and [48], the system approximating the FSI scenario most simply is the combination of a point mass, linear damper, and a linearly elastic spring. Fig. 3.1 illustrates this simplified model problem in in a monolithic version a) and a partitioned version b). Fig. 3.1 b) visualizes the decomposition into three subsystems and the explicit realization of interfaces (each creating an interface constraint equation). Fig. 3.1 is described in more detail during this subsection. The newly proposed simplified FSCI model problem's features can be summarized as follows: The coupling of a first-order ODE representing the fluid flow and a second-order ODE representing the structure reproduces the FSI problem. The FSI problem is extended to the FSCI problem by adding the algebraic ODE of the controller. In the simplified model problem, the combination of viscosity/inertia in one subsystem (fluid flow) and stiffness/inertia in the other (structure) also corresponds to the main characteristics of FSI problems. The FSI subproblem still dominates the physics since inertia is limited to the fluid flow and the structure. The controller is only adjusting the dynamics of the structure. Here the iterative/strong/implicit coupling described in section 2.4 is applied. The monolithic version in sub-figure a) results in the well-known single degree of freedom (SDoF) system

$$m\ddot{y}(t) + c\dot{y}(t) + ky(t) = u(t), \tag{3.1}$$

with its initial conditions according to Eq. (2.2)

$$\begin{aligned} y(0) &= y^{\text{init}}, \\ \dot{y}(0) &= \dot{y}^{\text{init}}. \end{aligned} \tag{3.2}$$

This is the linear, scalar version of Eq. (2.9). The variable $u(t)$

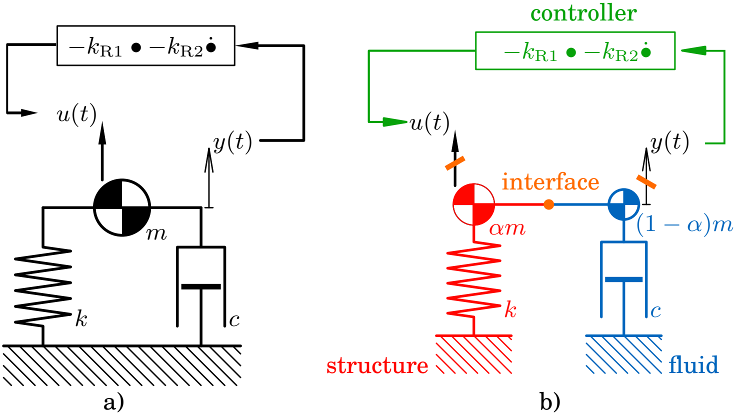

Figure 3.1: Simplified model problem: a) monolithic, b) partitioned.

on the right hand side represents the manipulation variable. Eq. (3.1) is equivalent to [31] p. 5, enhanced by a generic, but representative state-feedback controller. The state-feedback controller equation for $w(t) = 0$, which means, $e(t) = w(t) - y(t)$ is defined as

$$u(t) = -k_{\mathrm{R1}} e(t) - k_{\mathrm{R2}} \dot{e}(t). \tag{3.3}$$

The constant factors k_{R1} for the displacement and k_{R2} for the velocity in the manipulation variable u(t) are used to tune the controller, which is the basic PD control law. Inserting Eq. (3.3) into (3.1) one gets

$$m\ddot{y}(t) + (c + k_{\mathrm{R2}})\,\dot{y}(t) + (k + k_{\mathrm{R1}})\,y(t) = 0, \tag{3.4}$$

with the initial conditions from Eq. (3.2), which is a controlled SDoF system. In the following this is referred to as simplified model problem. The manipulation variable $u(t)$ is treated as Neumann boundary condition on the SDoF system, which corresponds to a disturbing force in this case. Therefore no additional displacement degree of freedom is added. This type of control results in pure force control, which also corresponds to the approach followed in CHAPTER 4.

3.1.1 Monolithic Approach

For the temporal discretization of the monolithic model problem the BDF1 (section 2.5) is applied. Applied to Eq. (3.4) this leads to the time discrete monolithic expression of the coupled system.

$$\begin{aligned} &\Big(m + (c + k_{\mathrm{R2}})\,\delta t + (k + k_{\mathrm{R1}})\,\delta t^2\Big)\, y^{n+1} \\ &- \big(2m + (c + k_{\mathrm{R2}})\,\delta t\big)\, y^n + m y^{n-1} = 0 \end{aligned} \tag{3.5}$$

and its discrete initial conditions

$$\begin{aligned} y^{-1} &= y^{\mathrm{init}} - \delta t \dot{y}^{\mathrm{init}}, \\ y^0 &= y^{\mathrm{init}}. \end{aligned} \tag{3.6}$$

Thus it is subsequently possible to derive statements, which reflect the choice of the controller parameters k_{R1} and k_{R2} for which the controlled system shows stable dynamics.

3.1.1.1 Analysis of the Time-Continuous Problem

The stability region Ω_{c} for the time-continuous, monolithic simplified model problem Eq. (3.4) is derived using its characteristic polynomial. The characteristic polynomial reads

$$p(s) = ms^2 + (c + k_{R2})s + (k + k_{R1}). \tag{3.7}$$

This is Eq. (3.4) transformed to the complex s-plane by a Laplace transform, where s is a complex number. The roots of Eq. (3.7) are defined as

$$\{s \in \mathbb{C} \mid p(s) = 0\}. \tag{3.8}$$

In this case asymptotically and BIBO stability coincide. The time-continuous stability region Ω_c results in

$$\begin{aligned} \Omega_\mathrm{c} &= \left\{ k_\mathrm{R1}, k_\mathrm{R2} \in \mathbb{R} \middle| \max_{i=1,2} \left\{ \mathrm{Re}\{s_i\} \right\} \leq 0 \right\} \\ &= \left\{ k_\mathrm{R1}, k_\mathrm{R2} \in \mathbb{R} \middle| k_\mathrm{R1} \geq -k \quad \wedge \quad k_\mathrm{R2} \geq -c \right\}. \end{aligned} \tag{3.9}$$

Herein s_i denote the two poles of the time-continuous problem, which are specified by its eigenvalues.

3.1.1.2 Analysis of the Time-Discrete Problem

In a similar way, the stability region Ω_d for the time-discrete, monolithic model problem Eq. (3.5) is determined. Its characteristic polynomial reads

$$\begin{aligned} p(z) = &\left(m + (c + k_\mathrm{R2})\, \delta t + (k + k_\mathrm{R1})\, \delta t^2 \right) z^2 \\ &- \left(2m + (c + k_\mathrm{R2})\, \delta t \right) z + m = 0. \end{aligned} \tag{3.10}$$

This is Eq. (3.5) transformed to the complex z-plane by the Z-Transform described in APPENDIX C. The roots of Eq. (3.10) are defined as

$$\{z \in \mathbb{C} \mid p(z) = 0\}. \tag{3.11}$$

The disturbance force $z(t)$ is not to be mixed up with the z from the Z-transform.

The two basic stability conditions change for the time-discrete case [40]. Consequently, the time-discrete region Ω_d formulated in the z-plane results in

$$\Omega_\mathrm{d} = \left\{ k_\mathrm{R1}, k_\mathrm{R2} \in \mathbb{R} \middle| \max_{i=1,2} \left\{ |z_i| \right\} \leq 1 \right\}. \tag{3.12}$$

Mapped back to the s-plane with Eq. (C.15) this reads

$$\begin{aligned} \Omega_\mathrm{d} &= \{k_\mathrm{R1}, k_\mathrm{R2} \in \mathbb{R} \Big| \frac{1}{\delta t} \ln \left(\max_{i=1,2} \{|z_i|\} \right) \leq 0\} \\ &= \{k_\mathrm{R1}, k_\mathrm{R2} \in \mathbb{R} \big| k_\mathrm{R1} \geq -k \\ &\wedge \quad k_\mathrm{R2} \geq -c - \delta t(k_\mathrm{R1} + k)\}. \end{aligned} \tag{3.13}$$

Herein z_i denote the two poles of the time-discrete problem, which are specified by its eigenvalues.

Clearly recognizable in Eq. (3.13) is the fact that the time-continuous stability region Ω_c representing real physics gets extended to an apparently larger, time-discrete stability region Ω_d. This has to be taken into account when conducting a simulation based controller design. The stability considerations performed here result in a stable system for all of the parameters of k_R1 and k_R2 that fulfill the criteria stated in Eq. (3.9) or Eq(3.13), depending if we are looking at the time continuous or the time discrete system. The selection of the optimal parameters, i.e. the controller design, is not conducted here explicitly, because it is not of interest for the following investigations. There exists a vast amount of state of the art possibilities how to select the optimal controller parameters for a PD controller in the literature (e.g. [40] p. 180 ff). One possibility for a concrete example is shown in the following in Sect. 3.4.

3.1.2 Partitioned Approach

The initial step of a partitioned approach is the decomposition of the multiphysics problem into single physics subproblems and appropriate interface constraints covering the interactions. The division in subsystems is referred to as partitioning [9] and is shown in Fig. 3.1 b).

A preparatory step for reaching a suitable partitioning of the simplified model problem is the reformulation of the ODE Eq. (3.1) as

$$\begin{aligned} &(\alpha m)\ddot{y}(t) + ((1-\alpha)m)\ddot{y}(t) + c\dot{y}(t) + kx(t) \\ &= u(t) + z(t). \end{aligned} \tag{3.14}$$

The disturbance force on the right hand side $z(t)$ has to be split up into $z_\mathrm{F}(t)$ and $z_\mathrm{S}(t)$, since Eq. (3.15) and (3.16), which are the partitioned equations, need a disturbance force each. In combination with Eq. (3.2) and Eq. (3.3) this leads finally to the partitioned, simplified model problem:

$$\big((1-\alpha)m\big)\,\ddot{y}_{\mathrm{F}}(t)+c\dot{y}_{\mathrm{F}}(t)=z_{\mathrm{F}}(t), \tag{3.15}$$

is referred to as the fluid subsystem (index F),

$$(\alpha m)\ddot{y}_{\mathrm{S}}(t)+ky_{\mathrm{S}}(t)=u_{\mathrm{S}}(t)+z_{\mathrm{S}}(t), \tag{3.16}$$

as the structural subsystem (index S) and

$$u_{\mathrm{C}}(t)=\,-k_{\mathrm{R1}}y_{\mathrm{C}}(t)-k_{\mathrm{R2}}\dot{y}_{\mathrm{C}}(t), \tag{3.17}$$

as controller subsystem (index C). The physical interaction is shifted to the interface constraints (index I)

$$\begin{aligned} y_{\mathrm{F}}(t)-y_{\mathrm{S}}(t)&=0,\\ z_{\mathrm{F}}(t)+z_{\mathrm{S}}(t)&=0,\\ y_{\mathrm{S}}(t)-y_{\mathrm{C}}(t)&=0,\\ u_{\mathrm{S}}(t)-u_{\mathrm{C}}(t)&=0. \end{aligned} \tag{3.18}$$

The initial conditions for the structure are given with

$$\begin{aligned} y_{\mathrm{S}}(0)&=y_{\mathrm{S}}^{\mathrm{init}},\\ \dot{y}_{\mathrm{S}}(0)&=\dot{y}_{\mathrm{S}}^{\mathrm{init}}. \end{aligned} \tag{3.19}$$

Thus, the structural domain is represented by the elastic spring k and the point mass share αm, the fluid domain by the linear damper c, and the point mass share $(1-\alpha)m$. The interface constraints cover the interactions between these two domains (FSI) and between structure and controller (SCI). $y(t)$ describes the displacement, which corresponds to the measured output. $z(t)$ is the disturbance (force) originating from the partitioning and $u(t)$ the manipulation variable. Eq. (3.18) formulate the interface constraint equations.

The parameter $\alpha\in[0,1)$ describes the mass distribution between fluid and structural subsystem, i.e.

$$\frac{m_{\mathrm{S}}}{m}=\alpha\quad\text{and}\quad\frac{m_{\mathrm{F}}}{m}=1-\alpha, \tag{3.20}$$

and allows to precisely quantify the added-mass effect [31], [20] and [98], which also applies to FSCI problems. Other "α"-parameters regarding the damping c and the stiffness k would be feasible ([31] p. 5), too. At this stage only one parameter α associated with the mass m is considered. In the dominating FSI subproblem the convergence properties of the relaxed iteration factor ${}_{\beta}A$ in the limit case $\delta t \to 0$ depend only on this one parameter [47] (section 3, p. 763).

The temporal discretization of the partitioned simplified model problem Eq. (3.15), (3.16), (3.17), (3.18) and (3.19), with the BDF1 scheme leads to the discrete, partitioned, simplified model problem. It consists of the discrete fluid Eq. (3.21), structural Eq. (3.22) and controller subsystem Eq. (3.23):

$$\begin{aligned} z_{\mathrm{F}}^{n+1} =& \frac{(1-\alpha)m + c\delta t}{\delta t^2} y_{\mathrm{F}}^{n+1} \\ & - \frac{(1-\alpha)m + c\delta t}{\delta t^2} y_{\mathrm{F}}^{n} - \frac{(1-\alpha)m}{\delta t} \dot{y}_{\mathrm{F}}^{n}, \\ z_{\mathrm{F}}^{n+1} =& \mathcal{G}_{\mathrm{F}}\left(y_{\mathrm{F}}^{n+1}\right), \end{aligned} \tag{3.21}$$

$$\begin{aligned} y_{\mathrm{S}}^{n+1} &= \frac{\delta t^2}{\alpha m + k\delta t^2} z_{\mathrm{S}}^{n+1} + \frac{\delta t^2}{\alpha m + k\delta t^2} u_{\mathrm{S}}^{n+1} \\ &\quad + \frac{\alpha m}{\alpha m + k\delta t^2} y_{\mathrm{S}}^{n} + \frac{\alpha m \delta t}{\alpha m + k\delta t^2} \dot{y}_{\mathrm{S}}^{n}, \\ y_{\mathrm{S}}^{n+1} &= \mathcal{G}_{\mathrm{S}}\left(z_{\mathrm{S}}^{n+1}, u_{\mathrm{S}}^{n+1}\right), \end{aligned} \tag{3.22}$$

$$\begin{aligned} u_{\mathrm{C}}^{n+1} &= -\frac{k_{\mathrm{R}1}\delta t + k_{\mathrm{R}2}}{\delta t} y_{\mathrm{C}}^{n+1} + \frac{k_{\mathrm{R}2}}{\delta t} y_{\mathrm{C}}^{n}, \\ u_{\mathrm{C}}^{n+1} &= \mathcal{G}_{\mathrm{C}}\left(y_{\mathrm{C}}^{n+1}\right) \end{aligned} \tag{3.23}$$

and the discrete interface equations

$$\begin{aligned} y_{\mathrm{F}}^{n+1} - y_{\mathrm{S}}^{n+1} &= 0, \\ \text{i.e.} \qquad \mathcal{I}_{\mathrm{FS},y}\left(y_{\mathrm{F}}^{n+1}, y_{\mathrm{S}}^{n+1}\right) &= 0, \end{aligned} \tag{3.24}$$

$$\begin{aligned} z_{\mathrm{F}}^{n+1} + z_{\mathrm{S}}^{n+1} &= 0, \\ \text{i.e.} \qquad \mathcal{I}_{\mathrm{FS},z}\left(z_{\mathrm{F}}^{n+1}, z_{\mathrm{S}}^{n+1}\right) &= 0, \end{aligned} \tag{3.25}$$

$$\begin{aligned} y_{\mathrm{S}}^{n+1} - y_{\mathrm{C}}^{n+1} &= 0, \\ \text{i.e.} \qquad \mathcal{I}_{\mathrm{SC},y}\left(y_{\mathrm{S}}^{n+1}, y_{\mathrm{C}}^{n+1}\right) &= 0, \end{aligned} \tag{3.26}$$

$$\begin{aligned} u_{\mathrm{S}}^{n+1} - u_{\mathrm{C}}^{n+1} &= 0, \\ \text{i.e.} \qquad \mathcal{I}_{\mathrm{SC},u}\left(u_{\mathrm{S}}^{n+1}, u_{\mathrm{C}}^{n+1}\right) &= 0. \end{aligned} \tag{3.27}$$

The operators $\mathcal{G}$ and $\mathcal{I}$ describe the input-output relation for the specific subsystem and the interface constraint for the specific coupling, respectively.

The FSI subproblem, i.e. the coupling between fluid and structure, converges to the solution of Eq. (3.21), (3.22), (3.24) and (3.25). The emerging system is the "fluid-structure (FS) subsystem", $\mathcal{G}_{\mathrm{FS}}\left(u_{\mathrm{S}}^{n+1}\right)$. Accordingly, the converged solution of the SCI subproblem, i.e. the coupling between structure and controller fulfills Eq. (3.22), (3.23), (3.26) and (3.27). This leads to a "structure-controller (SC) subsystem", $\mathcal{G}_{\mathrm{SC}}(z_{\mathrm{S}}^{n+1})$.

3.2 Extension of the Notation for the FSCI Problem

Before starting with further investigations concerning the FSCI problem, the notation introduced for the FSI problem in Sect. 2.4.4 has to be extended. In this example the controlling system is supposed to act with a force on a single node of the CSD subsystem. Thus in a first step the block of the CSD subsystem has to be extended. The extended block for the CSD subsystem is shown in Fig. 3.2 a). The additional input quantity u_{S}^{n+1} denotes the input force of the controller acting on the structure, which is a scalar value in this case. The CSD subsystem, described by the system transfer operator $\mathcal{G}_{\mathrm{S}}$ is now additionally depending on

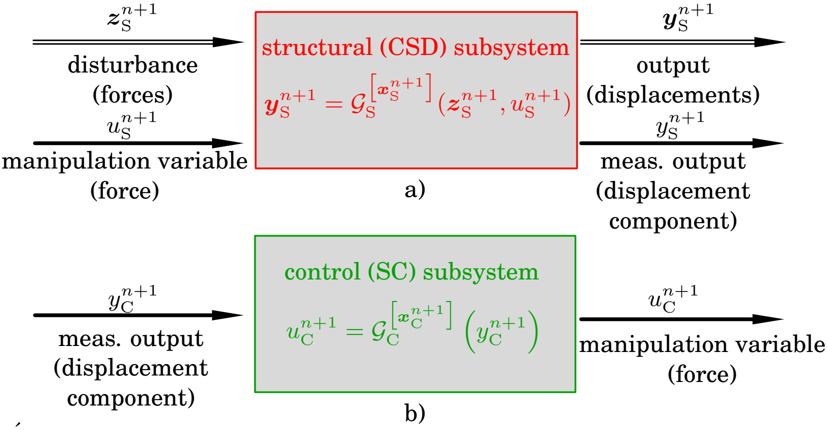

Figure 3.2: Single blocks for extended CSD a) and for SC b)

u_S^{n+1}. From the solution of the CSD subsystem the structural displacements $\boldsymbol{y}_\mathrm{S}^{n+1}$ on the interface and the measured output y_S^{n+1} can be gained and are the output quantities of the CSD block.

Fig. 3.2 b) shows the single block of the new subsystem involved now. The input to the SC subsystem is the measured output of y_C^{n+1}, which is a displacement component. The SC subsystem is also described by its system transfer operator $\mathcal{G}_\mathrm{C}$, which depends on the measured output y_C^{n+1} from its interface. The output of the SC system, u_C^{n+1}, referred to as manipulation variable, is a force. The description shown in Fig. 2.2 is consistent with the example treated in Sect. 3.4, considering the SC subsystem as a SISO and CFD and CSD subsystems as MIMO systems. Of course, it is possible to apply this notation to an arbitrary combination of SISO and MIMO systems. This only changes the type or arrows (double- or single-lined) used and if the quantities are written with bold characters or not.

With this extension of the notation initiated in Sect. 2.4.4, it is now possible to derive statements for the coupling for CFD, CSD, and SC subsystem, by the block diagram notation.

3.3 Alternatives of the Gauss–Seidel Pattern for Three Different Physical Fields

Three different alternatives for the serial GS pattern for the FSCI problem are described and applied to the partitioned simplified model problem consisting of Eq. (3.21)–(3.27).

The resulting nonlinear interface equation system can be solved in different ways. For each of those variants the limits of the unrelaxed ${}_1A$ and the relaxed ${}_\beta A$ iteration factors are derived and the optimal relaxation parameter β^* is calculated. The algorithms in pseudocode notation for the different alternatives can be found in APPENDIX A.

3.3.1 No Nesting FSCI

In the context of this subsection, the acronym FSCI also stands for the more specific iterative coupling scheme illustrated in Fig. 3.3, where the Gauss-Seidel communication pattern is realized without nesting of any subproblems, i.e., the coupled problem is solved with a single fixed-point iteration loop. This means only one interface equation system $\mathcal{I}_{\mathrm{FSC}}$ has to be solved. In the graphical representation as a block diagram, each of the physical fields and the interface equations are outlined by one of the blocks. The arrows describe the input and output quantities, which are passed between the blocks. Applying Eq. (2.32) to the partitioned, simplified model problem the equations of the algorithm condense down to

$$\begin{aligned}
{}^{k+1}y_{\mathrm{S}}^{n+1} &\overset{(3.22)}{=} \mathcal{G}_{\mathrm{S}}\left({}^{k}z_{\mathrm{S}}^{n+1}, {}^{k}u_{\mathrm{S}}^{n+1}\right) \\
&\overset{(3.25),(3.27)}{=} \mathcal{G}_{\mathrm{S}}\left(-{}^{k}z_{\mathrm{F}}^{n+1}, {}^{k}u_{\mathrm{C}}^{n+1}\right) \\
&\overset{(3.21),(3.23)}{=} \mathcal{G}_{\mathrm{S}}\left(-\mathcal{G}_{\mathrm{F}}\left({}^{k}y_{\mathrm{F}}^{n+1}\right), \mathcal{G}_{\mathrm{C}}\left({}^{k}y_{\mathrm{C}}^{n+1}\right)\right) \\
&\overset{(3.24),(3.26)}{=} \mathcal{G}_{\mathrm{S}}\left(-\mathcal{G}_{\mathrm{F}}\left({}^{k}y_{\mathrm{S}}^{n+1}\right), \mathcal{G}_{\mathrm{C}}\left({}^{k}y_{\mathrm{S}}^{n+1}\right)\right), \\
\text{i.e.} \qquad {}^{k+1}y_{\mathrm{S}}^{n+1} &= -\frac{(1-\alpha)m + (c + k_{R2})\delta t + k_{R1}\delta t^2}{\alpha m + k\delta t^2}\,{}^{k}y_{\mathrm{S}}^{n+1} + b^n, \\
\text{i.e.} \qquad {}^{k+1}y_{\mathrm{S}}^{n+1} &= {}_1A_{\mathrm{FSCI}}\;{}^{k}y_{\mathrm{S}}^{n+1} + b^n.
\end{aligned} \tag{3.28}$$

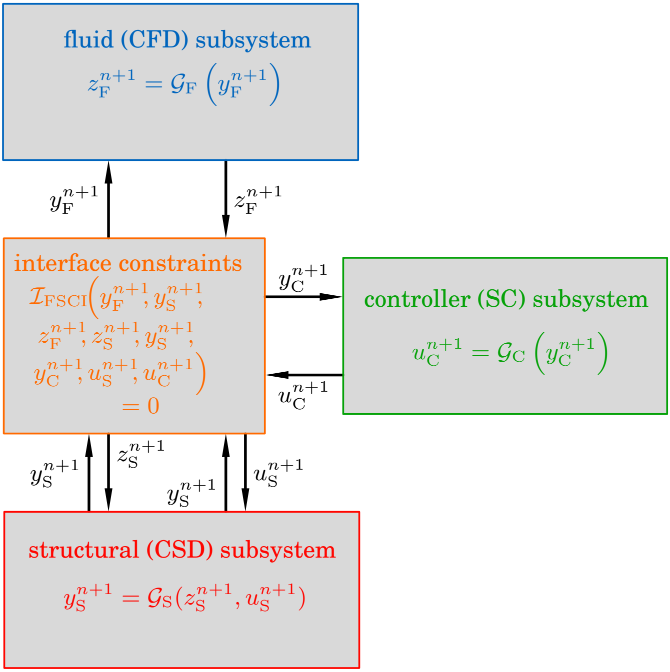

Figure 3.3: Block diagram for the FSCI scheme.

Herein b^n is the part remaining constant during the iteration process.

The limit of the iteration factor

$$\lim_{\delta t \to 0} \left\{ {}_1A_{\mathrm{FSCI}} \right\} = \frac{\alpha - 1}{\alpha}, \tag{3.29}$$

shows pure dependency on the mass distribution α.

Supplemented by relaxation, the FSCI scheme shown in Eq.

(3.28) is extended to

$$\begin{aligned}
{}^{k+1}y_{\mathrm{S}}^{n+1} &= \beta\mathcal{G}_{\mathrm{S}}\big(-\mathcal{G}_{\mathrm{F}}({}^{k}y_{\mathrm{S}}^{n+1}),\mathcal{G}_{\mathrm{C}}({}^{k}y_{\mathrm{S}}^{n+1})\big)\\
&\quad+(1-\beta)\,{}^{k}y_{\mathrm{S}}^{n+1},\\
\text{i.e.}\quad {}^{k+1}y_{\mathrm{S}}^{n+1} &= -\,\frac{(\beta-\alpha)m+\beta\big((c+k_{R2})\delta t+k_{R1}\delta t^{2}\big)-(1-\beta)k\delta t^{2}}{\alpha m+k\delta t^{2}}\\
&\quad {}^{k}y_{\mathrm{S}}^{n+1}+\beta b^{n},\\
\text{i.e.}\quad {}^{k+1}y_{\mathrm{S}}^{n+1} &= {}_{\beta}A_{\mathrm{FSCI}}\,{}^{k}y_{\mathrm{S}}^{n+1}+\beta b^{n}.
\end{aligned} \tag{3.30}$$

The limit of the iteration factor

$$\lim_{\delta t\to 0}\left\{{}_{\beta}A_{\mathrm{FSCI}}\right\}=\frac{\alpha-\beta}{\alpha}, \tag{3.31}$$

is now clearly determined by the mass distribution α and the relaxation parameter β.

According to Eq. (2.37) the optimal relaxation parameter becomes

$$\beta^{*}_{\mathrm{FSCI}}=\frac{\alpha m+k\delta t^{2}}{m+(c+k_{\mathrm{R2}})\,\delta t+(k+k_{\mathrm{R1}})\,\delta t^{2}}. \tag{3.32}$$

Each term in the denominator is positive, non-zero for physically relevant parameters and stable controller settings according to Eq. (3.9). Thus, it can always be found.

3.3.2 Nesting of the FSI Sub-Problem ([FS]CI)

The acronym [FS]CI denotes the specific iterative coupling scheme illustrated in Fig. 3.4 depicts the GS communication pattern with nesting of the FSI subproblem, which is indicated by bracketing [FS]. The nesting of sub-problems corresponds to the inclusion of bi-coupling schemes mentioned in [19]. As can be seen in Fig. 3.4, two interface constraint equations are to be set up. One for the FS subproblem (inner interface constraints) $\mathcal{I}_{\mathrm{FS}}$ and one for the overall coupling between the FS subsystem with the control subsystem (outer interface constraints) $\mathcal{I}_{[\mathrm{FS}]\mathrm{C}}$. At first the FS loop is iterated with constant manipulation variable until convergence. The converged values are used as information for the iterations of the outer loop. If the outer loop does not converge, the algorithm has to return to the inner loop. The inner and outer iteration loop have to converge before proceeding to the next time step. The scheme is again applied to the partitioned simplified model problem. Since the pure FSI is solved in its iteration loop, it is possible to calculate the best relaxation factor once for the FSI problem, involving two coupled fields and for the complete FSCI problem involving three coupled fields.

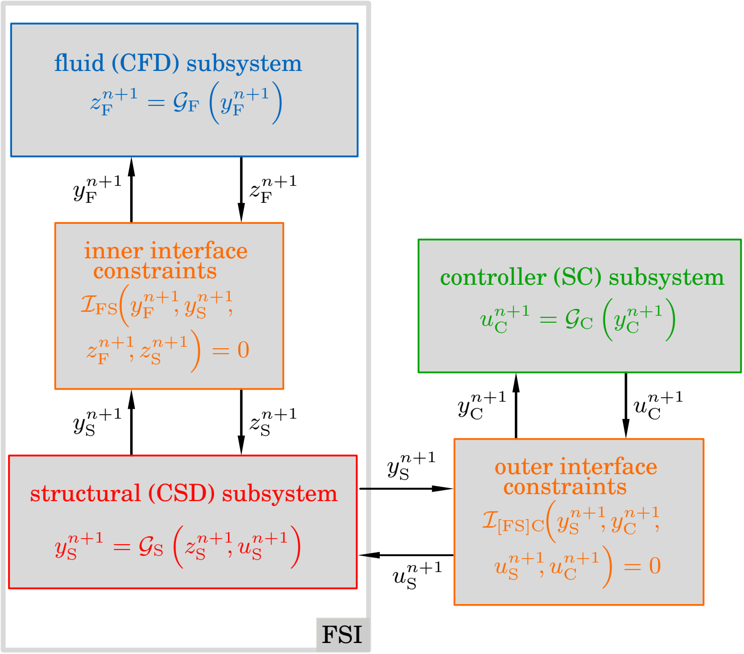

Figure 3.4: Block diagram for the [FS]CI scheme.

The inner FSI fixed-point iteration of the algorithm condenses down to

$$\begin{aligned}
{}_{l+1}{}^{k}y_{\mathrm{S}}^{n+1} &\overset{(3.22)}{=} \mathcal{G}_{\mathrm{S}}\left({}_{l}{}^{k}z_{\mathrm{S}}^{n+1}, {}^{k}u_{\mathrm{S}}^{n+1} = \text{const.}\right)\\
&\overset{(3.25)}{=} \mathcal{G}_{\mathrm{S}}\left(-{}_{l}{}^{k}z_{\mathrm{F}}^{n+1}, {}^{k}u_{\mathrm{S}}^{n+1} = \text{const.}\right)\\
&\overset{(3.21)}{=} \mathcal{G}_{\mathrm{S}}\left(-\mathcal{G}_{\mathrm{F}}\left({}_{l}{}^{k}y_{\mathrm{F}}^{n+1}\right), {}^{k}u_{\mathrm{S}}^{n+1} = \text{const.}\right)\\
&\overset{(3.24)}{=} \mathcal{G}_{\mathrm{S}}\left(-\mathcal{G}_{\mathrm{F}}\left({}_{l}{}^{k}y_{\mathrm{S}}^{n+1}\right), {}^{k}u_{\mathrm{S}}^{n+1} = \text{const.}\right),\\
\text{i.e.}\qquad {}_{l+1}{}^{k}y_{\mathrm{S}}^{n+1} &= -\frac{(1-\alpha)m + c\delta t}{\alpha m + k\delta t^{2}}\,{}_{l}{}^{k}y_{\mathrm{S}}^{n+1} + {}^{k}b^{n},\\
\text{i.e.}\qquad {}_{l+1}{}^{k}y_{\mathrm{S}}^{n+1} &= {}_{1}A_{\mathrm{FSI}}\;{}_{l}{}^{k}y_{\mathrm{S}}^{n+1} + {}^{k}b^{n}.
\end{aligned} \tag{3.33}$$

Herein the iteration counter l is used for the inner iteration loop and the iteration counter k for the outer iteration loop. For the inner FSI fixed point iteration the constant part is ${}^{k}b^{n}$.

The limit of the inner iteration factor

$$\lim_{\delta t \to 0}\left\{{}_{1}A_{\mathrm{FSI}}\right\} = \frac{\alpha - 1}{\alpha}, \tag{3.34}$$

shows pure dependency on the mass distribution α.

Supplemented by relaxation the inner FSI part of the scheme reads

$$\begin{aligned}
{}_{l+1}{}^{k}y_{\mathrm{S}}^{n+1} =& \beta\mathcal{G}_{\mathrm{S}}\big(-\mathcal{G}_{\mathrm{F}}({}_{l}{}^{k}y_{\mathrm{S}}^{n+1}), {}^{k}y_{\mathrm{S}}^{n+1} = \text{const.}\big)\\
&+ (1-\beta)\,{}_{l}{}^{k}y_{\mathrm{S}}^{n+1},\\
\text{i.e.}\quad {}_{l+1}{}^{k}y_{\mathrm{S}}^{n+1} =& -\frac{(\beta-\alpha)m + c\delta t - (1-\beta)k\delta t^{2}}{\alpha m + k\delta t^{2}}\,{}_{l}{}^{k}y_{\mathrm{S}}^{n+1} + \beta\,{}^{k}b^{n},\\
\text{i.e.}\quad {}_{l+1}{}^{k}y_{\mathrm{S}}^{n+1} =& {}_{\beta}A_{\mathrm{FSI}}\;{}_{l}{}^{k}y_{\mathrm{S}}^{n+1} + \beta\,{}^{k}b^{n}.
\end{aligned} \tag{3.35}$$

The limit of the inner iteration factor

$$\lim_{\delta t \to 0}\left\{{}_{\beta}A_{\mathrm{FSI}}\right\} = \frac{\alpha - \beta}{\alpha}, \tag{3.36}$$

now is obviously determined by the mass distribution α and the relaxation parameter β.

The optimal relaxation parameter according to Eq. (2.37) becomes

$$\beta^{*}_{\mathrm{FSI}} = \frac{\alpha m + k\delta t^{2}}{m + c\delta t + k\delta t^{2}}. \tag{3.37}$$

It can always be found since each term in the denominator is positive non-equal to zero for physically relevant parameters independent of the controller setting.

Assuming convergence, the inner FSI fixed-point iteration can be substituted by the equivalent FS subsystem $\mathcal{G}_{\mathrm{FS}}\left({}^{k}u_{\mathrm{S}}^{n+1}\right)$ for analyzing the outer [FS]CI fixed-point iteration. Consequently, this outer [FS]CI fixed-point iteration of the algorithm condenses down to

$$\begin{aligned}
{}^{k+1}y_{\mathrm{S}}^{n+1} &= \mathcal{G}_{\mathrm{FS}}\left({}^{k}u_{\mathrm{S}}^{n+1}\right)\\
&\overset{(3.27)}{=} \mathcal{G}_{\mathrm{FS}}\left({}^{k}u_{\mathrm{C}}^{n+1}\right)\\
&\overset{(3.23)}{=} \mathcal{G}_{\mathrm{FS}}\left(\mathcal{G}_{\mathrm{C}}\left({}^{k}y_{\mathrm{C}}^{n+1}\right)\right)\\
&\overset{(3.26)}{=} \mathcal{G}_{\mathrm{FS}}\left(\mathcal{G}_{\mathrm{C}}\left({}^{k}y_{\mathrm{S}}^{n+1}\right)\right),\\
\text{i.e.}\qquad {}^{k+1}y_{\mathrm{S}}^{n+1} &= -\frac{k_{R2}\delta t + k_{R1}\delta t^2}{m + c\delta t + k\delta t^2}\,{}^{k}y_{\mathrm{S}}^{n+1} + b^n,\\
\text{i.e.}\qquad {}^{k+1}y_{\mathrm{S}}^{n+1} &= {}_{1}A_{[\mathrm{FS}]\mathrm{CI}}\,{}^{k}y_{\mathrm{S}}^{n+1} + b^n.
\end{aligned} \tag{3.38}$$

Herein the factor b^n remains constant during all iterations. The limit of the outer iteration factor

$$\lim_{\delta t\to 0}\left\{{}_{1}A_{[\mathrm{FS}]\mathrm{CI}}\right\} = 0, \tag{3.39}$$

is always zero, independently of the parameter setting.

Supplemented by relaxation the outer [FS]CI part of the scheme reads

$$\begin{aligned}
{}^{k+1}y_{\mathrm{S}}^{n+1} &= \beta\mathcal{G}_{\mathrm{FS}}\big(\mathcal{G}_{\mathrm{C}}({}^{k}y_{\mathrm{S}}^{n+1})\big) + (1-\beta){}^{k}y_{\mathrm{S}}^{n+1},\\
\text{i.e.}\quad {}^{k+1}y_{\mathrm{S}}^{n+1} &= -\frac{\beta(k_{R2}\delta t + k_{R1}\delta t^2) - (1-\beta)(m + c\delta t + k\delta t^2)}{m + c\delta t + k\delta t^2}\,{}^{k}y_{\mathrm{S}}^{n+1}\\
&\quad + \beta b^n,\\
\text{i.e.}\quad {}^{k+1}y_{\mathrm{S}}^{n+1} &= {}_{\beta}A_{[\mathrm{FS}]\mathrm{CI}}\,{}^{k}y_{\mathrm{S}}^{n+1} + \beta b^n.
\end{aligned} \tag{3.40}$$

The limit of the outer iteration factor

$$\lim_{\delta t\to 0}\left\{{}_{\beta}A_{[\mathrm{FS}]\mathrm{CI}}\right\} = 1-\beta, \tag{3.41}$$

shows pure dependency on the relaxation parameter β.

The optimal relaxation parameter according to Eq. (2.37) becomes

$$\beta^{*}_{[\mathrm{FS}]\mathrm{CI}} = \frac{m + c\delta t + k\delta t^2}{m + \left(c + k_{\mathrm{R2}}\right)\delta t + \left(k + k_{\mathrm{R1}}\right)\delta t^2}. \tag{3.42}$$

Each summand in the denominator is positive and non-equal to zero for physically relevant parameters and stable controller settings according to Eq. (3.9). Thus, it can always be found.

3.3.3 Nesting of the SCI Sub-Problem (F[SC]I)

The acronym F[SC]I denotes the specific iterative coupling scheme illustrated in Fig. 3.5, where the GS communication pattern is depicted with nesting of the SCI subproblem, which is made clear by bracketing [SC]. Comparable to the [FS]CI problem, for the F[SC]I problem two interface equations are also to be set up. $\mathcal{I}_{\mathrm{SC}}$ for the inner and $\mathcal{I}_{\mathrm{F[SC]}}$ for the outer iteration loop. As already indicated, the solution procedure for the F[SC]I problem is done just the other way around like in the [FS]CI problem.

Accordingly, first, the SC loop is iterated applying a constant disturbance force until convergence. The converged values are used as information for the iterations of the outer loop. If the outer loop does not converge, the algorithm has to return to the inner loop. Before proceeding to the next time step, the inner and outer loop have to be converged. The scheme is again applied to the partitioned simplified model problem. The inner SCI fixed-point iteration of the algorithm condenses down to

$$\begin{aligned}
{}_{l+1}{}^{k}y_{\mathrm{S}}^{n+1} &\overset{(3.22)}{=} \mathcal{G}_{\mathrm{S}}\left({}^{k}z_{\mathrm{S}}^{n+1} = \text{const.}, {}_{l}{}^{k}u_{\mathrm{S}}^{n+1}\right) \\
&\overset{(3.27)}{=} \mathcal{G}_{\mathrm{S}}\left({}^{k}z_{\mathrm{S}}^{n+1} = \text{const.}, {}_{l}{}^{k}u_{\mathrm{C}}^{n+1}\right) \\
&\overset{(3.23)}{=} \mathcal{G}_{\mathrm{S}}\left({}^{k}z_{\mathrm{S}}^{n+1} = \text{const.}, \mathcal{G}_{\mathrm{C}}\left({}_{l}{}^{k}y_{\mathrm{C}}^{n+1}\right)\right) \\
&\overset{(3.26)}{=} \mathcal{G}_{\mathrm{S}}\left({}^{k}z_{\mathrm{S}}^{n+1} = \text{const.}, \mathcal{G}_{\mathrm{C}}\left({}_{l}{}^{k}y_{\mathrm{S}}^{n+1}\right)\right),
\end{aligned} \tag{3.43}$$

$$\text{i.e.} \qquad {}_{l+1}{}^{k}y_{\mathrm{S}}^{n+1} = -\frac{k_{R2}\delta t + k_{R1}\delta t^2}{\alpha m + k\delta t^2}\, {}_{l}{}^{k}y_{\mathrm{S}}^{n+1} + {}^{k}b^{n},$$

$$\text{i.e.} \qquad {}_{l+1}{}^{k}y_{\mathrm{S}}^{n+1} = {}_{1}A_{\mathrm{SCI}}\, {}_{l}{}^{k}y_{\mathrm{S}}^{n+1} + {}^{k}b^{n}.$$

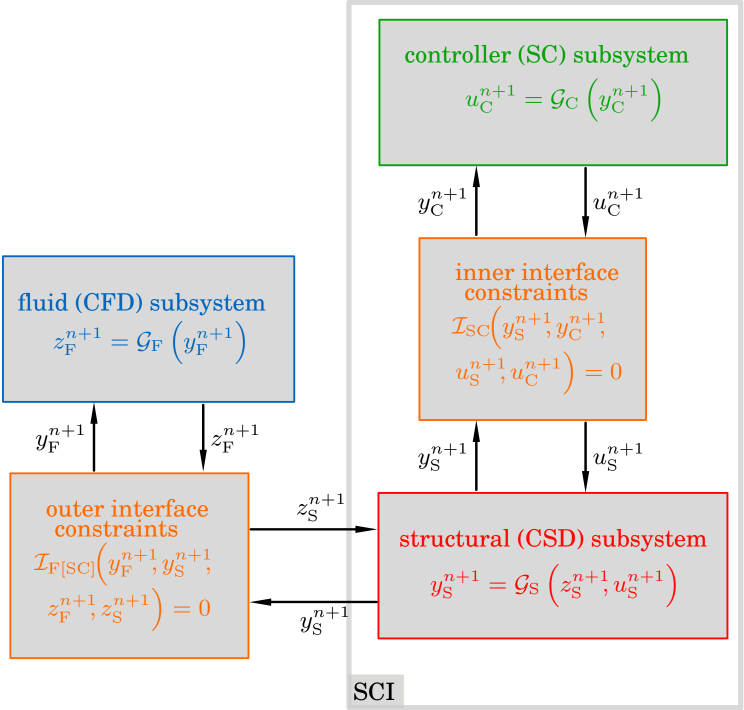

Figure 3.5: Block diagram for the F[SC]I scheme.

Again the iteration counter l is used for the inner iteration loop and the iteration counter k for the outer iteration loop. As defined for the FSCI and the [FS]CI problem, ${}^{k}b^{n}$ is the constant part of the inner iteration loop.

The limit of the inner iteration factor

$$\lim_{\delta t \to 0} \{{}_{1}A_{\mathrm{SCI}}\} = 0, \tag{3.44}$$

is always zero independently of the parameter setting.

Supplemented by relaxation the inner SCI part of the scheme reads

$$\begin{aligned}
&{}_{l+1}{}^{k}y_{\mathrm{S}}^{n+1} = \beta\mathcal{G}_{\mathrm{S}}\big({}^{k}z_{\mathrm{S}}^{n+1} = \text{const.}, \mathcal{G}_{\mathrm{C}}({}_{l}{}^{k}y_{\mathrm{S}}^{n+1})\big)\\
&\qquad + (1-\beta){}_{l}{}^{k}y_{\mathrm{S}}^{n+1},\\
\text{i.e.}\quad &{}_{l+1}{}^{k}y_{\mathrm{S}}^{n+1} = -\frac{\beta(k_{R2}\delta t + k_{R1}\delta t^{2}) - (1-\beta)(\alpha m + k\delta t^{2})}{\alpha m + k\delta t^{2}}\ {}_{l}{}^{k}y_{\mathrm{S}}^{n+1}\\
&\qquad +\beta{}^{k}b^{n},\\
\text{i.e.}\quad &{}_{l+1}{}^{k}y_{\mathrm{S}}^{n+1} = {}_{\beta}A_{\mathrm{SCI}}\ {}_{l}{}^{k}y_{\mathrm{S}}^{n+1} + \beta{}^{k}b^{n}.
\end{aligned} \tag{3.45}$$

The limit of the inner iteration factor

$$\lim_{\delta t\to 0}\left\{{}_{\beta}A_{\mathrm{SCI}}\right\} = 1-\beta, \tag{3.46}$$

shows pure dependency on the relaxation parameter β.

The optimal relaxation parameter becomes according to Eq. (2.37)

$$\beta^{*}_{\mathrm{SCI}} = \frac{\alpha m + k\delta t^{2}}{\alpha m + k_{\mathrm{R2}}\delta t + (k + k_{\mathrm{R1}})\,\delta t^{2}}. \tag{3.47}$$

αm and $(k + k_{\mathrm{R1}})\,\delta t^{2}$ in the denominator are positive and nonequal to zero for physically relevant parameters and stable controller settings according to Eq. (3.9).

Thus, the optimal relaxation factor can always be found by additionally requiring

$$k_{\mathrm{R2}}\delta t \neq -\big(\alpha m + (k + k_{\mathrm{R1}})\,\delta t^{2}\big)\ .$$

Assuming convergence, the inner SCI fixed-point iteration can accordingly be substituted by the equivalent SC subsystem $\mathcal{G}_{\mathrm{SC}}\left({}^{k}z_{\mathrm{S}}^{n+1}\right)$ for analyzing the outer F[SC]I fixed-point iteration. Consequently, this outer F[SC]I fixed-point iteration of the algorithm condenses down to

$$\begin{aligned}
{}^{k+1}y_{\mathrm{S}}^{n+1} &= \mathcal{G}_{\mathrm{SC}}\left({}^{k}z_{\mathrm{S}}^{n+1}\right) \\
&\overset{(3.25)}{=} \mathcal{G}_{\mathrm{SC}}\left(-{}^{k}z_{\mathrm{F}}^{n+1}\right) \\
&\overset{(3.21)}{=} \mathcal{G}_{\mathrm{SC}}\left(-\mathcal{G}_{\mathrm{S}}\left({}^{k}y_{\mathrm{F}}^{n+1}\right)\right) \\
&\overset{(3.24)}{=} \mathcal{G}_{\mathrm{SC}}\left(-\mathcal{G}_{\mathrm{F}}\left({}^{k}y_{\mathrm{S}}^{n+1}\right)\right), \\
\text{i.e.} \qquad {}^{k+1}y_{\mathrm{S}}^{n+1} &= -\frac{(1-\alpha)m + c\delta t}{\alpha m + k_{R2}\delta t + (k + k_{R1})\delta t^2}\ {}^{k}y_{\mathrm{S}}^{n+1} + b^n, \\
\text{i.e.} \qquad {}^{k+1}y_{\mathrm{S}}^{n+1} &= {}_1A_{\mathrm{F[SC]I}}\ {}^{k}y_{\mathrm{S}}^{n+1} + b^n.
\end{aligned} \tag{3.48}$$

The limit of the outer iteration factor

$$\lim_{\delta t \to 0} \left\{ {}_1A_{\mathrm{F[SC]I}} \right\} = \frac{\alpha - 1}{\alpha}, \tag{3.49}$$

shows pure dependency on the mass distribution α.

Supplemented by relaxation the outer F[SC]I part of the scheme reads

$$\begin{aligned}
{}^{k+1}y_{\mathrm{S}}^{n+1} &= \beta\mathcal{G}_{\mathrm{SC}}\left(-\mathcal{G}_{\mathrm{F}}\left({}^{k}y_{\mathrm{S}}^{n+1}\right)\right) + (1-\beta){}^{k}y_{\mathrm{S}}^{n+1}, \\
\text{i.e.} \quad {}^{k+1}y_{\mathrm{S}}^{n+1} &= -\ \frac{(\beta - \alpha)m + \beta c\delta t - (1-\beta)(k_{R2}\delta t + (k + k_{R1})\delta t^2)}{\alpha m + k_{R2}\delta t + (k + k_{R1})\delta t^2}\ {}^{k}y_{\mathrm{S}}^{n+1} \\
&\quad + \beta b^n, \\
\text{i.e.} \quad {}^{k+1}y_{\mathrm{S}}^{n+1} &= {}_\beta A_{\mathrm{F[SC]I}}\ {}^{k}y_{\mathrm{S}}^{n+1} + \beta b^n.
\end{aligned} \tag{3.50}$$

And the limit of the outer iteration factor

$$\lim_{\delta t \to 0} \left\{ {}_\beta A_{\mathrm{F[SC]I}} \right\} = \frac{\alpha - \beta}{\alpha}, \tag{3.51}$$

now is obviously determined by the mass distribution α and the relaxation parameter β.

The optimal relaxation parameter becomes according to Eq. (2.37)

$$\beta^*_{\mathrm{F[SC]I}} = \frac{\alpha m + k_{\mathrm{R2}}\delta t + (k + k_{\mathrm{R1}})\,\delta t^2}{m + (c + k_{\mathrm{R2}})\,\delta t + (k + k_{\mathrm{R1}})\,\delta t^2}. \tag{3.52}$$

It always exists since the denominator is positive and non-equal to zero for physically relevant parameters and stable controller settings according to Eq. (3.9).

From the simplified model problem, it can be concluded that all three types of Gauss-Seidel schemes show unconditional stability for reasonable physical parameters and stable controller settings. Furthermore, it was possible to derive the optimal relaxation parameters of β^*. It has to be kept in mind, that [31] p. 10 Eq. (48) states

$$\lim_{\substack{\delta t \to 0 \\ \alpha \to 0}} \{\beta^*\} = \lim_{\substack{\delta t \to 0 \\ \alpha \to 0}} \{\beta_{\mathrm{crit}}\} = 0. \tag{3.53}$$

This means a decreasing value of α, i.e., a decreasing amount of the structural mass results in a smaller value for β. [31] p. 11 concludes that an increased sensitivity w.r.t. β may lead to an increased number of iterations for small values of α, especially in cases with more than one degree of freedom (vector case), for which an optimal value of the relaxation parameter β^* generally cannot be found. This fact is also emphasized in [31] Section 4.4 for FSI and can be transferred to the FSCI case analogously. After the successful derivations for the simplified model problem, the schemes are subsequently applied to a multi-degree of freedom problem for further investigations, which have not been possible with the simplified model problem. This is especially concerning the robustness of the algorithms for multi-degree of freedom problems. It is very likely that the findings from the simplified model problem concerning stability also apply to multi-degree of freedom problems. For the calculation of the relaxation parameter the Aitken acceleration shortly mentioned in CHAPTER 2, proposed by [57] p. 66 for FSI is applied, which can be seen more in detail in the algorithms in APPENDIX A also written for the vector case.

3.4 Numerical Results for a Multi-Degree of Freedom FSCI Problem

The inspiration for the multi-degree of freedom FSCI experiment were the numerical benchmarks proposed in [94] and [100] p. 195-197. Since the investigations should go beyond the pure FSI effects study, the experimental setup had to be slightly modified. All in all, the principle arrangement remains the same and can be seen in Fig. 3.6.

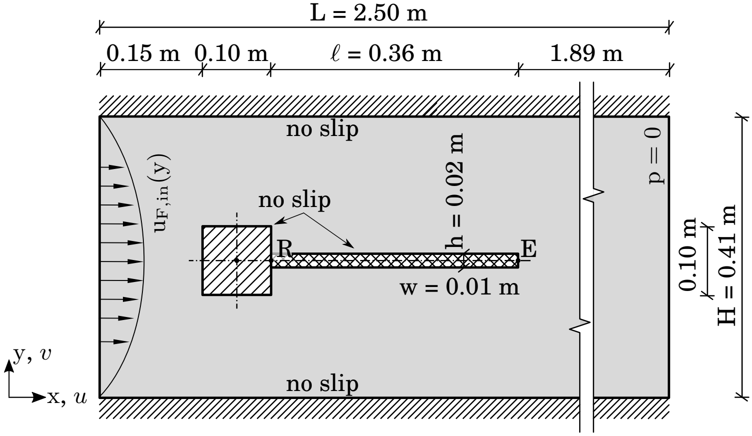

Figure 3.6: Dimensions and boundary conditions of the numerical FSCI experiment.

In contrast to the rigid cylinder in [94], a square, as suggested in [100], is placed in the channel. To this rigid square, an elastic flag (characters R to E) is attached. The square and flag are placed asymmetrically in the channel to stimulate a fast onset of the excitation mechanism depicted in Fig. 3.9. The phenomenology of the problem is described in [94] and [100].

In the following, we are actively trying to influence the dynamics of the structure, i.e., the CSD subsystem, by a controller, extending the FSI to the FSCI problem. The main objective of this is to reduce or in the best case entirely suppress the amplitude of the end-point displacement at point E. Similar to the simplified model problem, the manipulation variable is a Neumann boundary condition i.e. an external force, which is applied by the SC subsystem at the root point of the flag R to the CSD subsystem. For the design of the controller, a reduced order model is necessary ([96], [60]), which is exemplary shown in Fig. 3.8. This low-fidelity structural model was only used for the controller. In the coupled FSCI simulation, the structure was simulated like in classical FSI by the high-fidelity model depicted in Fig. 3.7.

3.4.1 Description of the Subsystems Involved

Just as mentioned before, the FSCI problem involves three subsystems, namely a fluid flow, a structural mechanics part and a controller.

At first the CFD subsystem is introduced. The main dimensions and the boundary conditions of the problem can be seen in Fig. 3.6. The time constant inlet velocity is described by the function

$$u_{F,in}(\mathrm{y}) = u_{F,max} 4\frac{\mathrm{y}}{H}\left(1-\frac{\mathrm{y}}{H}\right). \tag{3.54}$$

This is a quadratic parabola with $u_{\mathrm{F,max}}$ at its peak value. Herein

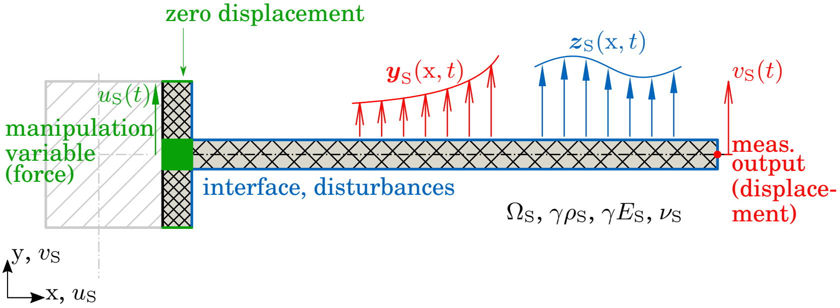

Figure 3.7: High-fidelity model to be solved in the coupled problem.

y is the coordinate running from the bottom of the channel to its width H. The material parameters for the fluid flow are chosen in accordance to the CFD3 specifications in [94], leading to a strongly unsteady flow with vortex shedding. This vortex shedding is additionally supported by the aforementioned eccentric placement of the square in the channel. Thus the following specifications are chosen: $\rho_F = 1000\ ^{\mathrm{kg}}/_{\mathrm{m}^3}$, $\mu_F = 1.0\ ^{\mathrm{kg \cdot m}}/_{\mathrm{s}^2}$ and $u_{\mathrm{F,max}} = 2\ ^{\mathrm{m}}/_{\mathrm{s}}$, which leads to a Reynolds number $Re = 200$. As can be seen in Fig. 3.9 an unstructured mesh of triangular elements (12515 elements and 6503 nodes) is used for the calculations. The mean element size is 0.002 m near the square and the flag and decreases to 0.02 m at the domain boundaries. It has to be pointed out, that Fig. 3.9 does not show the full length of the CFD domain. More information about the element formulation can be found in Sect. 2.2. The time step size is $\delta \mathrm{t} = 0.01$ s for all subsystems.

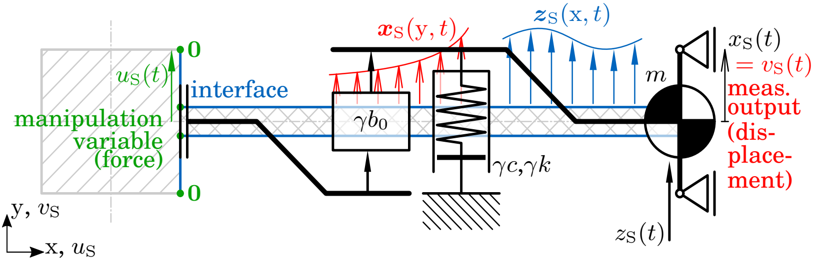

Figure 3.8: Low-fidelity model for the controller design.

Next, the CSD subsystem is presented. The CSD subsystem is represented by a high-fidelity multi-degree of freedom model, which is the initially suggested CSD system as proposed in [94]. The specifications of the high-fidelity model can be seen in Fig. 3.7.

Herein, $\boldsymbol{z}_{\mathrm{S}}(\mathrm{x}, t)$ is the disturbance force from the fluid flow and $\boldsymbol{y}_{\mathrm{S}}(\mathrm{x}, t)$ is the displacement of the structure at the interface. Again one can see that the manipulation variable $u_S(t)$, which is a force in this case, is applied only at the root point of the elastic flag and the displacement component in y-direction $v_{\mathrm{S}}(t)$ is measured solely at its tip. The special aspect of the high-fidelity model is the back part of the square (finely crosshatched), which is originally assumed to be rigid in [94], but is considered elastic in the current investigation. It is used to linearly distribute the root point excitation along the backside of the square to match the ALE boundary conditions of the fluid domain. Therefore a pseudo material with $\nu_{\mathrm{S}} = 0$ and $\rho_{\mathrm{S}} = 0$ is set, to avoid artificially introduced deformations and inertia effects at the back of

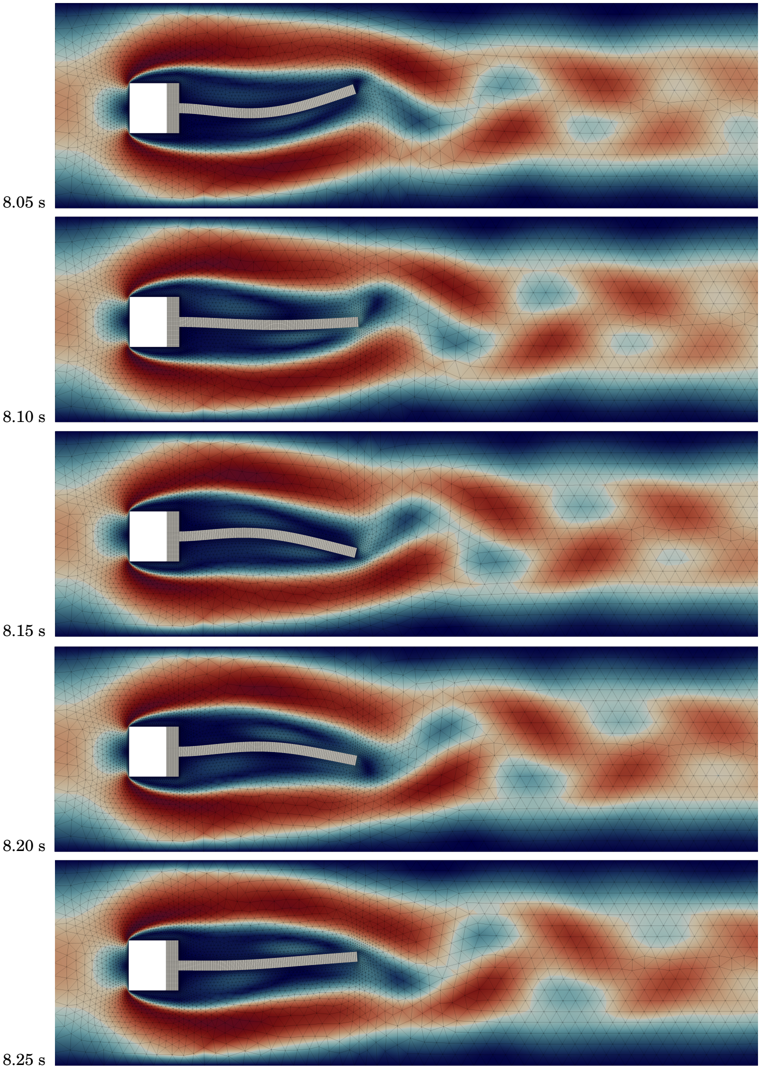

Figure 3.9: Deformed structure with velocity contours and deformed finite element mesh for the numerical experiment from 8.0 s to 8.25 s by snapshots in steps of 0.05 s.

the square. The problem is discretized by a structured mesh of 368 quadrilateral elements with an edge length of 0.005 m, which are described in Sect. 2.1.2.3. The material parameters are chosen as $\rho_{\mathrm{S}} = 1000\ {}^{kg}/_{m^3}$, $E_{\mathrm{S}} = 5.6\mathrm{e}6\ {}^{N}/_{m^2}$ and $\nu_{\mathrm{S}} = 0.4$. The values applied for the simulations match the CSD2 benchmark of [94] scaled by the factor of γ. The gravity constant is set to $g = 2\ {}^{m}/_{s^2}$ and is acting in x-direction. Fig. 3.9 shows an extract of the simulation results for 0.20 seconds by using the parameters for fluid flow and structural model described in this subsection ($\gamma = 1.0$) in order to show the deformation mechanism. The figure shows the deformed mesh, the high-fidelity CSD model and the velocity contours. The controller is not activated yet. The displacements at point E with and without activated controller are plotted in Figs. 3.11 and 3.12. The meshes on the interface of fluid and structure subsystem coincide, thus no additional mapping operation is necessary in this case.

The third subsystem consists of a low-fidelity CSD model implemented in the controller and the control law itself. In the low-fidelity CSD model, the overall structural dynamics are condensed to a SDoF system. The low fidelity model can be seen in Fig. 3.8. It has been derived from the high-fidelity multi-degree of freedom model. The structural model itself is approximated by a simple second-order ODE, which matches the boundary conditions of the high-fidelity model and is used by the controller to calculate the force $u_{\mathrm{S}}(t)$. The distributed displacements $\boldsymbol{y}_{\mathrm{S}}(\mathrm{x}, t)$ between points R and E are approximated by quadratic shape functions, which renders a good enough assumption for the dominant mode shape of the investigated problem (see Fig. 3.9). The distributed disturbance forces $\boldsymbol{z}_{\mathrm{S}}(\mathrm{x}, t)$ on the FSI interface are summed up to a single disturbance force $z_{\mathrm{S}}(t)$. If reduced-order model would not satisfy the prerequisites for successfully controlling the system (e.g., for more complex structures), a more advanced model-order reduction approach would be necessary. Since the major aim of the example presented here is to show the algorithmic treatment of the problem the assumptions made here are accurate enough, which also reflects in the results achieved with the reduced order model selected here. They are defined as $N_u(\mathrm{x}) = 1 - \left({}^{\mathrm{x}-\mathrm{x}_R}/_{\ell}\right)^2$ for the manipulation variable $u_{\mathrm{S}}(t)$ and $N_x(\mathrm{x}) = \left({}^{\mathrm{x}-\mathrm{x}_R}/_{\ell}\right)^2$ for the state variable $x_{\mathrm{S}}(t)$. Thus, the real

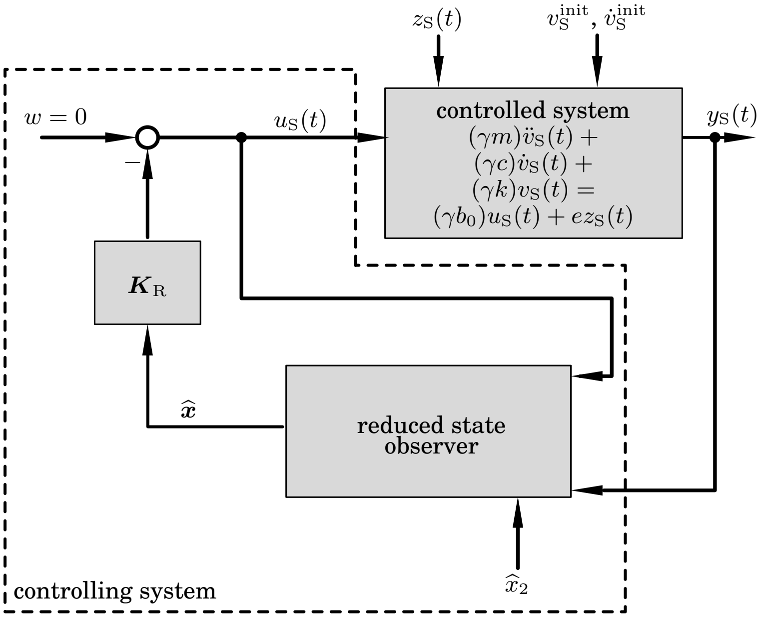

Figure 3.10: Block diagram for the controlled system with following state observer ([60] p. 334)

physics of the high-fidelity model reduces to

$$(\gamma m)\ddot{x}_S(t) + (\gamma c)\dot{x}_S(t) + (\gamma k)x_S(t) = (\gamma b_0)u_S(t) + z_S(t). \quad (3.55)$$

In the latter equation the single state $x_S(t)$ directly corresponds to the measured output $v_S(t)$, which is the displacement component in y-direction of the tip displacement at the end point E, resulting in $v_S(t) = x_S(t)$. The parameter b_0, which is associated with the manipulation variable at the root point R, the force $u_S(t)$, is used to replace the root point excitation, which avoids introducing an additional degree of freedom Since for this numerical example, zero damping is assumed and thus damping is not modeled in the CSD subsystem (high-fidelity model), it also follows for the low-fidelity model $c = 0$. Applying the PVW with a distributed cross sectional mass $\mu_S = \rho_S \mathrm{wh}$, where w is the width, h the height of the cross section and with $\widetilde{EI}$ is the distributed sectional stiffness, leads to

$$
\begin{aligned}
&\mu_{\mathrm{S}} \int_{\mathrm{x}_R}^{\mathrm{x}_E} N_x^2(\mathrm{x})\mathrm{dx}\, \ddot{x}_{\mathrm{S}}(t) + \widetilde{EI} \int_{\mathrm{x}_R}^{\mathrm{x}_E} N_x^2(\mathrm{x})\mathrm{dx}\, x_{\mathrm{S}}(t) \\
&= \mu_{\mathrm{S}} \int_{\mathrm{x}_R}^{\mathrm{x}_E} N_x(\mathrm{x})N_u(\mathrm{x})\mathrm{dx}\, \ddot{y}_{\mathrm{S}}(t) \\
&+\widetilde{EI} \int_{\mathrm{x}_R}^{\mathrm{x}_E} N_x(\mathrm{x})N_u(\mathrm{x})\mathrm{dx}\, u_{\mathrm{S}}(t) + \sum_i N_x(\mathrm{x}_i) z_{\mathrm{S,y}}(\mathrm{x}_i, t).
\end{aligned}
\tag{3.56}
$$

The last term of Eq. (3.56) denotes the discrete disturbance forces coming from the nodes i on the interface mesh of the fluid domain which are to be summed up here. The open parameters in Eq. (3.55) can be obtained as:

$$
\begin{aligned}
&m = \frac{\mu_{\mathrm{S}}\ell}{5} = \frac{\rho_{\mathrm{S}}\mathrm{wh}\ell}{5},\, k = \widetilde{EI}\frac{\ell}{5} = \frac{E_{\mathrm{S}}\mathrm{wh}^3}{4\ell^3}, \\
&b_0 = -\widetilde{EI}\frac{2\ell}{15} = \frac{E_{\mathrm{S}}\mathrm{wh}^3}{6\ell^3},\, z_{\mathrm{S}}(t) = \sum_i \left(\frac{\mathrm{x}_i - \mathrm{x}_R}{\ell}\right)^2 z_{\mathrm{S,y}}(\mathrm{x}_i, t).
\end{aligned}
\tag{3.57}
$$

Those approximations are applied to the centerline of the structure and have to be projected to the surfaces of the flag by proper projection operations. The time-discrete low-fidelity CSD model is finally given with the adapted time discretization (Eq. (3.22)) from the simplified model problem. The equivalent values to match the multi-degree of freedom model for m, c, k and b_0 can be found in Tab. 3.1. Those parameters can be scaled by the parameter γ accordingly.

With the low-fidelity CSD model, the controller can be designed. The Controller in this context means the control law, which is implemented, for example, in a microprocessor (controlling element in Fig. 2.2). Between this microprocessor and the actuator in the physical system, an amplifier device would be located. In Fig. 3.10 the amplifier, the actuator, and the measuring element are omitted because they are not necessary for the investigations made here. Although, the example shown here is a purely numerical experiment from the FSI community, which was utilized to test the algorithms developed for the simplified model problem in a multi-degree of freedom case; it could principally be build for a physical experiment. In this case, the input the actuator could be placed, for example, in the form of a linear motor or a smart material applying the manipulation variable (force $u_{\mathrm{S}}(t)$) to the root point of the flag marked green in Fig. 3.7 or marked by R in Fig. 3.6. The measurement of the flag's tip displacement (point E in Fig. 3.6) should be conducted contactless, so the dynamics of the flag are not influenced by the measurement device. In the physical experiment, the actuator's dynamics and the measurement apparatus would have to be taken into account in the controller design, which can be modeled by delay elements ([40] p. 184). This is not necessary for the investigations in this work thus optimal actuator and sensor dynamics are assumed.

In this work, a state-feedback control following state observer is implemented, which is state of the art for modern methods for controller design and is also used in the context of many applications in control theory. Herein, the controller state feedback matrix is specified via a linear-quadratic regulator approach (LQR) and the observer output-feedback matrix is set via pole placement as generally described in [60] and [96]. The block diagram can be seen in Fig. 3.10. The controlled system, which is seen by the controller, is represented by the equation

$$(\gamma m)\ddot{v}_{\mathrm{S}}(t) + (\gamma c)\dot{v}_{\mathrm{S}}(t) + (\gamma k)v_{\mathrm{S}}(t) = (\gamma b_0)u_{\mathrm{S}}(t) + e z_{\mathrm{S}}(t), \tag{3.58}$$

including the measured output $v_{\mathrm{S}}(t)$ (displacement), the manipulation variable $u_{\mathrm{S}}(t)$ (force), the disturbance force $z_{\mathrm{S}}(t)$ and the scaling factor γ. The system is rewritten in state-space representation introduced in Section 2.3, with $x_1(t) := v_{\mathrm{S}}(t)$ and $x_2(t) := \dot{v}_{\mathrm{S}}(t)$ being the entries in the state vector $\boldsymbol{x}(t) = [x_1(t)\ x_2(t)]^{\mathrm{T}}$, reading

$$\begin{bmatrix}\dot{x}_1\\ \dot{x}_2\end{bmatrix} = \begin{bmatrix}0 & 1\\ -\frac{k}{m} & -\frac{c}{m}\end{bmatrix}\begin{bmatrix}x_1\\ x_2\end{bmatrix} + \begin{bmatrix}0\\ \frac{b_0}{m}\end{bmatrix}u(t) + \begin{bmatrix}0\\ \frac{e}{m}\end{bmatrix}z(t), \tag{3.59}$$

$$\text{i.e.} \qquad \dot{\boldsymbol{x}} = \boldsymbol{A}\boldsymbol{x} + \boldsymbol{B}u(t) + \boldsymbol{E}z(t)$$

and the output equation

$$y(t) = \begin{bmatrix}1 & 0\end{bmatrix}\begin{bmatrix}x_1\\ x_2\end{bmatrix}, \tag{3.60}$$

$$\text{i.e.} \qquad y(t) = \boldsymbol{C}\boldsymbol{x}.$$

Since the system is fully controllable and fully observable, state-feedback control and state observer are possible. Thus a control law similar to the one presented for the model problem can be used. This is given by

$$u(t) = -k_{R1}x_1 - k_{R2}x_2 \tag{3.61}$$

or in short notation as

$$u(t) = -\boldsymbol{K}_R\boldsymbol{x}, \tag{3.62}$$

with $\boldsymbol{K}_R = [k_{R1}\ k_{R2}]$ being the constant state feedback matrix. Herein the constants in $\boldsymbol{K}_R$ are determined with the LQR approach described in detail in [60] Chapter 7. This is done in the general case by minimizing the quadratic cost functional

$$J(\boldsymbol{u}, \boldsymbol{x}_0) = \frac{1}{2}\int_0^\infty (\boldsymbol{x}^T\boldsymbol{Q}\boldsymbol{x} + \boldsymbol{u}^T\boldsymbol{R}\boldsymbol{u})\mathrm{dt}. \tag{3.63}$$

It involves user-definable weights $\boldsymbol{Q} \in \mathbb{R}^{2,2}$ related to state the $\boldsymbol{x}$ and $r \in \mathbb{R}^{1,1}$ for manipulation variable, i.e., the force $u(t)$. As it can be seen, in this case the matrix $\boldsymbol{R}$ reduces to a scalar, because the system has only one input $u(t)$. With an appropriate choice of $\boldsymbol{Q} \neq \boldsymbol{Q}(\gamma)$ and $r \neq r(\gamma)$ the state-feedback matrix becomes independent of γ, because also $\boldsymbol{A} \neq \boldsymbol{A}(\gamma)$, $\boldsymbol{B} \neq \boldsymbol{B}(\gamma)$ and $\boldsymbol{C} \neq \boldsymbol{C}(\gamma)$.

Since the displacement $v_{\mathrm{S}}(t)$, being state one, should be measured during the simulations, it is directly accessible $\big(x_1 = v_{\mathrm{S}}(t)\big)$. The second state should not be measured directly and thus needs an approximation. This approximation $x_2 \approx \widehat{x}_2$ is conducted from measurements of state one by a reduced state observer. The state-space representation, therefore, can be split up into one part for the measurement $v_{\mathrm{S}}(t)$ and a second one for the estimation $\widehat{x}_2$, by omitting the disturbance force $z(t)$, in the following way:

$$\begin{aligned} \dot{\widehat{\boldsymbol{x}}} &= \boldsymbol{A}\widehat{\boldsymbol{x}} + \boldsymbol{B}u, \\ \text{i.e.} \quad \left[\begin{array}{c} \dot{v}_{\mathrm{S}}(t) \\ \hline \dot{\widehat{x}}_2 \end{array}\right] &= \left[\begin{array}{cc} 0 & 1 \\ \hline -\frac{k}{m} & -\frac{c}{m} \end{array}\right] \left[\begin{array}{c} v_{\mathrm{S}}(t) \\ \hline \widehat{x}_2 \end{array}\right] + \left[\begin{array}{c} 0 \\ \hline \frac{b_0}{m} \end{array}\right] u(t). \end{aligned} \tag{3.64}$$

The reduced state observer equation can be written as follows:

$$\begin{aligned} \dot{\widetilde{x}}_2 =& -\frac{c}{m} - k_B\widetilde{x}_2 + \frac{b_0}{m}u(t) - (\frac{c}{m} + k_B)k_B - \frac{k}{m} \\ \widehat{x}_2 =& \widetilde{x}_2 + k_B v_{\mathrm{S}}(t) \end{aligned} \tag{3.65}$$

The value necessary for the output-feedback matrix k_B, which is a scalar value in this case, is calculated from a fictive system

$$\begin{aligned} \dot{x}_f &= -\frac{c}{m} x_f + u_f, \\ u_f &= -k_B x_f, \\ \rightarrow \quad \dot{x}_f &= -\big(\frac{c}{m} + k_B\big) x_f. \end{aligned} \tag{3.66}$$

By applying eigenvalue placement with the single eigenvalue of this system this results in

$$\begin{aligned} k_B &= -\frac{c}{m} - \lambda_B, \quad \text{where} \\ \lambda_B &< \mathrm{Re}\{\lambda\} = -\frac{c}{2m} \leq 0 \end{aligned} \tag{3.67}$$

has to hold, with λ being the eigenvalue of the fictive system.

Conducting the observer design and applying the BDF2 scheme results in

$$\begin{aligned} x_1^{n+1} &= v_\mathrm{S}^{n+1}, \\ [\mathrm{LHS}]\, \widetilde{x}_2^{n+1} &= -\frac{1}{\delta t}\Big(-2\widetilde{x}_2^{n} + \frac{1}{2}\widetilde{x}_2^{n-1}\Big) + [\mathrm{RHS}]\, y_S^{n+1}, \\ \widehat{x}_2^{n+1} &= \widetilde{x}_2^{n+1} + k_\mathrm{B} y_S^{n+1}, \\ u^{n+1} &= -k_\mathrm{R1} x_1^{n+1} - k_\mathrm{R2} \widehat{x}_2^{n+1}, \end{aligned} \tag{3.68}$$

where

$$\begin{aligned} [\mathrm{LHS}] &= \frac{3}{2\delta t} + \frac{c}{m} + k_\mathrm{B} + \frac{b_0}{m} k_\mathrm{R2} \text{ and} \\ [\mathrm{RHS}] &= -\left(\frac{c}{m} + k_\mathrm{B}\right) k_\mathrm{B} - \frac{k}{m} - \frac{b_0}{m}\left(k_\mathrm{R1} + k_\mathrm{R2} k_\mathrm{B}\right). \end{aligned} \tag{3.69}$$

For a parameter exploration to design the controller and the observer, the disturbance force $z_\mathrm{S}(t)$ is applied from recorded FSI simulations of the system. This results in the values summarized in Tab. 3.1

3.4.2 Residual Calculation and Numerical Accuracy

The overall coupled partitioned FSCI problem and the fluid subsystem were solved by an iterative approach. For the structural

Table 3.1: Values selected for controller parameters.

component	parameter	value	unit
controlled system	m	0.0144	kg
	c	0	$^{Ns}/_{m}$
	k	2.400549	$^{N}/_{m}$
	b_0	-1.600366	$^{N}/_{m}$
	e	0.01	1
state-feedback	$\boldsymbol{Q}$	$\boldsymbol{I}$	—
	r	1	—
	k_{R1}	-0.3028	1
	k_{R2}	-1.0027	s
state observer	λ_B	-2000	$^{rad}/_{s}$
	k_B	2000	$^{rad}/_{s}$

and the controller subsystem, a direct solver was used. For iterative solution procedures, the residual calculation and the accuracy of the solution play an important role in order to gain correct results [30] p. 201. In the following, a closer look is taken to the iterative solution of the interface equation system. For FSI, [57] shows to achieve the desired accuracy for the coupled problem using an iterative approach, the numerical accuracy of the solution of the subsystems has to be at least two orders of magnitude higher than the desired numerical accuracy of the coupled system. Thus, it makes sense to use the outcome of those investigations also for the FSCI problem.

Another crucial part is the calculation of the residual of the interface equation system. Since we are dealing with Dirichlet-Neumann coupling, it is obvious to calculate the residual vector $\boldsymbol{\mathcal{R}_y}$ from the interface displacements, which correspond to the mesh displacements $\boldsymbol{y}_\mathrm{F}$ of the fluid domain. This means

$$ {}^{k}\boldsymbol{\mathcal{R}_y} = {}^{k}\boldsymbol{y}_\mathrm{F} - {}^{k-1}\boldsymbol{y}_\mathrm{F}. \tag{3.70} $$

The convergence at the interface is achieved if

$$ \left\| {}^{k}\boldsymbol{\mathcal{R}_y} \right\| / \sqrt{N_\mathrm{dof,I}} \leq \varepsilon_\mathrm{I}. \tag{3.71} $$

Where $||...||$ denotes the L^2 norm of the residual vector and ε_I is the desired accuracy on the interface. The index k denotes the iteration counter. The residual is normalized by the square root of

Table 3.2: Recommendation for the numerical accuracy of solvers and interface iterations on basis of [57].

	FSI	FSCI	[FS]CI	F[SC]I
ε_{F}	$10^{-(p+2)}$	$10^{-(p+2)}$	$10^{-(p+4)}$	$10^{-(p+4)}$
ε_{S}	$10^{-(p+2)}$	$10^{-(p+2)}$	$10^{-(p+4)}$	$10^{-(p+4)}$
$\varepsilon_{\mathrm{I}}^{\mathrm{inner}}$	10^{-p}	10^{-p}	$10^{-(p+2)}$	$10^{-(p+2)}$
$\varepsilon_{\mathrm{I}}^{\mathrm{outer}}$	$--$	$--$	10^{-p}	10^{-p}

the number of degrees of freedom on the interface $N_{\mathrm{dof,I}}$ [57]. For the results in the following simulations, the numerical accuracy criteria can be found in Tab. 3.2. In this table, the proportions of values for the stopping criteria of the coupled simulations for the different variants of partitioned simulation patterns are listed. At first the overall desired numerical accuracy, which finally is to be achieved for the overall coupled simulation was selected in this case to be $p = 7$, resulting in a value of $\varepsilon_{\mathrm{I}} = 10^{-7}$ for the interface iterations. Afterwards the values of ε_{F} for the fluid solver and ε_{S} for the structural solver as well as for the inner interface iteration loop $\varepsilon_{\mathrm{I}}^{\mathrm{inner}}$ and the outer interface iteration loop $\varepsilon_{\mathrm{I}}^{\mathrm{outer}}$, were adopted according to the criteria described above.

3.4.3 Presentation and Interpretation of the Results

The simulations were conducted for 15 seconds and the measured output, i.e. the tip displacement (point E) in y-direction v_{S} of the elastic flag, has been plotted. The result for a pure FSI and a FSCI simulation with no nesting for a scaling factor $\gamma = 10^2$ and $\gamma = 10^4$ can be seen in Figs. 3.11 and 3.13. Additionally the results for the controlled system can be seen in an amplified version for $\gamma = 10^2$ in Fig. 3.12. One can see that the controller applied to the root point R of the flag can reduce the magnitude of the tip displacement at point E in the order of magnitude of almost 10^2. The vertical axes in Figs. 3.11 and 3.12 have a different scaling, but both figures show the same results for FSCI with LQR. Furthermore, the remaining oscillation in Fig. 3.12 is more regular than the one measured from the pure FSI simulation. Although the parameter setting is chosen to be optimal for

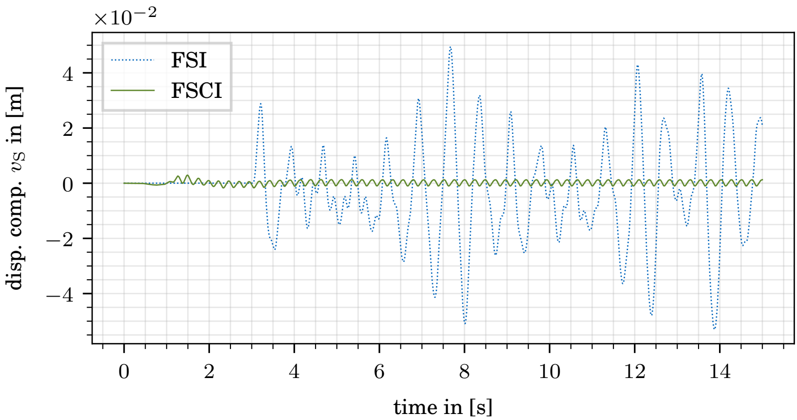

Figure 3.11: Displacement component v_S at point E for FSI and FSCI with LQR ($\gamma = 10^2$).

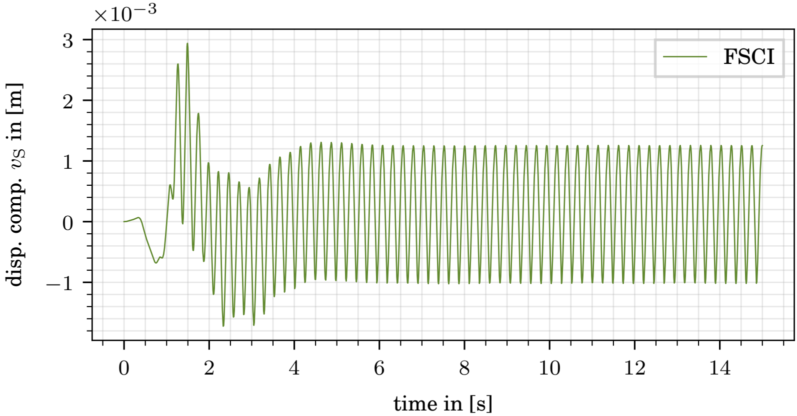

Figure 3.12: Displacement component v_S at point E for FSCI with LQR ($\gamma = 10^2$) (Zoomed view).

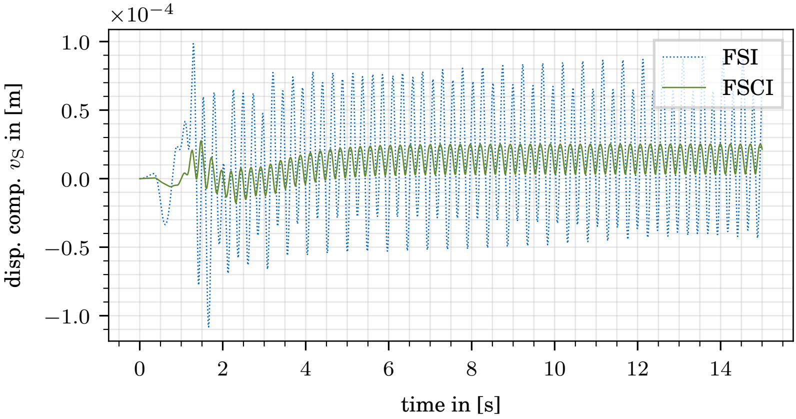

Figure 3.13: Displacement component v_S at point E for FSI and FSCI with LQR ($\gamma = 10^4$).

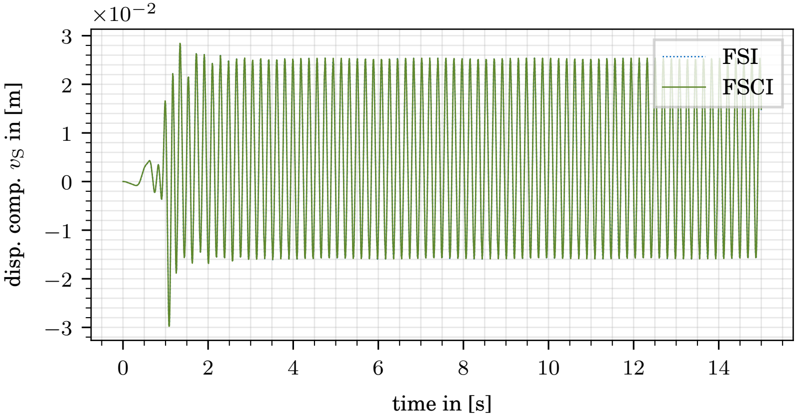

Figure 3.14: Displacement component v_S at point E for FSI and FSCI with LQR ($\gamma = 10^{-3}$).

the $\gamma = 10^2$, the controller still works for the value of $\gamma = 10^4$ because the structure behaves more inertial and is stiffer. Regarding the eigenvalues of the coupled system, this means that the structure's eigenfrequencies are dominating the overall behavior. It also follows that the number of interface iterations decreases. The added mass effect comes more into play by reducing the factor of γ, and the structural system becomes softer. This means the eigenfrequencies of the fluid flow start to dominate the system behavior, and the nonlinear behavior of the coupled system becomes more influential. It follows that a new controller design has to be conducted. For a value of $\gamma \leq 10^{-2}$, the structure is too soft and light to control its behavior by a force applied at its root-point R. Fig. 3.14 shows the results for such an example. Fig. 3.15 plots the overall number of interface iterations per time step for the different schemes applied to the numerical test example for the factor $\gamma = 10^2$ for the different coupling variants. For example, in the case of F[SC]I, we count the number of interface iterations for the [SC] loop (inner loop) first and add the number of interface iterations between [SC] and F (outer loop). The FSCI scheme needs a similar number of iterations as pure FSI. Tab. 3.2 shows one reason for this. For the FSCI problem, the number of coupling loops is the same as for the pure FSI prob-

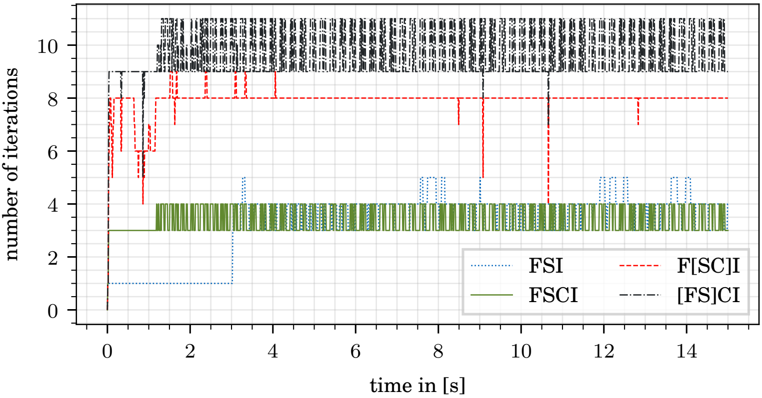

Figure 3.15: Total number of iterations per time step ($\gamma = 10^2$).

lem, and thus also the total number of interface iterations is almost equal. Looking closer at the number of interface iterations one can see, that the FSCI even needs fewer iterations at specific points than pure FSI. This is because the controller stabilizes the system leading to a more homogeneous oscillation with a smaller amplitude. Using the F[SC]I scheme increases the number of iterations almost by a factor of three and using the [FS]CI by almost a factor of four. According to Tab. 3.2 an additional loop and also a higher numerical accuracy in the solvers of the subsystems is needed, and the number of overall interface iterations increases. The reason that the F[SC]I requires fewer interface iterations than the [FS]CI version is the stabilizing behavior of the controller, which positively influences the outer FS loop. Conversely, the contrary effect occurs for the [FS]CI scheme.

3.5 Chapter Summary

This chapter discusses the algorithmic treatment and solution approaches to FSCI with iterative GS schemes. The aim was to conduct a fully coupled co-simulation of the FSCI problem, with the controller actively influencing the dynamics of the system.

The simplified model problem utilized in the first step is representative of the convergence behavior and stability for structural force control. Thus, all three developed variants of the Gauss-Seidel scheme prove unconditional stability for the simplified model problem in case of physically relevant parameters and stable controller settings. Furthermore, an optimal relaxation factor β^* could be determined for the simplified model problem. Hence, the simplified model problem is qualitatively capable of constituting the basic properties of the FSCI problem concerning stability and convergence. For the non-linear multi-degree of freedom problem, this means one can conclude from the simplified model problem that it should be possible to reduce the displacement significantly by applying a controller with an appropriate set of controller parameters. The schemes developed are supposed to converge in the multi-degree of freedom case, because Aitken acceleration is utilized instead of a constant relaxation factor. However, the simplified model problem only covers the main effects of the FSCI problem (e.g., the added mass effect), hence no detailed and quantitative conclusions concerning convergence patterns and stability issues can be drawn for the multi-degree of freedom problem.

Applying the variants of the GS scheme, developed by the simplified model problem, to a non-linear multi-degree of freedom problem in a second step showed promising results. A significant reduction of the flow-induced vibrations was possible. Simulations for different material parameter settings of the CSD subsystem also have shown the limits of the chosen controller type and design. Furthermore, they show the limits for system's controllability by applying a force at the flag's root point. Investigating the total number of iterations per time step illustrates that the FSCI scheme with no nesting is the best variant for controlling the selected multi-degree of freedom problem presented in this chapter.

Chapter 4

The Numerical Wind Tunnel for Civil Engineering Structures

This Chapter deals with the numerical wind tunnel and its particular application to civil engineering structures. In contrast to airplanes and cars, which are streamlined bodies, civil engineering structures are bluff bodies in most cases. When dealing with civil engineering structures in natural wind conditions, one has to keep an eye on the following points:

a) The turbulent characteristics of natural wind.

b) The large, spatial expansion of the object, i.e., building.

c) The possible interaction of the object with the fluid flow surrounding it.

Those three points mentioned above can pose problems for physical wind tunnels. This is especially the case for issues b) and c). For b) it is often not possible to fulfill all geometrical prerequisites of the building in an appropriate way, which is, for example, the case when dealing with thin and lightweight structures like membranes. To be able to investigate c), a fully elastic model is necessary, which needs exact modeling of the mass and stiffness distribution. This is possible with a numerical model but hardly or only with a lot of effort possible by a miniaturized physical model of the building. Additionally, only a limited number of measurement points can be set in the physical wind tunnel, which cannot be placed on arbitrary positions, because they might influence the fluid flow's behavior. The main advantage of the physical wind tunnel is the possibility of conducting many measurements in a short period, once the model is built and calibrated.

In the past years, the main bottleneck for the numerical wind tunnel has been the computation time. As shown in Section 2.6, this bottleneck could be reduced by the software applied in this thesis work. When looking at the increase in computation power in the past years, the problem of computation time is going to reduce even more in the next years. This is why the numerical wind tunnel can offer a serious alternative to the physical wind tunnel for the problems shown later in this chapter.

Although this work concentrates on the numerical wind tunnel, it has to be mentioned, that for a holistic approach in the design of civil engineering structures in the natural wind, parallel investigations with the strengths of both, the numerical and the physical wind tunnel should be taken into account.

4.1 Characteristic Dimensionless Numbers and Coefficients

This Section shortly introduces characteristic dimensionless numbers and coefficients which can be applied to characterize the behavior of the fluid flow or compare its action on an object. The dimensionless numbers of importance are the Reynolds number

$$\mathrm{Re} = \frac{b \cdot u_{\mathrm{F}}}{\nu_{\mathrm{F}}} \tag{4.1}$$

and the Strouhal number

$$\mathrm{St} = \frac{b \cdot f}{u_{\mathrm{F}}}. \tag{4.2}$$

Herein b is a characteristic length, for example the diameter of a cylinder, u_{F} is the velocity component in streamwise direction in the undisturbed flow, f is the vortex shedding frequency and ν_{F} is the kinematic viscosity of the fluid flow. By the Re number, it can be evaluated if the fluid flow shows turbulent or laminar characteristics. In the case of wind on the civil engineering structures treated in this work, typical values are in the region of $\mathrm{Re} = 5\mathrm{e}7$, which means the fluid flow is in the transcritical regime and shows highly turbulent characteristics. The St number is defined for several geometrical entities, e.g., cylinders or rectangles, and serves to investigate the vortex shedding frequency. In some cases, it depends on the Re number.

Another characteristic coefficient relevant for civil engineering structures is the drag coefficient $\mathrm{C_d}$. It is defined as

$$\mathrm{C_d} = \frac{2t_x}{\rho_{\mathrm{F}} u_{\mathrm{F}}^2 A}. \tag{4.3}$$

Herein t_x is the component of the traction vector in streamwise direction, ρ_{F} is the fluid density, u_{F} is the component of the velocity vector in streamwise direction in the undisturbed flow and A is a reference area. Typically A is chosen as the front face of the object the fluid flow is acting on. The drag coefficient depends on the height of z in which u_{F} is measured. Additionally, it can also depend on the Re for specific geometries.

The dimensionless number describing the vulnerability of a structure to vibrations is the Scruton number Sc. It describes the ratio of the structural damping, the structural mass and the mass of the air and is defined as

$$\mathrm{Sc} = \frac{2\Lambda m_{i,e}}{\rho_F b^2}. \tag{4.4}$$

Herein Λ is the structural damping described by the logarithmic decrement, $m_{i,e}$ is the equivalent structural mass per length, ρ_F is the density of air and b is a characteristic length.

4.2 Numerical Generation of Natural Wind

To be able to simulate the wind loads on structures the wind effects of the atmospheric boundary layer (ABL) near the ground have to be modeled. According to [49], this part of the atmosphere is referred to as surface layer, is characterized by constant shear stress distribution in the vertical direction, and extends to approximately 100 m above ground level. In the boundary layer, the shear stresses resulting from the friction of the earth and the temperature gradient dominate the wind effects. The latter are small compared to the friction forces at wind speeds, which are of interest for wind loads on structures and thus can be neglected. The terrain can be characterized by the roughness height z_0, which strongly influences the turbulent conditions near the structure and the structural wind loads. For example [2] Tab. NA.B.1 defines different terrain categories (I to IV) from which the value of z_0 can be specified. Since the temperature gradient can be neglected, from a methodological point of view, the surface layer can be meant to be neutrally stable. Applying the additional assumption of a homogeneous surface roughness in the upstream terrain, the variation of the mean velocity component $\overline{u}_{\mathrm{F}}$ can be approximated over the height z by the power law

$$\overline{u}_{\mathrm{F}}(\mathrm{z}) = \gamma \cdot \overline{u}_{\mathrm{F}}(\mathrm{z}_{\mathrm{ref}}) \left(\frac{\mathrm{z}}{\mathrm{z}_{\mathrm{ref}}} \right)^{\alpha}. \tag{4.5}$$

The values for γ, $\overline{u}_{\mathrm{F}}(\mathrm{z}_{\mathrm{ref}})$ and α can be found for example in [2] Fig. NA.A.1 and Tab. NA.B.1. If no design codes exist for the country the building is located in, measurements from weather stations nearby can be used to determine $\overline{u}_{\mathrm{F}}(\mathrm{z}_{\mathrm{ref}})$. An alternative for determining a value for α is a curve fit depending on z_0 for a logarithmic velocity profile, which is an alternative to the power-law in Eq. (4.5).

The mean velocity profile in Fig. 4.9 describes the component of the velocity in streamwise direction varying over hours or days. This variation results from the changes in the weather. In order to resolve the smaller time scales, i.e., minutes and seconds, time-resolved fluctuations are superimposed on the mean velocity profile. The velocity fluctuations u'_{F} are defined as

$$u'_{\mathrm{F}}(\mathrm{z}, t) = u_{\mathrm{F}}(\mathrm{z}, t) - \overline{u}_{\mathrm{F}}(\mathrm{z}). \tag{4.6}$$

In order to describe the properties of natural wind and especially of the fluctuating part, several characteristic statistic values can be computed for each component of $\boldsymbol{u}_{\mathrm{F}}$, e.g. in x-direction (refer also to APPENDIX B). The first value is the turbulence intensity

$$I_u = \frac{\sigma_u}{\overline{u}_{\mathrm{F}}}. \tag{4.7}$$

Table 4.1: Basic input parameters for [5].

wind field dimensions ℓ_{x}, ℓ_{y}, ℓ_{z}	70000 m, 600 m, 600 m
grid points $n_i = 2^{r_i}$	4096, 256, 256
grid width r_i	12 m, 8 m, 8 m
spectra	Kaimal
reference height z_{ref} *)	Sect. 4.5.1 and 4.6.1
roughness length z_0 **)	
mean velocity $\overline{u}$ at z_{ref} ***)	

The second one is the characteristic length scale or turbulence length

$$L_u^x = \overline{u}_{\mathrm{F}} \int_0^{\mathcal{T}} R_{uu} \mathrm{d}\tau \quad \forall R_{uu} > 0, \tag{4.8}$$

where R_{uu} is the auto correlation, described in Sect. B.6. Additionally, the energy spectrum $S_{uu}(f)$ can be investigated.

Those statistic indices can be computed for a time series gained from measurements or numerical simulations. Furthermore, [2] provides standard values for I_u and L_u^x in Tab. NA.B.4 for the different terrain categories.

The fluctuating inlet components are generated by a synthetic wind generator, which is presented in detail in [4] p. 8 -17 and is based on [64] and [65]. It is accessible on GitHub [5]. The most important input parameters for the inlet generator are:

*) z_{ref}: The reference height has to be specified as a positive real number and influences the turbulence length. It correlates with the turbulence length, i.e., for a higher turbulence length a larger value for the reference height has to be specified. Not to be confused with $\mathrm{z}_{\mathrm{ref}}$ from the exponential profile.

**) z_0: The value of the roughness length z_0 influences the turbulence intensity.

***) $\overline{u}(z_{\mathrm{ref}})$: The mean velocity component at z_{ref} in flow direction is used for initializing the parameters for the fluctuating component generation and is stored for the generation of the mean wind profile.

The fundamental sketch of the numerical wind tunnel, i.e., the CFD domain, with its dimensions, can be seen in Fig. 4.1. The fluctuations are superposed to the mean velocity profile, which is applied at the inlet. The boundary conditions are set to slip on the walls and top and no-slip on the bottom and the interface of the obstacle, i.e., the structure. At the outlet, the pressure is set to zero. The distances from the structure to the boundaries of the CFD domain are necessary to avoid spurious effects from the boundary conditions and retain the blockage ratio below 2%. The finite element mesh of the CFD domain with a sum of approx. 10e6 tetrahedral and triangular elements can be seen in Fig. 4.2. It is subdivided into three refinement regions, which gradually increase the mesh size from the near field of the structure, where the fluid flow has to be modeled very detailed, to the far-field. The extension of box 2 to the inlet is necessary to minimize the numerical dissipation of the turbulent profile applied to the inlet until it reaches the location of the structure. Tab. 4.2 lists the mean element sizes. The table can only give a rough overview because an unstructured meshing procedure has been applied, which means the element size might be locally smaller, but not

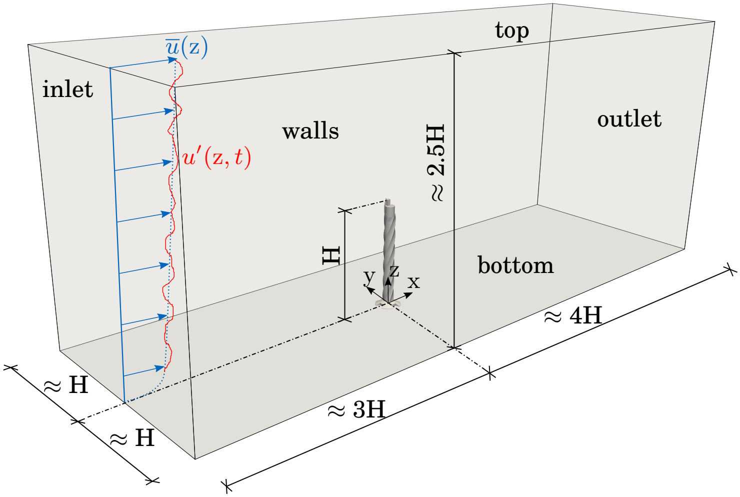

Figure 4.1: Dimensions ot the numerical wind tunnel.

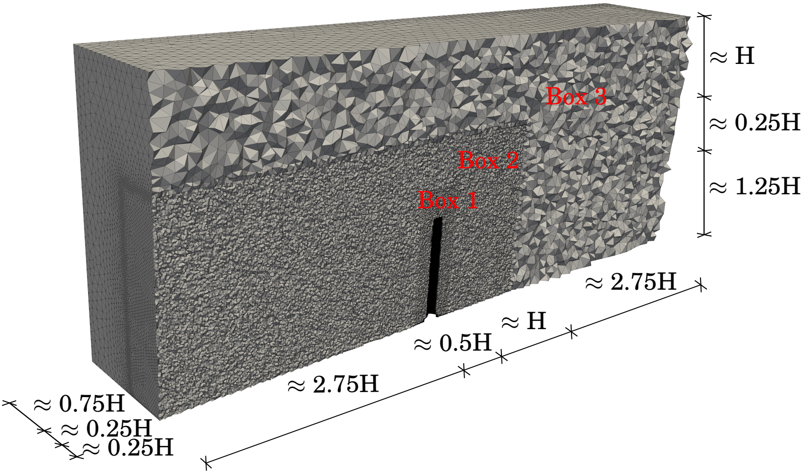

Figure 4.2: Fluid mesh with three refinement regions.

Table 4.2: Element sizes for the numerical wind tunnel. With box 1 in the near to box 3 in the far field.

Type	Mean element size
FSI interface	0.25 m
Box 1	2.0 m
Box 2	4.0 m
Box 3	16.0 m

larger than the sizes listed here. The mesh refinement has been investigated by convergence studies, which will be presented in detail in section 4.4.

In order to check the correct modeling of the wind conditions in the numerical wind tunnel, a simulation with an empty CFD domain, i.e., without any obstacle inside, was conducted. Except for omitting the obstacle, the mesh characteristics are the same, and a physical time of $T_{\mathrm{phys}} = 600$ s was simulated. The statistical data mentioned in Eq. (4.7), (4.8) and (B.7) can be computed for several points over the height z at position $\mathrm{x} = 0$ and $\mathrm{y} = 0$.

4.3 Wind Effects on High-Rise Civil Engineering Structures

This section discusses the significant effects of wind on high-rise, civil engineering structures. This section focuses on the effects which can occur, for example, for tower-like structures, chimneys, or skyscrapers. This work does not deal with bridges. Consequently, the wind effects, which are only valid for bridges, are omitted. [1] Appendix N provides a short overview of wind effects on bridges.

a) Buffeting: Buffeting oscillations are oscillations of the structure in the streamwise direction. Those oscillations can be amplified if the gust frequency matches one of the eigenfrequencies of the structure.

b) Vortex induced vibrations: A fluid flow, which is flowing around a bluff body, can cause periodic vortex shedding, which results in periodic forces. Fig. 3.9 shows an example for such periodic vortex shedding. These forces especially take effect in the cross-flow direction. If the vortex shedding frequency coincides with one of the eigenfrequencies of the structure, resonance effects can occur. As mentioned in section 4.1, the vortex shedding frequency can be described by the St number. By rewriting Eq. (4.2) to

$$\overline{u}_{\mathrm{F,crit}} = \frac{b f_{i,\perp}}{St}, \tag{4.9}$$

the critical velocity in streamwise direction can be computed. Herein the frequency $f_{i,\perp}$ is the eigenfrequency of the i^{th} eigenmode orthogonal to the flow direction. In most cases the lowest eigenfrequency is the critical one. For certain types of structures, [1] offers simplified formulas to calculate the displacements and forces from vortex induced vibrations. The amplitude of vortex induced vibrations can be reduced by adding damping to the structure.

c) Galloping: This type of wind effects are self-inducing vibrations, which can arise if a structure surrounded and influenced by a fluid flow sets itself in motion. This results in additional flow forces further exciting the structural motion.

In the case of galloping very large amplitudes are possible, which cannot be reduced by adding structural damping. Galloping starts if the critical galloping velocity

$$\overline{u}_{\mathrm{F,CG}} = \frac{2\mathrm{Sc}}{a_{\mathrm{G}}} f_{1,\perp} b, \tag{4.10}$$

is attained. The Sc is defined in Eq. (4.4), $f_{1,\perp}$ is the first eigenfrequency in perpendicular to the flow direction, b is a characteristic length and a_{G} is a stability value depending on the geometry. Values for a_{G} are suggested in [1] Tab. E.7. According to [1] galloping will not occur if:

$$\overline{u}_{\mathrm{F,CG}} > 1.25\overline{u}_{\mathrm{F}}(\mathrm{z}_{\mathrm{CG}}). \tag{4.11}$$

Herein $\overline{u}_{\mathrm{F}}(\mathrm{z}_{\mathrm{CG}})$ is the mean wind speed at the height where the galloping excitation forces are expected to occur. Additionally, an interaction of galloping with vortex induced vibrations is possible. This might be the case if

$$0.7 < \frac{\overline{u}_{\mathrm{F,CG}}}{\overline{u}_{\mathrm{F,crit}}} < 1.5. \tag{4.12}$$

If Eq. (4.12) holds, additional investigations, e.g. numerical simulations, are necessary.

4.4 Basic Convergence and Validation Study

Before carrying out simulations within turbulent wind conditions in this section, the results of a basic convergence and a validation study for the types of geometries investigated later are presented. This convergence study is an extension of the convergence studies carried out in [4], which utilized the implementation from [53], too. The geometries of interest are a cylinder and a hexagon. Fig. 4.3 shows a convergence study for St and $\mathrm{C_d}$. Therefore, CFD simulations with the geometry of the structure presented in section 4.6 with the mean velocity profile shown in Fig. 4.9 b) for $T_{\mathrm{phys}} = 600$ s and up to a number of $22\mathrm{e}6$ elements were performed. The angle of attack of the flow on the hexagon hereby varies over the height z. Consequently, the mesh with $8\mathrm{e}6$ elements is applied for simulations with the hexagon geometry and the mesh with $10\mathrm{e}6$ elements for the cylindrical geometries.

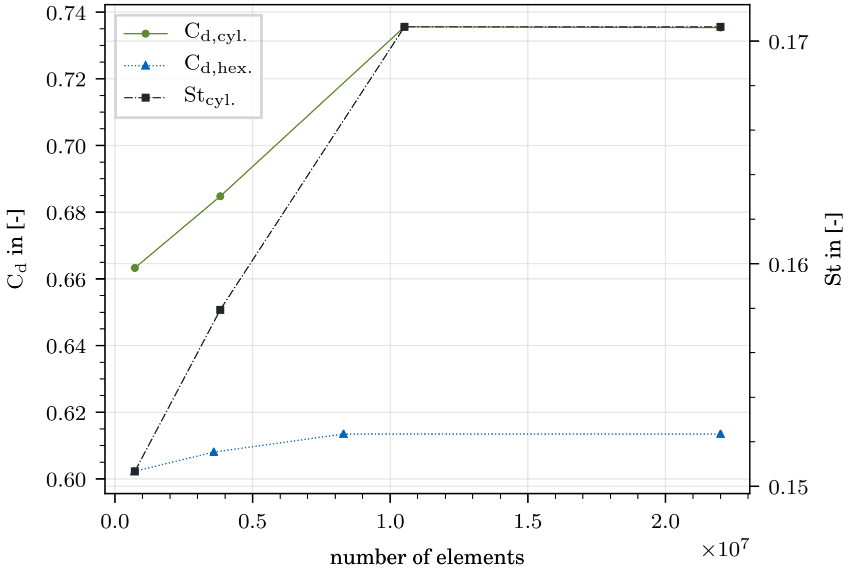

Figure 4.3: Convergence study for C_d and St.

For an additional validation, a similar simulation with the same fluid domain setup, but with the mean velocity profile shown in Fig. 4.9 a) was performed for the geometries presented in sections 4.5 and 4.6. The results of both simulations are compared to well-known measurements on real structures and in physical wind tunnels summarized by [83]. Fig. 4.4 and Fig. 4.5 show the St number and C_d coefficient in dependence of the Re number for a cylinder. The results for the St number and the C_d of the numerical simulation are within the variation range of the measurements. Not for all of the results in Fig. 4.4 and Fig. 4.5 measured in the physical wind tunnel, the reference point, where the velocity component u_F in the undisturbed flow was measured, is known. For the on-site measurements for built structures, it is documented. Here the reference velocity had been measured at the height of the obstacle. For consistency, this approach is followed for the simulations in this work, too.

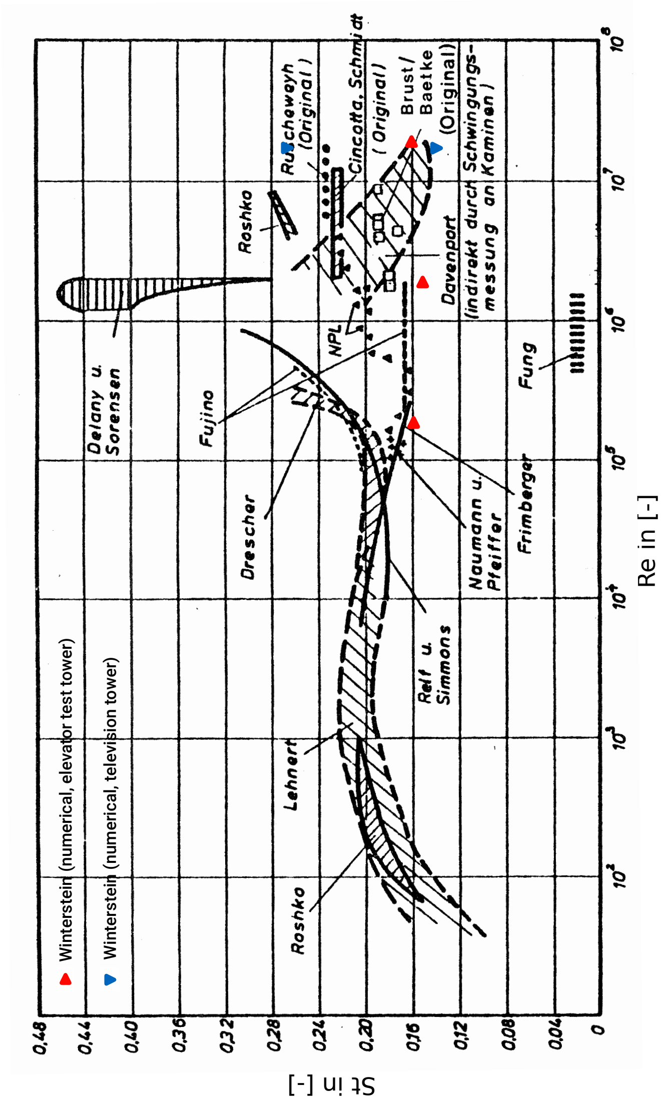

Figure 4.4: Strouhal number comparison from [83] p. 73.

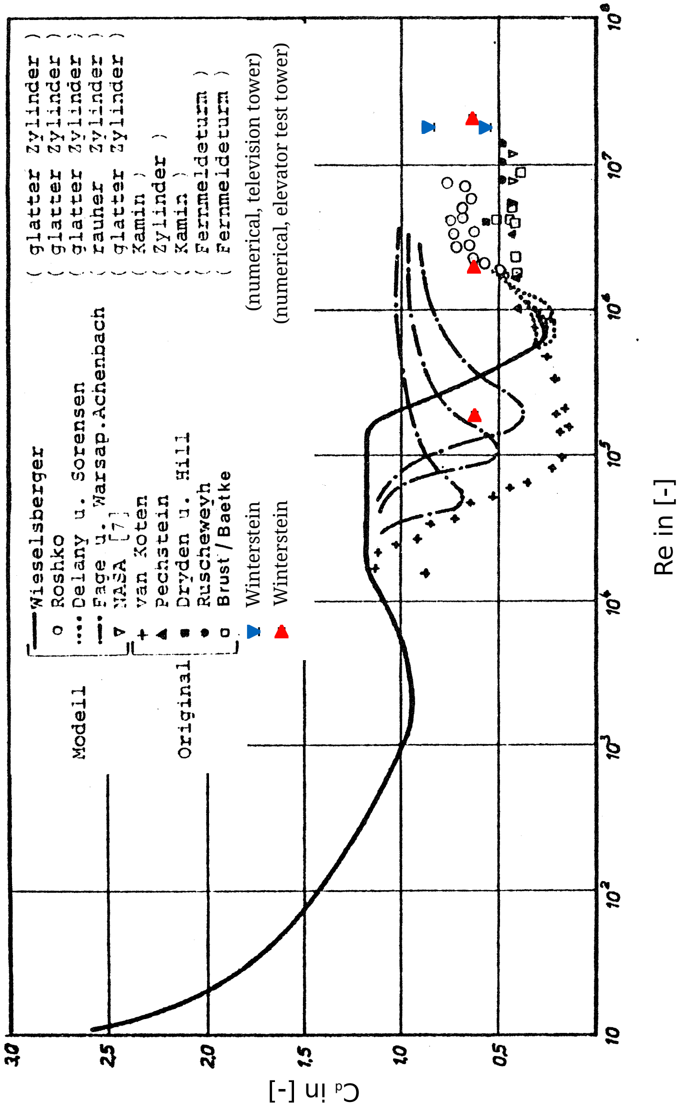

Figure 4.5: Drag coefficient comparison from [83] p. 73.

4.5 The Olympic Tower in Munich

This section deals with the wind-structure interaction of the Olympic Tower in Munich (OT). The OT was built from 1965 - 1968 and has a height of 291 m. Besides its usage as a television tower, it also serves as a viewing tower and accommodates a rotating restaurant.

This investigation serves as an additional validation case for the overall setup for the modeling of wind-structure interaction for high-rise, tower-like structures. The OT has been chosen, because in the years 1975 to 1984, very detailed studies concerning wind loads on the tower-like structures, mainly focused on the OT, had been carried out. Those studies also contained a very elaborate measurement campaign, including wind speeds and reaction moments. The results have been published as parts of ”Beiträge zur Anwendung der Aeroelastik im Bauwesen” [106]. In the following, one of these measurements' wind characteristics are modeled by the numerical inlet generator presented in section 4.2 and are applied as an inlet condition to the numerical wind tunnel. In the first step, the simulated results are compared to the characteristic, statistic values for the empty numerical wind tunnel. A detailed finite element model of the OT was placed in the numerical wind tunnel, and a fully coupled FSI simulation was performed in a second step. Finally, the results of the FSI simulation are compared to the measurements from [86] and [75], which were parts of [106].

4.5.1 Numerical Wind Generation for the Wind Acting on the Olympic Tower in Munich

For the numerical wind generation the velocities from ”Messung 50” (M50) in [86] p. 71 ff. from 13.11.1972 were analyzed at a height of $\mathrm{z} = 152$ m and $\mathrm{z} = 220$ m. This measurement was chosen because it has a high mean wind speed, the amplitude of the measured reaction moments is large and the measurement duration with $T_{\text{phys}} = 41.5$ min. is long. A basic sketch of the OT with its major dimensions, a height scale, and the position of the measurement devices is depicted in Fig. 4.6. The major wind direction in M50 is $253°$, the ten minute mean wind speed at a height of $\mathrm{z} = 220$ m is $24.2\ {}^{\mathrm{m}}/_{\mathrm{s}}$ and the maximum gust speed is

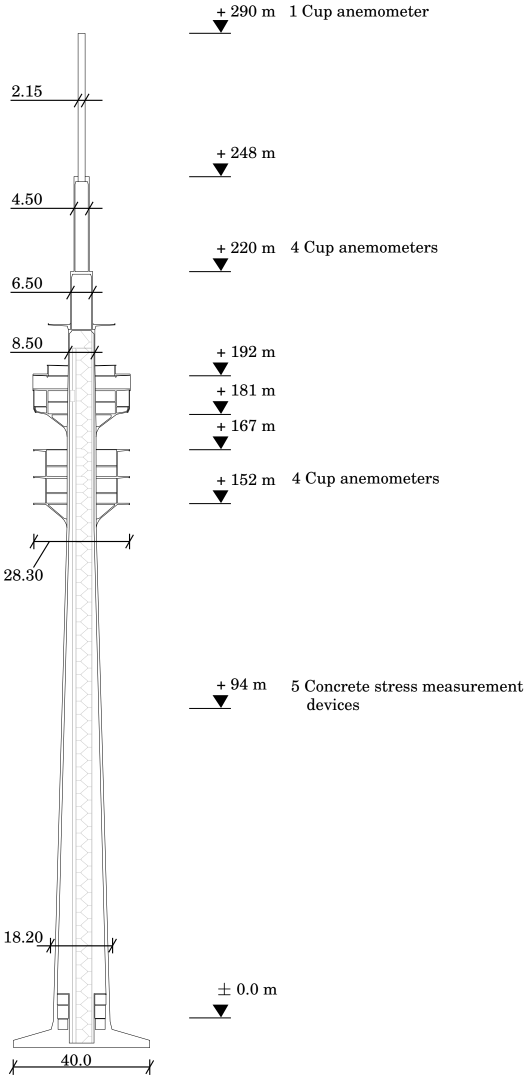

Figure 4.6: Fundamental sketch of the Olympic Tower in Munich with positions of the measurement devices.

37 m/s. Fig. 4.7 shows a basic map of the area around the OT. The position of the OT is marked by †. On basis of Fig. 4.7 the location

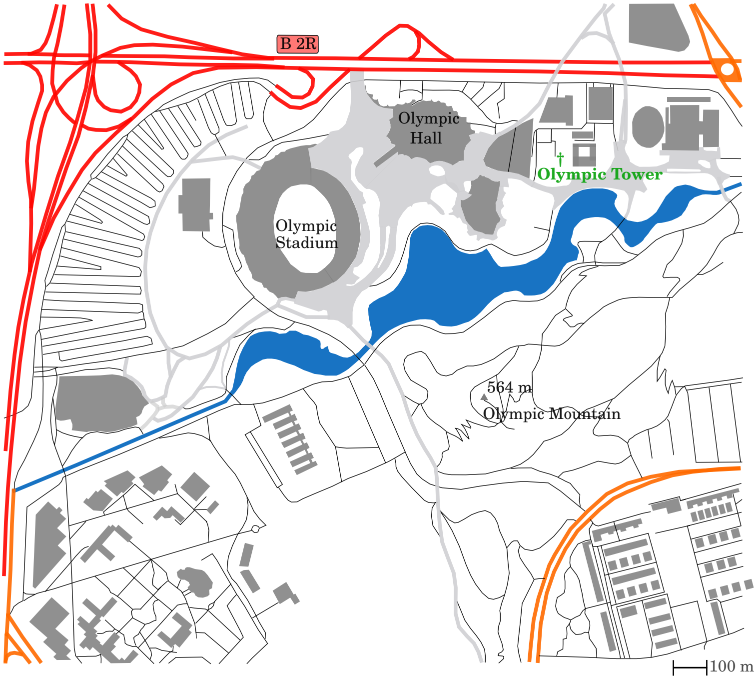

Figure 4.7: Map of the area around the Olympic Tower in Munich.

of the OT can be classified as a suburban or urban area, i.e. surface category III or IV according to [2] Tab. NA.B.1. This results in $z_0 = 0.30$ m for category III and $z_0 = 1.05$ m for category IV. Those values also serve as basis for the generation of the velocity fluctuations with the numerical inlet generator. For the power law describing the mean profile in Eq. (4.5) the exponent is to be set to $\alpha = 0.22$ for surface category III or to $\alpha = 0.30$ for category IV. The value for $\overline{u}_{\mathrm{F}}(\mathrm{z}_{\mathrm{ref}}) = \overline{u}_{\mathrm{F}}(220\ \mathrm{m})$ is set to 24.2 m/s. Different variants for different values of α of a numerical wind have been generated and investigated by simulations with an empty numerical wind tunnel. The results of the mean velocity superposed by the fluctuation components generated by the inlet generator for the empty numerical wind tunnel are depicted in Fig. 4.8. The characteristic statistical values for the results of the best matching results at coordinate $\mathrm{x} = \mathrm{y} = 0.0$ of the simulations with M50 are shown in Figs. 4.9, 4.10 and 4.11.

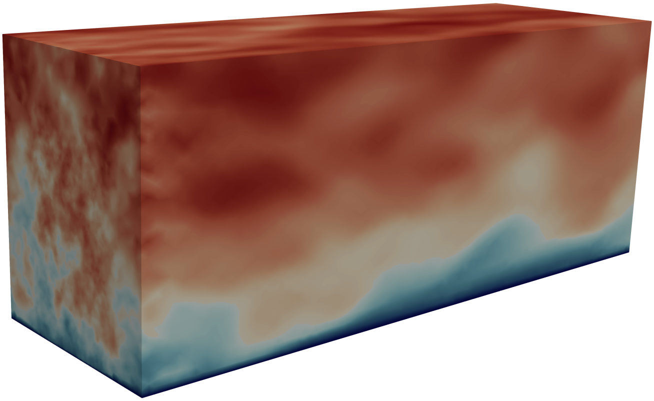

Figure 4.8: Numerical wind-tunnel with mean velocity and superposed fluctuating components.

Fig. 4.9 a) depicts the mean velocity profile with $\alpha = 0.30$ from the simulation at 50 points over the height z and also the theoretical profiles from [2] and the values from M50. The location of the building can be assigned to the terrain category IV, urban area. Fig. 4.10 shows the velocity spectra at the heights of $\mathrm{z} = 152$ m and $\mathrm{z} = 220$ m for the simulation and M50 and also includes the theoretical values from [49]. Fig. 4.11 a) depicts I_u for measurements and simulation compared to the theoretical values from [2]. In this case, the distribution of M50 over height is a mixture between the theoretical values from terrain cat. III and cat. IV, which is also mimicked by the numerically generated wind. Finally, Fig. 4.11 b) shows L_u^x. This type of characteristic statistical value is hard to be matched numerically. The theoretical values from [2] are, by far, not matching the values from M50. Two approaches are possible to deal with this kind of problem. The first one is to fit the values of L_u at certain points, as it is for example done in [4] p. 39 over time. In this case this could be conducted at

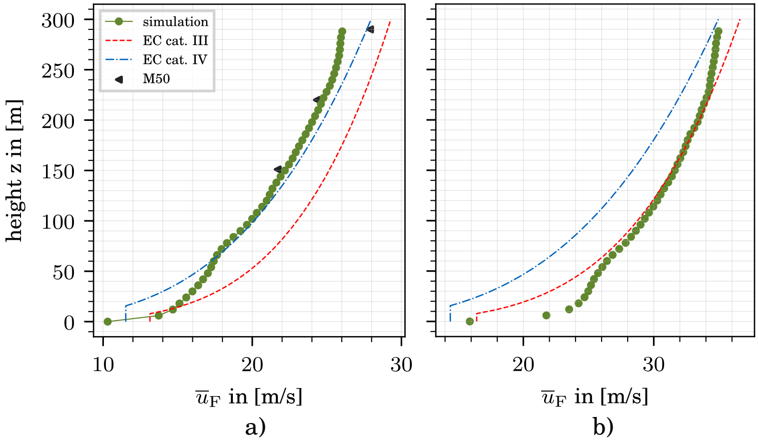

a) b)

Figure 4.9: Mean velocity profiles for a) OT and b) TkT. EC: Theoretical values from [2]; M50: Measurements from [86].

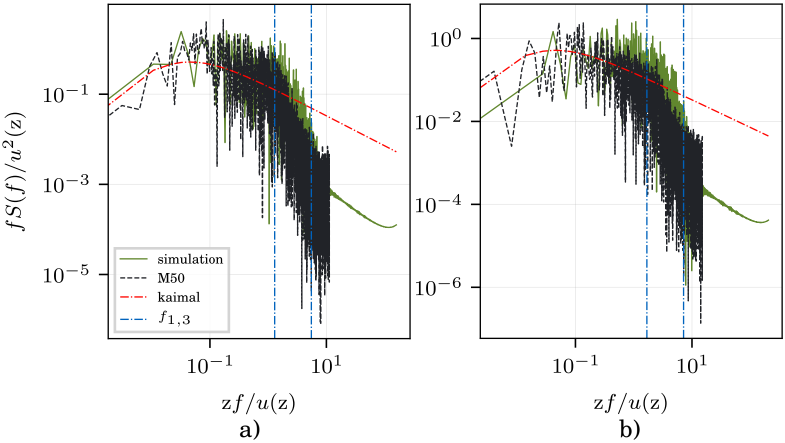

a) b)

Figure 4.10: Velocity spectra for a) $z = 151$ m and b) $z = 220$ m for the OT. M50: Measurements from [86]; Kaimal: Theoretical spectrum according to [49]; $f_{1,3}$: Eigenfrequencies of the structure.

z = 152 m and z = 220 m. If this is done, the distribution between

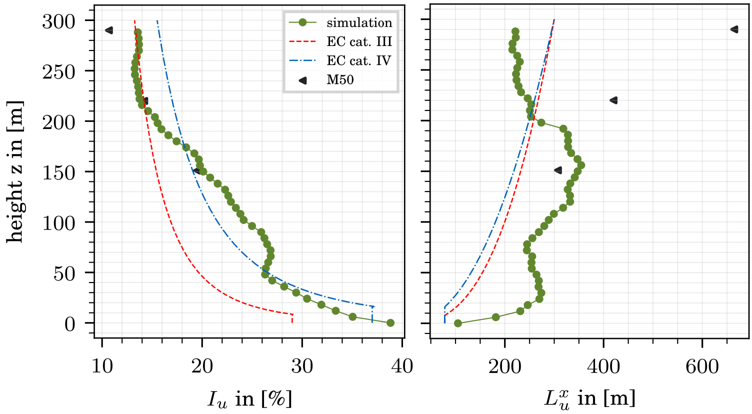

Figure 4.11: Turbulence intensity and turbulence length for the wind numerically generated for Munich. EC: Theoretical values from [2]; M50: Measurements from [86].

those points over z strongly varies, which is not realistic. The second possibility is shown in Fig. 4.11 b). Here the values are fitted the best way possible over z, which gave better results than only fitting points decidedly. The best results also shown in the figures in this section were obtained by setting the parameters for the roughness z_0 and reference height z_{ref} to 0.5 m and 80 m.

4.5.2 CSD Model of the Olympic Tower in Munich

The structural model of the OT is modeled by the FEM with the shell and beam elements presented in sections 2.1.2.1 and 2.1.2.2. The basis of the finite element model is the construction plans of the OT provided by the ”Stadtwerke München” (SWM), which contain several horizontal and one vertical cut. Those have been used to generate a three dimensional model. Additional information about the stiffness and mass distribution of the OT can be found in [85] p. 23 and [77] p. 28. The components and the main dimensions are depicted in Fig. 4.6 and Fig. 4.12 a) and b). It has to be distinguished between the main part made of concrete

($z = 0.0 - 248$ m) and the antenna ($z = 248 - 290$ m) made of steel. The concrete class according to [85] p. 21 is B450. Refer-

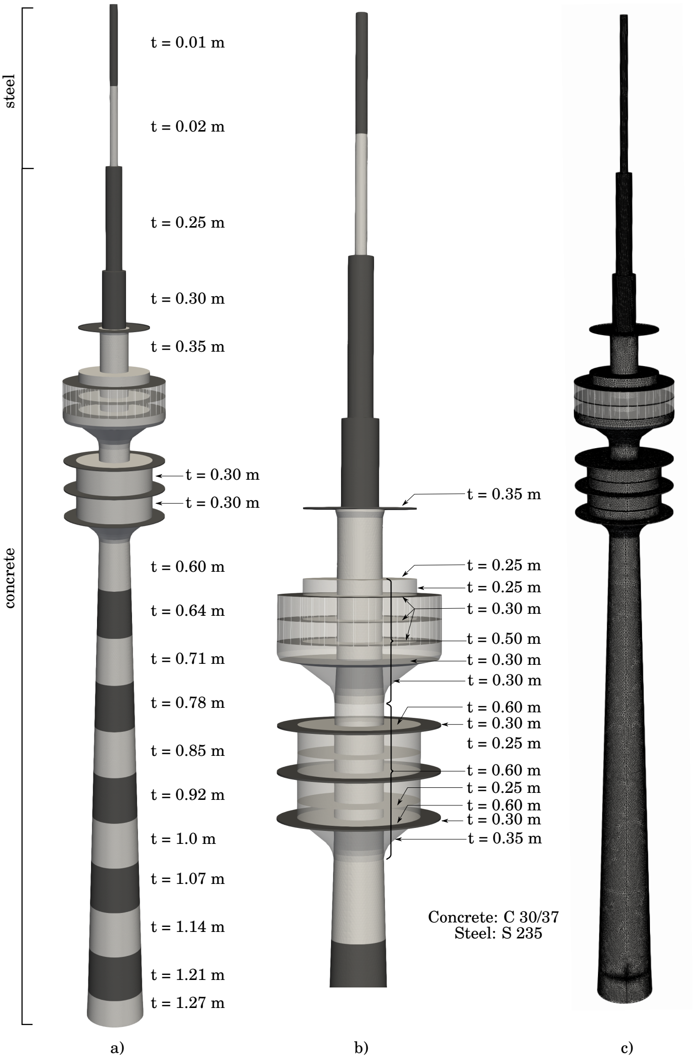

Figure 4.12: Olympic Tower in Munich materials and sections (a) and b)) and finite element mesh c).

ring to [17] p. 29, this corresponds to the concrete class C30/37 in the current European design code [3] with a mean secant Young's modulus $E_{\mathrm{cm,S}} = 33\mathrm{e}3$ MPa and $\nu_{\mathrm{S}} = 0.20$. For the steel part $E_{\mathrm{S}} = 21\mathrm{e}4$ MPa and $\nu_{\mathrm{S}} = 0.30$ is assumed. The shaft of the tower consists of an inner and an outer part, which basically can be seen in Fig. 4.6. The inner part is decoupled from the outer part to prevent stresses from the outer part's temperature changes. Thus the load-bearing behavior of the OT is fully dominated by the outer part, and the inner part does not need to be modeled. The thickness of the shaft varies from 1.3 m at $\mathrm{z} = 0.0$ m to 0.6 m at $\mathrm{z} = 145$ m. The variation of thickness is modeled by gradually varying the thickness of the shaft segments depicted in Fig. 4.12 a) in constant steps. The foundation does not need to be modeled explicitly, but as a Dirichlet boundary condition at $\mathrm{z} = 0.0$ m, rotations and displacements can be fixed. Detailed investigations concerning the foundation were performed in [77], which are also included in Tab. 4.3, showing that modeling the stiffness of the foundation does not have a significant effect in the case of the OT.

Another crucial part for modeling the correct dynamic behavior of a structure is the mass distribution. The self weight is calculated inherently in the finite element implementation. Therefore, the density of the concrete is set to $\rho_{\mathrm{S}} = 2600\ {}^{\mathrm{kg}}/{\mathrm{m}^3}$ and the density of steel is set to $\rho_{\mathrm{S}} = 7850\ {}^{\mathrm{kg}}/{\mathrm{m}^3}$. The additional dead load from building equipment and appliance as well as from non-load bearing walls is set to $4\ {}^{\mathrm{kN}}/{\mathrm{m}^2}$. Furthermore, 30% of the maximal assumed traffic load with $6\ {}^{\mathrm{kN}}/{\mathrm{m}^2}$ is applied to the slabs between $\mathrm{z} = 152$ m and $\mathrm{z} = 167$ m and $4\ {}^{\mathrm{kN}}/{\mathrm{m}^2}$ for the rest of the slabs. A dynamic eigenvalue analysis was performed to check the assumptions for stiffness and mass distribution. The finite element mesh consisting of $2.2\mathrm{e}5$ triangular shell elements is depicted in Fig. 4.12 c). A detailed view on the non-matching meshes at the interface between CFD and CSD subsystem for the OT are additionally visualized in Fig. 4.34 b). The results for the first five eigenfrequencies and their comparison with the measured and calculated reference values is summarized in Tab. 4.3. Because of the structure's symmetry, the first and second, and the third and fourth eigenfrequencies, are the same. In addition, Fig. 4.13 shows the first four eigenforms. The first two eigenforms (Fig. 4.13 a) and b)) are dominated by the concrete part and the third and fourth eigenforms (Fig. 4.13 c) and d)) are dominated by the

Table 4.3: Eigenfrequency comparison for the Olympic Tower in Munich.

Type	Eigenfrequencies in [Hz]		
	1 and 2	3 and 4	5
measured [75] p. 104	0.182	0.795	1.019
calculated clamped [77] p. 31	0.185	0.763	1.045
calculated elast. supported [77] p. 31	0.182	0.755	1.034
simulated	0.186	0.793	1.017

steel part. The structural damping is modeled by the Rayleigh coefficients (Eq. (2.12)). The values for the logarithmic decrement, the structural damping and the Rayleigh coefficients are summarized in Tab. 4.4. The values for the log. decrement have been suggested by [77], p. 34. The structure is lightly damped, and the eigenfrequencies computed by the dynamic eigenvalue analysis coincide with the damped eigenfrequencies. This coincidence has also been cross-checked by a numerical simulation, whereby the tower is deflected by a unit displacement of one meter applied on

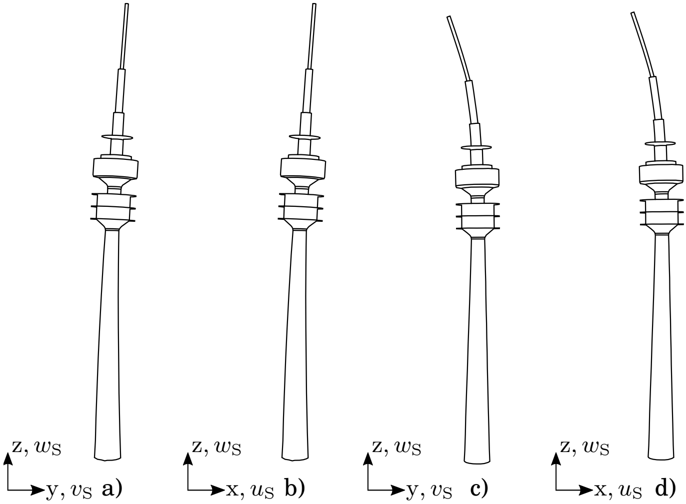

Figure 4.13: Dynamic eigenforms of the Olympic Tower in Munich (a) first to d) fourth eigenform).

Table 4.4: Log. decrement, damping ratio and Rayleigh coefficients for the OT.

Part	Λ	D	α_{R}	β_{R}
concrete	0.06	0.0095	0.0109	0.0084
steel	0.0025	0.0040	0.0188	0.0084

the slab at $\mathrm{z} = 192$ m letting the tower vibrate freely for several periods. The log. decrement and the first eigenfrequency can be measured. The values coincide with the proposed log. decrement and the result from the dynamic eigenvalue analysis.

4.5.3 FSI Simulations of the Olympic Tower in Munich

The simulation in the numerical wind tunnel is performed for a physical time $T_{\mathrm{phys}} = 41.5$ minutes. with a time step of $\delta t = 0.02$ s. A time series of the moments at the height $\mathrm{z} = 94$ m is written as an output in order to compare them with the measured values from M50. Fig. 4.14 and Fig. 4.15 show the longitudinal moment M_{y} and the lateral moment M_{x} for the simulation and M50. For more detailed investigations, it is of advantage to have a look at the frequency domain. A look at the frequency domain can be achieved by the Power Spectral Density (PSD) function, which is depicted for M_{y} in Fig. 4.16 and for M_{x} in Fig. 4.17 for the simulation and M50. The plots clearly show the first and second eigenfrequency. For the first resonance frequency, the simulation matches the measurements. In the higher frequency range, the spectrum of the simulation decreases a bit faster than the measurements, but also, the difference in the second resonance frequency is still acceptable. The first two eigenfrequencies dominate the interaction phenomenon. Thus the simulation should be able to map the behavior of the coupled problem accurate enough. It has to be mentioned that the data of M50 had to be digitized from the original publication. The result from this digitization is a non-uniform step size between the data points, which also influences the PSD's accuracy. Further investigations can be carried out by comparing the results of the simulation and measurements statistically. In the first step, the data for M_{y} from the simulation can be compared to the summary of measured values

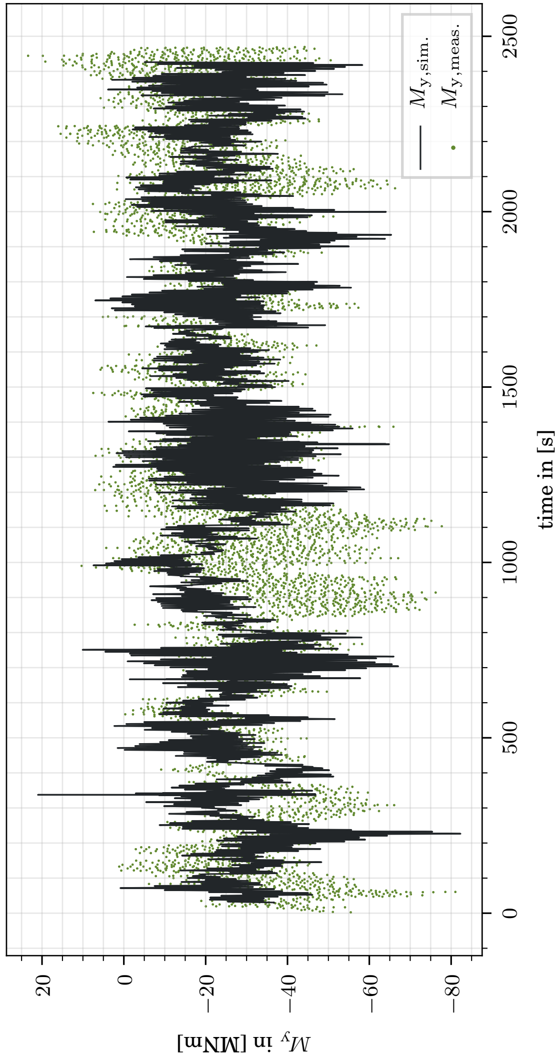

Figure 4.14: Longitudinal moment M_{y} of the simulation and M50.

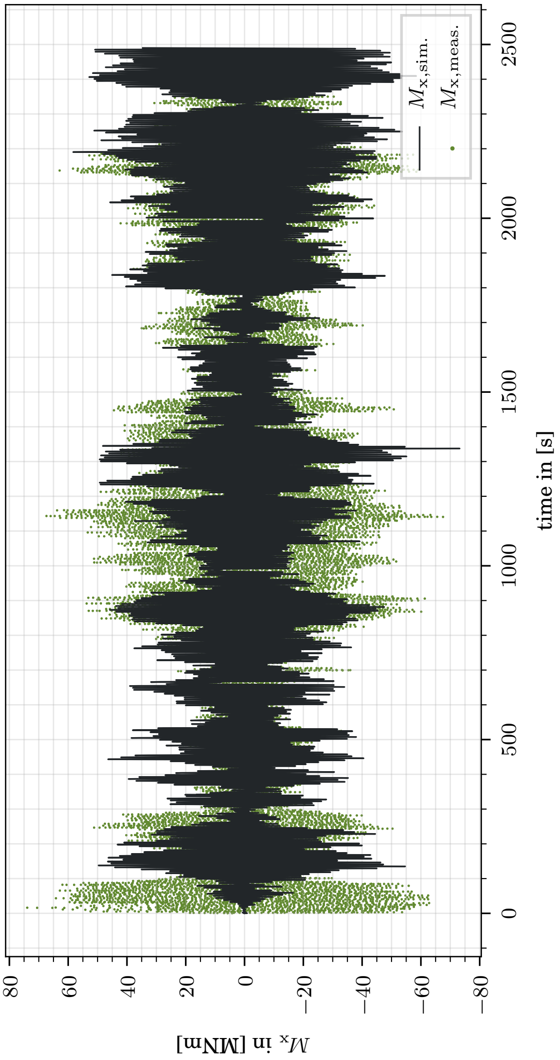

Figure 4.15: Lateral moment M_x of the simulation and M50.

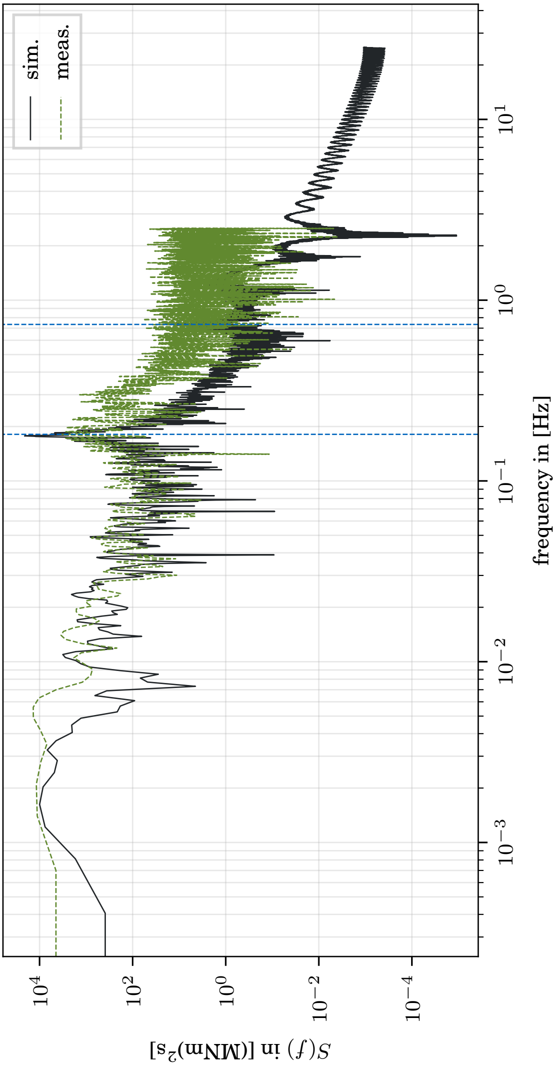

Figure 4.16: PSD longitudinal moment M_{y}. The dotted, vertical lines represent f_1,f_2 and f_3,f_4.

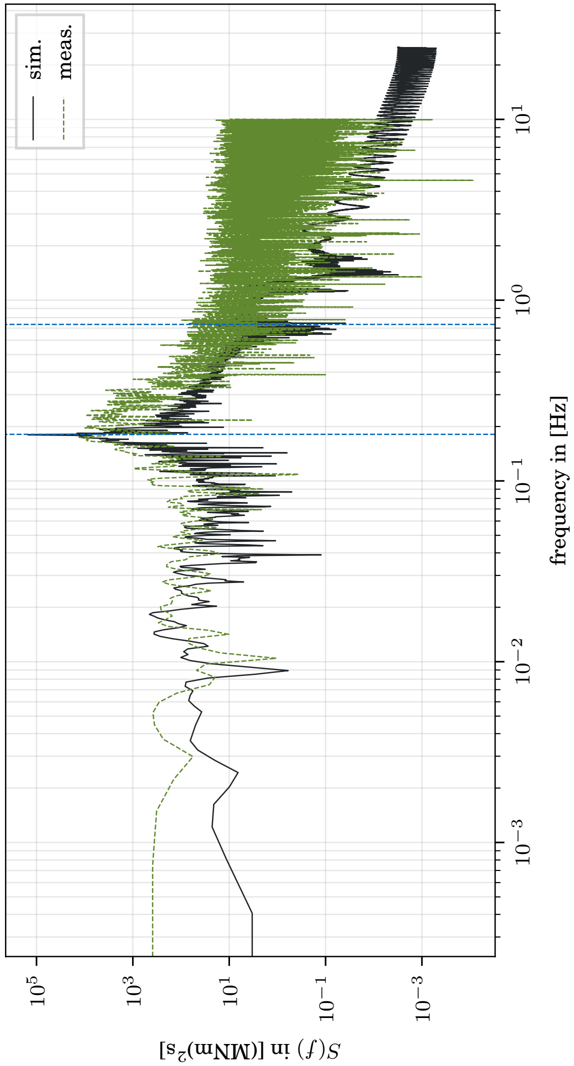

Figure 4.17: PSD lateral moment M_x. The dotted, vertical lines represent f_1,f_2 and f_3,f_4.

shown in the figures in [75] p. 105 and p. 106, which are included in this work as Fig. 4.18 for the mean value and Fig. 4.19 for the max value. Both figures also contain a linear regression line, the standard deviation σ, and the 95% fractile. The mean value of the moments of the simulations in Fig. 4.18, with the wind properties from M50, matches perfectly the regression curve. The values for the maximal moment in Fig. 4.19 are just above the line for 95% fractile, which is on the safe side.

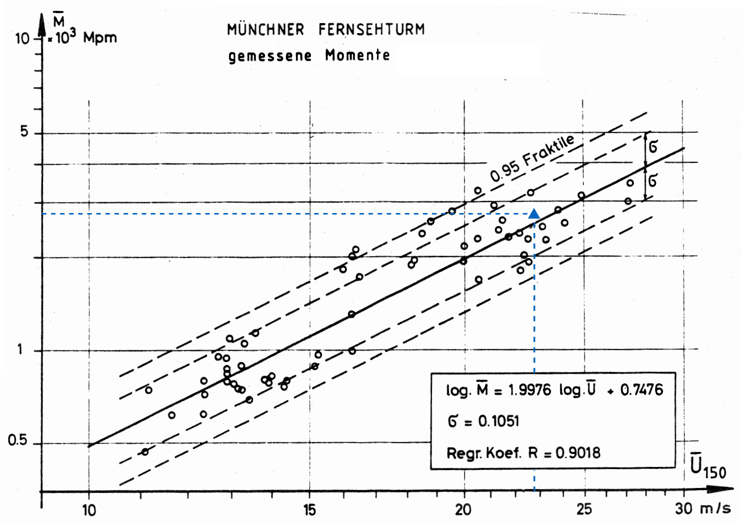

Figure 4.18: Regression of the mean, measured, longitudinal moment $\overline{\mathrm{M}} = \overline{M}_{\mathrm{y}}$ according to [75] p. 105. Measured values ○ and simulated value ▲.

Another question is, how much physical time T_{phys} has to be simulated in order to get statistically stationary results. The common consensus is, based on the energy spectrum of Van Der Hoven [99], to set $T_{\text{phys}} = 600$ s. Those ten minutes capture the micro meteorological effects, while the macro meteorological effects are captured by the mean velocity profile. In the case of the OT, simulated and measured data is available for $T_{\text{phys}} = 41.5$ minutes. Thus it is possible to inspect how the relative error between measurements and simulation develops over time. Fig. 4.20 compares the values for median, Root-Mean-

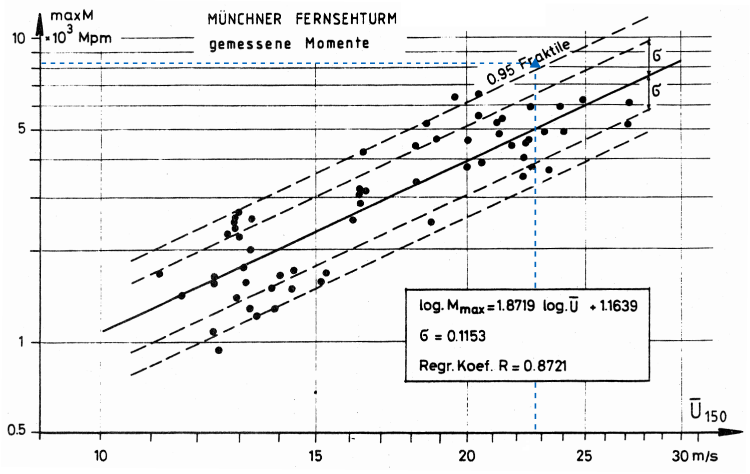

Figure 4.19: Regression of the maximal, measured, longitudinal moment $\mathrm{maxM} = M_{\mathrm{y,max}}$ according to [75] p. 106. Measured values • and simulated value ▲.

Square (RMS) and min/max amplitude for M_{x} and M_{y}. As reference data for the relative error calculation serve the statistical values calculated for the fully measured time of M50. Those are compared to the statistical quantities from the simulation after $T_{\mathrm{phys}} = \{300; 600; 900; 1200; 1500; 1800; 2100; 2400\}$ s.

The relative errors for all statistical quantities, except for $\widetilde{M}_{\mathrm{x}}$ are 20% or below after 600 s except for the value of $M_{\mathrm{x,max}}$. The value of $\widetilde{M}_{\mathrm{x}}$ is slightly oscillating over time, but remains below 20%. The lateral moment M_{x} is oscillating around zero, which can also be seen in Fig. 4.15. Whereby the values of the measurement show a slight shift, and positive and negative values are not distributed fully symmetric over time, as it is the case with the simulated values. The oscillation around zero leads to calculating the relative error with values close to zero, resulting in oscillations for the error's median value. Reasons for the slight shift in the measured values can be imperfections of the tower or deformations because of temperature, which can be significant according to several investigations made in the context of [106]. These effects were not taken into account within the numerical

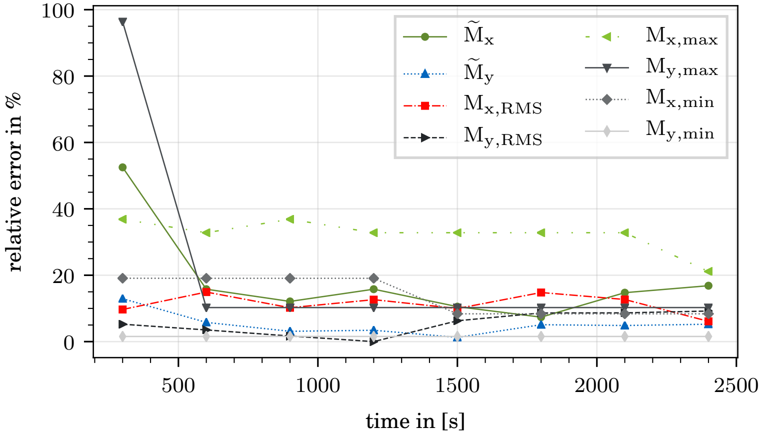

Figure 4.20: Relative error of selected statistical data for different simulation times. Median $\widetilde{(\cdot)}$, Root Mean Square (RMS) and min/max values for lateral moment M_x and longitudinal moment M_y.

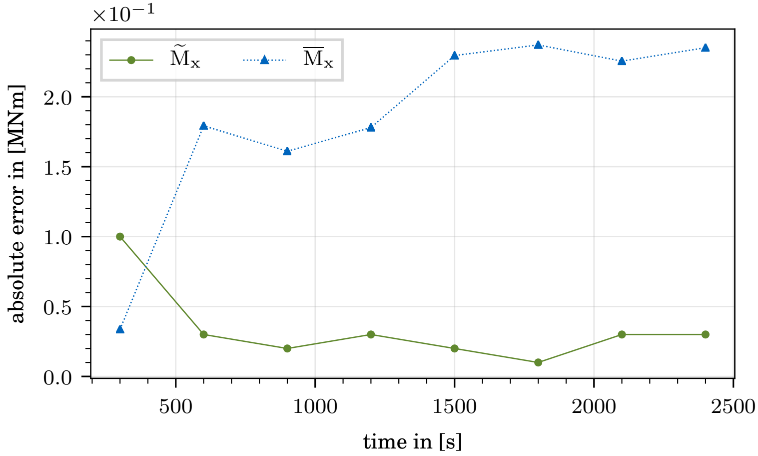

Figure 4.21: Absolute error of the lateral moment M_x for different simulation times. Comparison of median $\widetilde{(\cdot)}$ and mean $\overline{(\cdot)}$ value.

simulations. Fig. 4.21 shows the difference between median and mean value, where the mean and median value of the absolute error of the lateral moment M_x are compared over time. Because of the shift in the measured values and also some outliers in those values, the median value and not the mean value was utilized for the investigations made in this thesis work. According to [52] p. 77, 78 the median value behaves more robust against outliers and also more suitable if the values' distribution is not symmetric, as it is the case here.

All in all error between simulated and measured values of the statistical quantities investigated here, shows a decreasing tendency with increasing simulation time. Concerning the max/min values, the error depends on when the max or min value of relevance occurs in the dynamical process. Generally, it can be concluded a longer simulated physical time results in a smaller relative error. If one opposes the requirements for computation time and statistical accuracy, a value of the $T_\mathrm{phys} = 600$ s, offers the best compromise between them.

From the investigations carried out for the OT, it can be concluded that the generated wind and the numerical models set up can be applied to simulate the behavior of a tower-like structure in the natural wind within a reasonable amount of accuracy.

4.5.4 Acknowledgments

The detailed modeling of the OT would not have been possible without the help of Ms. Krikorian Maral from SWM, who provided the construction plans of the OT. Herewith her support is gratefully acknowledged.

4.6 The thyssenkrupp Elevator Test Tower in Rottweil

This section combines the algorithmic framework developed in CHAPTER 3 and the validation studies investigated in section 4.5 and applies them to the elevator test tower built by the thyssenkrupp elevator AG in Rottweil (Fig. 4.22).

The thyssenkrupp elevator test tower (TkT) has been designed by Prof. Werner Sobek. It was built by Ed. Züblin AG from 2014 - 2017 and serves as a testing environment for express and high-speed elevators. It mainly consists of a concrete tube containing several shafts for elevator testing and a hexagonal PTFE glass fiber membrane facade, which is mounted on a construction made of steel tubes. The transparency of the membrane changes over the height of the tower. The TkT has an overall height of 246 m. With a height of 231 m it also offers the highest viewing platform in Germany. Besides its architectural features, the TkT is currently the tallest building in the world, which can actively be stimulated to oscillate. The oscillations are initiated by a hybrid mass damper system (HMD) mounted at a height of 190 m in the form of a pendulum. Additionally, the HMD is used, in its passive mode, to reduce the structure's wind-induced vibrations, which provides a controlled testing environment for the elevators.

In this section the behavior of the TkT in natural wind conditions and its combination with the HMD is investigated.

4.6.1 Wind Conditions for the thyssenkrupp Elevator Test Tower

In contrast to the OT, no firm measurements of the wind conditions are available for the TkT. A different approach is necessary to find reasonable values for the natural wind, especially the mean velocity and the major wind direction. Three measurement points in the site's proximity have been compiled, to gain the macro meteorological data. Two of them are official measurement stations of the ”Deutscher Wetterdienst” (DWD), in Freudenstadt and Klippeneck. The raw data of the DWD's measurement stations are accessible from [32]. The DWD stations provide measurements for the hourly mean values for wind speed, gust speed, and wind direction. The third one is the privately operated measurement station of the ”Drachenfliegerverein Bösingen” (dfvb). In contrast to the DWD stations, the dfvb station provides values for the same data for a measurement interval of ten seconds. All of the measurement stations measure their values at $z_{\mathrm{ref}} = 10$ m. In addition to the measured data, simulated data provided by [69] has been taken into account. Unfortunately, no detailed information about the simulation concept is available. The simulated wind data also provides mean wind speed, gust speed, and wind direction at $\mathrm{z}_{\mathrm{ref}} = 10$ m as hourly mean values. The location of the tower and the measurement stations is marked on

Figure 4.22: The thyssenkrupp elevator test tower in Rottweil (Pictures: Winterstein).

the conceptual map in Fig. 4.23 by †. The airfield of Bösingen is located about six kilometers North-West of Rottweil and the DWD station of the Klippeneck approximately ten kilometers in the South-East. The DWD station of Freudenstadt is not on the map, because it is located approximately 25 km in the North-West of Rottweil. Concerning the macro meteorological aspects in this region over a longer period, this combination should lead to good results. This is also supported by the fact, that according to [2] Fig. NA.A.1, the building, and all the measurement stations are located in wind zone one. The raw wind data values provided by the measurement stations have been evaluated for a period between 2012 and 2018 because for this period, the data for all data

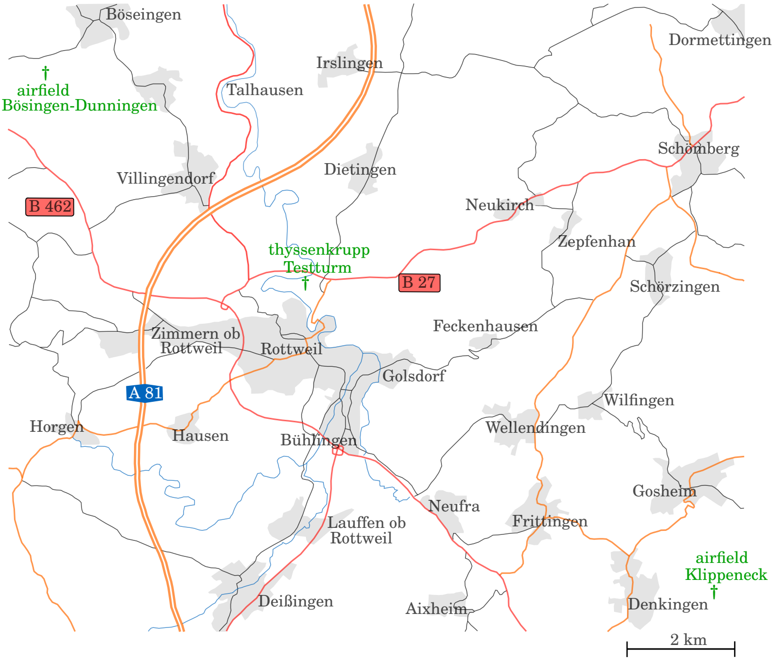

Figure 4.23: Map of the region around Rottweil. The important locations are marked green.

sets are fully available. The results are plotted as the wind rose plots in Fig. 4.24. The wind roses indicate the percentage occurrence of the daily mean velocity in each direction. The resolution of the data available for the station in Bösingen is finer than for the other stations, because of the shorter measurement interval. The major wind direction is South-West, i.e., approximately 230°. Having a look at Fig. 4.23 this means the wind blows most of the time across the town of Rottweil. The highest wind speeds are occurring in this direction, too. Taking into account the rest of the surrounding terrain this means terrain category III ([2] Tab. NA.B.1) can be assumed. This results in $\alpha = 0.22$ for the power law in Eq. (4.5). Before being able to generate the mean profile from the power law, a value for $\overline{u}_{\mathrm{F}}(\mathrm{z}_{\mathrm{ref}})$ has to be defined. Here the maximum measured mean value from 2012 - 2018 (Fig. 4.24)

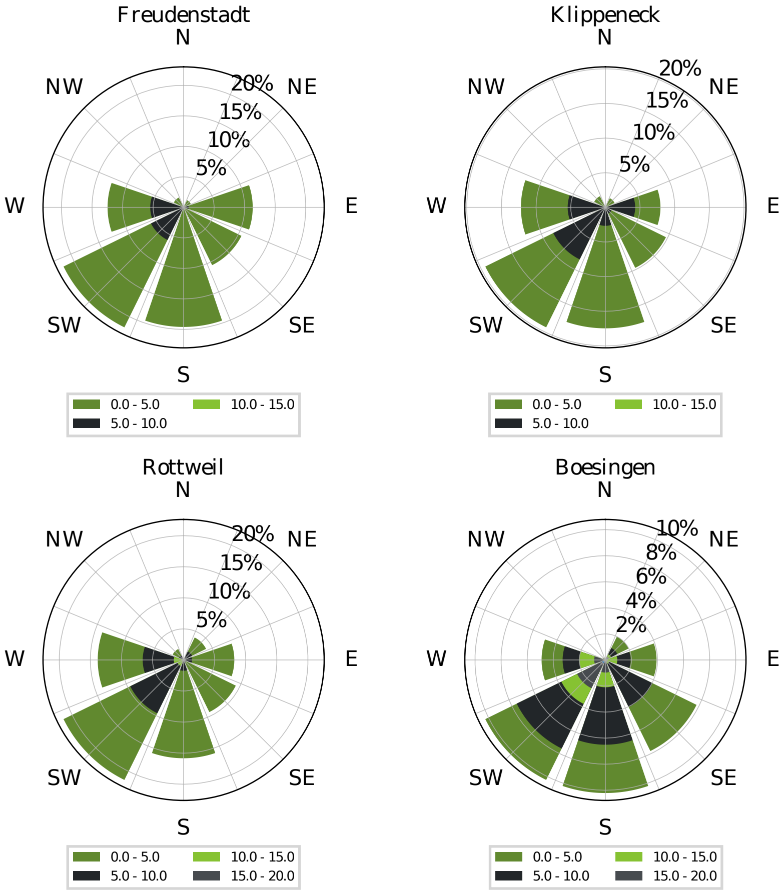

Figure 4.24: Wind roses for daily mean velocity in [$^{\mathrm{m}}/_{\mathrm{s}}$] from 2012/01/01 till 2018/12/31 at a height of ten meters.

is $\overline{u}_{\mathrm{F}}(10\ \mathrm{m}) = 20\ {}^{\mathrm{m}}/{}_{\mathrm{s}}$, which almost matches the proposed value from [2] Fig. NA.A.1, being $22.5\ {}^{\mathrm{m}}/{}_{\mathrm{s}}$ for wind zone one. The difference can be explained, because the value proposed in [2] must hold for a larger region in Germany, which is covered by wind zone one. Since a more detailed investigation has been made in this case, in the following $\overline{u}_{\mathrm{F}}(10\ \mathrm{m}) = 20{}^{\mathrm{m}}/{}_{\mathrm{s}}$ is defined as mean norm velocity $\overline{u}_{\mathrm{norm}}$. The terrain roughness near the structure in the main wind direction is similar to the one near the OT (refer to Fig. 4.7) and thus the same fluctuations generated by the numerical inlet generator as for the OT can be superposed to the mean profile proposed in this subsection. This turbulent fluctuations were generated by setting the input parameters for the inlet generator to 0.5 m for the roughness z_0 and 80 m for the reference height z_{ref}.

In a first step a simulation for $T_{\mathrm{phys}} = 600$ s with $\delta t = 0.02$ s for an empty numerical wind tunnel was performed. The results at $\mathrm{x} = \mathrm{y} = 0.0$ m can be seen in Fig. 4.9 b) for the mean velocity profile in Fig. 4.25 for the turbulence intensity and the turbulence length in streamwise direction. Fig. 4.26 additionally shows the velocity spectra at $\mathrm{z} = 190$ m and $\mathrm{z} = 246$ m, including also the structure's first two eigenfrequencies as vertical lines. The mod-

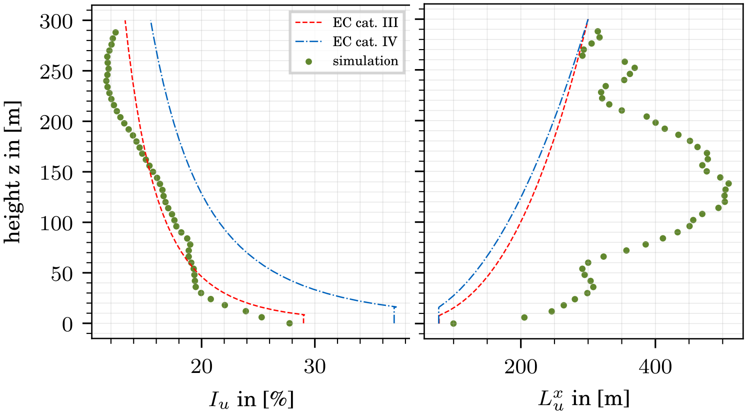

Figure 4.25: Turbulence intensity and turbulence length for the wind numerically generated for Rottweil. EC: Theoretical values from [2]

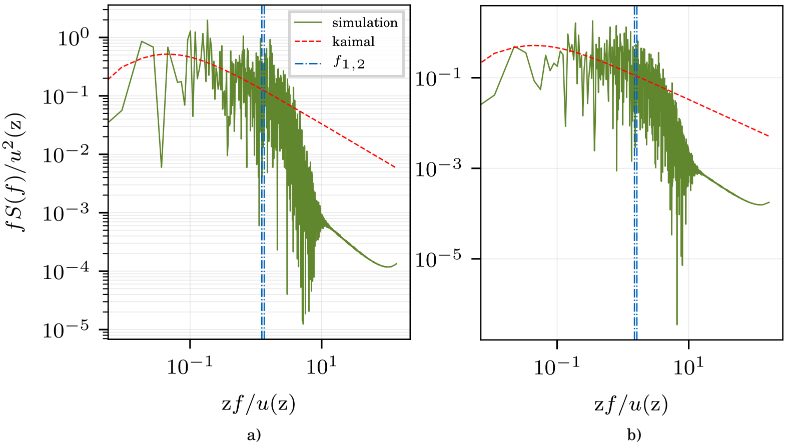

Figure 4.26: Velocity spectra for a) $z = 190$ m and b) $z = 246$ m for the TkT. Kaimal: Theoretical spectrum according to [49]; $f_{1,2}$: Eigenfrequencies of the structure.

eled mean velocity and turbulence intensity fit to the values proposed by [2], but again the difference to the values from [2] in the turbulence length can be observed. As it could be observed in the validation studies in Section 4.5, this difference does not have much impact on the results.

The numerical wind generated in this subsection can be applied in the following to the inlet of the numerical wind tunnel.

4.6.2 CSD Model of the thyssenkrupp Elevator Test Tower

The planning of the TkT has had followed the building information modeling (BIM) concept. BIM means a 3D model had been generated, including all information about the building. From this BIM model, the CSD finite element model was derived.

A conceptual sketch of the TkT with its major dimensions and labelings of its most important parts is depicted in Fig. 4.27 a). A more detailed view on the materials and cross sections can be seen in Fig. 4.28. Fig. 4.28 a) shows the membrane made from PTFE glass fiber fabrics and which is mounted on a supporting construction made from steel tubes depicted in Fig. 4.28 b). As

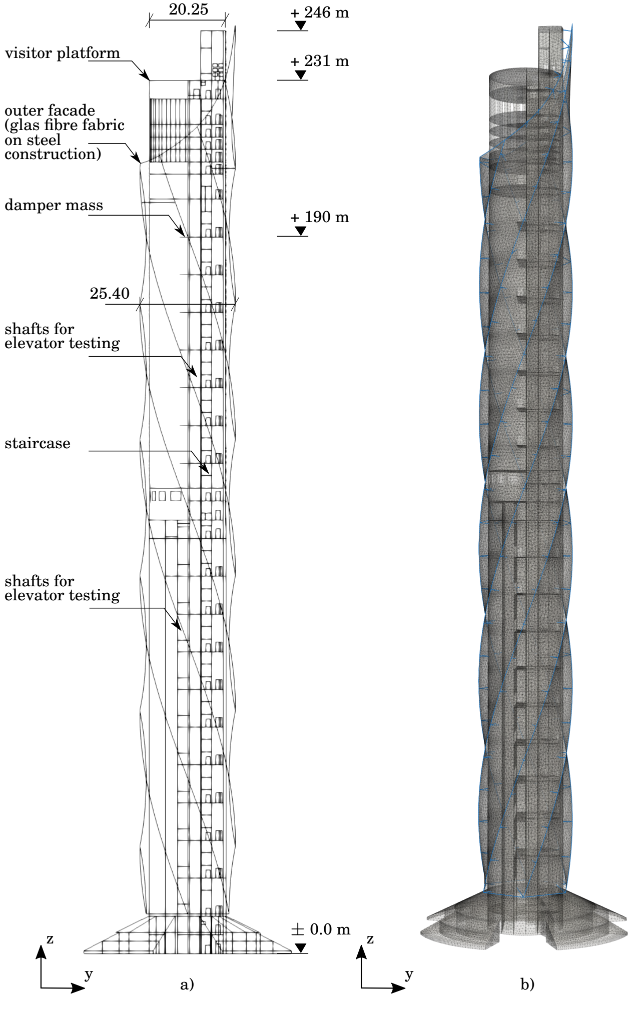

Figure 4.27: a) Schematic sketch with most important dimensions and parts of the TkT and b) finite element mesh.

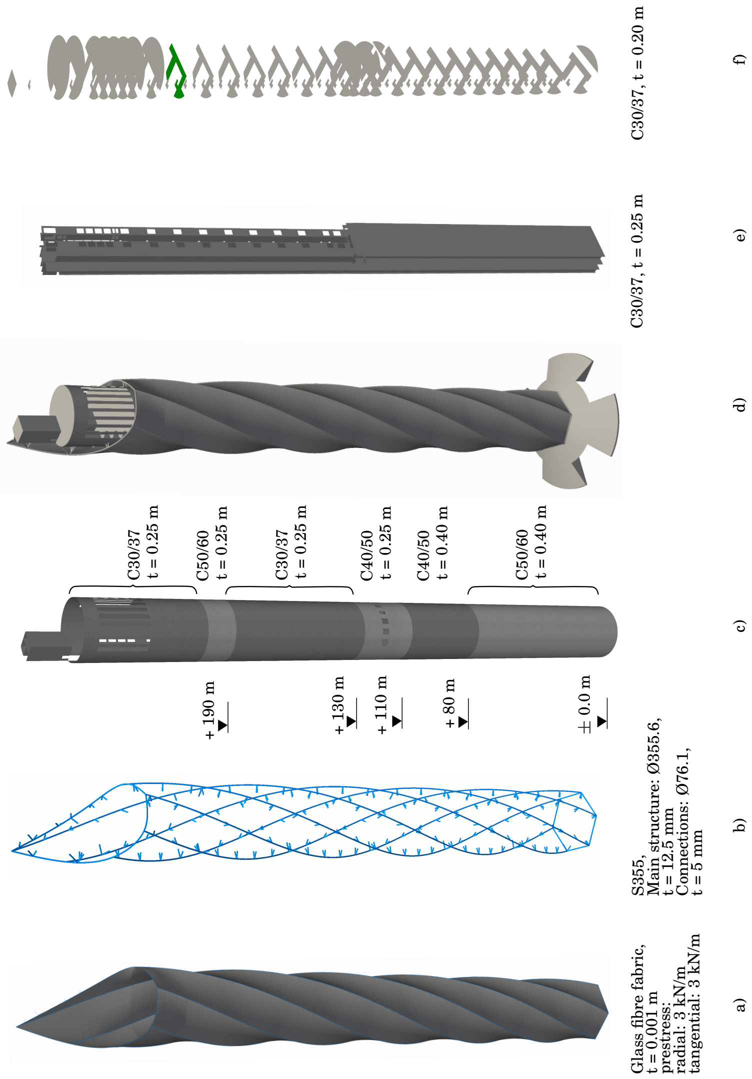

Figure 4.28: TkT cross-sections and materials.

shown later, the membrane and the steel structure hardly impact the overall dynamic behavior of the tower. However, they have to be modeled, because they mainly influence the shape of the building. The geometry of the building is important for its interaction with the fluid flow surrounding it. The exact built-in parts of the components of the fabric are confidential. It follows that typical values for an isotropic glass fiber fabric were applied. Applying those common values is accurate enough because no detailed investigations for the membrane are carried out in this work. The facade's load-bearing behavior is dominated by the steel structure. The material parameters for the membrane are set to $E_\mathrm{S} = 3000$ MPa, $\nu_\mathrm{S} = 0.22$ and $\rho_\mathrm{S} = 700\ ^{\mathrm{kg}}/_{\mathrm{m}^3}$. The isotropic prestress is set to $3\ ^{\mathrm{kN}}/_{\mathrm{m}}$. It has shown to be of advantage to model the membrane by the shell finite elements (2.1.2.1) and not by membrane elements. The shell elements are more robust to wrinkling problems occurring during the FSI simulations at the connection between membrane and beam elements (2.1.2.2), because of the bending part in the finite element formulation of the shell elements. The small beams connecting the steel structure with the concrete part are also modeled by beam finite elements. The connections between the steel and concrete structure are modeled fully clamped, i.e., without hinges. Since the overall dynamic behavior of the tower should be modeled and no details of the steel structure, this assumption is accurate enough. As shown later, it also does not have much impact on the global dynamic behavior of the structure.

In Fig. 4.28 c), e) and f) the concrete parts of the tower with their concrete classes according to [3] are depicted. The tower consists of different concrete classes. The whole concrete part is also modeled by the shell finite elements presented in 2.1.2.1. Finally Fig. 4.28 d) shows the complete structural model, which was meshed by $231\mathrm{e}3$ shell and $4\mathrm{e}3$ beam finite elements. The overall finite element mesh is depicted in Fig. 4.27 b). The tower also extends to $\mathrm{z} = -29.5$ m below ground level. This can be assumed as a fully clamped support, and thus the corresponding Dirichlet condition fixing displacement and rotation is applied to the bottom lines of the model at $\mathrm{z} = \pm 0.0$ m. By setting the secant Young's moduli $E_{\mathrm{cm,S}}$ defined in [3], the correct stiffness distribution of the structure can be modeled.

To model the correct mass distribution of the system, besides the self-weight of the load-bearing parts, the additional load from, e.g., steel constructions for the elevators, loading from building equipment and appliance, screed, and floor coverings have to be taken into account. Those are considered by a value of $4\ {}^{kN}\!/_{m^2}$ on all of the ceilings. Additionally, the traffic load in the building might also influence the eigenvalues of the structure. This type of loading is also considered by a value of $4\ {}^{kN}\!/_{m^2}$. This type of loading might vary in its magnitude, which results in only considering 30% of this type of loading in the calculations. Finally, the additional mass for the vibration reduction system has to be taken into account. It is placed at a height of 190 m and has a mass of 240 t.

The assumed mass and stiffness distribution is checked by dynamic eigenvalue analysis. The results are compared in Tab. 4.5 to measurements conducted by the GERB Schwingungsisolierungen GmbH & Co. KG, published in [68] p. 90. Three different variants were simulated. It can be observed that the damper mass and the facade construction do only have very little influence on the first four eigenfrequencies of the tower. The first four eigenforms, depicted in Fig. 4.29, are also fully dominated by the concrete part. In contrast to the OT, the TkT is not fully symmetric, due to its internal construction, which can be seen in Fig. 4.28 e) . To illustrate this, two cuts were set at the heights $z = 80$ m and $z = 190$ m. Those are depicted in Fig. 4.30. For those cross-sections, the center of gravity S and the principal axes were calculated. The principal axes differ with an angle of $10.3°$ from the x and y-axis, which is oriented in East-West, i.e., North-South direction. The slight difference in the internal structure over the height of the tower, i.e., red and black lines in Fig. 4.30, does

Table 4.5: Eigenfrequency comparison for the thyssenkrupp test tower.

Type	Eigenfrequencies in [Hz]			
	1	2	3	4
w/o membrane and damper mass	0.231	0.250	1.137	1.208
w/o membrane w/- damper mass	0.233	0.252	1.137	1.208
w/- membrane and damper mass	0.225	0.242	1.129	1.153
measured ([68] p. 90)	0.225	0.245	–	–

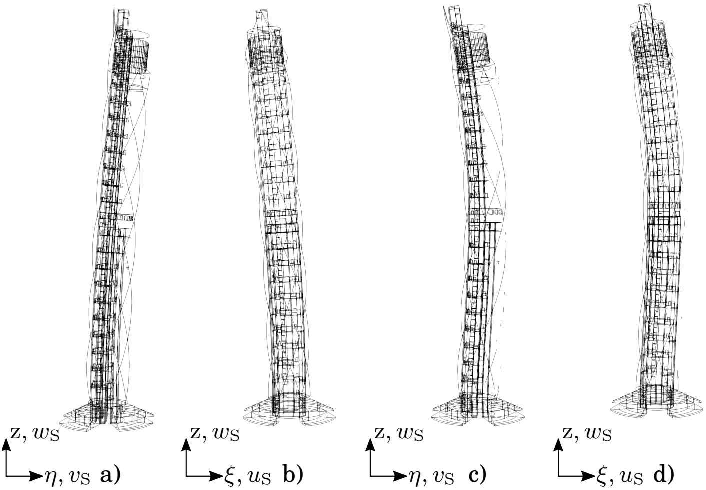

Figure 4.29: Dynamic eigenforms with membrane (a) first to d) fourth eigenform)

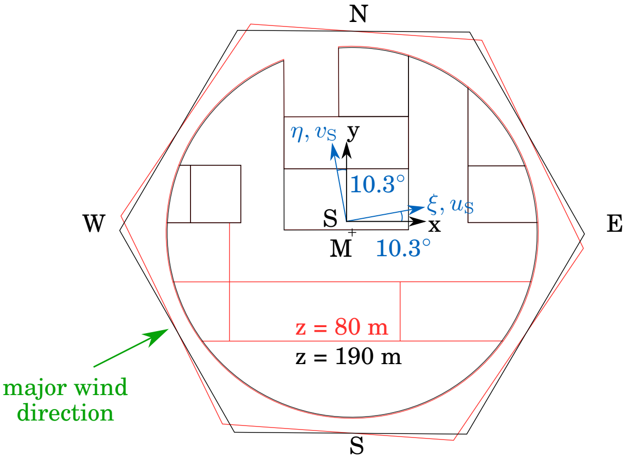

Figure 4.30: Horizontal cuts at $z = 80$ m and $z = 190$ m with principal axes ξ and η, center of gravity S, mid point M and major wind direction.

not have an effect on the angle between the coordinate systems. The eigenforms act in the direction of the principal axes ξ and η. When looking at the major wind directions, this leads to an unfavorable combination for vortex-induced lateral oscillations. Thus in the following, the simulations are performed w.r.t. the principal axes, i.e., the streamwise direction, is defined in ξ direction.

Before being able to carry out further numerical investigations, the structural damping has to be determined. The damping ratio with fixed damper has been measured in [68] p. 91 in North-South direction between 1.0% and 1.3% and in East-West direction between 1.2% and 1.3%. In the finite element model, the damping is modeled by the Rayleigh damping approach. The coefficients have been calculated for $D = 1.0\%$ for both principal directions with $\alpha_\mathrm{R} = 0.0179$ and $\beta_\mathrm{R} = 8.0\mathrm{e}{-3}$. The verification for the first two eigenfrequencies and the damping in both principal directions was performed by applying a unit displacement of one meter to the slab at $\mathrm{z} = 231$ m. From several oscillation periods of the free oscillation of the structure, the eigenfrequencies and the logarithmic decrement can be measured. The results coincide with the values in Tab. 4.5 for the eigenfrequencies and with the values from [68] p. 91 for the damping.

4.6.3 Wind Effects on the thyssenkrupp Elevator Test Tower

Resulting from its geometry, besides buffeting effects, the TkT is sensitive to vortex-induced vibrations. The St number for the cylindrical upper part, for $\mathrm{Re} = 5\mathrm{e}7$, which is valid here, is 0.17 (refer to Fig. 4.4). The potential critical velocity for the first eigenfrequency $f_1 = 0.225$ Hz and $b = 20.25$ m can be determined by Eq. (4.9) as $\overline{u}_\mathrm{F,crit} = 26.80\,\mathrm{m/s}$. If this velocity is reached at a height between 220 m and 231 m; the tower is subjected to vortex-induced vibrations. For the hexagonal part, the St number varies according to [88] p. 323 with the angle of attack, which varies in this case depending on the height above ground level z. Thus more detailed numerical investigations have to be carried out. In order to determine $\overline{u}_\mathrm{F,crit}$ for the hexagonal part, several simulations for $T_\mathrm{phys} = 600$ s with $\delta t = 0.02$ s were performed with the mean velocity profile shown in Fig. 4.9 b) without superposed fluctuations, varying the velocity at $\mathrm{z} = 190$ m such that values for $\mathrm{St} = \{0.13, 0.14, 0.15, 0.16, 0.18, 0.19\}$ are obtained. The lateral displacements v_S over time at $\mathrm{z} = 231$ m are shown in Fig. 4.31. To be able to find $\overline{u}_{\mathrm{F,crit}}$ the signals are compared in the frequency domain by calculating the PSD. From Fig. 4.32 it can be observed that the highest peak occurs for $\mathrm{St} = 0.13$, i.e. for $\overline{u}_\mathrm{F}(10\ \mathrm{m}) = 43.96\,{}^\mathrm{m}/_\mathrm{s} = \overline{u}_{\mathrm{F,crit}}$. Both values for $\overline{u}_{\mathrm{F,crit}}$, i.e., for the cylindrical and the hexagonal part, are likely to occur. Hence further investigations are carried out in the following with both values.

Before starting with extensive numerical studies a rough estimate for the maximal amplitude of the vortex induced vibrations can be obtained by Eq. (E7) from [1]. Inserting the values for the tower, it results in $v_\mathrm{max} = 0.68$ m at $\mathrm{z} = 231$ m.

The critical wind speed for galloping, according to Eq. (4.10) is $248.25\ {}^\mathrm{m}/_\mathrm{s}$. This wind speed is too high for the prevailing wind conditions at the building site, and thus galloping is not necessary to be taken further into account.

4.6.4 FSI Simulations thyssenkrupp Elevator Test Tower

Several FSI simulations with smooth inlet profile and turbulent inlet profile with different velocities and varying structural configurations for $T_\mathrm{phys} = 600$ s with $\delta t = 0.02$ s were performed in order to find the most unfavorable combination. The basis have been the preliminary studies carried out in 4.6.3. Before having a closer look at the results of those simulations, an additional remark concerning the modeling of the FSI interface, i.e., the interface between CFD and CSD subsystem, is necessary. The CFD domain needs a closed volume to produce correct results. Thus for the fluid mesh, the thickness of the membrane was modeled explicitly. This was not necessary over the full height, but only in the upper part of the tower. This assumption is applied because recirculation effects relevant to the FSI are likely to occur mainly in this area. The exact modeling can be seen in Fig. 4.33 and the non matching meshes of CFD and CSD domain in Fig. 4.34 a). Mapping the fluid forces from both sides from the CFD mesh to the CSD mesh in the upper part, the reaction forces from the CFD mesh of both sides (”interface FSI membrane outside and inside” in Fig. 4.33) are summed up before mapping them to the

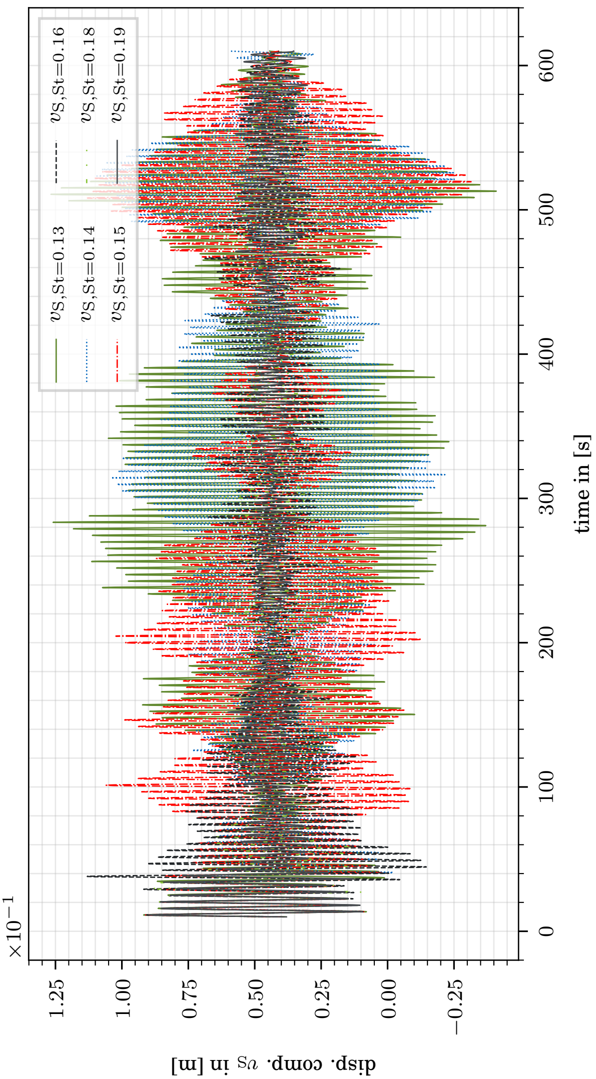

Figure 4.31: Structural displacement component v_S at top-level for different St numbers.

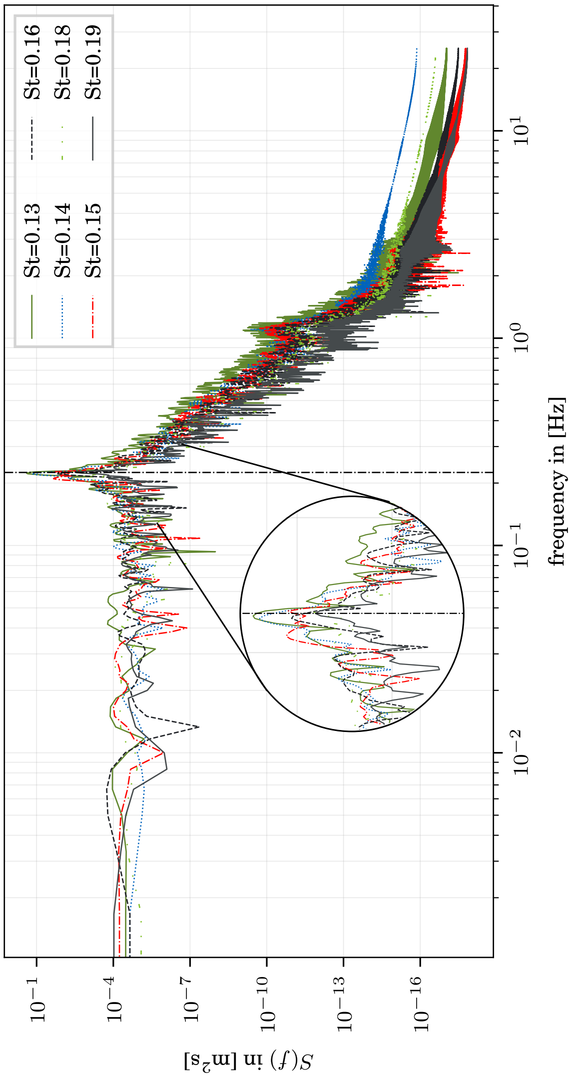

Figure 4.32: PSD function for structural displacement component v_{S} at top-level for different St numbers.

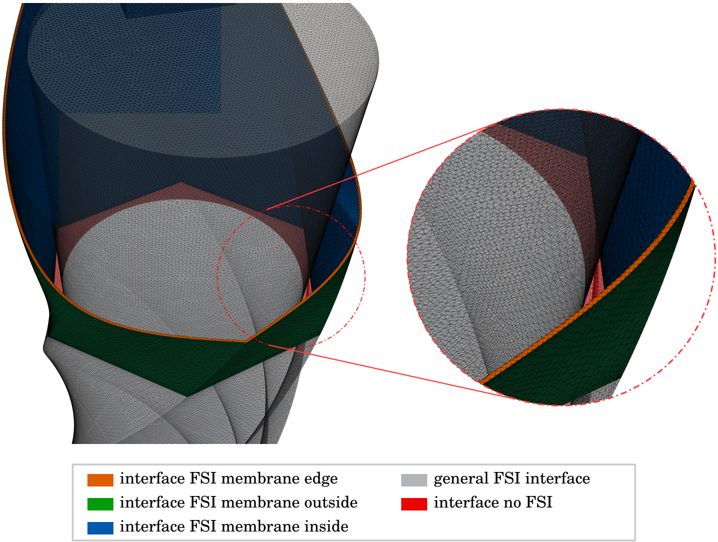

Figure 4.33: Detail of the fluid mesh for modeling the membrane at the top of the tower.

CSD mesh. The displacements from the CSD domain are mapped in the standard way, i.e. without summation. The reaction forces from the upper edge (colored orange in Fig. 4.33) are ignored and only displacements are mapped from the CSD to the CFD domain. In the region of the ”general FSI interface” the standard mapping procedure presented in Sect. 2.4 is applied. The region ”interface no FSI” is only needed for the CFD subsystem, to gain a watertight surface of the overall FSI interface. A no-slip boundary condition is applied to it. No mapping from the CFD to the CSD domain and the other way around is performed. This region has no fixed boundary conditions concerning the mesh motion but can move freely throughout the simulation. The same applies at the bottom part of the membrane, which is not depicted in Fig. 4.33. Furthermore, the membrane is assumed to be impermeable for air in the CFD finite element model, which is not the case in reality. Hence two limit value investigations have been carried out. In one case the membrane is completely omitted, which corresponds to a utterly permeable membrane (w/o membrane). It

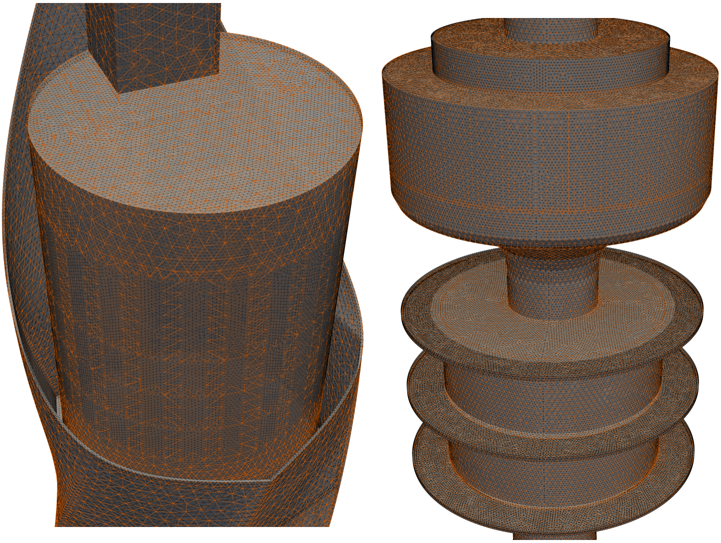
a) b)

Figure 4.34: Non-matching meshes at interface level. Black CFD and orange CSD mesh.

follows that only the concrete cylinder is simulated. In the other case, the membrane is assumed impermeable, and the structure is modeled with the membrane (w/- membrane).

The values which were applied to create the mean profile with the power law in Eq. (4.5), are summarized in Tab. 4.6. Visualizations of the FSI simulations by setting a cut in the x-z plane of the numerical wind tunnel can be seen in Fig. 4.35. Additionally, the stream lines around the TkT at $T_{\mathrm{phys}} = 500$ s are depicted in Fig. 4.36. The results for the displacement component in η-

Table 4.6: Value summary for creating the mean profiles for $\mathrm{z}_{\mathrm{ref}} = 10$ m.

Type	$\overline{u}_{\mathrm{F}}(10\ \mathrm{m})$	γ	α
$\overline{u}_{\mathrm{F,norm}}$	$20.0\,{}^{\mathrm{m}}/_{\mathrm{s}}$	0.77	0.22
$\overline{u}_{\mathrm{F,crit,hex}}$	$24.56\,{}^{\mathrm{m}}/_{\mathrm{s}}$	1.0	0.22
$\overline{u}_{\mathrm{F,crit,cyl}}$	$13.50\,{}^{\mathrm{m}}/_{\mathrm{s}}$	1.0	0.22

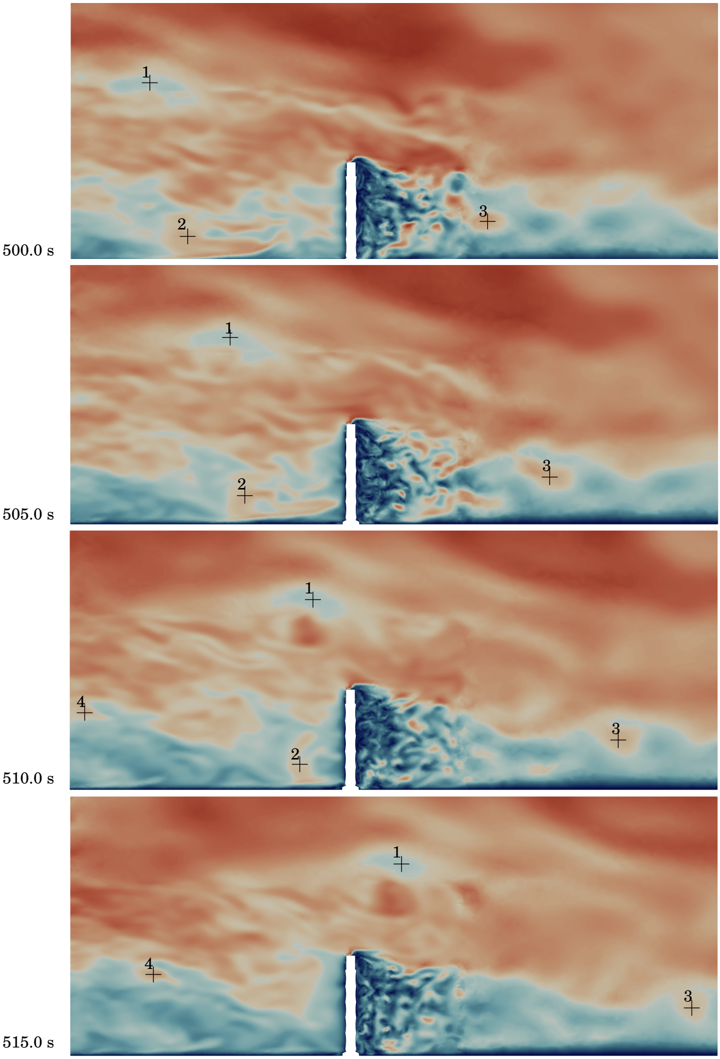

Figure 4.35: Slice of the numerical wind tunnel in the x-z plane. The motion of selected eddies is marked by numbered crosses.

direction at $z = 231$ m for the simulations w/o membrane, i.e. for a

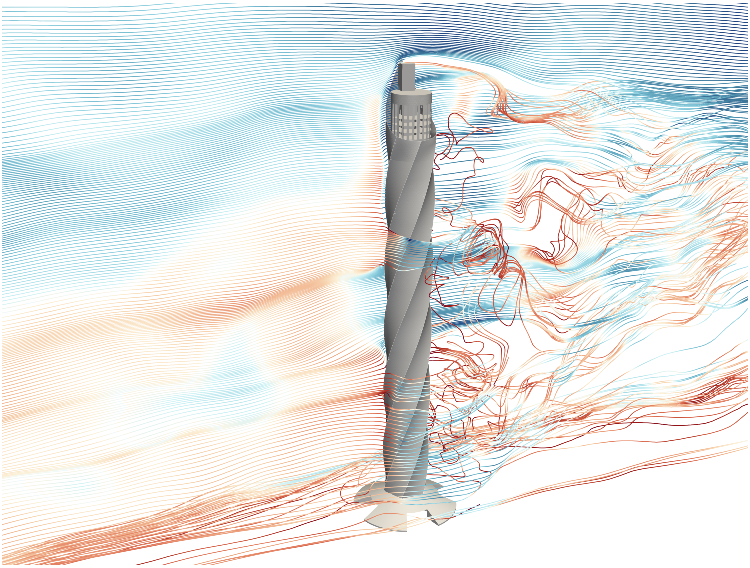

Figure 4.36: Streamlines with turbulent inlet around the TkT at $T_{\text{phys}} = 500$ s.

cylindrical geometry, are collected in Fig. 4.37 in the time domain and in Fig. 4.38 in the frequency domain. Those were computed with different velocity profiles applied to the inlet of the numerical wind tunnel. In the frequency domain, it can be observed that the critical velocity for the cylinder superimposed with the fluctuations from the inlet generator, results in the largest amplitudes for the lateral displacement.

Figs. 4.39 and 4.40 show the same summary for the variant with membrane, i.e. for a hexagonal geometry with varying attack angle in the lower part and a cylindrical geometry in the upper part.

Again different configurations of velocity profiles were applied to the inlet of the numerical wind tunnel. The amplitudes for the critical velocity for the cylindrical part and the norm velocity, each superimposed with the fluctuations, show the largest values. In contrast to the critical velocity for the cylinder, the norm velocity stimulates a broader frequency range to a higher extent (Fig. 4.40). Furthermore, it is observable from Figs. 4.38 and

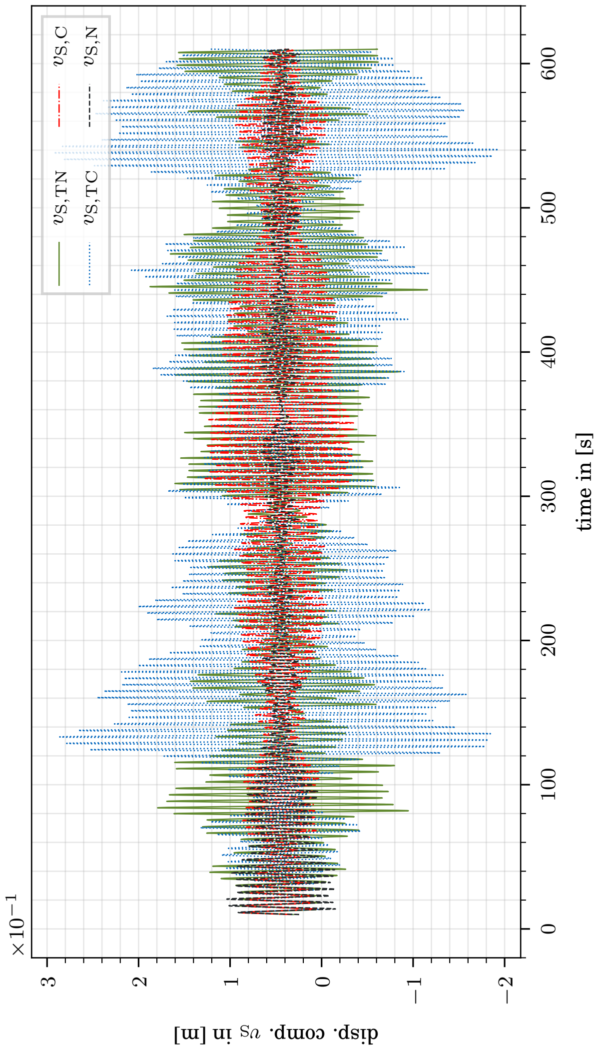

Figure 4.37: Structural displacement component v_{S} at $\mathrm{z} = 231$ m w/o membrane. TN: turbulent inlet with $\overline{u}_{\mathrm{F,norm}}$; N: non-turbulent inlet with $\overline{u}_{\mathrm{F,norm}}$; TC: turbulent inlet with $\overline{u}_{\mathrm{F,crit,cyl}}$; C: non-turbulent inlet with $\overline{u}_{\mathrm{F,crit,cyl}}$.

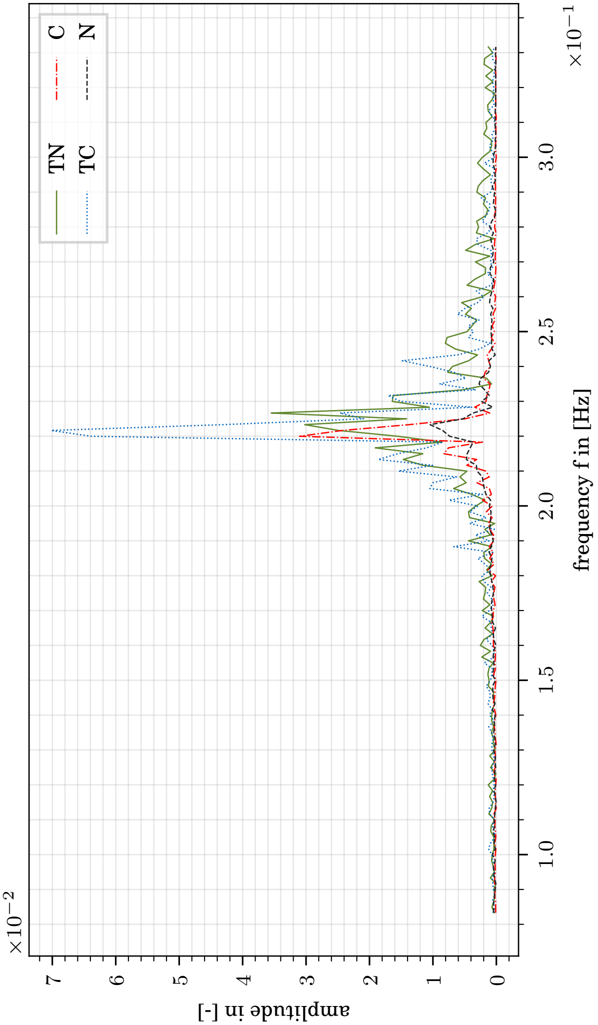

Figure 4.38: FFT structural displacement component v_S at $z = 231$ m w/o membrane. TN: turbulent inlet with $\overline{u}_{F,norm}$; N: non-turbulent inlet with $\overline{u}_{F,norm}$; TC: turbulent inlet with $\overline{u}_{F,crit,cyl}$; C: non-turbulent inlet with $\overline{u}_{F,crit,cyl}$.

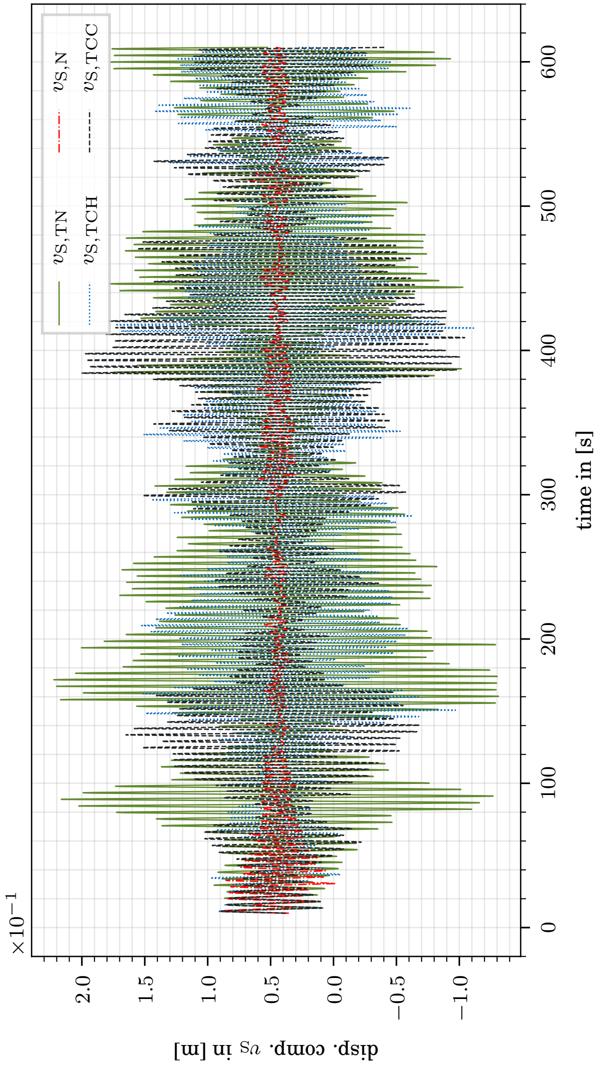

Figure 4.39: Structural displacement component v_S at z = 231 m w/- membrane. TN: turbulent inlet with $\overline{u}_{F,norm}$; N: non-turbulent inlet with $\overline{u}_{F,norm}$; TCH: turbulent inlet with $\overline{u}_{F,crit,hex}$; TCC: turbulent inlet with $\overline{u}_{F,crit,cyl}$.

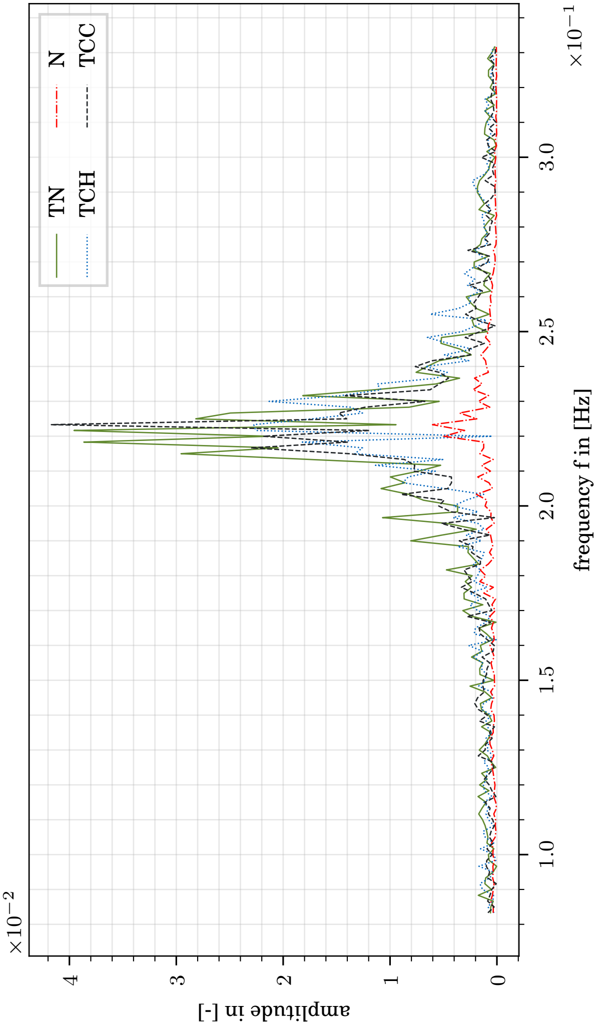

Figure 4.40: FFT of structural displacement component v_{S} at z = 231 m w/- membrane. TN: turbulent inlet with $\overline{u}_{\mathrm{F,norm}}$; N: non-turbulent inlet with $\overline{u}_{\mathrm{F,norm}}$; TCH: turbulent inlet with $\overline{u}_{\mathrm{F,crit,hex}}$; TCC: turbulent inlet with $\overline{u}_{\mathrm{F,crit,cyl}}$.

4.40, that it is not enough, in this case, to perform simulations with a mean profile with no fluctuations superposed to it, i.e., a smooth profile. Looking at the absolute values of the amplitudes in Figs. 4.37 and 4.39 the maximum value w/o membrane is 0.23 m and w/- membrane 0.18 m. This corresponds to about 30% of the rough approximation calculated from [1], which shows that those formulas lead to results far on the safe side.

4.6.5 CFD vs. FSI and Weak vs. Strong Coupling

Before dealing with the coupled simulation of fluid, structure and HMD, two additional considerations might be of interest.

The first question is if it is enough to perform only CFD simulations or measurements on a rigid model in the physical wind-tunnel. In the case of the numerical simulation, the code available might not be capable of performing FSI simulations. In the physical wind tunnel modeling issues for a fully aeroelastic model can occur. In both cases, one might be tempted not to perform complex FSI simulations or measurements, but to perform only pure CFD simulations or measurements on a rigid model. Comparing a pure CFD and an FSI simulation serves, to check if this makes sense for such a structure like the TkT. The results for the reaction forces at $\mathrm{z} = 0.0$ m of this study can be seen in Fig. 4.41. The values of the reaction forces in the streamwise direction of the CFD simulation are more significant than the ones for reaction forces for the FSI simulation, but all in all, both of them show the same overall tendency. The reaction forces in the cross-stream direction differ entirely. This is because the vortex-induced vibrations are a the dynamic effect of the interaction between fluid flow and structure, which cannot be modeled without taking into account the dynamic behavior of the structure, which is the case in a CFD simulation or when measuring without an aeroelastic model.

The second question is if the results are accurate enough if only weakly coupled FSI simulations are performed in this case. Therefore, one strongly and one weakly coupled simulation was carried out with the smooth velocity profile with norm velocity for $T_{\mathrm{phys}} = 600$ s and $\delta t = 0.02$ s. The results for the displacement component in η-direction at $\mathrm{z} = 231$ m are depicted in Fig. 4.42 in the frequency domain.

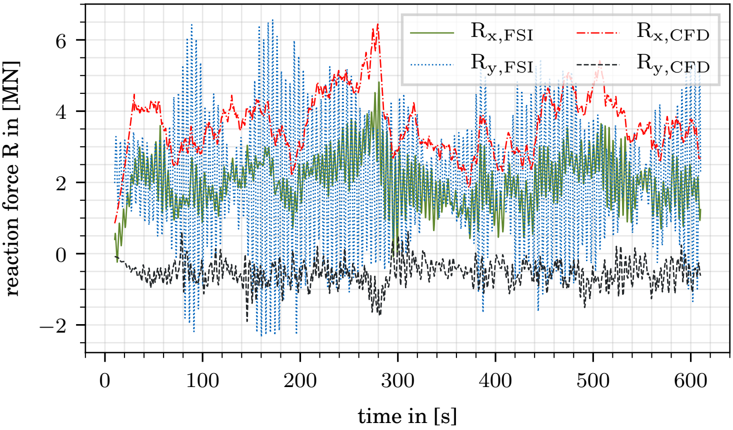

Figure 4.41: Reaction force components at $z = 0.0$ m for FSI and CFD with turbulent inlet, with $\overline{u}_{\mathrm{F,norm}}$, structure w/- membrane.

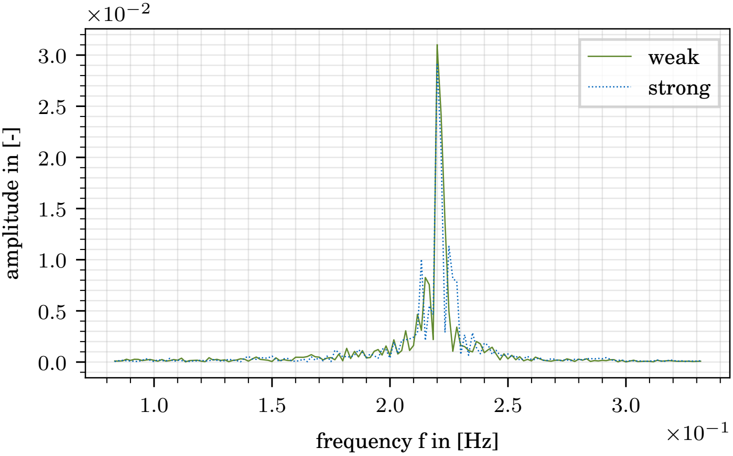

Figure 4.42: Comparison of weak and strong coupling by a FFT with non-turbulent inlet, $\overline{u}_{\mathrm{F,crit,cyl}}$.

In this case, the weak coupling is capable of modeling the primary frequency content, except for some smaller deviations. On the one hand, it can be concluded from this subsection, that a pure CFD analysis, which corresponds to a rigid model in the physical wind tunnel is not capable of modeling all effects of wind on a structure like the TkT. On the other hand, it is not necessary to perform strongly coupled FSI simulations. The results from section 4.5 also obtained for turbulent wind conditions by weak coupling, emphasize this. Hence an FSI simulation with a weak coupling applying the predictor proposed by [31] is accurate enough for structures like the TkT. [4] also showed the excellent performance of the predictor presented in [31] for a different type of structure.

4.6.6 Artificial Oscillations and Oscillation Reduction of the thyssenkrupp Test Tower

A special feature of the TkT is the HMD mounted in the form of a pendulum with a mass of 240 t at the height of 190 m $\big($marked green in Fig. 4.28 f)$\big)$. The pendulum is incorporated for two reasons. Firstly, it reduces the tower's wind-induced vibrations, acting as a passive system, to guarantee predictable testing conditions for the elevators. Secondly, it can be used to excite the tower to actively oscillate with amplitudes up to 0.20 m at $\mathrm{z} = 231$ m in ξ or η direction, to test the elevators in those conditions. In the passive mode, the HMD principally works like an open-loop control with adaptive filtering, i.e., without a feedback loop. This is why a reduced-order model of the system like in CHAPTER 3 is not necessary here ([79] p. 10). Although no feedback loop is necessary for the investigations made in this work, the algorithm implemented in the real structure has a feedback loop. According to [68] p. 89, the reason for the feedback-loop is the safety concept applied for the HMD. Theoretically, the actuator force is only strong enough to archive the desired tower oscillations. Though the artificial oscillations in combination with the deflections caused by wind, might lead to deformations causing fatigue issues. This is why an emergency shutdown is incorporated in the control algorithm, which deactivates the actuators, and the HMD switches to its passive mode. The emergency shutdown is based on the control loop sensors measuring the tower displacements, making a feedback loop necessary. In the investigations made in this work, the emergency shutdown system was not investigated in detail, because no access to the explicit control algorithm of the emergency shutdown system could be granted. In the case of the HMD system's mechanical failure, it is also possible to uncouple the pendulum's dampers from the structure. Fig. 4.44 shows the block diagram for the principal control law of the TkT. The feedback loop is grayed out, because it does not play a role for the investigations in this work. This is, why the structural control system behaves like an open-loop control. The disturbance z_{C} acting on the HMD block is the tower displacement. In the best case, the top displacement $v_{\mathrm{S,top}}$ of the tower should be zero with activated HMD, i.e. $w = 0.0$ m. This cannot be achieved by open-loop control, because of the wind forces z_{S} on the tower. Thus the passive part of the HMD is designed by the empiric formulas in Eq. (4.17) and Eq. (4.18), to get as close as possible to the desired value of w.

A basic sketch of the HMD can be seen in Fig. 4.43. The pendulum can be actively actuated by linear motors, with a maximum force of 40 kN and a maximum stroke of ± 0.60 m, mounted in the principal directions. The linear motors are connected

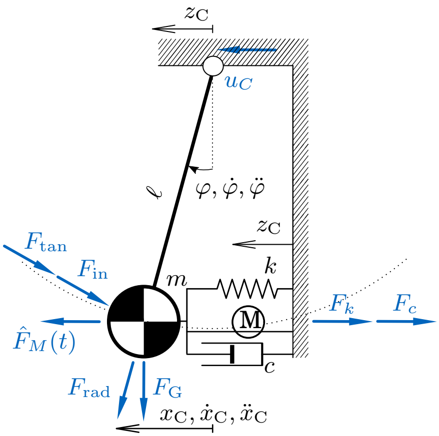

Figure 4.43: Schematic model for hybrid mass damper (HMD).

hinged to the building and the center of gravity of the pendulum

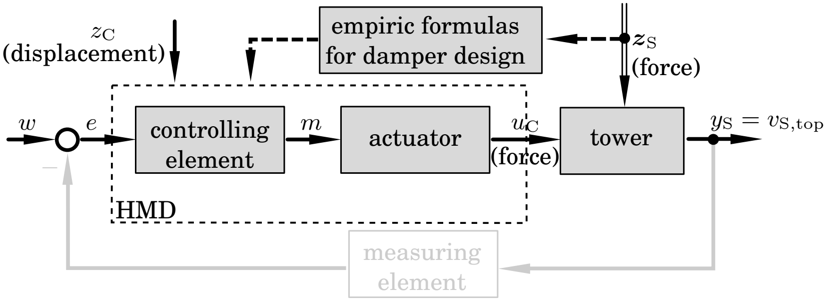

Figure 4.44: Schematic block diagram for the control algorithm of the TkT.

mass to avoid parasitic forces. The passive damper elements of the HMD system are permanently activated, which makes the passive system available in the case of power failures. [68] p. 86 - 89 offers more detailed information about the pendulum, its control algorithm, and the safety concept. The ODE of the HMD in Eq. (4.14) can be derived from the sketch in Fig. 4.43 the following way:

$$\begin{aligned} F_G &= m \cdot g \\ F_{tan} &= F_G \cdot \sin(\varphi) \\ F_{rad} &= F_G \cdot \cos(\varphi) \\ F_k &= k \cdot \ell \cdot \sin(\varphi) \\ F_c &= c \cdot \ell \cdot \sin(\dot{\varphi}) \\ F_{in} &= m \cdot \ddot{\varphi} \cdot \ell \end{aligned} \tag{4.13}$$

The sum of forces with assumption of small displacements (i.e. $\sin(\varphi) \approx \varphi$, $\cos(\varphi) \approx 1$) leads to the differential equation depending on $x_C(t)$:

$$\begin{aligned} & m\ddot{x}_C(t) + c\dot{x}_C(t) + \Big(\frac{mg}{\ell} + k\Big) x_C(t) \\ & = \hat{F}_M(t) - m\ddot{z}_C(t) + c\dot{z}_C(t) + kz_C(t). \end{aligned} \tag{4.14}$$

The prescribed velocity $\dot{z}_C$ can be calculated by time integration from Eq. (2.45) from the prescribed displacement z_C. The circular eigenfrequency of the freely oscillating pendulum is defined as:

$$\omega = \sqrt{\frac{g}{\ell}}. \tag{4.15}$$

No additional spring elements are mounted to the system, which results in $k = 0$. For the coupled simulation performed later, the algorithm from CHAPTER 3 is applied. Hence the force from the HMD subsystem is to be applied as a Neumann boundary condition to the nodes of the CSD subsystem marked green in Fig. 4.28 f). Therefore, the support force $u_{\mathrm{C}}(t)$ of the pendulum can be calculated as

$$u_{\mathrm{C}}(t) = mg\frac{x_{\mathrm{C}}(t)}{\ell}. \tag{4.16}$$

This force is distributed uniformly to all nodes belonging to the mesh of the slab in the CSD domain, the HMD is mounted to, i.e. $\boldsymbol{u}_{\mathrm{S},i} = u_{\mathrm{C}}$. This is also indicated by the double arrow in Fig. 4.44.

The value of the mass is fixed to 240 t, which corresponds to 0.6% of the building's overall mass. It follows that, the remaining parameters to be selected for the HMD are the damping ratio of the damper elements and the length of the pendulum. The prerequisites for the selection of those parameters according to [68] are:

a) Increase the structural damping to decrease the amplitude of the wind-induced vibrations.

b) Constrain the motions the damper mass motions to a value less than 0.60 m.

c) Gain the demanded top displacement of the tower of ± 0.20 m by the maximum actuator forces of 40 kN.

The basic criteria for selecting the parameters to tune the pendulum, i.e., calculating the damping coefficient c and the pendulum length ℓ can be found in [78] p. 830. Those are:

$$D_{\mathrm{opt}} = \sqrt{\frac{3\mu}{8(1+\mu)^2}} \tag{4.17}$$

and

$$\ell_{\mathrm{opt}} = \frac{(1+\mu)g}{4\pi^2 f_1^2}. \tag{4.18}$$

Herein μ is the mass ratio between the mass of the building and the mass of the damper, g is the gravity constant and f_1 is the first eigenfrequency of the structure. With $\mu = 0.6\%$ this results in $D_{\mathrm{opt}} = 0.05$ and $\ell_{\mathrm{opt}} = 4.93$ m.

In a first step, the ± 0.20 m oscillation of the tower in η-direction at $\mathrm{z} = 231$ m excited by the HMD was simulated. Fig. 4.45 shows the results for the displacement component and the displacements of the HMD mass in this direction. The corresponding forces applied to the HMD are depicted in Fig. 4.46. This simulation was performed in a partitioned way, excluding the CFD subsystem. In this case, a weak and a strong coupling approach leads to the same results. It is possible to excite the tower to the demanded amplitude, without exceeding the maximum admissible mass displacement of 0.60 m. Additionally, this simulation can be taken into account to measure the structural damping with locked and unlocked HMD. Fig. 4.47 shows the amplification function and the phase shift for both cases. When activating the HMD, the structural damping increases to 2.0%. Finally, an FSCI simulation for the case of the tower with membrane for $\overline{u}_{\mathrm{F,norm}}$ was performed. Therefore also a weak coupling with the predictor from [31] was applied. For the case of

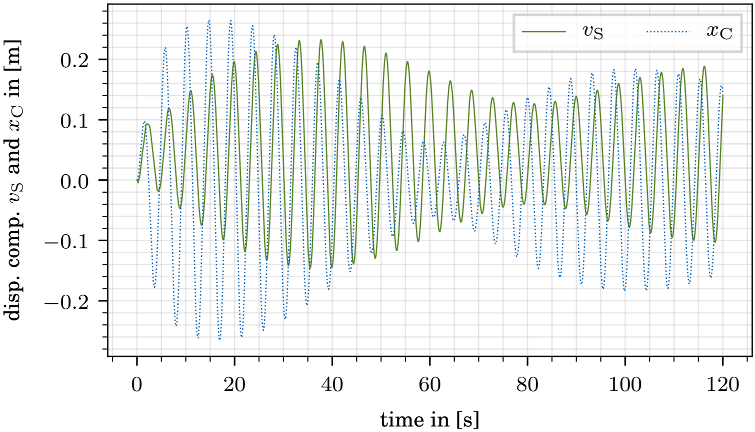

Figure 4.45: Structural displacement component v_S at $\mathrm{z} = 231$ m and HMD displacement x_C.

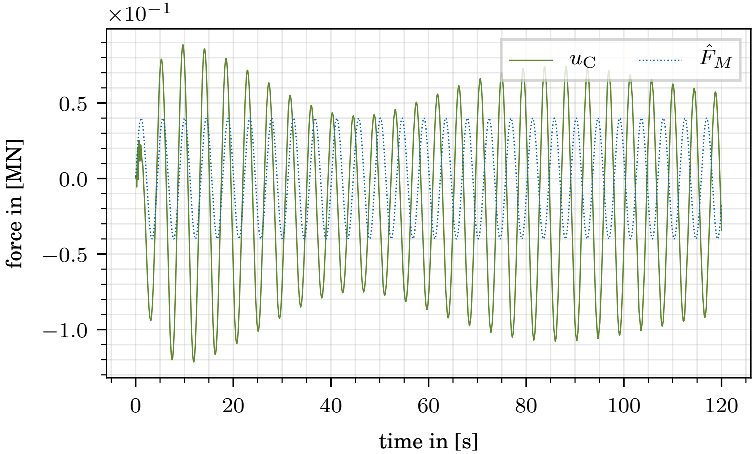

Figure 4.46: Force applied to the HMD $\hat{F}_M$ and reaction force y_C applied to the structure.

the TkT this leads to good results. An additional testing of the FSCI algorithm from CHAPTER 3 with strong coupling for a prototypical high-rise building was performed in [105] and [76]. Fig. 4.48 shows the results displacement component in η-direction at $z = 231$ m w/- and w/o activated HMD. The same results transformed to the frequency domain are depicted in Fig. 4.49.

The HMD fully annihilates the frequency of 0.225 Hz which leads to a significant reduction of the top displacements of the tower. When checking the displacements of the HMD itself in Fig. 4.50 it can also be observed, that the displacements of the HMD do not exceed the maximum admissible value of 0.60 m. It can be concluded from this subsection it is possible to apply the algorithm developed in CHAPTER 3 to a complex problem like the TkT and to comply by a simulation that all the prerequisites posed to the structure, and the HMD can be fulfilled.

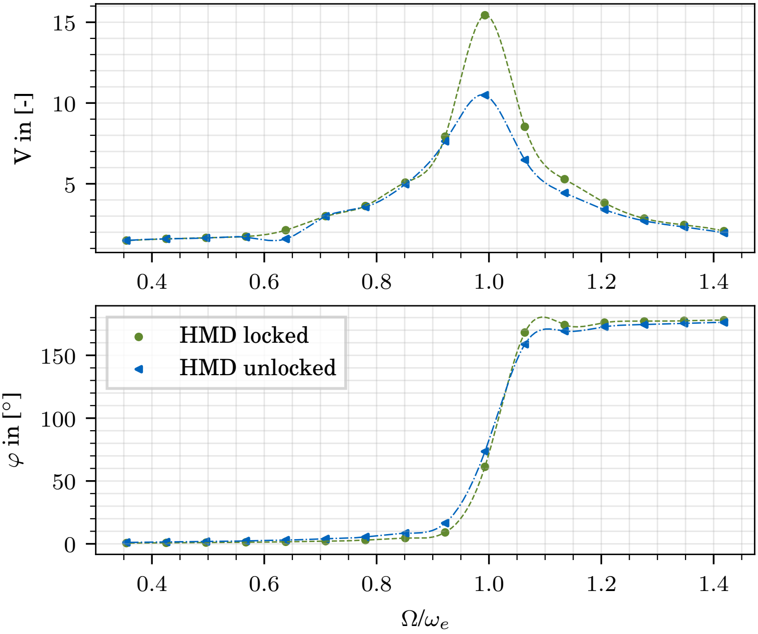

Figure 4.47: Amplification function and phase shift with locked and unlocked HMD.

4.6.7 Procedure for the Numerical Wind Generation

Summing up the experience from the wind generation for the OT and the TkT, the schematic procedure shown in Fig. 4.51 can be proposed. In the case on-site measurements are available, the characteristic values (L_u^x, I_u and $\overline{u}$) are computed for the measurement and from the design codes, because the measurement values might only be available at certain points over the height.

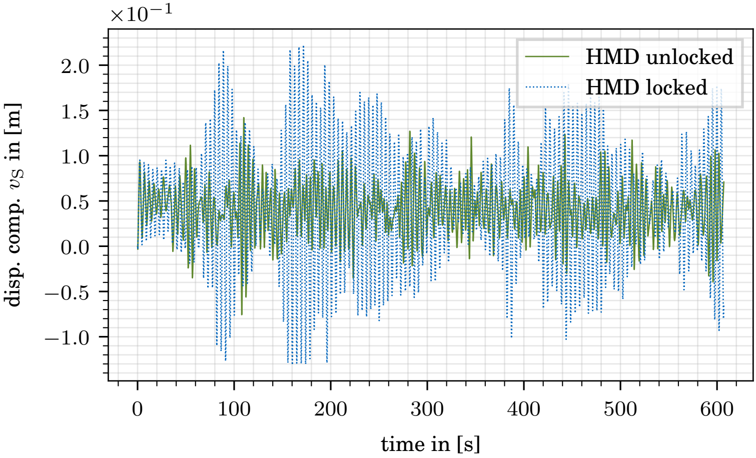

Figure 4.48: Displacement component v_{S} at $\mathrm{z} = 231$ m with unlocked HMD and locked HMD, applying a turbulent inlet profile with $\overline{u}_{\mathrm{F,norm}}$.

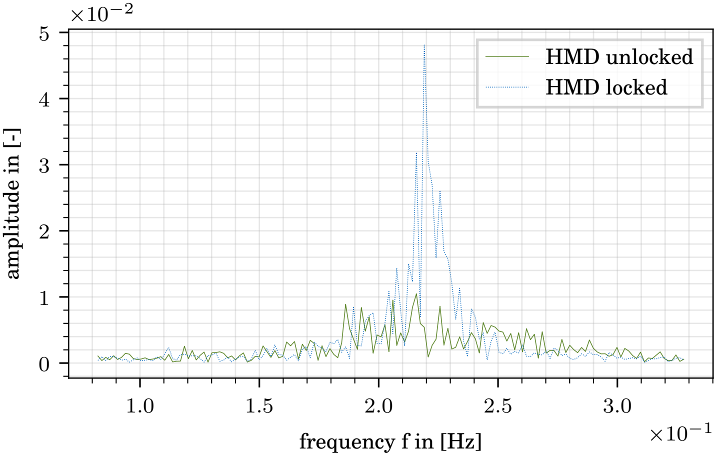

Figure 4.49: FFT of the displacement component v_{S} at $\mathrm{z} = 231$ m with unlocked and locked HMD, applying a turbulent inlet profile with $\overline{u}_{\mathrm{F,norm}}$.

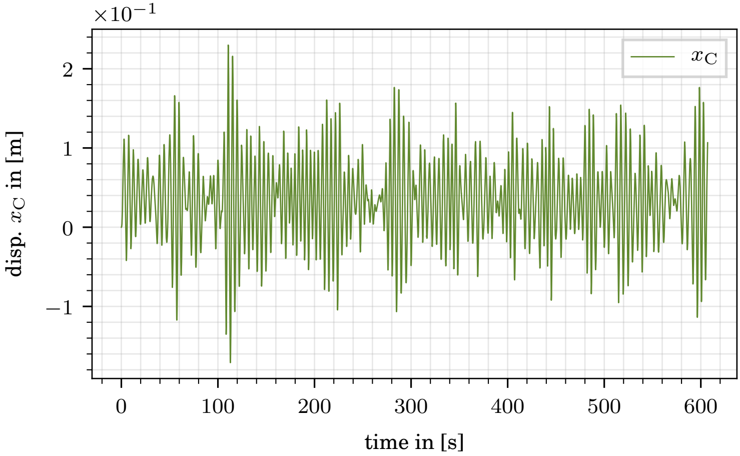

Figure 4.50: Displacement x_C of the HMD mass, applying a turbulent inlet profile with $\overline{u}_{F,\mathrm{norm}}$.

Additionally, the values from the design codes ensure that typical problems with measurements (on-site measurements or from measurement stations) can be identified at this point, which can be, for example:

- outliers,
- wrong or unknown units,
- changes in the units throughout the measurement period,
- manipulation or failures of the measurement devices,
- errors in the data analysis,
- timestamp issues.

All of the examples listed above also arose in the context of this work. If there are no on-site measurements available, other data sources have to be used. The quality of such data sources is assessed in Tab. 4.7. It can be observed that the design codes are a solid basis, but do not provide any information about the major wind direction. Thus it is suggested to utilize measurements from surrounding measurement stations or macro-meteorological simulations as additional data sources. Those provide information for the major wind direction and often better data for the mean wind speed $\overline{u}$.

4.6.8 Acknowledgments

The investigations which were carried out for the TkT, would not have been possible without the help of the following people. Herewith I want to thank them very much for their support:

- Prof. Werner Sobek, Dipl.-Ing. Holger Hinz and Dipl.-Ing. Dieter Möhrle, from Werner Sobek Stuttgart AG, for providing the full BIM model.
- Dr.-Ing. Christian Meinhardt, from GERB Schwingungsisolierungen GmbH & Co. KG, for the helpful discussions on the telephone and for providing additional measurement data.
- Dipl.-Ing. Hardy Stimmer, from thyssenkrupp Business Services GmbH, for the uncomplicated permission to use the data in connection with the tower.
- B.Eng. Jonas Buck, from Ed. Züblin AG, for the uncomplicated permission to use the data in connection with the tower.
- Prof. Karsten Moritz, from Taiyo Europe GmbH, for providing detailed data for the steel and the membrane construction.
- Mr. Rainer Thieringer, from Drachenfliegerverein Bösingen, for giving me full access to their wind data.

4.7 Chapter Summary

This chapter applied the numerical wind tunnel to two types of a slender, high-rise, tower-like structures: a television tower and an elevator test tower. A basic convergence and validation study for pure CFD, successfully extending and confirming the results

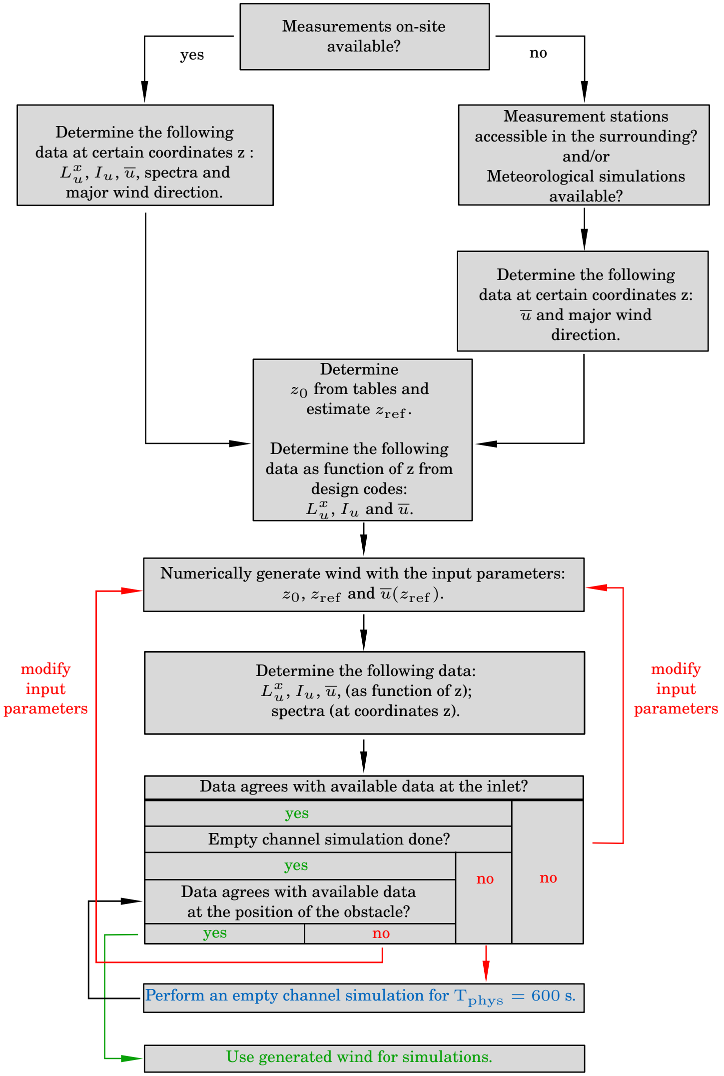

Figure 4.51: Procedure for the numerical wind generation. The Computationally expensive part marked blue.

Table 4.7: Means of assessment of numerically generated wind.

Data	Data sources			
	on-site measurements	measurements from surrounding measurement stations	macro-meteorological simulations	design codes
major wind direction	+++	++	++	O
I_u	+++	O	O	+
L_u^{x}	+++	O	O	+
velocity spectra	+++	O	O	+
$\overline{u}$	+++	++	++	+

Symbol	Assessment
+++	optimal
++	work well
+	appropriate
O	unavailable

from [4] and [26]. Based on those studies, fully coupled FSI simulations with a numerically generated wind-inlet were performed for the television tower. Since a lot of measurement data is available, it was possible to utilize this data to generate a reasonable inlet profile by the synthetic inlet generator [5]. The results of the FSI simulations correspond well to the available on-site measurements. Based on the studies on the television tower, a meaningful wind-inlet was generated on the basis of measurements from different measurement stations and one macro meteorological simulation for the elevator test tower. Different FSI simulations were performed for different configurations of the elevator test tower, to find the most unfavorable configurations concerning vortex-induced vibrations. Finally, a successful application of the algorithm presented in CHAPTER 3 was possible for the simulation of the elevator test tower, including an HMD device.

Chapter 5

Conclusions and Outlook

In this thesis work, the multiphysics problem of the interaction of high-rise, tower-like civil engineering structures with the natural wind, including systems for vibration mitigation of wind-induced vibrations was investigated, by a numerical approach.

Therefore, in a first step, the algorithmic treatment of the interaction between fluid flow, structure, and an open or closed-loop controller, based on a Gauss-Seidel pattern, is presented in CHAPTER 3. It was successfully tested by the modification of a well-known benchmark case from the FSI community. Thus its applicability is not limited to civil engineering structures but is generally possible for different types of FSCI problems.

In a second step the findings from CHAPTER 3 were applied in CHAPTER 4 to the thyssenkrupp elevator test tower in Rottweil in combination with the numerical wind tunnel, including the synthetic inlet generator developed in [4]. The application to real-world problems also contained a validation study conducted for the Olympic Tower in Munich. This validation study compared simulated results from the numerical wind tunnel with on-site measurements, which had been conducted for the Olympic Tower. The results from simulations and measurements match well. Additionally, this study served as a successful test for the simulation setup for multiphysics problems like FSI, implemented in [53].

Thus the same setup was applied to the thyssenkrupp elevator test tower combined with the algorithm for FSCI. Several FSI studies concerning the critical wind speed and the influence of the natural wind's turbulent characteristics on the flow-induced vibrations of the thyssenkrupp elevator test tower were performed. Those included the comparison of wind data from different measurement stations with a macro meteorological simulation, to be able to model reasonable wind conditions. The FSI simulations, which were conducted, showed that it is not enough to perform simulations with a smooth velocity inlet profile. Still, the turbulent characteristics of natural wind have to be modeled to get meaningful results. Furthermore, applying a weak coupling with the predictor introduced in [31] resulted in the optimal combination between accuracy and computational cost for problems with a small to medium added mass effect. Those results also substantiate the findings by [4], which had led in the same direction. Finally, the algorithm for FSCI could successfully be applied to the combination of the thyssenkrupp elevator test tower with an HMD. The large number of coupled simulations performed throughout this thesis work up to a physical time up to 41.5 minutes also showed that it is possible to conduct useful numerical studies for those kinds of multiphysics problems with a manageable amount of computational cost.

A recommendation for future research is more validation studies comparing numerical results with on-site measurements and physical wind tunnel testing. For example, the data published in [106] offers much potential for such studies. Additionally, the coupling of macro and micrometeorological models and the modeling of the surrounding terrain are of interest for a better modeling of the wind conditions. Concerning the aspect of the inclusion of structural control into FSI simulations, i.e., FSCI, further investigations concerning more advanced control strategies are possible. Furthermore, the extension of the SC subsystem from a SISO to a MIMO system is worth to be investigated. Additionally, the general concepts presented in CHAPTER 3, which were applied to an example from civil engineering, can be applied for problems from other engineering disciplines, like, for example, for problems from mechanical engineering.

Appendix A

Algorithms

This Appendix shows the algorithms for FSCI, [FS]CI, and F[SC]I in pseudo code notation, which is in accordance with Sect. 3.2.. Those have also been published in a slightly different notation in [104]. The algorithms are written generically, to make them applicable to general FSCI problems. Thus the measured output and the quantities of the SC subsystem (index C) are written as vectors in order to cover MIMO systems. As mentioned in Sect. 2.3 in this work only SISO systems for the SC subsystem are taken into account. This means vector quantity $\boldsymbol{y}_{\mathrm{S,meas}}^{n+1}$ and the quantities of the SC subsystem (index C) in the pseudo-code become scalar quantities.

Algorithm 1 Pseudocode for the partitioned FSCI scheme (no nesting).

```
// initialize states, i.e. set ICs ...
${}^{k_{\mathrm{end}}}\boldsymbol{x}_{\mathrm{F}}^{0} \longleftarrow \boldsymbol{x}_{\mathrm{F}}^{\mathrm{init}}$; ${}^{k_{\mathrm{end}}}\boldsymbol{x}_{\mathrm{S}}^{0} \longleftarrow \boldsymbol{x}_{\mathrm{S}}^{\mathrm{init}}$; ${}^{k_{\mathrm{end}}}\boldsymbol{x}_{\mathrm{C}}^{0} \longleftarrow \boldsymbol{x}_{\mathrm{C}}^{\mathrm{init}}$
time loop ...
for $n \longleftarrow 0$ to $n \longleftarrow n_{\mathrm{end}} - 1$ do
    // predict displacements and measured output ...
    ${}^{0}\boldsymbol{y}_{\mathrm{S}}^{n+1} \longleftarrow {}^{k_{\mathrm{end}}}\boldsymbol{y}_{\mathrm{S}}^{n}$; ${}^{0}\boldsymbol{y}_{\mathrm{S,meas}}^{n+1} \longleftarrow {}^{k_{\mathrm{end}}}\boldsymbol{y}_{\mathrm{S,meas}}^{n}$
    // interface iteration loop, i.e. FSCI loop ...
    for $k \longleftarrow 0$ to $k \longleftarrow k_{\mathrm{max}}$ do
        // map displacements from solid to fluid ...
        // and copy measured output from solid to controller...
        ${}^{k}\boldsymbol{y}_{\mathrm{F}}^{n+1} \longleftarrow \mathcal{M}_{\boldsymbol{y}}\left({}^{k}\boldsymbol{y}_{\mathrm{S}}^{n+1}\right)$; ${}^{k}\boldsymbol{y}_{\mathrm{C}}{}^{n+1} \longleftarrow {}^{k}\boldsymbol{y}_{\mathrm{S,meas}}{}^{n+1}$
        // solve fluid and controller in parallel ...
        ${}^{k}\boldsymbol{z}_{\mathrm{F}}^{n+1} \longleftarrow \mathcal{G}_{\mathrm{F}}^{\left[{}^{k}\boldsymbol{x}_{\mathrm{F}}^{n+1}\right]}\left({}^{k}\boldsymbol{y}_{\mathrm{F}}^{n+1}\right)$
        ${}^{k}\boldsymbol{u}_{\mathrm{C}}^{n+1} \longleftarrow \mathcal{G}_{\mathrm{C}}^{\left[{}^{k}\boldsymbol{x}_{\mathrm{C}}^{n+1}\right]}\left({}^{k}\boldsymbol{y}_{\mathrm{C}}^{n+1}\right)$
```

Algorithm 1 continued

```
        // map forces from fluid to solid ...
        // and copy control input from controller to solid ...
        ${}^{k}\boldsymbol{z}_{\mathrm{S}}^{n+1} \longleftarrow \mathcal{M}_{\boldsymbol{z}}\left({}^{k}\boldsymbol{z}_{\mathrm{F}}^{n+1}\right)\ {}^{k}\boldsymbol{u}_{\mathrm{S}}^{n+1} \longleftarrow {}^{k}\boldsymbol{u}_{\mathrm{C}}^{n+1}$
        // solve solid ...
        $\begin{bmatrix} {}^{k}\boldsymbol{y}_{\mathrm{S}}^{n+1} \\ {}^{k}\boldsymbol{y}_{\mathrm{S,meas}}^{n+1} \end{bmatrix} \longleftarrow \mathcal{G}_{\mathrm{S}}^{\left[{}^{k}\boldsymbol{x}_{\mathrm{S}}^{n+1}\right]}\left({}^{k}\boldsymbol{z}_{\mathrm{S}}^{n+1}, {}^{k}\boldsymbol{u}_{\mathrm{S}}^{n+1}\right)$
        // calculate residuum of displacements
        // and measured output ...
        ${}^{k}\mathcal{R}_{\boldsymbol{y}}^{n+1} \longleftarrow {}^{k}\boldsymbol{y}_{\mathrm{S}}^{n+1} - {}^{k-1}\boldsymbol{y}_{\mathrm{S}}^{n+1}$
        ${}^{k}\mathcal{R}_{\boldsymbol{y}_{\mathrm{meas}}}^{n+1} \longleftarrow {}^{k}\boldsymbol{y}_{\mathrm{S,meas}}^{n+1} - {}^{k-1}\boldsymbol{y}_{\mathrm{S,meas}}^{n+1}$
        ${}^{k}\boldsymbol{\mathcal{R}}_{\boldsymbol{y},\boldsymbol{y}_{\mathrm{meas}}}^{n+1} := \left[{}^{k}\mathcal{R}_{\boldsymbol{x}}^{n+1}\ {}^{k}\mathcal{R}_{\boldsymbol{y}_{\mathrm{meas}}}^{n+1}\right]$
        // check for convergence ...
        ${}^{k}\varepsilon^{n+1} \longleftarrow \left\|{}^{k}\boldsymbol{\mathcal{R}}_{\boldsymbol{y},\boldsymbol{y}_{\mathrm{meas}}}^{n+1}\right\| / \sqrt{n_{dof}}$
        if ${}^{k}\varepsilon^{n+1} < {}^{\max}\varepsilon$ then
            break
        end if
        // update Aitken factor
        if $k = 0$ then
            ${}^{0}\beta^{n+1} \longleftarrow {}^{\mathrm{init}}\beta$
        else
            ${}^{k}\beta^{n+1} \longleftarrow {}^{k-1}\beta^{n+1} \frac{{}^{k-1}\boldsymbol{\mathcal{R}}_{\boldsymbol{y},\boldsymbol{y}_{\mathrm{meas}}}^{n+1\ \mathrm{T}}\left({}^{k-1}\boldsymbol{\mathcal{R}}_{\boldsymbol{y},\boldsymbol{y}_{\mathrm{meas}}}^{n+1} - {}^{k}\boldsymbol{\mathcal{R}}_{\boldsymbol{y},\boldsymbol{y}_{\mathrm{meas}}}^{n+1}\right)}{\left\|{}^{k-1}\boldsymbol{\mathcal{R}}_{\boldsymbol{y},\boldsymbol{y}_{\mathrm{meas}}}^{n+1} - {}^{k}\boldsymbol{\mathcal{R}}_{\boldsymbol{y},\boldsymbol{y}_{\mathrm{meas}}}^{n+1}\right\|^{2}}$
        end if
        // update displacements and measured output ...
        ${}^{k+1}\boldsymbol{y}_{\mathrm{S}}^{n+1} \longleftarrow {}^{k}\boldsymbol{y}_{\mathrm{S}}^{n+1} + {}^{k}\beta^{n+1}\ {}^{k}\mathcal{R}_{\boldsymbol{y}}^{n+1}$
        ${}^{k+1}\boldsymbol{y}_{\mathrm{S,meas}}^{n+1} \longleftarrow {}^{k}\boldsymbol{y}_{\mathrm{S,meas}}^{n+1} + {}^{k}\beta^{n+1}\ {}^{k}\mathcal{R}_{\boldsymbol{y}_{\mathrm{meas}}}^{n+1}$
    end for
end for
```

Algorithm 2 Pseudocode for the partitioned F[SC]I scheme (nesting of [SC] subsystem)

```
// initialize states, i.e. set ICs ...
${}^{k_\mathrm{end}}\boldsymbol{x}_\mathrm{F}^{0} \longleftarrow \boldsymbol{x}_\mathrm{F}^\mathrm{init}$; ${}^{k_\mathrm{end}}_{l_\mathrm{end}}\boldsymbol{x}_\mathrm{S}^{0} \longleftarrow \boldsymbol{x}_\mathrm{S}^\mathrm{init}$; ${}^{k_\mathrm{end}}_{l_\mathrm{end}}\boldsymbol{x}_\mathrm{C}^{0} \longleftarrow \boldsymbol{x}_\mathrm{C}^\mathrm{init}$
// time loop ...
for $n \longleftarrow 0$ to $n \longleftarrow n_\mathrm{end} - 1$ do
    // predict displacements and measured output ...
    ${}^{0}_{l_\mathrm{end}}\boldsymbol{y}_\mathrm{S}^{n+1} \longleftarrow {}^{k_\mathrm{end}}_{l_\mathrm{end}}\boldsymbol{y}_\mathrm{S}^{n}$; ${}^{0}_{l_\mathrm{end}}\boldsymbol{y}_\mathrm{S,meas}^{n+1} \longleftarrow {}^{k_\mathrm{end}}_{l_\mathrm{end}}\boldsymbol{y}_\mathrm{S,meas}^{n}$
    // outer interface iteration loop, i.e. F[SC]I loop ...
    for $k \longleftarrow 0$ to $k \longleftarrow k_\mathrm{max}$ do
        // map displacements from solid to fluid ...
        ${}^{k}\boldsymbol{y}_\mathrm{F}^{n+1} \longleftarrow \mathcal{M}_{\boldsymbol{y}}\left({}^{k}_{l_\mathrm{end}}\boldsymbol{y}_\mathrm{S}^{n+1}\right)$
        // solve fluid ...
        ${}^{k}\boldsymbol{z}_\mathrm{F}^{n+1} \longleftarrow \mathcal{G}_\mathrm{F}^{\left[{}^{k}\boldsymbol{x}_\mathrm{F}^{n+1}\right]}\left({}^{k}\boldsymbol{y}_\mathrm{F}^{n+1}\right)$
        // map forces from fluid to solid ...
        ${}^{k}\boldsymbol{z}_\mathrm{S}^{n+1} \longleftarrow \mathcal{M}_{\boldsymbol{z}}\left({}^{k}\boldsymbol{z}_\mathrm{F}^{n+1}\right)$
        // predict measured output ...
        ${}^{k}_{0}\boldsymbol{y}_\mathrm{S,meas}^{n+1} \longleftarrow {}^{k}_{l_\mathrm{end}}\boldsymbol{y}_\mathrm{S,meas}^{n+1}$
        // inner interface iteration loop, i.e. SCI loop ...
        for $l \longleftarrow 0$ to $l \longleftarrow l_\mathrm{max}$ do
            // copy measured output from solid to controller ...
            ${}^{k}_{l}\boldsymbol{y}_\mathrm{C}^{n+1} \longleftarrow {}^{k}_{l}\boldsymbol{y}_\mathrm{S,meas}^{n+1}$
            // solve controller ...
            ${}^{k}_{l}\boldsymbol{u}_\mathrm{C}^{n+1} \longleftarrow \mathcal{G}_\mathrm{C}^{\left[{}^{k}_{l}\boldsymbol{x}_\mathrm{C}^{n+1}\right]}\left({}^{k}_{l}\boldsymbol{y}_\mathrm{C}^{n+1}\right)$
            // copy control input from controller to solid ...
            ${}^{k}_{l}\boldsymbol{u}_\mathrm{S}^{n+1} \longleftarrow {}^{k}_{l}\boldsymbol{u}_\mathrm{C}^{n+1}$
            // solve solid ...
            $\begin{bmatrix} {}^{k}_{l}\boldsymbol{y}_\mathrm{S}^{n+1} \\ {}^{k}_{l}\boldsymbol{y}_\mathrm{S,meas}^{n+1} \end{bmatrix} \longleftarrow \mathcal{G}_\mathrm{S}^{\left[{}^{k}_{l}\boldsymbol{x}_\mathrm{S}^{n+1}\right]}\left({}^{k}\boldsymbol{z}_\mathrm{S}^{n+1}, {}^{k}_{l}\boldsymbol{u}_\mathrm{S}^{n+1}\right)$
            // calculate residuum of measured output ...
            ${}^{k}_{l}\mathcal{R}_{\boldsymbol{y}_\mathrm{meas}}^{n+1} \longleftarrow {}^{k}_{l}\boldsymbol{y}_\mathrm{S,meas}^{n+1} - {}^{k}_{l-1}\boldsymbol{y}_\mathrm{S,meas}^{n+1}$
            // check for inner convergence ...
            ${}^{k}_{l}\varepsilon^{n+1} \longleftarrow \left\|{}^{k}_{l}\mathcal{R}_{\boldsymbol{y}_\mathrm{meas}}^{n+1}\right\| / \sqrt{n_{dof}}$
            if ${}^{k}_{l}\varepsilon^{n+1} < {}_{\mathrm{max}}\varepsilon$ then
                break
            end if
```

Algorithm 2 continued

```
            // update inner Aitken factor ...
            if $l = 0$ then
                ${}^{k}_{0}\beta^{n+1} \longleftarrow {}_{\text{init}}\beta$
            else
                if $\dim\left\{{}^{k}_{l}\mathcal{R}^{n+1}_{\boldsymbol{y}_\text{meas}}\right\} = 1$ then
                    ${}^{k}_{l}\beta^{n+1} \longleftarrow {}^{k}_{l-1}\beta^{n+1} \frac{{}^{k}_{l-1}\mathcal{R}^{n+1}_{y_\text{meas}}}{{}^{k}_{l-1}\mathcal{R}^{n+1}_{y_\text{meas}} - {}^{k}_{l}\mathcal{R}^{n+1}_{y_\text{meas}}}$
                else
                    ${}^{k}_{l}\beta^{n+1} \longleftarrow {}^{k}_{l-1}\beta^{n+1} \frac{{}^{k}_{l-1}\mathcal{R}^{n+1}_{\boldsymbol{y}_\text{meas}}{}^{\mathrm{T}}\left({}^{k}_{l-1}\mathcal{R}^{n+1}_{\boldsymbol{y}_\text{meas}} - {}^{k}_{l}\mathcal{R}^{n+1}_{\boldsymbol{y}_\text{meas}}\right)}{\left\|{}^{k}_{l-1}\mathcal{R}^{n+1}_{\boldsymbol{y}_\text{meas}} - {}^{k}_{l}\mathcal{R}^{n+1}_{\boldsymbol{y}_\text{meas}}\right\|^{2}}$
                end if
            end if
            // update measured output ...
            ${}^{k}_{l+1}\boldsymbol{y}^{n+1}_{\text{S,meas}} \longleftarrow {}^{k}_{l}\boldsymbol{y}^{n+1}_{\text{S,meas}} + {}^{k}_{l}\beta^{n+1}\,{}^{k}_{l}\mathcal{R}^{n+1}_{\boldsymbol{y}_\text{meas}}$
        end for
        // calculate residuum of displacements ...
        ${}^{k}\mathcal{R}^{n+1}_{\boldsymbol{y}} \longleftarrow {}^{k}_{l_\text{end}}\boldsymbol{y}^{n+1}_{\text{S}} - {}^{k-1}_{l_\text{end}}\boldsymbol{y}^{n+1}_{\text{S}}$
        // check for outer convergence ...
        ${}^{k}\varepsilon^{n+1} \longleftarrow \left\|{}^{k}\mathcal{R}^{n+1}_{\boldsymbol{y}}\right\| / \sqrt{n_{dof}}$
        if ${}^{k}\varepsilon^{n+1} < {}^{\max}\varepsilon$ then
            break
        end if
        // update outer Aitken factor ...
        if $k = 0$ then
            ${}^{0}\beta^{n+1} \longleftarrow {}^{\text{init}}\beta$
        else
            if $\dim\left\{{}^{k}\mathcal{R}^{n+1}_{\boldsymbol{y}}\right\} = 1$ then
                ${}^{k}\beta^{n+1} \longleftarrow {}^{k-1}\beta^{n+1} \frac{{}^{k-1}\mathcal{R}^{n+1}_{\boldsymbol{y}}}{{}^{k-1}\mathcal{R}^{n+1}_{\boldsymbol{y}} - {}^{k}\mathcal{R}^{n+1}_{\boldsymbol{y}}}$
            else
                ${}^{k}\beta^{n+1} \longleftarrow {}^{k-1}\beta^{n+1} \frac{{}^{k-1}\mathcal{R}^{n+1\,\mathrm{T}}_{\boldsymbol{y}}\left({}^{k-1}\mathcal{R}^{n+1}_{\boldsymbol{y}} - {}^{k}\mathcal{R}^{n+1}_{\boldsymbol{y}}\right)}{\left\|{}^{k-1}\mathcal{R}^{n+1}_{\boldsymbol{y}} - {}^{k}\mathcal{R}^{n+1}_{\boldsymbol{y}}\right\|^{2}}$
            end if
        end if
        // update displacements and measured output ...
        ${}^{k+1}_{l_\text{end}}\boldsymbol{y}^{n+1}_{\text{S}} \longleftarrow {}^{k}_{l_\text{end}}\boldsymbol{y}^{n+1}_{\text{S}} + {}^{k}\beta^{n+1}\,{}^{k}\mathcal{R}^{n+1}_{\boldsymbol{y}}$
        ${}^{k+1}_{l_\text{end}}\boldsymbol{y}^{n+1}_{\text{S,meas}} \longleftarrow {}^{k}_{l_\text{end}}\boldsymbol{y}^{n+1}_{\text{S,meas}}$
    end for
end for
```

Algorithm 3 Pseudocode for the partitioned [FS]CI scheme (nesting of [FS] subsystem)

```
// initialize states, i.e. set ICs ...
${}^{k_\text{end}}_{l_\text{end}}\boldsymbol{x}^0_\text{F} \longleftarrow \boldsymbol{x}^\text{init}_\text{F}$; ${}^{k_\text{end}}_{l_\text{end}}\boldsymbol{x}^0_\text{S} \longleftarrow \boldsymbol{x}^\text{init}_\text{S}$; ${}^{k_\text{end}}\boldsymbol{x}^0_\text{C} \longleftarrow \boldsymbol{x}^\text{init}_\text{C}$
// time loop ...
for $n \longleftarrow 0$ to $n \longleftarrow n_\text{end} - 1$ do
    // predict displacements and measured output ...
    ${}^{0}_{l_\text{end}}\boldsymbol{y}^{n+1}_\text{S} \longleftarrow {}^{k_\text{end}}_{l_\text{end}}\boldsymbol{y}^{n}_\text{S}$; ${}^{0}_{l_\text{end}}\boldsymbol{y}^{n+1}_\text{S,meas} \longleftarrow {}^{k_\text{end}}_{l_\text{end}}\boldsymbol{y}^{n}_\text{S,meas}$
    // outer interface iteration loop, i.e. [FS]CI loop ...
    for $k \longleftarrow 0$ to $k \longleftarrow k_\text{max}$ do
        // copy measured output from solid to controller ...
        ${}^{k}\boldsymbol{y}^{n+1}_\text{C} \longleftarrow {}^{k}_{l_\text{end}}\boldsymbol{y}^{n+1}_\text{S,meas}$
        // solve controller ...
        ${}^{k}\boldsymbol{u}^{n+1}_\text{C} \longleftarrow \mathcal{G}_\text{C}^{\left[{}^{k}\boldsymbol{x}^{n+1}_\text{C}\right]}\left({}^{k}\boldsymbol{y}^{n+1}_\text{C}\right)$
        // copy control input from controller to solid ...
        ${}^{k}\boldsymbol{u}^{n+1}_\text{S} \longleftarrow {}^{k}\boldsymbol{u}^{n+1}_\text{C}$
        // predict displacements ...
        ${}^{k}_{0}\boldsymbol{y}^{n+1}_\text{S} \longleftarrow {}^{k}_{l_\text{end}}\boldsymbol{y}^{n+1}_\text{S}$
        // inner interface iteration loop, i.e. FSI loop ...
        for $l \longleftarrow 0$ to $l \longleftarrow l_\text{max}$ do
            // map displacements from solid to fluid ...
            ${}^{k}_{l}\boldsymbol{y}^{n+1}_\text{F} \longleftarrow \mathcal{M}_{\boldsymbol{y}}\left({}^{k}_{l}\boldsymbol{y}^{n+1}_\text{S}\right)$
            // solve fluid ...
            ${}^{k}_{l}\boldsymbol{z}^{n+1}_\text{F} \longleftarrow \mathcal{G}_\text{F}^{\left[{}^{k}_{l}\boldsymbol{x}^{n+1}_\text{F}\right]}\left({}^{k}_{l}\boldsymbol{y}^{n+1}_\text{F}\right)$
            // map forces from fluid to solid ...
            ${}^{k}_{l}\boldsymbol{z}^{n+1}_\text{S} \longleftarrow \mathcal{M}_{\boldsymbol{z}}\left({}^{k}_{l}\boldsymbol{z}^{n+1}_\text{F}\right)$
            // solve solid ...
            $\begin{bmatrix} {}^{k}_{l}\boldsymbol{y}^{n+1}_\text{S} \\ {}^{k}_{l}\boldsymbol{y}^{n+1}_\text{S,meas} \end{bmatrix} \longleftarrow \mathcal{G}_\text{S}^{\left[{}^{k}_{l}\boldsymbol{x}^{n+1}_\text{S}\right]}\left({}^{k}_{l}\boldsymbol{z}^{n+1}_\text{S}, {}^{k}\boldsymbol{u}^{n+1}_\text{S}\right)$
            // calculate residuum of displacements ...
            ${}^{k}_{l}\mathcal{R}^{n+1}_{\boldsymbol{y}} \longleftarrow {}^{k}_{l}\boldsymbol{y}^{n+1}_\text{S} - {}^{k}_{l-1}\boldsymbol{y}^{n+1}_\text{S}$
            // check for inner convergence ...
            ${}^{k}_{l}\varepsilon^{n+1} \longleftarrow \left\|{}^{k}_{l}\mathcal{R}^{n+1}_{\boldsymbol{y}}\right\| / \sqrt{n_{dof}}$
            if ${}^{k}_{l}\varepsilon^{n+1} < {}_\text{max}\varepsilon$ then
                break
            end if
```

Algorithm 3 continued

```
      // update inner Aitken factor ...
      if $l = 0$ then
        ${}^{k}_{0}\beta^{n+1} \longleftarrow {}_{\text{init}}\beta$
      else
        if $\dim\left\{{}^{k}_{l}\mathcal{R}_{\boldsymbol{y}}^{n+1}\right\} = 1$ then
          ${}^{k}_{l}\beta^{n+1} \longleftarrow {}^{k}_{l-1}\beta^{n+1}\frac{{}^{k}_{l-1}\mathcal{R}_{\boldsymbol{y}}^{n+1}}{{}^{k}_{l-1}\mathcal{R}_{\boldsymbol{y}}^{n+1}-{}^{k}_{l}\mathcal{R}_{\boldsymbol{y}}^{n+1}}$
        else
          ${}^{k}_{l}\beta^{n+1} \longleftarrow {}^{k}_{l-1}\beta^{n+1}\frac{{}^{k}_{l-1}\mathcal{R}_{\boldsymbol{y}}^{n+1\,\mathrm{T}}\left({}^{k}_{l-1}\mathcal{R}_{\boldsymbol{y}}^{n+1}-{}^{k}_{l}\mathcal{R}_{\boldsymbol{y}}^{n+1}\right)}{\left\|{}^{k}_{l-1}\mathcal{R}_{\boldsymbol{y}}^{n+1}-{}^{k}_{l}\mathcal{R}_{\boldsymbol{y}}^{n+1}\right\|^{2}}$
        end if
      end if
      // update displacements ...
      ${}^{k}_{l+1}\boldsymbol{y}_{\text{S}}^{n+1} \longleftarrow {}^{k}_{l}\boldsymbol{y}_{\text{S}}^{n+1} + {}^{k}_{l}\beta^{n+1}\,{}^{k}_{l}\mathcal{R}_{\boldsymbol{y}}^{n+1}$
    end for
    // calculate residuum of measured output ...
    ${}^{k}\mathcal{R}_{\boldsymbol{y}_{\text{meas}}}^{n+1} \longleftarrow {}^{k}_{l_{\text{end}}}\boldsymbol{y}_{\text{S,meas}}{}^{n+1} - {}^{k-1}_{l_{\text{end}}}\boldsymbol{y}_{\text{S,meas}}{}^{n+1}$
    // check for outer convergence ...
    ${}^{k}\varepsilon^{n+1} \longleftarrow \left\|{}^{k}\mathcal{R}_{\boldsymbol{y}_{\text{meas}}}^{n+1}\right\| / \sqrt{n_{dof}}$
    if ${}^{k}\varepsilon^{n+1} < {}^{\max}\varepsilon$ then
      break
    end if
    // update outer Aitken factor ...
    if $k = 0$ then
      ${}^{0}\beta^{n+1} \longleftarrow {}^{\text{init}}\beta$
    else
      if $\dim\left\{{}^{k}\mathcal{R}_{\boldsymbol{y}_{\text{meas}}}^{n+1}\right\} = 1$ then
        ${}^{k}\beta^{n+1} \longleftarrow {}^{k-1}\beta^{n+1}\frac{{}^{k-1}\mathcal{R}_{y_{\text{meas}}}^{n+1}}{{}^{k-1}\mathcal{R}_{y_{\text{meas}}}^{n+1}-{}^{k}\mathcal{R}_{y_{\text{meas}}}^{n+1}}$
      else
        ${}^{k}\beta^{n+1} \longleftarrow {}^{k-1}\beta^{n+1}\frac{{}^{k-1}\mathcal{R}_{\boldsymbol{y}_{\text{meas}}}^{n+1}{}^{\mathrm{T}}\left({}^{k-1}\mathcal{R}_{\boldsymbol{y}_{\text{meas}}}^{n+1}-{}^{k}\mathcal{R}_{\boldsymbol{y}_{\text{meas}}}^{n+1}\right)}{\left\|{}^{k-1}\mathcal{R}_{\boldsymbol{y}_{\text{meas}}}^{n+1}-{}^{k}\mathcal{R}_{\boldsymbol{y}_{\text{meas}}}^{n+1}\right\|^{2}}$
      end if
    end if
    // update displacements and measured output ...
    ${}^{k+1}_{l_{\text{end}}}\boldsymbol{y}_{\text{S}}^{n+1} \longleftarrow {}^{k}_{l_{\text{end}}}\boldsymbol{y}_{\text{S}}^{n+1}$
    ${}^{k+1}_{l_{\text{end}}}\boldsymbol{y}_{\text{S,meas}}^{n+1} \longleftarrow {}^{k}_{l_{\text{end}}}\boldsymbol{y}_{\text{S,meas}}{}^{n+1} + {}^{k}\beta^{n+1}\,{}^{k}\mathcal{R}_{\boldsymbol{y}_{\text{meas}}}^{n+1}$
  end for
end for
```

Appendix B

Calculation of Descriptive Statistics

This Appendix provides the definitions of discrete statistical data for a time series $\{x_k\}_{k=0}^{N-1}$. When applying B.4, B.5 and B.6 to a time series of turbulent velocities, only the fluctuating part u' is to be used for the calculations.

B.1 Mean Value

The mean value is computed as

$$\overline{x} = \frac{1}{N} \sum_{k=0}^{N-1} x_k. \tag{B.1}$$

B.2 Median Value

The median value is computed as

$$\tilde{x} = \begin{cases} x_{\frac{N-1}{2}} & \text{for } N \text{ odd} \\ 0.5(x_{\frac{N}{2}-1} + x_{\frac{N}{2}}) & \text{for } N \text{ even} \end{cases} \tag{B.2}$$

B.3 Root Mean Square (RMS)

The quadratic mean is computed as

$$\overline{x}^2 = \frac{1}{N}\sum_{k=0}^{N-1} x_k^2 \tag{B.3}$$

and from this the Root Mean Square (RMS) is calculated as

$$\mathrm{RMS} = \sqrt{\overline{x}^2}. \tag{B.4}$$

B.4 Standard Deviation

The standard deviation is calculated as

$$\sigma_x = \sqrt{\sum_{k=0}^{N-1} \frac{|x_k|^2}{N}}. \tag{B.5}$$

B.5 Spectral Density

The spectral density can be calculated at $f = {}^{m}/_{T}$ from the discrete Fourier transform (DFT)

$$\hat{x}_m = \frac{1}{N}\sum_{k=0}^{N-1} x_k \mathrm{exp}\left(\frac{-2\pi i m k}{N}\right), \quad m = 0 \ldots N-1, \tag{B.6}$$

as

$$S_{xx,m} = \frac{1}{2T}\overline{|\hat{x}_m|^2} = S_{xx}(f) = S(f). \tag{B.7}$$

According to [4] $S_{xx}(f)$ is calculated by subdividing the total time series into subintervals (usually eight to 16 values), evaluating Eq. (B.6) on the subintervals and averaging its results afterwards.

B.6 Auto Correlation

The auto correlation for $\tau = m\delta t$ is calculated as

$$R_{xx,m} = \frac{1}{\sigma_x^2 N}\sum_{k=0}^{N-1} x_k x_{m+k \bmod N}. \tag{B.8}$$

Appendix C

Integral Transform Methods

This Appendix gives a short introduction to the basic integral transform methods commonly applied in control theory. It is only possible to give a very rough overview, which, by far, cannot be complete. For more details, the interested reader is referred to [39], which is a very detailed textbook about integral transform methods.

C.1 The Laplace-Transform

This is a short introduction into the Laplace-Transform on the basis of [40] p. 401. The Laplace-Integral associates the function $f(t)$, which is in most technical applications a function of time, to the complex function $F(s)$. This is referred to as Laplace-Transform. $f(t)$ is called original function and $F(s)$ transformed function. This relation is written as

$$F(s) = \mathcal{L}\{f(t)\}. \tag{C.1}$$

The transformation rule is

$$F(s) = \int_0^\infty f(t)\mathrm{e}^{-st}\mathrm{d}t, \tag{C.2}$$

where $s \in \mathbb{C}$ is a complex number. The Laplace domain is also referred to as the frequency domain and the original domain as the time domain. In the context of the classical approach for controller design in control theory, in general the design is entirely performed in the frequency domain, and no transformation back to the time domain is necessary. This is why the transformation rule back to the time domain is not treated here.

Subsequently, two important examples for the application of the Laplace-Transform are given, which are advantageous when applying it to equations of dynamic systems.

C.1.1 Differentiation

$f(t)$ is a continuous function. Its derivative is defined as $f'(t) = \frac{\mathrm{d}}{\mathrm{d}t} f(t)$. The transformation is carried out by applying Eq. (C.2). With

$$\int u'v = [uv] - \int uv', \tag{C.3}$$

it follows

$$\begin{aligned} \mathcal{L}[f'(t)] &= \int_0^\infty f'(t)\mathrm{e}^{-st}\mathrm{d}t \\ &= -f(0) + \underbrace{s\int_0^\infty f(t)\mathrm{e}^{-st}\mathrm{d}t}_{s\mathcal{L}[f(t)]}. \end{aligned} \tag{C.4}$$

Thus the rule

$$\mathcal{L}[f'(t)] = s\mathcal{L}[f(t)] - f(0), \tag{C.5}$$

applies, which states that a derivative in the time domain results in a multiplication in the Laplace domain. This also holds for higher order derivatives and Eq. (C.5) can be generalized as

$$\mathcal{L}[f^n(t)] = s^n\mathcal{L}[f(t)] - s^{n-1}f(0) - s^{n-2}f'(0) - \ldots - sf^{n-2}(0) - f^{n-1}(0). \tag{C.6}$$

C.1.2 Integration

$g(t)$ is defined as the integral of $f(t)$, with $g(t) = \int_0^t f(\tau)\mathrm{d}\tau$ and $g(0) = 0$. Inserting $g(t)$ into Eq. (C.5) one obtains:

$$\mathcal{L}\Big[\int_0^t f(\tau)\mathrm{d}\tau\Big] = \frac{1}{s}\mathcal{L}[f(t)]. \tag{C.7}$$

Thus the integration is performed in the Laplace domain by carrying out divisions.

C.2 The Z-Transform

In analogy to the Laplace-Transform for continuous functions $f(t)$, for discrete sequences $f(k)$ the Z-transform exists. This section summarizes the most important aspects concerning this work, from [60] Chapter 12. The sampled function $f(k)$ is described by a sequence of Dirac δ impulses as

$$f^*(t) = \sum_{k=0}^{\infty} f(kT)\delta(t - k\Delta t). \tag{C.8}$$

Herein $f^*(t)$ is a function of the continuous time t, which is only different from zero at the sampling points $t = k\Delta t$. Applying the Laplace transform to Eq. (C.8) it follows

$$F^*(s) = \sum_{k=0}^{\infty} f(kT)\mathrm{e}^{-ks\Delta t}. \tag{C.9}$$

The values of $\mathrm{e}^{-ks\Delta t}$ are complex numbers, depending on the sampling time Δt and the summation index k. $\mathrm{e}^{s\Delta t}$ is replaced by the complex variable z, which results in

$$z = \mathrm{e}^{s\Delta t}. \tag{C.10}$$

is the sampling time, but in the context of numerical time integration the discrete time step is δt. Applying Eq. (C.10) to Eq. (C.9) and introducing the new function

$$F(z) = F^*(s)|_{\mathrm{e}^{s\Delta t}=z}, \tag{C.11}$$

the Z-Transform is defined as

$$F(z) = \sum_{k=0}^{\infty} f(k)z^{-k}. \tag{C.12}$$

In accordance to the Laplace transform this is often written as

$$F(z) = \mathcal{Z}\{f(k)\}. \tag{C.13}$$

An additional important aspect is the relation of the system poles s_i of the transfer function of the time continuous and time discrete system z_i. This relation is defined as

$$z_i = \mathrm{e}^{s_i \Delta t}, \tag{C.14}$$

which is the map between the s-plane and the z-plane and the other way around

$$s_i = \frac{1}{\Delta t} \ln(z_i). \tag{C.15}$$

Appendix D

Dynamic System Modeling in Control Theory

This Appendix gives a short introduction into the modeling of dynamic systems in control theory. Therefore, a simple, well-known mechanical example is chosen, which is also shown in the standard literature (e.g., [40] p. 40 ff., [96] p. 2 ff. and [61] p. 290). The block referred to in the following is the "controlled system" block in the basic block diagram in Fig. 2.2. When modeling dynamic systems in one of the forms presented in this Appendix, in control theory, a lot of different tools for system assessment and controller design exist, which are afterwards easily applicable. The controller design, which corresponds to the "controlling element" block in Fig. 2.2 is not part of the explanations done here, but can for example be seen in CHAPTER 3. The problem to

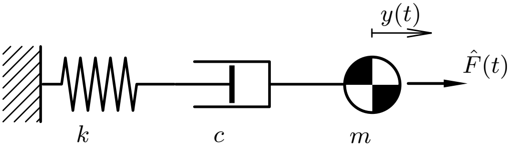

Figure D.1: Mechanical example for a dynamic system.

be modeled is shown in Fig. D.1 with its differential equation

$$m\ddot{y}(t) + c\dot{y}(t) + ky(t) = \hat{F}(t). \tag{D.1}$$

The system output $y(t)$ is the system displacement and the system input $u(t)$ is the external force $\hat{F}(t)$. The two standard modeling approaches (one in the frequency and one in the time domain) from control theory, which are physically equivalent, are presented for this system in the following Sections.

D.1 Modeling in the Frequency Domain

The modeling of dynamic systems in the frequency domain is the classical approach in control theory. It takes advantage of the Laplace transform (APPENDIX C) and mostly is applied to SISO systems. Additionally, several standard system types depending on their differential equation, are defined. Since the system's type of ODE presented in Eq. (D.1) applies to many technical applications; this system can be characterized as one of those standard system types. It is referred to as PT_2 element, or in words, delay element of second order. In a first step the Eq. (D.1) is transformed to the frequency domain by the Laplace transform. It reads then

$$(ms^2 + cs + k)Y(s) = U(s). \tag{D.2}$$

Eq. (D.2) is often written in the following generalized notation

$$(T^2s^2 + 2DTs + 1)Y(s) = KU(s), \tag{D.3}$$

with

$$T = \sqrt{\frac{m}{k}}\ ; D = \frac{c}{2\sqrt{mk}}\ ; K = \frac{1}{k}. \tag{D.4}$$

From Eq. (D.4) the system transfer function can be obtained as

$$G(s) = \frac{Y(s)}{U(s)} = \frac{K}{T^2s^2 + 2DTs + 1}. \tag{D.5}$$

After the system is written in this kind of notation, it is directly possible to apply the tools for system analysis and controller design of control theory. Two examples of such tools are shown in the following. Firstly it is directly possible to depict the system

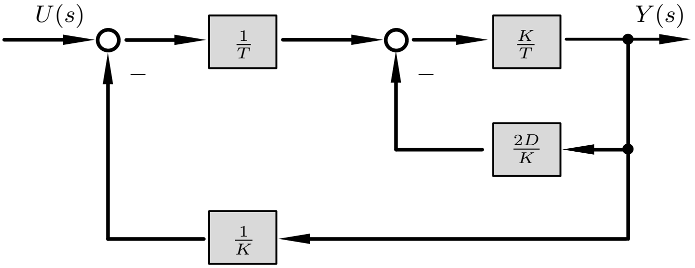

Figure D.2: Block diagram for the system in the frequency domain.

in block diagram notation, as shown in Fig. D.2. Secondly the system behavior and a basic stability analysis can be performed. For the purpose of the stability analysis, the system is subjected to the load depicted in Fig. D.3, to investigate its step function response. Inserting the angular eigenfrequency, defined as $\omega = {}^1\!/_T$, into Eq. (D.5) results in

$$G(s) = \frac{K\omega^2}{s^2 + 2D\omega s + \omega^2}. \tag{D.6}$$

The system poles, describing the system eigen behavior, can be

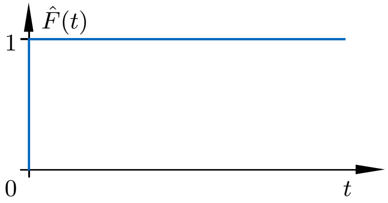

Figure D.3: Step function excitation.

calculated by solving the characteristic equation $s^2+2D\omega s+\omega^2 = 0$. The system poles are for this example:

$$s_{1/2} = -\omega(D \pm \sqrt{D^2 - 1}). \tag{D.7}$$

The system poles can be depicted in the s-plane, which is shown in Fig. D.4 for different values of the damping coefficient D. Fig.

D.4 also shows the equivalent system reaction in the time domain for comparison. It can be seen; the system is stable if the

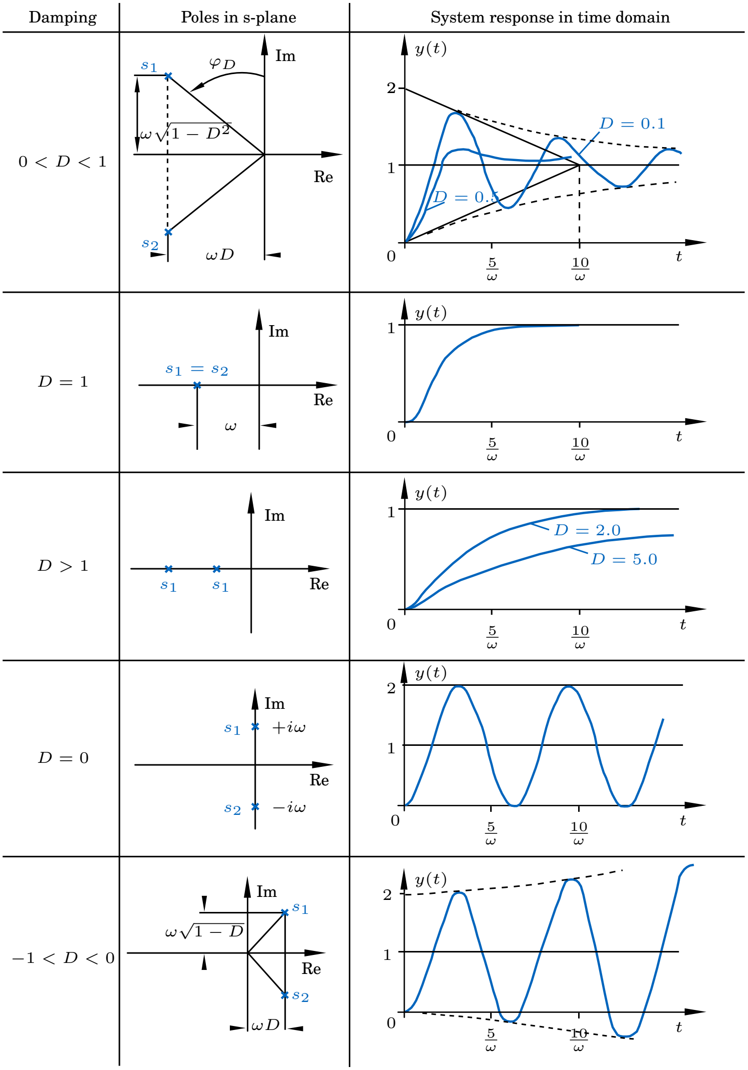

Figure D.4: System behavior in the s-plane and time domain, adapted from [97] p. 103.

poles are located in the negative real half-plane of the s-plane. Even if the system itself is stable, applying a closed-loop control to the system will shift the system poles. In the best case, the poles are shifted further into the negative real half-plane; in the worst case, they are shifted to the positive real half-plane making the system unstable. Several other additional techniques for stability assessment exist (e.g., the Nyquist criterion), which can be used for more detailed investigations, which are not necessary to be applied in this work. Therefore, the reader is referred to the literature. For most civil engineering structures, it is hardly possible to make the system unstable by applying a closed-loop control. The reason for this is that the necessary forces are, in most cases, too high to be applied by a suitable actuator. This is only likely to happen in combination with additional external forces (like wind) acting in an unfavorable way on the structure.

D.2 Modeling in the Time Domain

A physically equivalent representation of the system in the time domain is the state-space representation introduced in Section 2.3. Therefore Eq. (D.1) is rewritten with $u(t) = \hat{F}(t)$ as

$$\ddot{y}(t) = \frac{1}{m}(u(t) - c\dot{y} - ky), \tag{D.8}$$

which can be directly be depicted in block diagram notation as shown in Fig. D.5. The state variables can be defined as

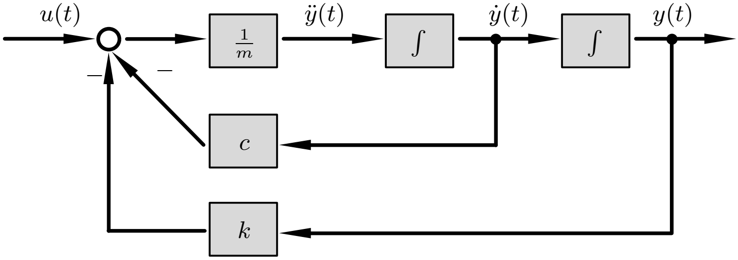

Figure D.5: Block diagram for the system in the time domain.

$$\begin{aligned} x_1(t) =& y(t) \text{ and} \\ x_2(t) =& \dot{y}(t). \end{aligned} \tag{D.9}$$

The state variables have a physical meaning. $x_1(t)$ describes the deformation and is thus a measure for the spring force, and $x_2(t)$ is a measure for the damper force. With the definitions of the state variables the system can be represented in state-space representation as

$$\begin{aligned} \dot{x}_1(t) =& x_2(t) \text{ and} \\ \dot{x}_2(t) =& -\frac{k}{m}x_1(t) - \frac{c}{m}x_2(t) + \frac{1}{m}u(t), \end{aligned} \tag{D.10}$$

which reads in matrix notation

$$\begin{aligned} \begin{bmatrix} \dot{x}_1 \\ \dot{x}_2 \end{bmatrix} &= \begin{bmatrix} 0 & 1 \\ -\frac{k}{m} & -\frac{c}{m} \end{bmatrix} \begin{bmatrix} x_1 \\ x_2 \end{bmatrix} + \begin{bmatrix} 0 \\ \frac{1}{m} \end{bmatrix} u(t), \\ \text{i.e.} \qquad \dot{\boldsymbol{x}} &= \boldsymbol{A}\boldsymbol{x} + \boldsymbol{B}u \end{aligned} \tag{D.11}$$

and the output equation

$$\begin{aligned} y(t) &= \begin{bmatrix} 1 & 0 \end{bmatrix} \begin{bmatrix} x_1 \\ x_2 \end{bmatrix}, \\ \text{i.e.} \qquad y &= \boldsymbol{C}\boldsymbol{x}. \end{aligned} \tag{D.12}$$

The tools from literature for controller design, stability considerations, and system analysis can be directly applied if the dynamic system is written in this notation. Here a SISO system is shown, but the principle can easily be applied to MIMO systems, which is according to [73] one of the advantages of the state-space representation.

Bibliography

[1] DIN EN 1991-1-4:2010-12, Eurocode 1: Einwirkungen auf Tragwerke - Teil 1-4: Allgemeine Einwirkungen - Windlasten; Deutsche Fassung EN 1991-1-4:2005 + A1:2010 + AC:2010.

[2] DIN EN 1991-1-4/NA:2010-12, Nationaler Anhang - National festgelegte Parameter - Eurocode 1: Einwirkungen auf Tragwerke - Teil 1-4: Allgemeine Einwirkungen - Windlasten.

[3] DIN EN 1992-1-1:2011-01, Eurocode 2: Bemessung und Konstruktion von Stahlbeton- und Spannbetontragwerken - Teil_1-1: Allgemeine Bemessungsregeln und Regeln für den Hochbau; Deutsche Fassung EN 1992-1-1:2004 + AC:2010.

[4] M. S. Andre. *Aeroelastic modeling and simulation for the assessment of wind effects on a parabolic trough solar collector*. Dissertation, Technische Universität München, 2018.

[5] M. S. Andre. https://github.com/msandre/windgen, 2020.

[6] S. Badia and R. Codina. Algebraic pressure segregation methods for the incompressible Navier-Stokes equations. *Archives of Computational Methods in Engineering*, 15(3):1–52, 2007.

[7] K.-J. Bathe. *Finite element procedures*. K.J.Bathe, United States, Watertown, MA, 2014.

[8] K.-J. Bathe and E. L. Wilson. Solution methods for eigenvalue problems in structural mechanics. *International Journal for Numerical Methods in Engineering*, 6(2):213–226, 1973.

[9] K.-J. Bathe and H. Zhang. Finite element developments for general fluid flows with structural interactions. *International Journal for Numerical Methods in Engineering*, 60(1):213–232, 2004.

[10] K.-J. Bathe, H. Zhang, and Y. Yan. The solution of Maxwell's equations in multiphysics. *Computers & Structures*, 132:99–112, 2014.

[11] T. Belytschko, W. K. Liu, B. Moran, and K. I. Elkhodary. *Nonlinear finite elements for continua and structures*. CourseSmart. John Wiley & Sons Inc, Hoboken, New Jersey, 2014.

[12] M. Bischoff. *Theorie und Numerik einer dreidimensionalen Schalenformulierung*. Dissertation, Universität Stuttgart, 1999.

[13] M. Bischoff, K.-U. Bletzinger, W. A. Wall, and E. Ramm. Models and Finite Elements for Thin-Walled Structures. In E. Stein, editor, *Encyclopedia of computational mechanics*, volume 172, page 79. Wiley, Chichester, 2004.

[14] K.-U. Bletzinger, M. Bischoff, and E. Ramm. A unified approach for shear-locking-free triangular and rectangular shell finite elements. *Computers & Structures*, 75(3):321–334, 2000.

[15] A. Bogaers, S. Kok, B. D. Reddy, and T. Franz. Quasi-Newton methods for implicit black-box FSI coupling. *Computer Methods in Applied Mechanics and Engineering*, 279:113–132, 2014.

[16] P. Bucher. *Development and Implementation of a Parallel Framework for Non-Matching Grid Mapping*. Master's thesis (unpublished), Technische Universität München, 2017.

[17] Bundesministerium für Verkehr, Bau und Stadtentwicklung. Richtlinie zur Nachrechung von Straßenbrücken im Bestand (Nachrechnungsrichtlinie), 2011.

[18] H.-J. Bungartz, F. Lindner, B. Gatzhammer, M. Mehl, K. Scheufele, A. Shukaev, and B. Uekermann. preCICE – A fully parallel library for multi-physics surface coupling. *Computers & Fluids*, 141:250–258, 2016.

[19] H.-J. Bungartz, F. Lindner, M. Mehl, and B. Uekermann. A plug-and-play coupling approach for parallel multi-field simulations. *Computational Mechanics*, 55(6):1119–1129, 2015.

[20] P. Causin, J. F. Gerbeau, and F. Nobile. Added-mass effect in the design of partitioned algorithms for fluid–structure problems. *Computer Methods in Applied Mechanics and Engineering*, 194(42-44):4506–4527, 2005.

[21] A. J. Chorin. Numerical Solution of the Navier-Stokes Equations. *Mathematics of Computation*, 22(104):745, 1968.

[22] A. J. Chorin. On the Convergence of Discrete Approximations to the Navier-Stokes Equations. *Mathematics of Computation*, 23(106):341, 1969.

[23] R. Codina. Pressure Stability in Fractional Step Finite Element Methods for Incompressible Flows. *Journal of Computational Physics*, 170(1):112–140, 2001.

[24] R. Codina. Stabilized finite element approximation of transient incompressible flows using orthogonal subscales. *Computer Methods in Applied Mechanics and Engineering*, 191(39-40):4295–4321, 2002.

[25] O. Colomés, S. Badia, R. Codina, and J. Principe. Assessment of variational multiscale models for the large eddy simulation of turbulent incompressible flows. *Computer Methods in Applied Mechanics and Engineering*, 285:32–63, 2015.

[26] J. Cotela Dalmau, E. Oñate, and R. Rossi. *Applications for turbulence modeling in civil engineering*. PhD. Thesis, UPC Barcelona, Barcelona, 2016.

[27] P. Dadvand, R. Rossi, and E. Oñate. An Object-oriented Environment for Developing Finite Element Codes for Multidisciplinary Applications. *Archives of Computational Methods in Engineering*, 17(3):253–297, 2010.

[28] A. de Boer, A. H. van Zuijlen, and H. Bijl. Comparison of conservative and consistent approaches for the coupling of non-matching meshes. *Computer Methods in Applied Mechanics and Engineering*, 197(49-50):4284–4297, 2008.

[29] J. Degroote, K.-J. Bathe, and J. Vierendeels. Performance of a new partitioned procedure versus a monolithic procedure in fluid–structure interaction. *Computers & Structures*, 87(11-12):793–801, 2009.

[30] W. G. Dettmer. *Finite Element Modelling of Fluid Flow with Moving Free Surfaces and Interfaces Including Fluid-Solid Interaction*. Dissertation, University of Wales Swansea, School of Engineering, 2004.

[31] W. G. Dettmer and D. Perić. A new staggered scheme for fluid-structure interaction. *International Journal for Numerical Methods in Engineering*, 93(1):1–22, 2013.

[32] Deutscher Wetterdienst DWD. Climate Data Center - CDC (https://cdc.dwd.de/), 2020.

[33] J. Donéa and A. Huerta. *Finite element methods for flow problems*. Wiley, Chichester and Hoboken, NJ, 2003.

[34] J. Donéa, A. Huerta, J.-P. Ponthot, and A. Rodriguez-Ferran. Arbitrary Lagrangian-Eulerian Methods. In E. Stein, editor, *Encyclopedia of computational mechanics*, volume 39, page 657. Wiley, Chichester, 2004.

[35] J. Donéa, A. Huerta, J.-P. Ponthot, and A. Rodríguez-Ferran. Arbitrary Lagrangian-Eulerian Methods. In

E. Stein, R. de Borst, and T. J. R. Hughes, editors, *Encyclopedia of Computational Mechanics Second Edition*, volume 64, pages 1–23. John Wiley & Sons, Ltd, Chichester, UK, 2017.

[36] C. A. Felippa and B. Haugen. A unified formulation of small-strain corotational finite elements: I. Theory. *Computer Methods in Applied Mechanics and Engineering*, 194(21-24):2285–2335, 2005.

[37] C. A. Felippa, K. C. Park, and C. Farhat. Partitioned Analysis of Coupled Mechanical Systems. *Computer Methods in Applied Mechanics and Engineering*, Special issue on Fluid-Structure Interaction(190):3247–3270, 2001.

[38] C. A. Felippa, K. C. Park, and M. R. Ross. A Classification of Interface Treatments for FSI. In H.-J. Bungartz, M. Mehl, and M. Schäfer, editors, *Fluid Structure Interaction II*, volume 73 of *Lecture Notes in Computational Science and Engineering*, pages 27–51. Springer Berlin Heidelberg, Berlin, Heidelberg, 2010.

[39] O. Föllinger. *Laplace-, Fourier- und z-Transformation*. VDE-Verl., Berlin Offenbach, 10. aufl. edition, 2011.

[40] O. Föllinger, U. Konigorski, B. Lohmann, G. Roppenecker, and A. Trächtler. *Regelungstechnik: Einführung in die Methoden und ihre Anwendung*. VDE-Verl., Berlin, 12., völlig neu bearb. aufl. edition, 2016.

[41] P. Gamnitzer, V. Gravemeier, and W. A. Wall. Time-dependent subgrid scales in residual-based large eddy simulation of turbulent channel flow. *Computer Methods in Applied Mechanics and Engineering*, 199(13-16):819–827, 2010.

[42] C. W. Gear. *Numerical initial value problems in ordinary differential equations*. Prentice-Hall series in automatic computation. Prentice-Hall, Englewood Cliffs, NJ, 2. print edition, 1971.

[43] W. Hamilton. *On quaternions, or on a new system of imaginaries in algebra*. Dublin, 2000.

[44] G. A. Holzapfel. *Nonlinear solid mechanics: A continuum approach for engineering*. Wiley, Chichester, repr edition, 2010.

[45] T. J. Hughes. Multiscale phenomena: Green's functions, the Dirichlet-to- Neumann formulation, subgrid scale Multiscale phenomena: Green's functions, the Dirichlet-to-Neumann formulation, subgrid scale models, bubbels and the origins of stabilized methods. *Computer Methods in Applied Mechanics and Engineering*, 127:387–401, 1995.

[46] T. J. Hughes, G. R. Feijóo, L. Mazzei, and J.-B. Quincy. The variational multiscale method—a paradigm for computational mechanics. *Computer Methods in Applied Mechanics and Engineering*, 166(1-2):3–24, 1998.

[47] M. M. Joosten, W. G. Dettmer, and D. Perić. Analysis of the block Gauss-Seidel solution procedure for a strongly coupled model problem with reference to fluid-structure interaction. *International Journal for Numerical Methods in Engineering*, 78(7):757–778, 2009.

[48] M. M. Joosten, W. G. Dettmer, and D. Perić. On the temporal stability and accuracy of coupled problems with reference to fluid-structure interaction. *International Journal for Numerical Methods in Fluids*, 64(10-12):1363–1378, 2010.

[49] J. C. Kaimal, J. C. Wyngaard, Y. Izumi, and O. R. Coté. Spectral characteristics of surface-layer turbulence. *Quarterly Journal of the Royal Meteorological Society*, 98(417):563–589, 1972.

[50] K.-T. Kim and K.-J. Bathe. The Bathe subspace iteration method enriched by turning vectors. *Computers & Structures*, 186:11–21, 2017.

[51] F. Koschnick. *Geometrische Locking-Effekte bei Finiten Elementen und ein allgemeines Konzept zu ihrer Vermeidung*. Dissertation, Technische Universität München, 2004.

[52] R. Kosfeld, H. F. Eckey, and M. Türck. *Deskriptive Statistik - Grundlagen - Methoden - Beispiele - Aufgaben*. Springer-Verlag, Berlin Heidelberg New York, 2016.

[53] KRATOS Multiphysics. https://github.com/kratosmultiphysics.

[54] S. Krenk. *Non-linear modeling and analysis of solids and structures*. Cambridge University Press, Cambridge, 2009.

[55] D. Kuhl. *Stabile Zeitintegrationsalgorithmen in der nichtlinearen Elastodynamik dünnwandiger Tragwerke*. Dissertation, Universität Stuttgart, 1996.

[56] A. Kupzok. *Modeling the Interaction of Wind and Membrane Structures by Numerical Simulation*. Dissertation, Technische Universität München, 2009.

[57] U. Küttler and W. A. Wall. Fixed-point fluid–structure interaction solvers with dynamic relaxation. *Computational Mechanics*, 43(1):61–72, 2008.

[58] C. Lerch. *Analysis of Gauss-Seidel Fixed-Point Formulations for an Iteratively Coupled Model Problem with Reference to Fluid-Structure-Control Interaction*. Honorous project (unpublished), Technische Universität München, 2016.

[59] C. Lerch. *Implementation and Assessment of Partitonend Schemes (Co-Simulation) for Closed-Loop Structural Control in Computational Fluid-Structure Interaction*. Master's thesis (unpublished), Technische Universität München, 2016.

[60] J. Lunze. *Regelungstechnik 2: Mehrgrößensysteme, digitale Regelung*. Springer-Lehrbuch. Springer, Berlin, 6., neu bearbeitete aufl. edition, 2010.

[61] J. Lunze. *Regelungstechnik 1: Systemtheoretische Grundlagen, Analyse und Entwurf einschleifiger Regelungen : mit 425 Abbildungen, 76 Beispielen, 179 Übungsaufgaben sowie einer Einführung in das Programmsystem MATLAB*. Lehrbuch. Springer, Berlin, 11., überarbeitete und ergänzte auflage edition, 2016.

[62] M. Lyly, R. Stenberg, and T. Vihinen. A stable bilinear element for the Reissner-Mindlin plate model. *Computer Methods in Applied Mechanics and Engineering*, 110(3-4):343–357, 1993.

[63] L. E. Malvern. *Introduction to the mechanics of a continuous medium*. EPS, Prentice-Hall series in engineering of the physical sciences. Prentice-Hall, Englewood Cliffs, NJ, [nachdr.] edition, 1969.

[64] J. Mann. The spatial structure of neutral atmospheric surface-layer turbulence. *Journal of Fluid Mechanics*, 273:141–168, 1994.

[65] J. Mann. Wind field simulation. *Probabilistic Engineering Mechanics*, 13(4):269–282, 1998.

[66] J. E. Marsden and T. J. R. Hughes. *Mathematical Foundations of Elasticity*. Dover Civil and Mechanical Engineering. Dover Publications, Newburyport, 2012.

[67] U. M. Mayer, A. Popp, A. Gerstenberger, and W. A. Wall. 3D fluid–structure-contact interaction based on a combined XFEM FSI and dual mortar contact approach. *Computational Mechanics*, 46(1):53–67, 2010.

[68] C. Meinhardt. *Applikation eines hybriden Tilgersystems für ein 246 m hohes Gebäude: 6. VDI-Fachtagung : Würzburg, 17. und 18. April 2018*, volume 2321 of *VDI-Berichte*. VDI-Verlag GmbH, Düsseldorf, 2018.

[69] meteoblue AG. www.meteoblue.com, 2020.

[70] A. Michalski. *Simulation leichter Flächentragwerke in einer numerisch generierten atmosphärischen Grenzschicht*. Dissertation, Technische Universität München, 2010.

[71] A. Mini. *Implementation and evaluation of mesh-updating strategies for computational fluid-struture interaction*. Master's Thesis (unpublished), Technische Universität München, München, 2014.

[72] A. Mini, C. Lerch, R. Wüchner, and K.-U. Bletzinger. Computational Closed-Loop Control of Fluid-structure Interaction (FSCI) for Lightweight Structures. *PAMM*, 16(1):15–18, 2016.

[73] R. Nordmann. *Mechatronische Systeme im Maschinenbau*. Vorlesungen Mechatronik & Maschinenakustik. Shaker, Aachen, 2001.

[74] K. Nozawa and T. Tamura. Numerical prediction of pressure on a high-rise building immersed in a turbulent boundary layer using les. *Summaries to Technical Papers of Annual Meeting, Japan Association for Wind Engineering*, 2003:84–84, 2003.

[75] H. Panggabean. Schwingungsverhalten von Turmartigen Tragwerken unter aerodynamischer Belastung. In F. H. Wittmann and G. I. Schueller, editors, *Beiträge zur Anwendung der Aeroelastik im Bauwesen*, volume 10. München, 1975 - 1984.

[76] M. Péntek, A. Winterstein, M. Vogl, P. Kupás, K.-U. Bletzinger, and R. Wüchner. A multiply-partitioned methodology for fully-coupled computational wind-structure interaction simulation considering the inclusion of arbitrary added mass dampers. *Journal of Wind Engineering and Industrial Aerodynamics*, 177:117–135, 2018.

[77] C. Petersen. Schwingungen turmartiger Bauwerke im böigen Wind unter Berücksichtigung der vertikalen Phasenkorrelation am Beispiel des Müncher Fernsehturms. In F. H. Wittmann and G. I. Schueller, editors, *Beiträge zur Anwendung der Aeroelastik im Bauwesen*, volume 7. München, 1975 - 1984.

[78] C. Petersen. *Dynamik der Baukonstruktionen*. Vieweg, Braunschweig, korrigierter nachdruck edition, 2000.

[79] A. Preumont. *Vibration Control of Active Structures - An Introduction*. Springer Science and Business Media, Berlin Heidelberg, 2011.

[80] J. Principe, R. Codina, and F. Henke. The dissipative structure of variational multiscale methods for incompressible flows. *Computer Methods in Applied Mechanics and Engineering*, 199(13-16):791–801, 2010.

[81] A. Rasheed, O. San, and T. Kvamsdal. Digital Twin: Values, Challenges and Enablers From a Modeling Perspective. *IEEE Access*, 8:21980–22012, 2020.

[82] J. W. S. Rayleigh. *The Theory of Sound Volume 2*. Cambridge University Press, 1878.

[83] H. Ruscheweyh. *Beitrag zur Windbelastung hoher kreiszylinderähnlicher schlanker Bauwerke im natürlichen Wind bei Reynoldszahlen bis Re=1,4x10e7*. Dissertation, RWTH Aachen, 1974.

[84] K. B. Sautter. *Dynamic simulation of rock-fall protection nets: Implementation and validation of large deformation finite elements in an open-source code*. Master's thesis (unpublished), Technische Universität München, 2017.

[85] F. X. Schneider. Wind- und Betonspannugsmessungen am Olympiaturm München. In F. H. Wittmann and G. I. Schueller, editors, *Beiträge zur Anwendung der Aeroelastik im Bauwesen*, volume 1. München, 1975 - 1984.

[86] F. X. Schneider, F. H. Wittmann, and H. Panggabean. Zusammenstellung der im Verlauf mehrerer Jahre am Münchner Fernsehturm durchgeführten Wind- und Schwingungsmessungen. In F. H. Wittmann and G. I. Schueller, editors, *Beiträge zur Anwendung der Aeroelastik im Bauwesen*, volume 4. München, 1975 - 1984.

[87] S. Sicklinger, V. Belsky, B. Engelmann, H. Elmqvist, H. Olsson, R. Wüchner, and K.-U. Bletzinger. Interface Jacobian-based Co-Simulation. *International Journal for Numerical Methods in Engineering*, 98(6):418–444, 2014.

[88] H. Sockel. *Aerodynamik der Bauwerke*. Vieweg+Teubner Verlag, Wiesbaden, 1984.

[89] K. Stein, T. Tezduyar, and R. Benney. Mesh Moving Techniques for Fluid-Structure Interactions With Large Displacements. *Computer Methods in Applied Mechanics and Engineering*, 70(1):58, 2003.

[90] G. Strang. *Computational science and engineering*. Wellesley-Cambridge Press, Wellesley, Mass., 2. print edition, 2012.

[91] Y. Tamura and A. Kareem. *Advanced Structural Wind Engineering -*. Springer Science and Business Media, Berlin Heidelberg, 2013.

[92] R. Temam. *Navier–Stokes Equations: Theory and Numerical Analysis*, volume v.343 of *AMS Chelsea Publishing*. American Mathematical Society, Providence, 2001.

[93] P. D. Thomas and C. K. Lombard. Geometric Conservation Law and Its Application to Flow Computations on Moving Grids. *AIAA Journal*, 17(10):1030–1037, 1979.

[94] S. Turek and J. Hron. Proposal for Numerical Benchmarking of Fluid-Structure Interaction between an Elastic Object and Laminar Incompressible Flow. In H.-J. Bungartz and M. Schäfer, editors, *Fluid-Structure Interaction*, volume 53 of *Lecture Notes in Computational Science and Engineering*, pages 371–385. Springer-Verlag GmbH, Berlin Heidelberg, 2006.

[95] B. Uekermann. *Partitioned Fluid-Structure Interaction on Massively Parallel Systems*. Dissertation, Technische Universität München, 2016.

[96] H. Unbehauen. *Regelungstechnik II: Zustandsregelungen, digitale und nichtlineare Regelsysteme*. Studium Technik. Vieweg+Teubner Verlag, Wiesbaden, 8., vollständig überarbeitete und erweiterte auflage edition, 2000.

[97] H. Unbehauen. *Regelungstechnik I: Klassische Verfahren zur Analyse und Synthese linearer kontinuierlicher Regelsysteme, Fuzzy-Regelsysteme*. Vieweg+Teubner Verlag / GWV Fachverlage GmbH Wiesbaden, Wiesbaden, 15., überarbeitete und erweiterte auflage edition, 2008.

[98] E. H. van Brummelen. Added Mass Effects of Compressible and Incompressible Flows in Fluid-Structure Interaction. *Computer Methods in Applied Mechanics and Engineering*, 76(2):021206, 2009.

[99] I. van der Hoven. Power Spectrum of Horizontal Wind Speed in the Frequency Range from 0.0007 to 900 Cycles per Hour. *Journal of Meteorology*, 14(2):160–164, 1957.

[100] W. A. Wall. *Fluid-Struktur-Interaktion mit stabilisierten Finiten Elementen*. Dissertation, Universität Stuttgart, 1999.

[101] W. A. Wall, editor. *Trends in computational structural mechanics: Papers presented at the International Conference Trends in Computational Structural Mechanics, held May 20 - 23, 2001 at Schloss Hofen, Lake Constance*. CIMNE, Barcelona, Spain, 1. ed. edition, 2001.

[102] T. Wang. *Development of Co-Simulation Environment and Mapping Algorithms*. Dissertation, Technische Universität München, 2015.

[103] P. Wilson. *Advanced Shell Finite Elements: Formulation, Implementation, Validation and Structural Modelling*. Master's thesis (unpublished), Technische Universität München, 2017.

[104] A. Winterstein, C. Lerch, K.-U. Bletzinger, and R. Wüchner. Partitioned simulation strategies for fluid–structure–control interaction problems by Gauss–Seidel formulations. *Advanced Modeling and Simulation in Engineering Sciences*, 5(1):3247, 2018.

[105] A. Winterstein, M. Péntek, K.-U. Bletzinger, and R. Wüchner. Gekoppelte numerische Simulation zur Bewertung von Reduktionsmassnahmen bei windinduzierten Schwingungen. In Windtechnologische Gesellschaft (WTG) e.V., editor, *Aufbruch zu neuen Methoden im Windingenieurwesen*, number 16. Windtechnologische Gesellschaft (WTG) e.V., 2019.

[106] F. H. Wittmann and G. I. Schueller, editors. *Beiträge zur Anwendung der Aeroelastik im Bauwesen*. München, 1975 - 1984.

[107] R. Wüchner. *Mechanik und Numerik der Formfindung und Fluid-Struktur-Interaktion von Membrantragwerken*. Dissertation, Technische Universität München, 2006.

[108] R. Wüchner. *Computational Wind-Structure Interaction - Modeling, Simulation and Validation*. Habilitation, Technische Universität München, 2017.

[109] O. C. Zienkiewicz, R. L. Taylor, and J. Zhu. *The finite element method*. Elsevier Butterworth-Heinemann, Amsterdam, 6. ed., repr edition, 2010.

Bisherige Titel der Schriftenreihe

Band	Titel
1	Frank Koschnick, *Geometrische Lockingeffekte bei Finiten Elementen und ein allgemeines Konzept zu ihrer Vermeidung*, 2004.
2	Natalia Camprubi, *Design and Analysis in Shape Optimization of Shells*, 2004.
3	Bernhard Thomée, *Physikalisch nichtlineare Berechnung von Stahlfaserbetonkonstruktionen*, 2005.
4	Fernaß Daoud, *Formoptimierung von Freiformschalen - Mathematische Algorithmen und Filtertechniken*, 2005.
5	Manfred Bischoff, *Models and Finite Elements for Thin-walled Structures*, 2005.
6	Alexander Hörmann, *Ermittlung optimierter Stabwerkmodelle auf Basis des Kraftflusses als Anwendung plattformunabhängiger Prozesskopplung*, 2006.
7	Roland Wüchner, *Mechanik und Numerik der Formfindung und Fluid-Struktur-Interaktion von Membrantragwerken*, 2006.
8	Florian Jurecka, *Robust Design Optimization Based on Metamodeling Techniques*, 2007.
9	Johannes Linhard, *Numerisch-mechanische Betrachtung des Entwurfsprozesses von Membrantragwerken*, 2009.
10	Alexander Kupzok, *Modeling the Interaction of Wind and Membrane Structures by Numerical Simulation*, 2009.
11	Bin Yang, *Modified Particle Swarm Optimizers and their Application to Robust Design and Structural Optimization*, 2009.

Band	**Titel**
12	Michael Fleischer, *Absicherung der virtuellen Prozesskette für Folgeoperationen in der Umformtechnik*, 2009.
13	Amphon Jrusjrungkiat, *Nonlinear Analysis of Pneumatic Membranes - From Subgrid to Interface*, 2009.
14	Alexander Michalski, *Simulation leichter Flächentragwerke in einer numerisch generierten atmosphärischen Grenzschicht*, 2010.
15	Matthias Firl, *Optimal Shape Design of Shell Structures*, 2010.
16	Thomas Gallinger, *Effiziente Algorithmen zur partitionierten Lösung stark gekoppelter Probleme der Fluid-Struktur-Wechselwirkung*, 2011.
17	Josef Kiendl, *Isogeometric Analysis and Shape Optimal Design of Shell Structures*, 2011.
18	Joseph Jordan, *Effiziente Simulation großer Mauerwerksstrukturen mit diskreten Rissmodellen*, 2011.
19	Albrecht von Boetticher, *Flexible Hangmurenbarrieren: Eine numerische Modellierung des Tragwerks, der Hangmure und der Fluid-Struktur-Interaktion*, 2012.
20	Robert Schmidt, *Trimming, Mapping, and Optimization in Isogeometric Analysis of Shell Structures*, 2013.
21	Michael Fischer, *Finite Element Based Simulation, Design and Control of Piezoelectric and Lightweight Smart Structures*, 2013.
22	Falko Hartmut Dieringer, *Numerical Methods for the Design and Analysis for Tensile Structures*, 2014.
23	Rupert Fisch, *Code Verification of Partitioned FSI Environments for Lightweight Structures*, 2014.
24	Stefan Sicklinger, *Stabilized Co-Simulation of Coupled Problems Including Fields and Signals*, 2014.

Band	Titel
25	Majid Hojjat, *Node-based parametrization for shape optimal design*, 2015.
26	Ute Israel, *Optimierung in der Fluid-Struktur-Interaktion - Sensitivitätsanalyse für die Formoptimierung auf Grundlage des partitionierten Verfahrens*, 2015.
27	Electra Stavropoulou, *Sensitivity analysis and regularization for shape optimization of coupled problems*, 2015.
28	Daniel Markus, *Numerical and Experimental Modeling for Shape Optimization of Offshore Structures*, 2015.
29	Pablo Suárez, *Design Process for the Shape Optimization of Pressurized Bulkheads as Components of Aircraft Structures*, 2015.
30	Armin Widhammer, *Variation of Reference Strategy - Generation of Optimized Cutting Patterns for Textile Fabrics*, 2015.
31	Helmut Masching, *Parameter Free Optimization of Shape Adaptive Shell Structures*, 2016.
32	Hao Zhang, *A General Approach for Solving Inverse Problems in Geophysical Systems by Applying Finite Element Method and Metamodel Techniques*, 2016.
33	Tianyang Wang, *Development of Co-Simulation Environment and Mapping Algorithms*, 2016.
34	Michael Breitenberger, *CAD-integrated Design and Analysis of Shell Structures*, 2016.
35	Önay Can, *Functional Adaptation with Hyperkinematics using Natural Element Method: Application for Articular Cartilage*, 2016.
36	Benedikt Philipp, *Methodological Treatment of Non-linear Structural Behavior in the Design, Analysis and Verification of Lightweight Structures*, 2017.
37	Michael Andre, *Aeroelastic Modeling and Simulation for the Assessment of Wind Effects on a Parabolic Trough Solar Collector*, 2018.

Band	Titel
38	Andreas Apostolatos, *Isogeometric Analysis of Thin-Walled Structures on Multipatch Surfaces in Fluid-Structure Interaction*, 2018.
39	Altuğ Emiroğlu, *Multiphysics Simulation and CAD-Integrated Shape Optimization in Fluid-Structure Interaction*, 2019.
40	Mehran Saeedi, *Multi-Fidelity Aeroelastic Analysis of Flexible Membrane Wind Turbine Blades*, 2017.
41	Reza Najian Asl, *Shape Optimization and Sensitivity Analysis of Fluids, Structures, and their Interaction Using Vertex Morphing Parametrization*, 2019.
42	Ahmed Abodonya, *Verification Methodology for Computational Wind Engineering Prediction of Wind Loads on Structures*, 2020.
43	Anna Maria Bauer, *CAD-Integrated Isogeometric Analysis and Design of Lightweight Structures*, 2020.